Study and realization of an UWB microwave radar based on phase conjugation

Lucio Bellomo

UNIVERSITÉ DU SUD TOULON VAR

École Doctorale Sciences Fondamentales et Appliquées (364)

Institut Méditerranéen d'Océanologie (MIO)

Thèse présentée par :

Lucio Bellomo

soutenue le : **16 février 2012**

pour obtenir le grade de Docteur en Électronique
Spécialité : Télécommunications et Télédétection

Étude et réalisation d'un RADAR ULB à conjugaison de phase en micro-ondes

Thèse dirigée par :

M. SAILLARD Marc	Professeur, MIO
M. PIOCH Sébastien	Maître de Conférence, MIO

Jury :

M. DAUVIGNAC Jean-Yves	Rapporteur	Professeur, LEAT
M. DUCHÊNE Bernard	Rapporteur	Chargé de Recherche au CNRS, L2S
M. BELKEBIR Kamal	Examinateur	Maître de Conférence, Institut Fresnel
M. MASSA Andrea	Examinateur	Professeur, Università di Trento
M. DE ROSNY Julien	Examinateur	Chargé de Recherche au CNRS, Institut Langevin
M. SAILLARD Marc	Examinateur	Professeur, MIO
M. BARBARESCO Frédéric	Membre invité	Thales Air Systems

UNIVERSITÉ DU SUD TOULON VAR

PhD dissertation

Lucio Bellomo

Mediterranean Institute of Oceanography (MIO)

Study and Realization of an UWB Microwave RADAR based on Phase Conjugation

---

Thesis advisor: **Marc Saillard**

Thesis co-advisor: **Sébastien Pioch**

Thesis committee

Jean-Yves Dauvignac	*Reviewer*
Bernard Duchêne	*Reviewer*
Kamal Belkebir	*Member*
Andrea Massa	*Member*
Julien de Rosny	*Member*
Marc Saillard	*Member*
Frédéric Barbaresco	*Invited Member*

Defended on february 16th 2012 at USTV

Si sta come
d'autunno
sugli alberi
le foglie
(Giuseppe Ungaretti - Soldati)

Remerciements

Si le choix de la langue anglaise pour ce manuscrit est motivé par l'espoir, peut-être vain, qu'un public plus vaste puisse y accéder, lorsque je pense aux remerciements c'est le français qui tout naturellement s'impose. Ce travail n'aurait pas existé sans l'opportunité que la recherche publique en France m'a offerte. En ce sens, mon malheureux pays, l'Italie, aurait beaucoup à apprendre.

C'est en effet très simplement que ma relation avec le LSEET (désormais intégré dans le MIO), le laboratoire d'accueil de la thèse, s'est mise en place. Attiré par les thématiques de recherche affichées sur le site internet, je n'avais contacté le directeur, M. Philippe Fraunié, qu'avec un très faible espoir d'être reçu. Et pourtant, je suis ici aujourd'hui pour le remercier de l'ouverture d'esprit dont il a fait preuve en me rencontrant ce jour-là.

M. Marc Saillard a rapidement pris la relève par affinité de profil scientifique. Pratiquement sans me connaître, il a lui aussi misé sur moi, et ce, même après une première tentative de financement échouée. Marc, on se rend très vite compte d'avoir affaire à un homme hors du commun. J'avais ressenti cela dès la première rencontre. Et en effet j'ai découvert une personne douée d'une intelligence parfois déstabilisante, d'une volonté étourdissante, d'une passion entraînante. Au fur et à mesure que je me liais émotivement à l'Université du Sud Toulon-Var et à la terre du Var, j'ai été sincèrement ravi, et même un peu fier, que Marc se soit engagé politiquement pour leur essor. Je considère le simple fait d'avoir travaillé, ou bien d'avoir réussi à travailler, avec lui, comme une véritable réussite. Je le remercie de tout cœur, au delà de toute formalité, pour tout ce qu'il a voulu partager avec moi. Ses enseignements, académiques et non, sont inoubliables pour moi.

Suit, ne serait-ce qu'en ordre chronologique, M. Sébastien Pioch, co-encadrant de ces travaux. Séb "Il Professore". Je n'ai jamais connu quelqu'un de pareil : sans doute il appartient à une autre époque. J'ai découvert un oxymore vivant, un garçon solide comme une falaise mais tendre dans l'âme, un travailleur rigoureux aux éclats déjantés, un esprit inébranlable cependant extrêmement sensible. Séb a été pour moi un vrai guide, certes dans le sens purement scientifique, mais aussi sur le plan "bricolage" (combien de vis à visser, de soudure ratées, d'aller-retour chez Leroy Merlin ...?) et surtout sur celui humain. Sa chaleur, parfois peut-être exagérée, a veillé sur mes fatigues de doctorant. Et d'ami.

Je tiens à remercier également M. Eric Spano, vrai concepteur de l'électronique du prototype RADAR. L'accueil enthousiaste qu'il m'a réservé reste parmi les beaux moments de la thèse.

Ma reconnaissance va aux membres du jury. Je suis honoré qu'ils aient accepté cette tâche. D'abord les rapporteurs, M. Jean-Yves Dauvignac et M. Bernard Duchêne : j'espère que la qualité de mon travail va pouvoir recompenser leur effort. M. Andrea Massa et M. Julien de Rosny, que j'ai eu la chance d'écouter lors de conférences et rencontres diverses. Et un merci particulier à M. Kamal Belkebir, qui m'a offert une disponibilité inégalable en m'ouvrant les portes, entre autres, du merveilleux monde de la diffraction inverse.

La DGA, mécène scientifique, et le CNRS qui ont financé la thèse ; ainsi que Thales, représenté par M. Frédéric Barbaresco et co-financeur du projet, trouvent tout à fait leur place parmi ces remerciements. J'ai pu, grâce à leur soutien, me procurer le matériel électronique nécessaire et présenter mes travaux lors de plusieurs congrès internationaux, ce que j'ai particulièrement apprécié.

Viennent maintenant mes collègues du LSEET que j'ai cotoyés durant ces années. Toutefois, si leurs noms figurent ici, ce n'est pas par la bête application d'une règle. C'est parce qu'ils ont donné de la couleur à l'espace et au temps. Didier et Stephane, pour la force, presque violence, avec laquelle on a imaginé un monde différent ensemble, la mer comme cadre, tout autour. Fabienne, au-delà du rôle administratif, pour les "gueulantes" et parfois même les disputes, toujours à bout de nerfs comme on l'aime. Joël pour les blagues et Yves pour les conseils précieux, souvent hors du temps réglementaire. Et Anne, pour la foi aveugle, sans doute insensée, qu'elle a eu en moi. Par elle j'exauce un de ces rêves d'enfant qu'avec le temps on n'ose plus s'avouer.

Je songe aussi à Francine et Yann, qui il y a longtemps m'ont réappris à croire en moi-m̂eme et à exiger de la vie autant de bonheur que possible. Le hasard de les avoir rencontrés est peut-être le plus ancien parmi ceux qui ont contribué à ce que j'écrive ces mots, aujourd'hui.

Enfin, je m'adresse à ma famille. Merci pour la discrétion que vous avez sue garder malgré vous, pleine de patience envers moi qui en mérite si peu. Merci de m'avoir appris l'indépendance, en même temps que le respect. Ma soeur, mon papà et ma mamma. Et puis, Sophie, sans qui j'aurais quitté depuis longtemps cet effort, ainsi que bien d'autres ...

Table of Contents

Introduction

The development of the classical theory of electromagnetism at the end of the 19^{th} century by, among others, James C. Maxwell, Heinrich R. Hertz and Oliver Heaviside has marked a turning point in the history of mankind. So, the availability of a physical model describing the propagation of electromagnetic waves and their interaction with matter has paved the way to applications that have positively changed the daily life of billions of people. Wired and wireless telecommunications, medical imaging and healing techniques, radio and television, G.P.S.: these are but a few of them.

Although usually not addressed to such a wide public, a number of striking applications is founded on the following observation: in presence of an obstacle, the characteristics of a propagating electromagnetic wave are altered (*e.g.* its wavefront shape is modified). Since the nature of this alteration depends on the properties of the obstacle, it can in principle be possible to retrieve at least some of them from the observation of the "modified" wave. The definition of the so-called *inverse problem* can then be drawn: the characterization of one or more *scatterers* (the obstacles) from the knowledge of the *total field* (the "modified" wave) generated by the interaction of the *incident field* (the illuminating wave) with the scatterers. In case both the total and the incident field can be measured, their difference, called the *scattered field*, constitutes the data to be inversed. Non-destructive testing of building materials, again medical imaging, geophysical prospection, anti-personal landmine detection, and to some extent also RADAR are examples of such applications.

As it is formulated, the inverse problem is a non-linear and ill-posed problem: there is no guarantee that a solution exists, is unique, and is continuous when noise affects the data [1]. Two different approaches arise then to tackle the problem. When only the detection and localization of the scatterers is of interest, a *qualitative* inversion is carried out. In a way, the sought quantity is now the distribution of the induced currents over the support of the scatterer, and it can be shown that their relation with the data is linear. On the other hand, when a *quantitative* characterization is needed (shape, composition), more complicated mathematical tools are deployed to transform the problem into a well-posed one. Yet, the non-linear character remains and the existence of multiple local solutions may lead to untrustworthy results.

Among the qualitative approaches, the potentialities of Time Reversal techniques have been clear since the first reports at the end of the '80s [2]. These methods, based on the time reversal invariance of the propagation equation, allow in effect to build waves selectively

focusing onto different scatterers by a simple and "blind" manipulation of the data. An effective detector is thus built by observing the distribution of the backpropagated field over space. Namely, the DORT method [3] as well as the re-interpretation of the MUSIC algorithm in the frame of deterministic scattering [4, 5], have led to impressive results especially in cluttered and multi-target scenarii.

Concerning quantitative inverse scattering, gradient-based methods have proven to be effective in retrieving the properties of the scatterers. Maxwell's equations are here directly used to measure the misfit, in the sense of a given norm, between the scattered field data and an estimation obtained from a guessed profile of the scatterer. This misfit is then minimized through a conjugate gradient algorithm interpreted in a variety of ways [6–8]. Nonetheless, due to the ill-posedness of the initial problem, these methods are extremely sensitive to noise and clutter, and give meaningful results only when the amount of information contained in the data is sufficiently large with respect to the parameters to be reconstructed. Taking into account, within the inversion process, any a priori known information about the scatterer (shape, minimum allowable permittivity value, etc.) helps then in regularizing the problem, increasing the confidence level of the results.

This work aims at giving an experimental proof of the effectiveness of the aforementioned techniques under realistic operational conditions. The data are gathered through a prototype made of a small linear array of linearly-polarized ultrawideband antennas of the exponentially tapered slot type (ETSA), whose realization covers by itself an important portion of the PhD duration. The accent is put on the experimental behavior of these methods when only a small aperture angle is available. Subsurface sensing and, in general, applications where only a partial access to the sounded medium is possible are therefore targeted. To somehow counteract such limitations, a large frequency band (from 2 to 4 GHz) is used. This is also motivated by the overwhelming progress in nanoelectronics and by the innovative antenna design solutions making such bandwidths easily available in modern systems. Concerning in particular quantitative inverse problems, only few attempts to experimentally image extended targets with small arrays and/or with non-standard antennas (i.e. horn or wire antennas) have yet been reported in literature [9–11]. Hence the originality of the thesis.

Furthermore, an attempt is made to build a bridge between qualitative and quantitative inversion methods. In case of cluttered media, namely, the latter are known to be poorly effective due to the small Signal-to-Clutter Ratio of the scattered field. Using the incident field issued from the DORT method, which focuses onto the targets of interest, might then be a good solution to increase the robustness of the inversion algorithms. A quantitative inverse scheme replacing the "raw" incident and scattered fields with the respective DORT fields is thus proposed.

The manuscript is articulated as follows. The first chapter is dedicated to the description of the prototype that will be operated throughout the manuscript. The hardware architec-

ture comprises two antenna arrays, one of which is equipped with a beamforming network. It is therefore possible to perform complete Time Reversal experiments, as shown in the second chapter. The signal processing steps necessary to exploit the system and to improve its performances are also presented. They include the antenna modeling strategy and a drift correction algorithm aimed at compensating mainly the thermal drift affecting the data during their acquisition.

The exploitation begins with the following chapter, focused on qualitative inversion. Particular attention is cast into the theoretical background of the DORT method, validated through a number of experimental setups. The performances are systematically compared with those obtained through the classical Kirchhoff migration method, and with the results of another Time Reversal-based method known as Time Reversal-MUSIC. Different ways of exploiting frequency diversity, as well as different geometric configurations, are also investigated. In addition, the experimental results from a measurement campaign targeting Through-The-Wall imaging are shown.

The quantitative inversion framework is presented in the third chapter. An effort is first made to understand the origin of the ill-posedness of the inverse problem from a theoretical point of view. Follows an explanation of the concept of available information associated to the data, extremely important in applications with small arrays and a limited number of views. Then, the selected inversion algorithm, the so-called Modified^2 Gradient Algorithm introduced by Belkebir and Tijhuis in [12], is detailed. In order to apply it to the experimental data, the adaptation to the 2.5D configuration, including an accurate calibration step, must be performed. Finally, for a number of configurations and targets, the experimental inversion results are presented.

In the last chapter, the DORT concept is applied to the quantitative inversion frame, thus somehow merging the benefits of the methods developed in the two previous chapters. The inversion scheme modified accordingly is tested on a linear array configuration where the target of interest is embedded in a cluttered medium. The same applications are targeted, namely medical imaging or subsurface sensing. Synthetic data-only are used to inquire on the effectiveness of the approach.

Publications

A number of publications witnesses the work carried out during these three years. Their list follows:

Book chapters

- L. Bellomo, M. Saillard, S. Pioch, F. Barbaresco, and M. Lesturgie, "Waveform design based on Phase Conjugation and Time Reversal", in *Waveform Design and Diversity for Advanced RADAR Systems*, IET, 2012, to be published

Journal articles

- L. Bellomo, S. Pioch, M. Saillard, and E. Spano, "Time Reversal Experiments in the Microwave Range: Description of the RADAR and results", *Progress In Electromagnetic Research*, vol. 104, 427-448, 2010

Invited conferences

- L. Bellomo, K. Belkebir, M. Saillard, S. Pioch, and P. Chaumet, "Inverse Scattering Using a Time Reversal RADAR", 2010 URSI International Symposium on Electromagnetic Theory (EMTS), 381-384, Berlin, 2010
- K. Belkebir, L. Bellomo, S. Pioch, M. Saillard, and P. Chaumet, "Microwave imaging using a time-reversal radar system", 2009 International Conference on Electromagnetics in Advanced Applications (ICEAA), Torino, 2009

Conference proceedings

- R. Dubroca, N. Fortino, J-Y. Dauvignac, L. Bellomo, S. Pioch, M. Saillard, T. Lepetit, J. de Rosny, C. Prada, P.Millot, N.Maaref, and B.Boudamouz, "Time Reversal-Based Processing for Human Targets Detection in Realistic Through-The-Wall Scenarios", 2011 European Microwave Week (EuMW-EuRAD), Manchester, 2011
- L. Bellomo, M. Saillard, S. Pioch, K. Belkebir, and P. Chaumet, "Microwave imaging in cluttered media with an Ultrawideband Time Reversal-based prototype", 2011 Symposium on Progress in Electromagnetic Research (PIERS), Marrakech, 2011
- L. Bellomo, S. Pioch, M. Saillard, and E. Spano, "An S-band Ultrawideband Time Reversal-based RADAR for Imaging in Cluttered Media", 2010 IEEE International Symposium on Phased Array Systems and Technology, Boston, 2010
- L. Bellomo, S. Pioch, M. Saillard, and E. Spano, "Microwave-range Imagery with an Ultrawideband Time Reversal-based RADAR", 2010 European Microwave Week (EuMW-EuRAD), Paris, 2010
- L. Bellomo, M. Saillard, S. Pioch, K. Belkebir, and P. Chaumet, "An Ultrawideband Time Reversal-based RADAR for Microwave-range Imaging in Cluttered Media", 13$^{\text{th}}$ International Conference on Ground Penetrating Radar (GPR), Lecce, 2010

Notation

i	imaginary unit
$e^{+i\omega t}$	time dependency convention
$\vec{r}$	vector notation
$\mathbf{v}$	one-dimensional array (vector) notation
$\mathbf{V}$	two or more-dimensional array notation
$\mathbf{1}_k$	vector with all zeros except 1 in the k^{th} position
$\text{sinc}(x)$	$\sin(x)/x$
$\|\cdot\|$	Euclidean norm (norm-2), if not indicated with an index
(I)FT, (I)FFT	(Inverse) Fourier Transform, (Inverse) Fast Fourier Transform
$(\cdot)^*$	conjugate operator
$(\cdot)^T$	transpose operator
$(\cdot)^H$	conjugate transpose operator

Chapter 1

Microwave imaging prototype

Building a Time Reversal-based RADAR was an already kicked-off project at LSEET when the PhD started [13]. Although some remarkable results existed in acoustics [14–16] and the foundations of a theoretical frame had been established in electromagnetics [17–23], only a few experiments had been reported in the latter domain [24–30]. Joining my PhD supervisor's *savoir-faire* [6, 7, 31] to this background had led to the idea of exploiting Time Reversal for improving the quantitative reconstruction of objects located in cluttered or random media [32].

All this had converged to the choice of building a microwave prototype with the following characteristics:

1. linear antenna array with transmit/receive capability;

2. ultrawideband working frequency range;

3. easeness of acquisition of multi-view multi-static data;

4. possibility of experimentally retransmit the waveforms issued from Time Reversal-based methods.

The linear array choice follows directly from the established LSEET's expertise in current-measuring RADAR's [33, 34] also working with linear arrays; more particularly, it targets buried objects and *ground penetrating RADAR* applications [35]. From the inverse scattering point of view, the ultrawideband is required as a countermeasure to the limited aperture of a small linear array in order not to limit too much the accessible portion of the spectral support of the electromagnetic contrast (cfr. §3.4). Specification 3. arises from the will of studying subspace methods such as DORT [3, 20], Time Reversal-MUSIC [5, 36], or Linear Sampling Method [37–39] which all need the knowledge of the multi-static data matrix of the array. The latter requirement is finally interesting in order to be able to observe and analyze the super-resolution phenomena associated to Time Reversal [40, 41].

In this chapter, an overview of the state of the art of the existing wideband prototypes is first given. Then, the retained solution is described in detail. Further on, the general yet fundamental signal processing operations performed on the measured data are presented, finally followed by the description of the procedure used for the experimental retransmission.

1.1 State of the art

Let us briefly recall and describe here the hardware solutions employed in some of the most representative electromagnetic Time Reversal-based prototypes recently reported. Due to the particular interest in wideband solutions, this review deliberately discards narrowband applications (that is, purely Phase Conjugation ones), particularly explored since a long time in the RADAR community since the seminal Van Atta patent [42] (which describes a wideband approach, though) up to nowadays [26, 43–48].

As the Time Reversal-Phase Conjugation duality [44, 49] holds, at least for propagative waves [50], two different instrumental approaches can be distinguished. In the first one, experiments are achieved directly in the time domain with an Arbitrary Waveform Generator (AWG) at transmission and a Digital Sampling Oscilloscope (DSO) at reception. The second approach is the stepped-frequency one with systems based on the use of a Vector Network Analyzer (VNA) both as signal source and receiver.

1.1.1 Time domain implementation

Concerning the time domain approach, some of the first publications come from Mathias Fink's group [24, 25] in 2004 and 2006. Here, working at the central frequency 2.45 GHz, bandwidths of 2 MHz and 150 MHz, respectively, are reported. They are achieved with an AWG, a DSO and thanks to commercially-available general purpose IQ transceivers performing the baseband-RF (Tx) and RF-baseband (Rx) conversions. Later articles [27,30] report larger bandwidths (more than 2 GHz at around 1.5 GHz central frequency) made possible by the availability of more rapid AWG's and DSO's thus making obsolete the use of external transceivers. Another remarkable experiment concerns an HF over-the-horizon RADAR based on a double-pass Time Reversal strategy, where the much lower frequencies (bandwidth approximately going from 3 MHz, due to the antennas used, to 20 MHz) easily allow the use of the AWG/DSO architecture [51].

Finally, a common characteristic of these experiments is the use of one single active antenna as Time Reversal Mirror (TRM). Nevertheless, a virtual array can be built in virtue of Maxwell's equations linearity by switching ON/OFF or displacing the active antenna [25].

1.1.2 Stepped-frequency implementation

The first report of a frequency domain Time Reversal system is most probably [52]. The architecture used is very similar to the one presented in this chapter, with an antenna

array and a vector modulator per channel to experimentally steer the array and create the waveform to be retransmitted. Nevertheless, a very narrowband is used (2 MHz) and the phase conjugation law is the one of the central frequency 2.45 GHz. In other papers, a stepped-frequency acquisition over a given frequency band and pulse synthesis are rather performed, while retransmission is only done numerically. The bandwidths are instead very wide, *e.g.* 10 GHz in [28] and 6.5 GHz in [29].

Dually with respect to the time-domain approach, the time coherency is here retrieved by recombining all the frequencies *via* a Fourier Transform.

1.1.3 Time Reversal through dispersive optical fibers

Yet another, completely different approach exists. In 1999, Coppinger *et al.* [53] reported the experimental demonstration of broadband TR by employing dispersive optical fibers. The idea consists in generating an optical pulse with a laser and first letting it run through a fiber with negative dispersion module D_1 and length L_1: the effect is a delayed pulse with more delay corresponding to the higher wavelengths. At its output, an electro-optical modulator modulates the amplitude of the resulting pulse with the RF signal that has to be time reversed. Then, the signal propagates through another fiber of length L_2, with positive dispersion index D_2 this time, which will delay more and more lower wavelengths until they will lead in time with respect to the higher ones (which were the leading ones at the fiber input). As a result, when $D_2L_2 = -2D_1L_1$, the initial optical pulse as well as the RF signal have been reversed in time; after a final fiber, whose role is to stretch in time the RF signal, a complete TR can be observed. Similar results and the possible implementation of an antenna array based on this technology have also been published in [54].

There are mainly two drawbacks to this solution. First, very long fibers (some kilometers!) are needed to time reverse wideband RF signals. Second, it only works with TR: in other words, it is impossible to process the received data to "arbitrarily" beamform the following transmitted wave. Since we want to use antenna arrays to investigate techniques such as DORT, based on a Singular Value Decomposition (SVD) of the multi-static matrix, the latter drawback prevents us from adopting this implementation.

1.2 Prototype description

Excluding the optical solution, it might seem that the approaches in §1.1.1 and §1.1.2 are rather equivalent, given today's technology, for what concerns bandwidth availability and easeness of implementation of experimental beamforming. Nevetheless, for a comparable frequency band, both cost and dynamic range still seem more favorable in the former case. Given this, and also in order to provide the LSEET with an instrument that other teams might be interested in using[1], the stepped frequency implementation has been chosen, with

[1]Namely, the team developing the current-measuring RADAR, which works at VHF.

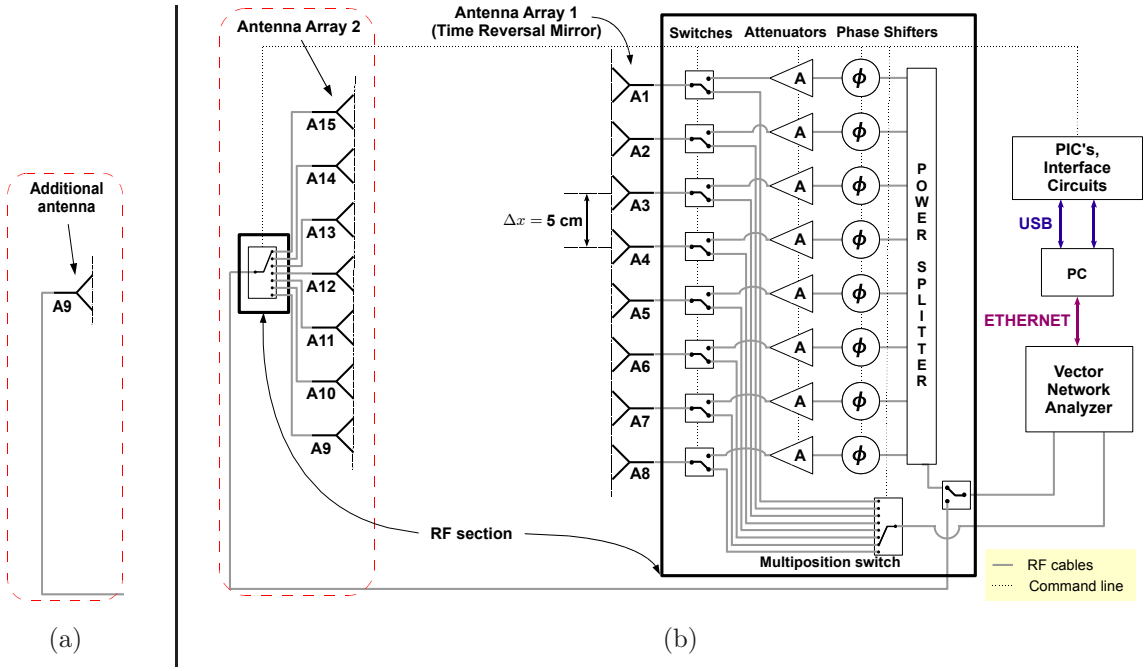

Figure 1.1: *Prototype architecture. (a) Additional antenna (A_9) present in the initial architecture later replaced by (b) a second antenna array. In both architectures, the antenna array-1 acts as TRM.*

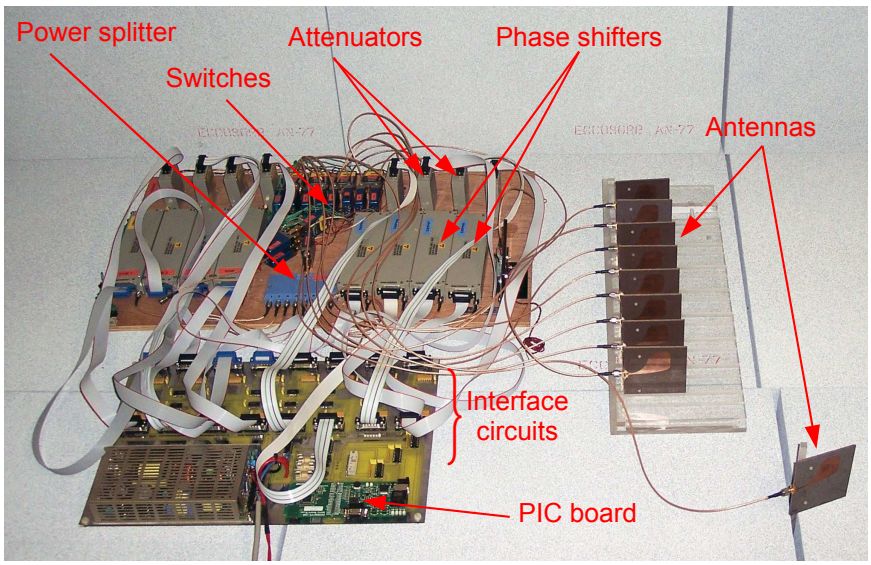

Figure 1.2: *Photograph of the prototype in the TRM array + additional antenna version (Fig. 1.1(a)).*

a frequency band going from 2 to 4 GHz.

1.2.1 RF section

The initial architecture of the prototype is presented in Fig. 1.1(a), and a photograph is shown in Fig. 1.2. The system is built around the VNA, a two-port Rohde & Schwarz ZVB8

able to work from 300 kHz to 8 GHz and acting both as RF signal source and receiver. The TRM is made of an array of 8 antennas, each of them connected to the VNA *via* two possible paths selected through a single-pole double-throw (SPDT) electromechanical switch. The first path, called MUX path, is a simple connection through a single-pole 8-throw (SP8T) 50 Ω-terminated switch (Multiposition switch in Fig. 1.1); the MUX path provides small losses (≈4 dB at 3 GHz) and allows to select the active antenna. The other path, the A/Φ path, is responsible of the beamforming implementation *via* a pair of numerically-controlled attenuator (A) and phase shifter (Φ) followed by an 8-channel power splitter. Note that since all the components are passive and reciprocal, both TX and RX beamforming can be realized. On the other hand, the array-2 only presents an SP7T switch to select the active antenna, giving an overall path loss (including cables) of ≈6.25 dB at 3 GHz.

In order to perform experiments in transmission configurations and to measure focusing spots, one additional antenna, directly connected to the VNA, was present in the initial architecture (Fig. 1.1(a)). It has later been replaced by a second 7-antenna array without beamforming capabilities but equipped with a Multiposition switch[2] (Fig. 1.1(b)).

A summary of the electric characteristics of the RF components is given in Tab. 1.1. Attenuators come from Waveline; they have an attenuation range of 32 dB and 8 control bits, giving a rather linear-in-dB resolution of 0.125 dB/LSB. Phase shifters, also from Waveline, assure a phase shifting range of more than 360 deg with 10 control bits, giving a linear resolution of 0.35 deg/LSB (see Tab. 1.2). The insertion losses are 2.75 dB for the former (at minimum attenuation) and 6 dB for the latter; including power splitter (9 dB nominally plus 0.8 dB insertion losses), switches and cables, the losses of the whole A/Φ path amount to ≈21 dB at 3 GHz.

The antennas are antipodal symmetric Exponentially Tapered Slot (ETS) antennas, printed on a Duroid substrate of permittivity $\varepsilon_r = 2.2$ and dimensions 8 cm × 9 cm (length × height). They show very good input impedance matching (SWR < 2) in the [2–18] GHz frequency band and radiate a vertically-polarized (perpendicular to the plane of Fig. 1.1(a)) electric field [55]. Antennas based on the same design have also been employed in [29,56]. As shown in Fig. 1.1, when used within an array, they have usually been spaced of $\Delta x = 5$ cm, equivalent to $\lambda_0/2$ at 3 GHz. This allows a good compromise between antenna coupling, which has more impact for a smaller Δx, and grating lobes, which are more of an issue for larger Δx values. In particular, at the worst case frequency 4 GHz, grating lobes are present at end-fire for a pointing angle of 30 deg, rather hard to obtain in our "long-and-narrow" anechoic chamber (see §1.2.3).

Finally, the systems operates in the [2-4] GHz band. The lower limit was imposed by the adaptation of the antennas, which were available before the whole project began; the upper limit results from a trade-off between performances and cost of all the other RF components.

[2]There were originally 8 antennas in the second array, too. Unfortunately, one channel of the SP8T switch has broken, leaving us with seven usable channels only.

	SPDT switch	SP8T switch	Power splitter	A	Φ	Antennas
Frequency operating range (GHz)	[0-4]	[0-4]	[2-4]	[2-8]	[2-4]	[2-18]
Insertion loss/Gain @ 3 GHz (dB)	-0.1	-0.1	-0.8	-2.75	-6	+3

Table 1.1: *Main electrical characteristics of the RF components.*

	A	Φ
Attenuation/phase shift range	32 dB	360 deg
Number of bits	8	10
Resolution	0.125 dB/LSB	0.35 deg/LSB

Table 1.2: *More electrical characteristics of attenuators and phase shifters.*

Concerning the VNA frequency step, it must be chosen in such a way that the alias-free distance range be at least equal to the total electric length of the "longest" prototype path. Indeed, with reference to Fig. 1.1, the longest path is the array-2 one, comprising one 5 m and one 2 m cables (the SP8T siwth electrical length is negligible). Adding to this the length of the chamber (almost 2 m, see §1.2.3), multiplying by two to handle the retrodiffusion measurement case, and keeping into account the dielectric constant of our cables (approximately 1.9 and 1.4 for the 2 m and 5 m cables, respectively), the maximum length is:

$$2\left(2\sqrt{1.9}+5\sqrt{1.4}+2\right)\ \text{m} \approx 21.5\ m\ . \tag{1.1}$$

This value must be compared with the alias-free range associated to a given frequency step, Δf. This gives:

$$\frac{1}{2}\left(\frac{c_0}{\Delta f}\right) \leq 25\ \text{m}\ \Rightarrow\ \Delta f \leq 7.1\ \text{MHz}\ , \tag{1.2}$$

where $c_0 = 30$ cm/ns is the speed of light in vacuum and the 1/2 factor comes from the alias-free requirement. Being a little conservative, we have finally chosen $\Delta f = 5$ MHz (401 points between 2 GHz and 4 GHz).

1.2.2 Drive and control electronics

The entire system can be controlled from a PC. For this purpose, a Matlab-based Graphical User Interface (GUI) has been developed. It can autonomously perform a complete data acquisition or a Phase Conjugation/DORT retransmission.

There are three connections handled by Matlab's Instrument Control Toolbox, one to the VNA (Ethernet) and two to the PIC microcontrollers (one USB cable per PIC) driving the RF components of each of the arrays (see Fig. 1.1(b)). The way these connections are set and handled in Matlab is described in §A.

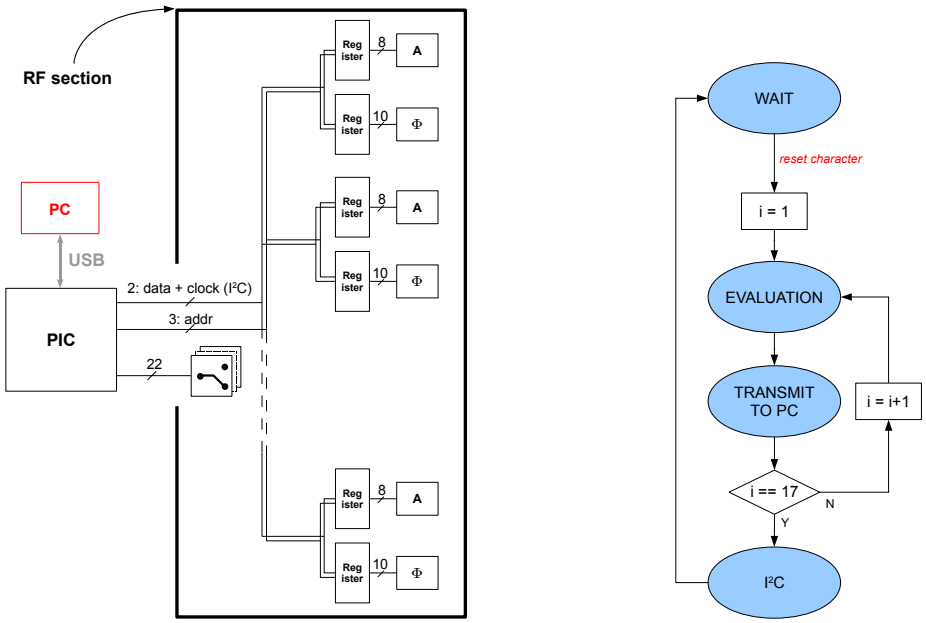

(a) (b)

FIGURE 1.3: *(a) Simplified schematization of the way the PC controls the RF components through the PIC microcontroller. (b) State machine implemented in the PIC microcontroller.*

The VNA is remote-controlled in order to set the features of a frequency sweep (n. of frequencies, IF filter bandwidth, n. of averages), to trigger it and to read the measurement into the PC.

With reference to the PIC driving the TRM array, in FIG. 1.3(a) one can schematically see the PIC connections to the switches (SPDT's and SP8T's) and to attenuators and phase shifters. They were designed, together with the electronic board layout, by Marc Bianchieri-Astier during its Master 2 internship [13]. The switches are connected to the PIC through a simple buffer (not shown in the figure). In order to implement the wanted attenuation/phase shift, the channel is addressed through three bits (1 to 8) and A/Φ couples controlled with the I^2C protocol through two wires: one carries a clock signal, the other the data sent bit after bit (a first byte representing the address of either the attenuator or the phase shifter, followed by two bytes containing the code giving the wanted attenuation/phase shift as described in §1.8).

A communication protocol between PIC, PC and RF components has been established. It has a "server" side in Matlab and a "client" side running in the PIC (coded in a special PIC-adapted C language, cfr. §A). The PIC state machine is depicted in FIG. 1.3(b). After initialization the PIC is in the *wait* state; when a reset character (arbitrarily chosen and known to both Matlab and the PIC) is read, a counter i is initialized and the *evaluation* state is reached. Two bytes are now read, decoded (a binary to decimal conversion is needed), and sent back to the PC in the *transmit to PC* state for verification. This loop is repeated 17 times, 1 for the switches and 2×8 times for all the attenuators and phase

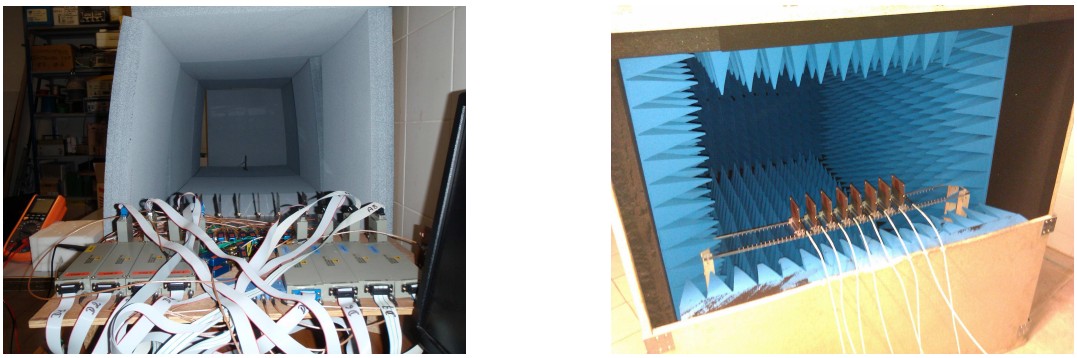

(a) (b)

FIGURE 1.4: *Photographs of the anechoic chambers built at LSEET with (a) flat and (b) pyramidal absorbing panels.*

shifters. Once this is done, the PIC finally goes to the I^2C state: the PIC drives its outputs connected to the switches and uses the I^{2}C protocol to communicate with attenuators and phase shifters one after the other. Notice that during the I^{2}C communication, after writing the attenuation/phase shift code into the component, the PIC reads back the code for verification. The whole cycle approximately takes 2 seconds.

1.2.3 The anechoic chamber

A first anechoic chamber was built with flat absorbing panels (FIG. 1.4(a)) with dimensions 1.8×0.6×0.6 m^3 (length×width×height). It was used for the initial validation of the prototype. Nevertheless, as soon as the first quantitative inverse scattering experiments were realized, the need for pyramidal panels, much more effective in absorbing electromagnetic waves under grazing angle incidences, became impellent in order to recreate free-space conditions. A second chamber with pyramidal panels has then been built (FIG. 1.4(b)), whose internal (exploitable) dimensions are 1.4×0.8×0.8 m^3. This chamber is provided of a door and of a removable panel on the TRM side, and it is completely rigidified by a 3 cm-thick wood shell. Furthermore, two plexiglas supports (one of them is visible in FIG. 1.4(b)) have been realized in order to achieve a precise positioning of the array antennas. The second anechoic chamber was financed by the Institut Fresnel in Marseille; the plexiglas support was realized by the Laboratoire d'Électronique, Antennes et Télécommunications (LEAT) in Nice-Sophia Antipolis.

1.3 Measurement configurations

For a given configuration, a 2-port VNA measures 4 S-parameters defined, with reference to FIG. 1.5, as

$$\begin{bmatrix} b_1 \\ b_2 \end{bmatrix} = \begin{bmatrix} S_{11} & S_{12} \\ S_{21} & S_{22} \end{bmatrix} \begin{bmatrix} a_1 \\ a_2 \end{bmatrix} , \tag{1.3}$$

where $(a_i, b_i)|_{i=1,2}$ are the so-called power waves [57], and conventionally the 1st index stands for the receiving port and the 2nd for the transmitting one.

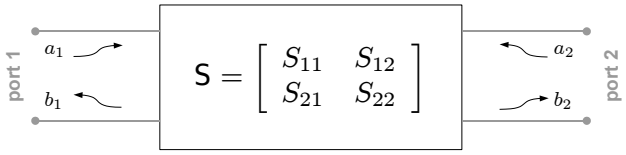

Figure 1.5: *Definition of the S-parameters for a 2-port network.*

In practice, if the signal received by antenna A_j when antenna A_k transmits has to be measured, the VNA port 1 must be connected to A_k and the port 2 to A_j. As a result, using the formalism in (1.3), the following quantities are obtained:

$$\begin{bmatrix} S_{kk} & S_{jk} \\ S_{kj} & S_{jj} \end{bmatrix}, \tag{1.4}$$

among which the desired S_{jk} appears. This notation is used throughout the manuscript.

With respect to the architecture in Fig. 1.1, the system can be used in one of the following configurations.

1.3.1 Reflection

In this configuration, the TRM antennas act both as sources and receivers, array-2 is not active. The following 8×8 inter-element matrix $\mathbf{K}^{\text{reflec}}$ can be measured at each frequency:

$$\mathbf{K}^{\text{reflec}} = \begin{bmatrix} S_{11} & S_{12} & \cdots & S_{18} \\ S_{21} & S_{22} & & S_{28} \\ \vdots & & \ddots & \vdots \\ S_{81} & S_{82} & \cdots & S_{88} \end{bmatrix} \tag{1.5}$$

The path losses, L_{path}, associated to the reflection configuration can be evaluated. For retrodiffusion measurements, *i.e.*, for the diagonal elements of $\mathbf{K}^{\text{reflec}}$, the signal runs twice through the TRM MUX path; hence, $L_{\text{path}} \approx 8$ dB at 3 GHz. For all the other terms, there is a MUX path followed by an A/Φ path, giving $L_{\text{path}} \approx 25$ dB at 3 GHz (Tab. 1.3). Notice that since all the prototype RF components are passive and reciprocal, if the wave propagation medium is reciprocal (in the sense of Lorentz), then $\mathbf{K}^{\text{reflec}}$ is symmetric.

1.3.2 Transmission

The TRM antennas act in this case as sources and array-2 antennas as receivers (or vice versa), giving the following 7×8 $\mathbf{K}^{\text{transm}}$ matrix:

$$\mathbf{K}^{\text{transm}} = \begin{bmatrix} S_{91} & S_{92} & \cdots & S_{98} \\ S_{101} & S_{102} & & S_{108} \\ \vdots & & \ddots & \vdots \\ S_{151} & S_{152} & \cdots & S_{158} \end{bmatrix} \tag{1.6}$$

	MUX path	**A/Φ path**	**array-2 path**	**Reflection**		**Transmission**	**Full**
				S_{jj}	S_{jk}	S_{jl}	S_{ll}
L_{path} **@ 3 GHz (dB)**	4	21	6.25	8	25	10.25	12.5

TABLE 1.3: *Path loss, L_{path}, for the different paths and measurement configurations. j and k indices cover the TRM array ($j,k = 1,8$), l is for the array-2 antennas ($l = 9,15$).*

Concerning path losses, for any element of $\mathbf{K}^{\text{transm}}$ the signal runs through the MUX path of the TRM and through the array-2 path. The result is $L_{\text{path}} \approx 10.25$ dB at 3 GHz. With the same assumptions made for the reflection configuration, $\mathbf{K}^{\text{transm}}$ is theoretically a symmetric matrix.

1.3.3 Full

It is in principle possible to merge the reflection and transmission configurations above, giving a 15×15 $\mathbf{K}^{\text{full}}$ matrix. Nevertheless, the architecture in FIG. 1.1(b) does not allow to record the array-2 inter-element responses, except for the retrodiffusion coefficients $S_{ll}|_{l=9,15}$. Indeed, it could have been possible to build a second TRM equipped with A/Φ pairs instead of the "simple" array-2 of FIG. 1.1(b). The full matrix could have then be measured, but at the price of a reduced dynamic range due to the additional components. The choice has been therefore made to have only one TRM while optimizing the dynamic range, extremely important for imaging low-scattering objects. Finally, the global measurable matrix $\mathbf{K}^{\text{full}}$ is

$$\mathbf{K}^{\text{full}} = \left[\begin{array}{cccc|cccc} S_{11} & S_{12} & \cdots & S_{18} & S_{19} & S_{110} & \cdots & S_{115} \\ S_{21} & S_{22} & & S_{28} & S_{29} & S_{210} & & S_{215} \\ \vdots & & \ddots & \vdots & \vdots & & \ddots & \vdots \\ S_{81} & S_{82} & \cdots & S_{88} & S_{89} & S_{810} & \cdots & S_{815} \\ \hline S_{91} & S_{92} & \cdots & S_{98} & S_{99} & \circ & \cdots & \circ \\ S_{101} & S_{102} & & S_{108} & \circ & S_{1010} & & \circ \\ \vdots & & \ddots & \vdots & \vdots & & \ddots & \vdots \\ S_{151} & S_{152} & \cdots & S_{158} & \circ & \circ & \cdots & S_{1515} \end{array}\right], \tag{1.7}$$

where the symbol '$\circ$' stands for an unavailable measurement. The retrodiffusion terms belonging to array-2 ($S_{ll}|_{l=9,15}$) have $L_{\text{path}} = 12.5$ dB at 3 GHz.

1.4 Dynamic range

For scattering experiments, where very low-level signals must often be sensed, it is essential to configure the VNA to have a dynamic range as wide as possible. Indeed, the signal power level to observe might be very low for small and/or far targets. At the same time a good measurement precision is needed, especially in the framework of quantitative inverse scattering (see §3).

1.4.1 VNA output power

To optimize the dynamic range, defined as the ratio between the measurement power available at the test port and the noise floor of the receiver, the first VNA parameter to set is the output power level, P_{out}. Despite one would tend to use the maximum VNA power level not to waste any of the available dynamic range, a too high value would produce non-linearity errors affecting the measurement precision. To understand why these errors come into play, consider a VNA calibration procedure (TOSM calibration, for instance) run with a power level beyond the receiver linear range. Since harmonics and spurious tones are created by the non-linearity, at each frequency the calibration coefficients will correct for them, too. Nonetheless, when real measurements are performed with passive devices as ours, which by definition attenuate the signal, the power level at the receiver is lower than the one seen during calibration. As a result, despite there is no non-linearity in the receiver now, the calibration coefficients tend to correct for it, *i.e.*, a wrong calibration is applied. In practice, the VNA should be operated at a power level below the 0.1 dB receiver compression point to have negligible non-linearity errors [58].

To verify up to what P_{out} value the VNA can be used, the receiver compression level must be evaluated. This is done by measuring, with the uncalibrated VNA, the S_{21} (transmission configuration) and the S_{11} (reflection configuration) with an open circuit and a thru connector, respectively, directly connected to the VNA test port, at three different P_{out} levels: -20 dBm (10 μW), +13 dBm (20 mW), and +14 dBm (25 mW). At -20 dBm the receiver is considered in its linear range, as stated in the VNA datasheet and which we have verified with a power sweep; +13 dBm is the maximum nominal output power reported in the datasheet. To sense the compression level, the ratio between the linear-range measurement (-20 dBm) and the non-linear ones must be observed:

$$\frac{S_{j1}|_{-20\ dBm}}{S_{j1}|_{+13\ dBm}} \quad \text{and} \quad \frac{S_{j1}|_{-20\ dBm}}{S_{j1}|_{+14\ dBm}}, \qquad j = 1, 2\ . \tag{1.8}$$

The results for the transmission and reflection configurations are in Fig. 1.6 (a) and (b), respectively. At +13 dBm the receiver is below the 0.1 dB compression point throughout the entire [2-4] GHz band, except for two small sub-bands in the reflection case centered at 3.725 and 3.905 GHz, where an excess ≤ 0.015 dB is measured. At +14 dBm the receiver is more often, and more deeply, beyond the 0.1 dB compression point. According to these results, the VNA has been operated at $P_{\text{out}} = +13$ dBm, although it would have been enough to further back-off of as few as 0.5 dB to *always* stay beyond 0.1 dB compression.

1.4.2 VNA Noise floor

Concerning the noise floor (NF), the ZVB8 datasheet reports a value ≤ -110 dBm, obtained with an IF filter bandwidth of 10 Hz. For a trade-off between measurement speed and dynamic range, the IF filter bandwidth has been set to 200 Hz, giving a $L_{\text{IF}} = 10\log_{10}(200/10) = 20$ dB dynamic range reduction.

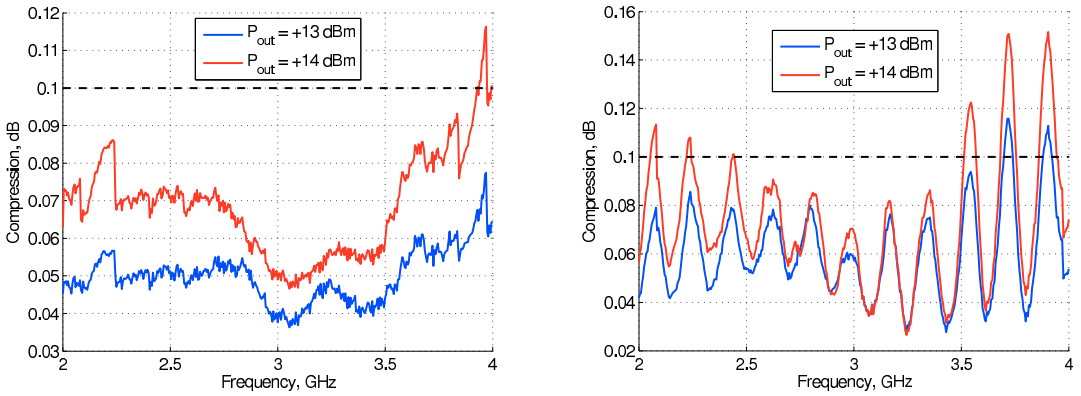

(a) transmission configuration, S_{21}

(b) reflection configuration, S_{11}

FIGURE 1.6: *Measurement of the compression of the VNA receiver port in the cases (a) of transmission (S_{21}) and (b) of reflection (S_{11}) measurements.*

For experiments involving only active sources, *e.g.*, Time Reversal of the field radiated by an active antenna (see §2.2), the dynamic range DR can therefore be evaluated, which gives, at 3 GHz,

$$\begin{aligned} DR &= P_{\text{out}} - (NF + L_{\text{IF}} + L_{\text{path}}) \\ &= +13 \text{ dBm} - (-110 \text{ dBm} + 20 \text{ dB} + 10.25 \text{ dB}) = 92.75 \text{ dB} , \end{aligned} \tag{1.9}$$

where L_{path} is necessarily related to the transmission configuration (see TAB. 1.3).

1.4.3 Thermal drift

For scattering experiments, an additional element must be taken into account to evaluate the available dynamic range. As detailed later in §1.6, two measurements must be performed in order to retrieve an exploitable scattered field term, $E^{\text{s}} \triangleq S^{\text{s}}_{jk}$: the incident field, $E^{\text{i}} \triangleq S^{\text{i}}_{jk}$, measured without the target, and the total field, $E \triangleq S_{jk}$, measured with the target present in the scene. This is referred to as *differential measurement* technique, since the difference $E - E^{\text{i}}$ gives the scattered field one works with [10, 11, 29]. Nonetheless, despite a long (at least an hour) VNA warm up time, a temperature drift has systematically been experienced. Such drift is responsible of an altered precision between two identical measurements performed at different times. And a certain amount of time is indeed needed, for instance to fill the incident field $\mathbf{K}^{\text{i}}$ matrix before measuring the total field one, $\mathbf{K}$. Inspired by [59], it is possible to model the effect of such a drift as follows:

$$\begin{cases} E^{\text{i}} = \tilde{E}^{\text{i}} + w_1 \\ E = \tilde{E}^{\text{i}} + \tilde{E}^{\text{s}} + \Delta E + w_2 \end{cases} \quad \Rightarrow \quad E^{\text{s}} = \tilde{E}^{\text{s}} + \underbrace{\Delta E}_{\text{drift}} + \underbrace{w_2 - w_1}_{\text{noise}} , \tag{1.10}$$

where the quantities topped with '$\sim$' represent the ideal quantities in the absence of drift, and $w_j|_{j=1,2}$ are the VNA noise realizations related to its NF. Two effects can therefore be distinguished:

- the necessity of performing differential measurements results in a 3 dB dynamic range loss due to the term $w_2 - w_1$;
- temperature drift causes an additional "noise" term, ΔE, that affects the dynamic range as well. This can be further split into two contributions. Indeed, since the drift physically acts on the incident field, ΔE is the sum of an incident field drift term, ΔE^{i}, and of another term representing its effect onto the scattered field:

$$\Delta E = \Delta E^{\mathrm{i}} + \mathcal{S}(\Delta E^{\mathrm{i}}) \ , \tag{1.11}$$

  where $\mathcal{S}$ is the linear scattering operator relying incident and scattered fields ($\tilde{E}^{\mathrm{s}} = \mathcal{S}(\tilde{E}^{\mathrm{i}})$).

Overall, the temperature drift term may or not be larger than the "classical" $w_2 - w_1$ term. This of course depends dramatically on the time between the total and incident field measurements. On this purpose, it has rather paradoxically been found that not doing any average in the VNA gives a cleaner scattered field after difference, and this is because a lesser amount of time has flown between the two measurements. Nevertheless, for a common 8×8 $\mathbf{K}$ matrix recorded with an IF filter bandwidth of 200 Hz, it appears that the thermal drift noise is higher than the VNA noise floor, hence imposing the final dynamic range as shown in FIG. 1.7.

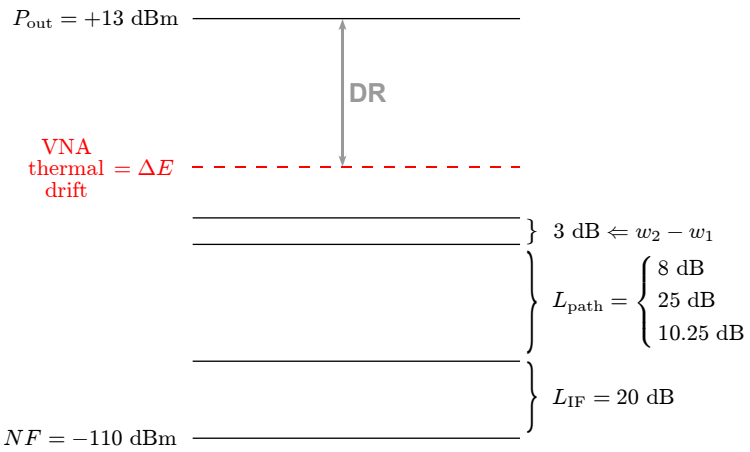

FIGURE 1.7: *Schematization of the dynamic range for scattering experiments. According to experimental evidence for typical measurements, the thermal drift is higher than the "augmented" NF. Notice also that since the drift is signal-dependent, the dynamic range finally depends on the amplitude of the incident field.*

In order to further understand the drift phenomenon, the following experiment has been performed. For a single antenna couple, *e.g.* S_{46}, the incident field in absence of scatterers has first been recorded twice in very rapid succession (about 5 s). Then, during a whole night, $N = 50$ total field measurements, with a time step $\delta t = 15$ min, have been recorded as well. The scatterer is a small metallic cylinder (radius equal to 3.1 mm) placed at around 75 cm from the couple of antennas. Finally, this results in $E_1^{\mathrm{i}} \approx E_2^{\mathrm{i}} \triangleq E^{\mathrm{i}}$ and $E_n|_{n=1,50}$,

giving the scattered fields $E_n^{\mathrm{s}} = E_n - E^{\mathrm{i}}$. The assumption is that, due to their rapid succession, the incident field measurements are practically indetical, *i.e.*, the thermal drift amount is lower than the VNA NF, whereas a sensible drift-induced difference is observable in the total, hence scattered, fields.

Before presenting the results, let us adapt the model in (1.10)-(1.11) in the case of the present experiment. It is assumed that the drift effect is linear with respect to the time δt between two measurements. Then, for the N consecutive measurements with the same time interval, one obtains

$$\Delta E^{\mathrm{i}} = n\delta E^{\mathrm{i}} \quad \Rightarrow \quad E_n^{\mathrm{s}} = \tilde{E}^{\mathrm{s}} + n\left[\delta E^{\mathrm{i}} + \mathcal{S}(\delta E^{\mathrm{i}})\right] \ , \tag{1.12}$$

where δE^{i} is the variation of the incident field during the δt. VNA noise has been neglected for conciseness.

In Fig. 1.8(a) the time-domain complex envelopes (or analytical signals) in dB of some of the measured signals are shown. In particular, it can be clearly seen how, with respect to the $E_1^{\mathrm{i}} - E_2^{\mathrm{i}}$ difference (black curve), the bunch of scattered fields E_n^{s} (from dark to bright green corresponding to a growing n) is stronger even at the very first time instants ($t < 4$ ns) where the target echo is not yet arrived. The hypothesis that the thermal drift cumulated in a $\delta t = 15$ min overrules the VNA NF is then validated (*cf.* Fig. 1.7).

Fig. 1.8(b) shows the amplitude of the largest normalized E_n^{s} sample, that is, $\max_t(E_n^{\mathrm{s}}/E_1^{\mathrm{s}})$ within two separate time windows depicted in Fig. 1.8(a): the direct antenna coupling window (bottom subfigure) and the target echo window (top subfigure). In the former window, there is not any scattered field yet - the target echo only arrives later. The observed signal is then $n\delta E^{\mathrm{i}}$ in (1.12), whose rather linear behavior confirms the drift-linearity assumption made in (1.12). On the other end, the curve pertaining to the target echo contains the three contributions in (1.12). Since it is practically constant - barely a 20 % variation in more than $N\delta t \approx 12$ hours -, it can be assumed that $\tilde{E}^{\mathrm{s}} \gg n\left[\delta E^{\mathrm{i}} + \mathcal{S}(\delta E^{\mathrm{i}})\right]$, which basically means that for these target and configuration there is still sufficient dynamic range to observe the scattered field even after 12 hours.

Another interesting result is presented in Fig. 1.9. Here, two consecutive scattering (or total) field measurements have been subtracted, giving the green curves $E_n^{\mathrm{s}} - E_{n-1}^{\mathrm{s}}$. Since, as just observed, the drift effect is practically linear in time, the mean of such signals can be computed at any t. The result is the red thick curve, which with respect to (1.12) is nothing but $\delta E^{\mathrm{i}} + \mathcal{S}(\delta E^{\mathrm{i}})$. It is interesting to observe that this curve is partially correlated to the incident field one (blue line), *e.g.* within the antenna direct coupling window ($t < 4$ ns), whereas there is no correlation with the scattered field curve (black line). Indeed, since the scatterer is small and relatively far from the antenna, its scattered field is rather isotropic and very small, giving $\mathcal{S}(\delta E^{\mathrm{i}}) \approx S_0 E^{\mathrm{i}} \ll E^{\mathrm{i}}$, where S_0 is the isotropic scattering matrix coefficient.

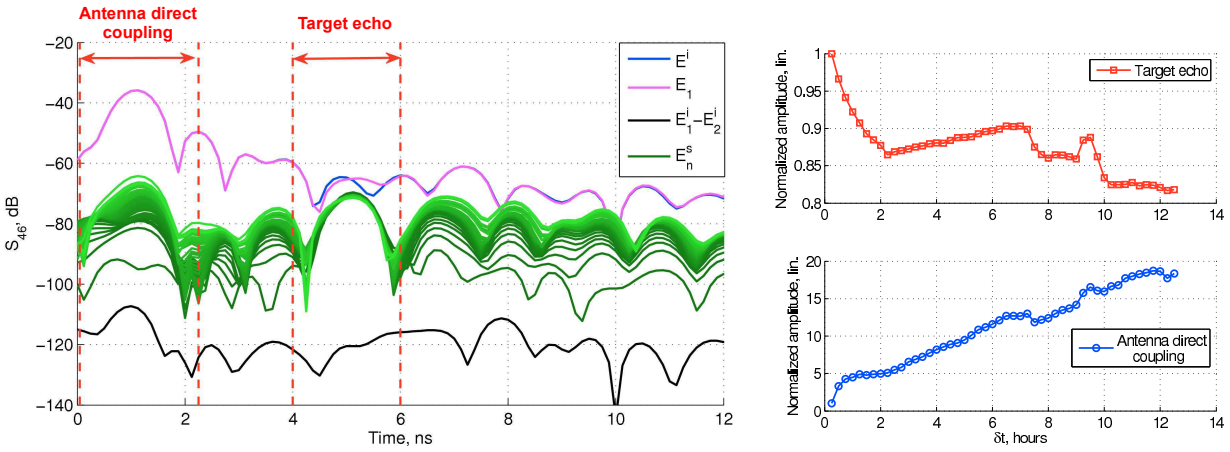

(a) (b)

FIGURE 1.8: *(a) Time-domain complex envelopes in dB of E^{i} (blue line), E_1 (magenta), $E^{\mathrm{i}}_1 - E^{\mathrm{i}}_2$ (black) representing a sort of noise floor, and E^{s}_n (from dark to bright green corresponding to a growing n). (b) Linear amplitude of the largest E^{s}_n sample within the target echo (red line, top) and the direct antenna coupling (blue line, bottom) "windows". Comparing the amplitude scales, a rather linear behavior can be appreciated in the latter, well corresponding to the model in (1.12), whereas the target echo "window" exhibits a rather constant value.*

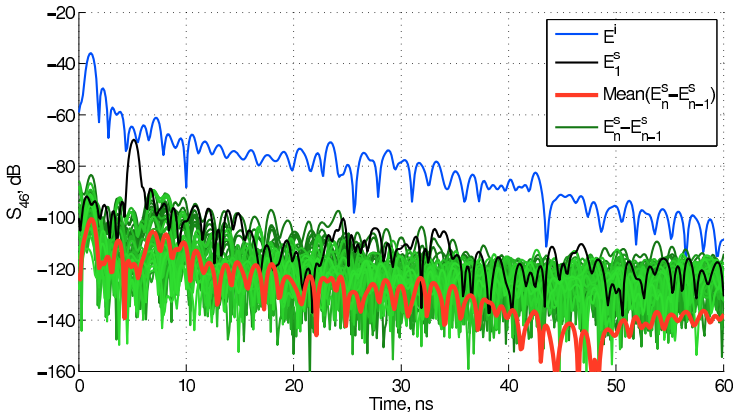

FIGURE 1.9: *Time-domain complex envelopes in dB of E^{i} (blue line), E^{s}_1 (black), $E^{\mathrm{s}}_n - E^{\mathrm{s}}_{n-1}$ (from dark to bright green corresponding to a growing n), and their mean value at each time instant.*

1.5 VNA Calibration

The VNA calibration is an essential task for obtaining precise measurements. Since any configuration (see §1.3) necessitates both retrodiffusion and transmission measurements, the TOSM calibration type has always been used. This method, employing a Short (S), Open (O), Match (M), and Thru (T) connector set (also called *standards*) applied to both ports of the VNA, is one of the most complete and accurate existing calibration methods.

Concerning the interface at which the calibration must be performed, a fundamental

choice has to be made. In effect, calibrating the VNA means setting its phase origin at the connector where the standards are applied. Hence, especially for scattering measurements, it seems natural to calibrate the VNA at the connectors of the array antennas, since, by doing so, the data measured by the VNA would directly represent the wave propagation from the transmitting to the receiving antenna. Nonetheless, two major problems arise:

- taking for instance the reflection configuration in §1.3, assuming reciprocity, and considering that the retrodiffusion parameters $S_{jj}|_{j=1,\dots,8}$ are obtained "for free" when measuring any $(j,k)^{\text{th}}, j \neq k$ antenna pair, there are $C_8^2 = 8!/2!(8-2)! = 28$ different antenna couples to be tested to fill the 8×8 $\mathbf{K}$ matrix. This means 28 different TOSM calibrations, each of them lasting ≈ 3 minutes, which apart from the obvious "manual effort" cover a long time with respect to the VNA thermal drift issue previously mentioned.
- as shown in Tab. 1.3, up to 25 dB path loss exist for a tranmission measurement involving the TRM array. Such a loss must be subtracted from the VNA dynamic range during calibration and greatly affects the precision of the calibration factors calculated. The result is then an imprecise calibration giving imprecise measurements.

Due to the last item, then, not even an 8-port VNA would solve the issue, despite its capability of calibrating all 8 ports simultaneously. The solution found consists in calibrating the VNA at its own test ports, and in retrieving the wave propagation part of the measurement by using the transfer matrix formalism as explained next.

1.5.1 Extraction of the propagating medium through the use of the transfer matrices

Among the configurations in §1.3, the example of a reflection configuration involving the TRM array, *i.e.*, S_{jk} $(j \neq k,\ j,k \leq 8)$, is used here. Fig. 1.10 shows that the VNA actually measures the cascade of three 2-port networks, the k^{th} MUX path, the propagating medium, and the j^{th} A/Φ path. The overall measurement is the S-parameters matrix $\mathbf{S}$, whereas the sub-network matrices are, respectively, $\mathbf{S}_k^{\text{MUX}}$, $\mathbf{S}^{\text{air}}$, and $\mathbf{S}_j^{\text{A}/\Phi}$.

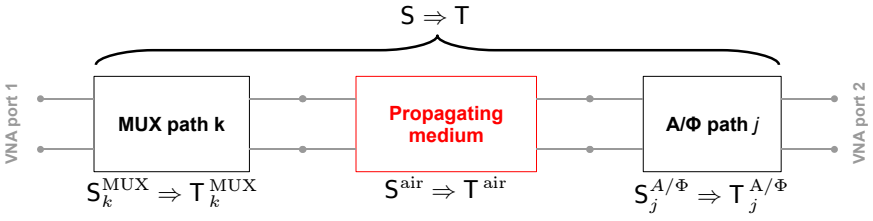

Figure 1.10: *Cascade of 2-port networks for a reflection measurement configuration (S_{jk}) involving the TRM array.*

Nevertheless, the only sought contribution is the one of the propagation medium, $\mathbf{S}^{\text{air}}$. In order to extract it, the following procedure is used.

1. Each prototype path is characterized by direct measurement, resulting in a full database composed of $\mathbf{S}_k^{\mathrm{MUX}}|_{k=1,\ldots,8}$, $\mathbf{S}_j^{\mathrm{A}/\Phi}|_{j=1,\ldots,8}$, and $\mathbf{S}_l^{\mathrm{arr2}}|_{l=1,\ldots,7}$ (the latter, representing the array-2 path for the antenna A_l, is needed for transmission configurations involving array-2).

2. Each of these matrices, and the overall $\mathbf{S}$ matrix, are transformed into the respective *transfer matrices* $\mathbf{T}$ (T-matrices) [60], according to the relationships

$$\begin{bmatrix} a_1 \\ b_1 \end{bmatrix} = \mathbf{T} \begin{bmatrix} b_2 \\ a_2 \end{bmatrix} \;\Rightarrow\; \begin{cases} \begin{bmatrix} T_{11} & T_{12} \\ T_{21} & T_{22} \end{bmatrix} = \begin{bmatrix} \dfrac{1}{S_{21}} & -\dfrac{S_{22}}{S_{21}} \\ \dfrac{S_{11}}{S_{21}} & -\dfrac{det(\mathbf{S})}{S_{21}} \end{bmatrix} \\ \begin{bmatrix} S_{11} & S_{12} \\ S_{21} & S_{22} \end{bmatrix} = \begin{bmatrix} \dfrac{T_{21}}{T_{11}} & \dfrac{det(\mathbf{T})}{T_{11}} \\ \dfrac{1}{T_{11}} & -\dfrac{T_{12}}{T_{11}} \end{bmatrix} \end{cases} . \tag{1.13}$$

3. Thanks to T-matrices, since sub-networks can be easily cascaded through a simple multiplication, the T-matrix containing the propagation medium contribution, $\mathbf{T}^{\mathrm{air}}$, is obtained as

$$\mathbf{T} = \mathbf{T}_k^{\mathrm{MUX}}\, \mathbf{T}^{\mathrm{air}}\, \mathbf{T}_j^{\mathrm{A}/\Phi} \;\Rightarrow\; \mathbf{T}^{\mathrm{air}} = \left[\mathbf{T}_k^{\mathrm{MUX}}\right]^{-1} \mathbf{T} \left[\mathbf{T}_j^{\mathrm{A}/\Phi}\right]^{-1} . \tag{1.14}$$

4. Finally, $\mathbf{T}^{\mathrm{air}}$ is recast back into the respective S-matrix by using (1.13).

Two remarks concerning the use of T-matrices must be done:

- using T-matrices for cascading 2-port networks is an exact technique, *i.e.*, one does not introduce any error due, for instance, to disadaptation between consecutive networks (T-parameters, like S-parameters, do not depend on the characteristic impedance value and keep into account the actual impedance seen at the port of a component);
- T-matrices, like S-matrices, are a rigorous tool only if all the considered networks are linear with respect to input power. Such is the case for our components when using the VNA at $P_{\mathrm{out}} = +13$ dBm.

An example of the effectiveness of this technique is given in Fig. 1.11 for an S_{11} measurement without targets (incident field). Since this is a retrodiffusion measurement, the signal runs twice through the same path, the MUX path, shown in Fig. 1.11(a) (*cf.* Fig. 1.1). In the raw signal acquired by the VNA, whose time-domain complex-envelop in dB is plotted in Fig. 1.11(b), it is possible to individuate all the reflections due to the desadaptation between consecutive components, whose arrival times well correspond with their electrical path lengths (taken twice because of the retrodiffusion configuration). The resulting time-domain signal after applying the transmission matrix technique is in Fig. 1.11(c): the

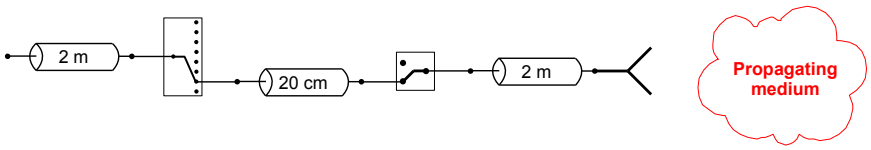

(a)

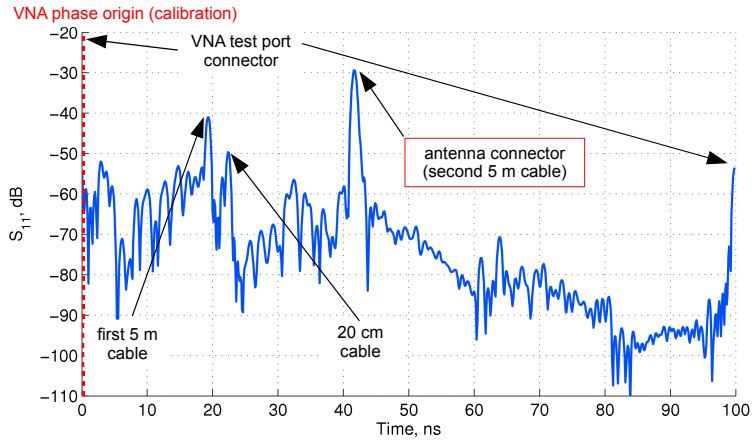

(b)

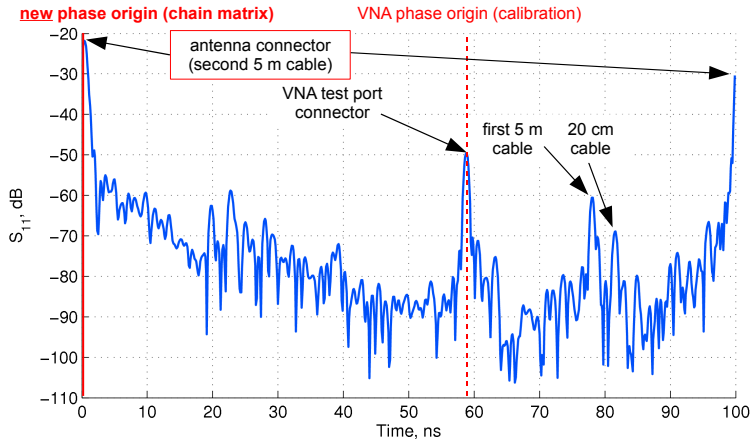

(c)

Figure 1.11: *Example of the effectiveness of the transmission matrix technique. For the S_{11} incident field measurement corresponding to the path in (a), the raw time-domain signal is in (b). After applying the chain matrix technique, the propagating medium portion of the signal is extracted, giving (c) with its new phase (time) origin. Notice that the switches in (a) have a negligible electrical length.*

new phase origin (t=0 ns) corresponds to the antenna connector interface (t≈43 ns in Fig. 1.11(b)), while all the desadaptation reflections have been time-shifted accordingly.

As a conclusion, by employing the transfer matrix formalism, only one calibration, not depending on the given measurement configuration, is required. This dramatically simplifies the utilization of the prototype. There is a price to pay, though, and it is the introduction of an error due to the VNA thermal drift described in §1.4.3. This happens because while the path database is measured once, at a given temperature, humidity, etc., it is systematically

used for retrieving the propagation part of the signal measured at - in principle different - ambient conditions. Nevertheless, it has been found that such an error is tolerable with respect to the precision given by the VNA and required by our algorithms. From now on, unless otherwise specified, any time-domain scattered signal will be plotted after the application of the technique just described.

1.6 Signal processing for scattering measurements

This paragraph is intended to cover all the signal processing that is systematically applied to the raw measured scattering data before utilizing it for any of the methods described in the following chapters (DORT, inverse scattering, etc.).

1.6.1 Differential measurements for antenna direct coupling reduction

As already mentioned in §1.4.3, for scattering measurements a differential mode is chosen. This means that for a given scattering experiment, two measurements are performed, the total field, E, with the targets in place and the incident field, E^{i}, without them. Then, their difference, $E^{\mathrm{s}} \triangleq E - E^{\mathrm{i}}$, called scattered field, is used [11, 29]. Indeed, although it is the scattered signal that is of interest, the incident field is in practice most often so high to "shadow" the scattered one, which *e.g.* for electrically small diffracting objects can be very small.

Although this can be easily understood for a transmission configuration (the emitting antenna directly illuminates the receiving one), it also true in reflection due to the *antenna direct coupling*. Such contribution can be identified as any signal transmitted by the emitting antenna and "sensed" at the receiving one beside the diffraction process. A special case is the reflection, due to imperfect adaptation, at the antenna connector in the case of a retrodiffusion measurement. In the time-domain, this contribution typically *precedes* the arrival of the scattered field echo and can therefore be filtered out. Nevertheless, due to all the imperfect adaptations in the prototype paths (see Fig. 1.11), the direct coupling signal enters the receiving channel and reverberates; at each connector reflection it loses power and finally vanishes below the VNA noise floor after some ns.

Let us observe both phenomena for each of the three possible signal types (*cf.* §1.3), namely a) retrodiffusion, $S_{jj}|_{j=1\ldots8}$ and $S_{ll}|_{l=9\ldots15}$, b) TRM array reflection, $S_{jk}|_{j,k=1\ldots8}$, and c) transmission, $S_{jl}|_{j=1\ldots8;l=9\ldots15}$. The time-domain complex envelope in the case of the scattering of a metallic cylinder is shown in Fig. 1.12. In a) and b), the direct antenna coupling is immediately visible during the initial 2-3 ns, whereas at ≈4 ns (corresponding to 2×60 cm=120 cm round-trip distance) the target echo appears, followed by the reverberation in the respective prototype channels. Notice how the differential measurement reduces by ≈40 dB the initial coupling contribution, letting the scattering signature emerge. On

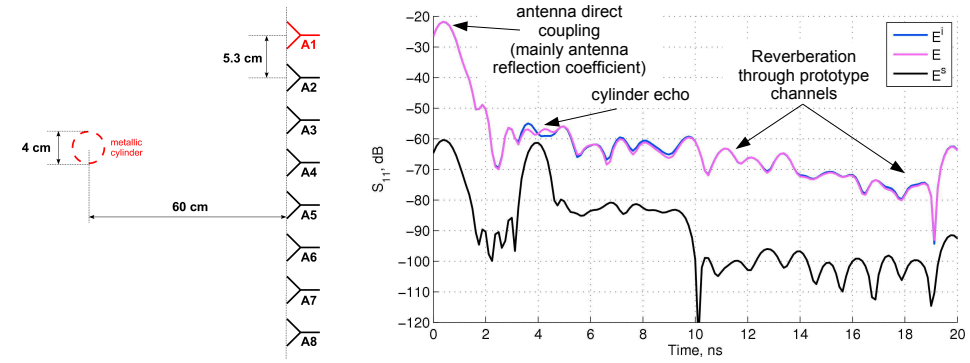

(a) retrodiffusion configuration, S_{11}

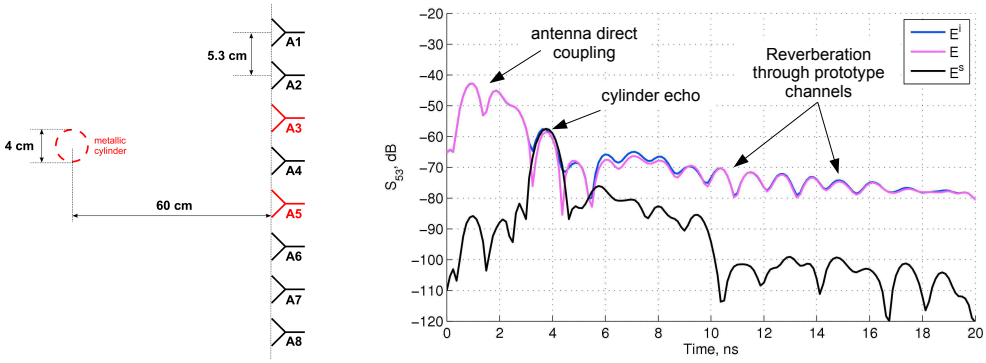

(b) reflection configuration, S_{53}

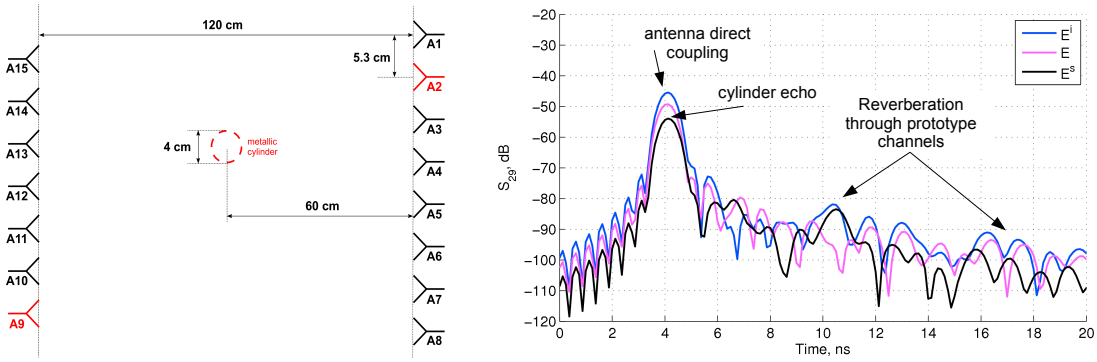

(c) transmission configuration, S_{29}

Figure 1.12: *Measured time-domain complex envelope of a (a) retrodiffusion, (b) reflection, and (c) transmission signals, in the case of the scattering of a metallic cylinder.*

the other hand, for the transmission configuration (Fig. 1.12(c)), nothing is received by A_2 until the direct signal (incident field) emitted by A_9 and the scattering contribution both arrive almost at the same time. Here again, using the $E - E^s$ difference helps in retrieving the target echo.

1.6.2 FFT window and time-gating

There is a simple signal processing routine, common to any of these configurations, that is applied to the raw signals measured by the VNA. It can be described as follows for a

generic couple of total/incident field measurements, $E(\omega)$ and $E^{\mathrm{i}}(\omega)$:

1. apply the transfer matrix technique in §1.5.1 to retrieve the "air" part of each measurement,
$$\begin{cases} E(\omega) \to E^{\mathrm{air}}(\omega) \\ E^{\mathrm{i}}(\omega) \to E^{\mathrm{i;air}}(\omega) \end{cases} ; \tag{1.15}$$

2. evaluate the scattered field by taking the difference
$$E^{\mathrm{s;air}}(\omega) = E^{\mathrm{air}}(\omega) - E^{\mathrm{i;air}}(\omega) \ ; \tag{1.16}$$

3. through an FFT frequency-domain window, $W_\omega(\omega)$, go to time domain:
$$E^{\mathrm{s;air}}(\omega) W_\omega(\omega) \quad \longrightarrow \quad e^{\mathrm{s;air}}(t) * w_\omega(t) \ ; \tag{1.17}$$

4. apply a time-gate, $w_t(t)$, to remove the initial and final parts of the signal, containing direct antenna coupling and parasite reverberations in the prototype channels, respectively:
$$\left[e^{\mathrm{s;air}}(t) * w_\omega(t)\right] w_t(t) \ ; \tag{1.18}$$

5. go back to the frequency domain (no additional FFT window is needed since $w_t(t)$ already acts as such):
$$\left[e^{\mathrm{s;air}}(t) * w_\omega(t)\right] w_t(t) \quad \longrightarrow \quad \left[E^{\mathrm{s;air}}(\omega) W_\omega(\omega)\right] * W_t(\omega) \ . \tag{1.19}$$

Some details on the choice of $W_\omega(\omega)$ and $w_t(t)$ are presented next. Concerning the former, the choice must be done by observing its time-domain transform, $w_\omega(t)$, and its impact on the scattered signal through the time-convolution in (1.17). The classical trade-off between main lobe width *vs.* side lobe attenuation drives the choice. The first controls the achievable time - hence space - resolution; the second the impact, in the time domain, of strong echoes "polluting" small ones. With reference to Fig. 1.12, the required side lobe attenuation is driven by the ratio between antenna direct coupling residual after difference and minimum detectable target echo. The worst case is the retrodiffusion case, where the amplitude of the antenna coupling signal is the highest. In Fig. 1.12(a), for instance, it is around -60 dB, whereas the noise floor appears at around -100 dB. This gives a 40 dB ratio at a minimum time distance of 2 ns (corresponding to a target at a distance of 30 cm). Fig. 1.13 shows two windows satisfying this requirement: the *hann* and the *lanczos* (or *sinc*) windows, the latter being the one used for plotting Fig. 1.13. On the other hand, their main lobes reach an attenuation of 3 dB (half power) at, respectively, 0.5 and 0.42 ns, giving a space resolution of 10.5 and 9 cm, respectively[3]. Unless otherwise stated, the *lanczos*

[3]This distance must of course be compared to the measurement configuration. For instance, given a retrodiffusion measurement and two identical targets placed on the same antenna-target line, the actual resolution is halved.

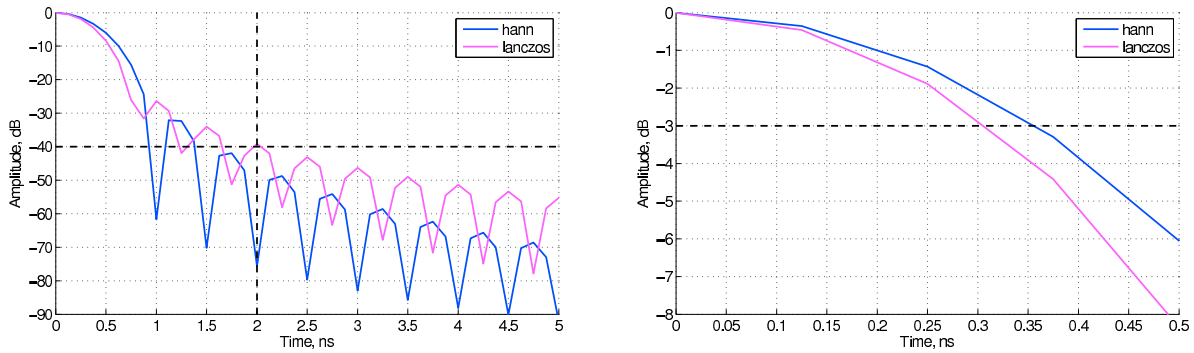

(a) (b)

FIGURE 1.13: *FFT of two frequency-domain windows $W_\omega(\omega)$ (hann and lanczos windows) satisfying (a) the side lobe attenuation requirement of 40 dB at $t = 2$ ns. In (b), the space resolution can be derived from the main lobe attenuation at 3 dB.*

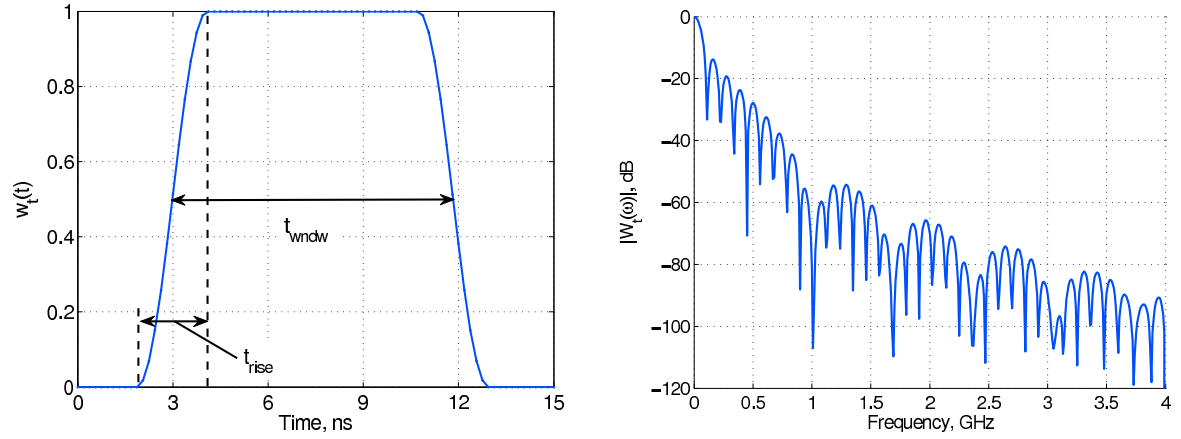

(a) (b)

FIGURE 1.14: *Tukey (tapered-cosine) window chosen as time-gate window in (a) time domain and (b) its FT.*

window has been adopted, which writes as

$$W_\omega(\omega) = \begin{cases} 0\ , & 0 \le \omega < \omega_m \\ sinc\left(\dfrac{2\,(\omega - \omega_m)}{\omega_M - \omega_m} - 1\right)\ , & \omega_m \le \omega \le \omega_M \end{cases}\ , \tag{1.20}$$

where $\omega_m = 2\pi\ 2{\cdot}10^9$ rad/s and $\omega_M = 2\pi\ 4{\cdot}10^9$ rad/s, corresponding to the lower and higher frequencies used, respectively.

As for the time-gating window, $w_t(t)$, it has no particular requirement. A good choice seems to be the *tukey* (or tapered-cosine) window, which has the advantage of having a flat "plateau" surrounded by cosine-shaped rise and fall parts. As a consequence, outside of the rise/fall part, the signal integrity is preserved. An example is given in FIG. 1.14, both in time and frequency domain. The start and stop time instants, t_{start} and t_{stop}, resepectively, within which the signal is gated must be chosen. With respect to the former, the goal is to

cut off the direct antenna coupling signal present in the first time instants. In the worst case (S_{18}), this effect has a duration equal to twice the antenna array length (2×35 cm) divided by c_0, *i.e.*, approximately 2.3 ns. Assuming that coupling from the farthest antennas is already sufficiently low, and exploiting the attenuation of the rise part of $w_t(t)$, we have set $t_{\text{start}} = 2$ ns. This ultimately sets a blind detection range of 30 cm in reflection and 60 cm in transmission. Instead of directly setting t_{stop}, it is preferable to deal with the mid-height length t_{wndw} in FIG. 1.14(a). It must be large enough to contain all the scattering signature and small enough to cut out all the signal queue containing reverberation in the prototype channels. Generally, a good enough value is around 9 ns (equivalent to 135 cm antenna-target distance in reflection and twice in transmission). Finally, the tapering parameter α, defined as the ratio between the lengths of the tapered (both rise and fall) and the constant portions of the window, is fixed as a function of the signal bandwidth f_{bw} (2 GHz):

$$\alpha = \frac{2\,t_{\text{rise}}}{t_{\text{wndw}} - t_{\text{rise}}}, \text{ where } t_{\text{rise}} = 3/f_{\text{bw}} \ , \tag{1.21}$$

where the factor '3' has been chosen to impose a rise/fall speed (or *slew-rate*) slightly lower than the one belonging to a pulse with bandwidth f_{bw} and already "slowed up" by the application of $W_\omega(\omega)$.

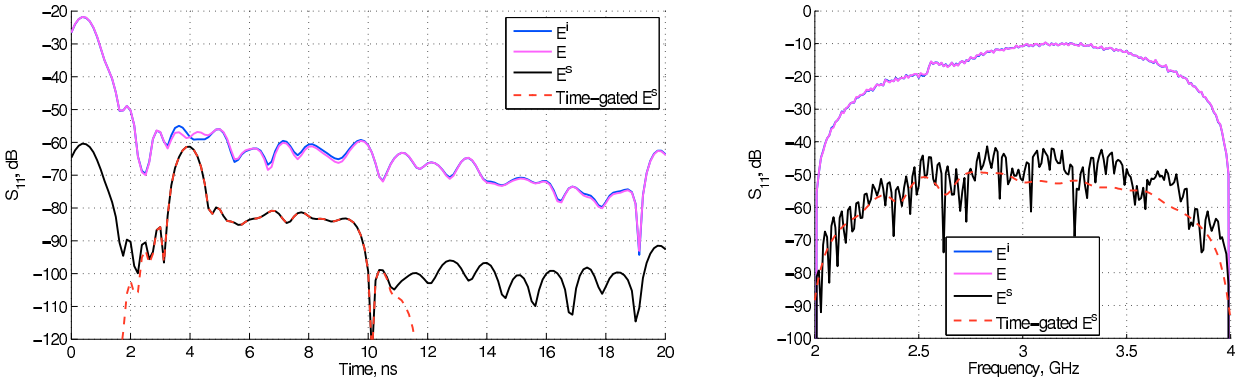

(a) (b)

FIGURE 1.15: *Effect of signal processing in the (a) time and (b) frequency domain for the retrodiffusion S_{11} measurement shown in* FIG. *1.12(a).*

In FIG. 1.15 an example of the effect of the signal processing routine is presented. The measurement configuration is the one in FIG. 1.12(a). The total, incident, and scattered fields are shown, and the effect of the time-gating is also visible (red dashed trace). Notice that the signals are plotted after the application of the FFT frequency-domain window, $W_\omega(\omega)$, which explains why in FIG. 1.15(b) the low and high frequency ends are dumped.

1.6.3 Drift correction

As described in §1.4.3, for scattering measurements the VNA thermal drift overules the theoretically available dynamic range, thus imposing the minimum detectable signal level.

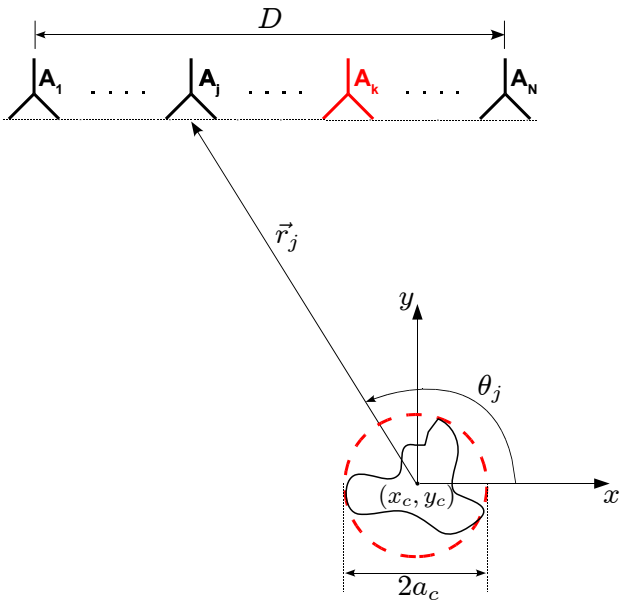

FIGURE 1.16: *Reflection setup used as reference for the drift correction algorithm.*

To mitigate this problem, a drift correction algorithm has recently been reported which has proven to be effective for the almost circular setup of Institut Fresnel [59, 61] and even for a measurement line [62].

The correction algorithm is based on the work by Bucci and co-workers in [63], whose underlying hypotheses are:

- the target is sufficiently far from the antennas (at least $\lambda_0/2$);
- antennas are considered isotropic;
- the center (x_c, y_c) and the radius a_c of the smallest circle (sphere for 3D scatterers) encircling the target support are known (see FIG. 1.16)[4]. This of course implies clean-enough data to be able to retrieve such parameters by any of the methods presented in §2 or even in §3.

The authors have shown that, for a given source and at a given frequency, the scattered field measured at different locations has a limited spatial bandwidth, provided the field used for the bandwidth computation is the so-called *reduced* field [64]. This is defined by extracting from the raw data an analytically computed phase function ψ. In free-space, with an $e^{i\omega t}$ time-dependency, and for a measurement line along the x-axis [64], the reduced field associated to the source A_k is given by

$$\tilde{E}_k(\omega; x_j) \triangleq E_k(\omega; x_j) e^{i\psi(x_j)}, \quad \text{where} \quad \psi(x_j) = k_0 \sqrt{r_j^2 - a_c^2} - k_0 a_c cos^{-1}\left(\frac{a_c}{r_j}\right), \quad (1.22)$$

x_j and r_j are the x-coordinate and the target distance belonging to the receiver A_j (FIG. 1.16), and $k_0 = 2\pi/\lambda_0$ is the wavenumber in vacuum.

[4]If multiple targets are present, the position and the radius must be evaluated with respect to the smallest circle encircling *all* the targets.

Given this definition, the correction is applied for each transmitting antenna A_k and at each frequency ω. With reference to the drift model developed and analyzed in (1.10)-(1.12), it simply writes as

$$\tilde{E}_k^{\mathrm{s;corr}}(\omega; x_j) = \tilde{E}_k(\omega; x_j) - be^{i\phi}\tilde{E}_k^{\mathrm{i}}(\omega; x_j) \ , \tag{1.23}$$

where for notation simplicity (b, ϕ) is used instead of $(b_k(\omega), \phi_k(\omega))$. The value of this complex coefficient is determined by minimizing the spatial bandwidth of the corrected scattered field, $B_k(\omega)$, that can be obtained by [65, 66]

$$B_k^2(\omega; b, \phi) = \frac{\int_{-\infty}^{\infty} \kappa_x^2 |\hat{E}_k^{\mathrm{s;corr}}(\omega; \kappa_x)|^2 d\kappa_x}{\int_{-\infty}^{\infty} |\hat{E}_k^{\mathrm{s;corr}}(\omega; \kappa_x)|^2 d\kappa_x} \ , \tag{1.24}$$

where $\hat{E}_k^{\mathrm{s;corr}}(\omega; \kappa_x)$ is the spatial Fourier Transform along x_j of $\tilde{E}_k^{\mathrm{s;corr}}(\omega; x_j)$ defined as

$$\hat{E}_k^{\mathrm{s;corr}}(\omega; \kappa_x) = \int_{-\infty}^{\infty} \tilde{E}_k^{\mathrm{s;corr}}(\omega; x_j) e^{i\kappa_x x_j} dx_j \ . \tag{1.25}$$

1.6.3.1 Implementation of the algorithm

To the best of our knowledge, the drift correction algorithm just described was only applied in [59] and [62]. In both cases, a bistatic setup with a single pair of Tx/Rx antennas is used, so that a *virtual* array is obtained by displacing each of them. A circular array with an aperture angle $\theta \approx 260$ deg and $N = 261$ receiving antenna positions is built in the first case, a linear one with $\theta \approx 70$ deg and $N = 41$ in the second. With respect to this configurations, the present setup presents two additional difficulties:

- antennas are directive enough to require taking into account their radiation pattern;
- very small aperture angle and number of receiving antennas are available, θ varying from 50 to 20 deg according to the target-array distance, and $N = 8$.

The first item invalidates the isotropicity hypothesis under which the bandwidth limitedness result is obtained. Thus, since anisotropicity alters the scattered field measured by the receiving antennas, the field should be brought back to the one measured by hypothetical isotropic antennas. On top of this, since a *real* antenna array is used here, antennas do couple each other, resulting in an altered radiation pattern that should be compensated as well. The second point, on the other hand, might be very limiting since with a small array as the one utilized here, one has access only to a very poor spatial frequency resolution ($\Delta\kappa_x = 2\pi/L$, L being the array length - see FIG. 1.16).

The sequence of operations performed to implement the drift correction while dealing with the aforementioned issues is presented next. Every step is performed for each transmitting antenna A_k and at each frequency ω, by considering all the receiving antennas at once. The index k and the receiving antenna dependency x_j have been removed for simplicity.

1. starting from the quantities in (1.15) and removing for conciseness the subscript "air", the total and incident reduced fields, $\tilde{E}(\omega)$ and $\tilde{E}^{\mathrm{i}}(\omega)$, are calculated according to (1.22);

2. assuming an antenna radiation pattern $RP(\omega) \triangleq RP(\omega; \vec{r}_j)$ taking into account the coupling effects is experimentally retrieved (the way this is done is described in detail in §1.7.2), an antenna pattern correction is applied so to recreate the needed isotropicity requirement on the receiving antennas

$$\frac{\tilde{E}(\omega)}{RP(\omega)} \quad \text{and} \quad \frac{\tilde{E}^{\mathrm{i}}(\omega)}{RP(\omega)} \; ; \tag{1.26}$$

3. using (1.25), the spatial spectra $\hat{E}(\omega)$ and $\hat{E}^{\mathrm{i}}(\omega)$ are obtained;

4. "half" of the time-gating detailed in (1.17),(1.18), and (1.19) is performed. By "half", we mean that $\sqrt{w_t(t)}$ is used, since - similarly to the root raised cosine filtering used in telecommunication systems - the other "half" will be applied after the drift correction. Notice that this step implies an IFFT, the actual application of $\sqrt{w_t(t)}$, and a final FFT back to the frequency domain;

5. apply the correction by minimizing the bandwidth in (1.24); the minimization is performed through a Polak-Ribière Conjugate Gradient algorithm whose step search is simply dealt with Matlab's `min` function, and the final corrected scattered field is $\hat{E}^{\mathrm{s;corr}}(\omega)$;

6. through an inverse spatial FFT the corrected reduced scattered field, $\tilde{E}^{\mathrm{s;corr}}(\omega)$, is retrieved;

7. the antenna radiation pattern is applied back

$$\tilde{E}^{\mathrm{s;corr}}(\omega) RP(\omega) \; ; \tag{1.27}$$

8. the reduced field phase factor in (1.22) is removed, giving $E^{\mathrm{s;corr}}(\omega)$;

9. the other "half" of the time-gating is performed (implying other frequency $\rightarrow$ time $\rightarrow$ frequency FFTs).

Notice that the FFT frequency-domain window $W_\omega(\omega)$ in (1.20) can only be applied at step 4., whereas at step 9. a rectangular window (equivalent to no window) can be used. Indeed, it is necessary to use an FFT window with low temporal sidelobes *before* the time-gating of step 4., whereas at step 9. the strong antenna direct coupling signal has already been gated out and a rectangular FFT window is sufficient. Finally, the need for the "half" time-gating can be justified as follows. It is important, in step 4., to use a time-gate *before* the actual correction. In effect, the correction being run *at each frequency*, all the time instants contribute to the final minimizing (b, ψ) value. It is therefore necessary to cut out those initial and final parts of the signal containing residual antenna direct coupling and reverberation through the prototype channels, which would otherwise influence the correction. Nevertheless, steps 7. and 8. act separately on each frequency component, thus

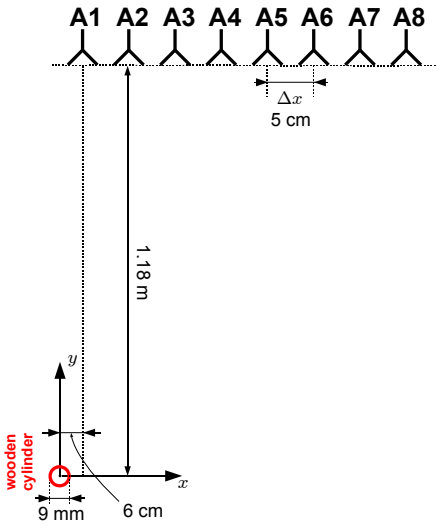

FIGURE 1.17: *Reflection measurement setup used to test the drift correction algorithm.*

partially "polluting" (when observing $E^{\mathrm{s;corr}}$ in the time domain) the time-gating of step 4. The result is an imperfect gating at the initial and final time instants, that must be cleaned out by applying the other "half" of the time-gate.

Experimental results

In order to validate the algorithm, we have used the measurement setup in FIG. 1.17, consisting of a reflection configuration where the scattering object is a wooden cylinder with radius $r_c = 4.5$ mm, relative permittivity $\varepsilon_r \approx 2$, and placed at a distance 1.16 m from the measurement line. Let us first study the characteristics of the discrete spatial spectrum $\hat{E}^{\mathrm{s;corr}}(\omega)$ in (1.25). The resolution $\Delta\kappa_x$ and the maximum accessible frequency K_x can be written as

$$\Delta\kappa_x = \frac{2\pi}{(N-1)\Delta x} = \frac{2\pi}{(N-1)\lambda_0/2} = \frac{2}{N-1}k_0 \ , \tag{1.28a}$$

and

$$K_x = \left\lceil \frac{N}{2} - 1 \right\rceil \Delta\kappa_x \approx k_0 \ , \tag{1.28b}$$

where Δx is the spacing between the antennas considered equal to $\lambda_0/2$ at 3 GHz (see FIG. 1.1). Notice how small is the resolution $\Delta\kappa_x$ given the few available antennas ($N = 8$).

In FIG. 1.18, some results are presented. In (a) and (b), for A_4 as transmitting antenna and A_8 as receiving one (S_{84}), the time- and frequency-domain signals before and after the correction are shown, respectively. The gain in dynamic range, especially visible in the time-domain plot, reaches up to 10 dB; as a result, the corrected frequency-domain scattered field (green full line) is considerably smoother than the time-gated uncorrected signal (red dashed line), testifying a lesser amount of noise in the signal. FIG. 1.18(c) shows the effect of the correction on the spatial spectrum at 3 GHz, again for A_4 as transmitting antenna. While a reduction of the sidelobes can indeed be observed for all indices but one,

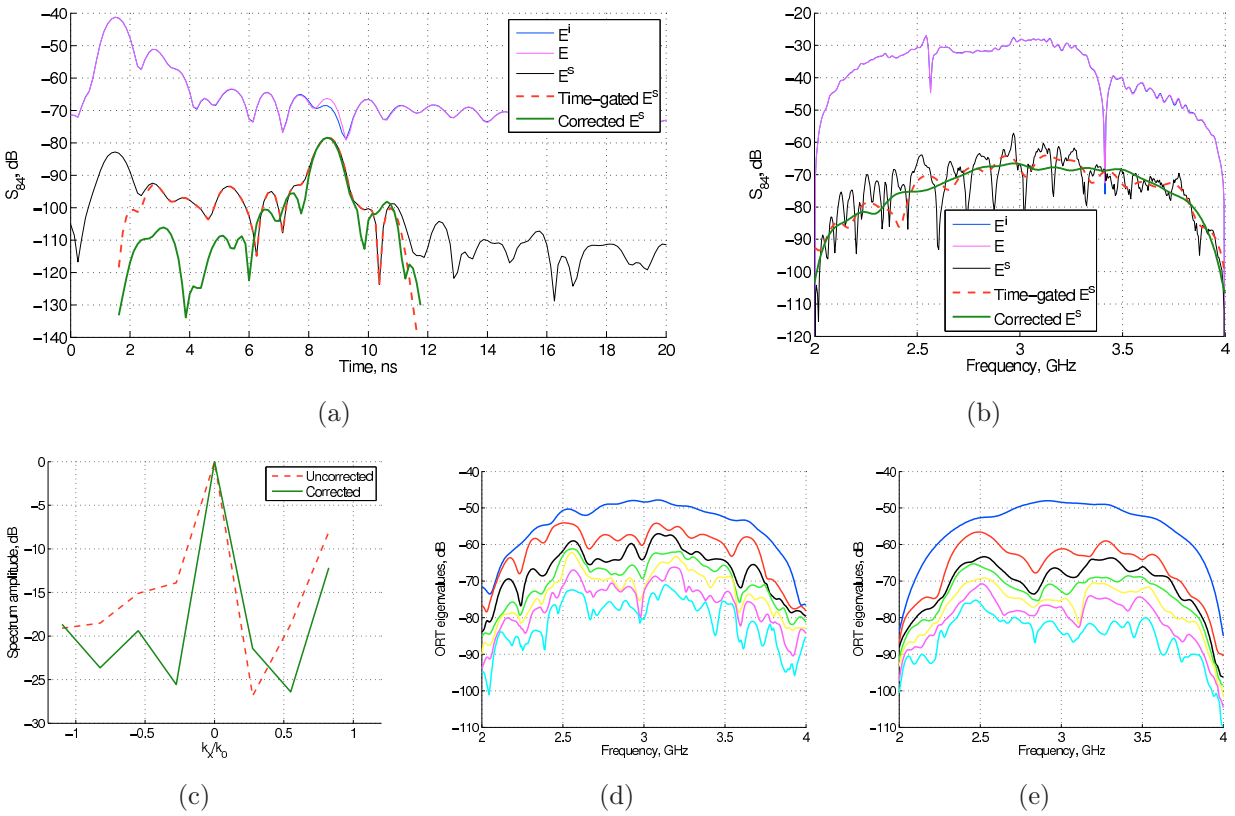

Figure 1.18: *Impact of the drift correction algorithm for the setup in* Fig. *1.17. (a) and (b) are the time- and frequency-domain S_{84} signals before and after the correction. In (c) the spatial spectrum bandwidth reduction at 3 GHz can be appreciated. In all these cases, A_4 is the transmitting antenna. (d) and (e) finally show the DORT eigenvalues distribution as a function of frequency without and with the drift correction, respectively.*

it can be noticed how poor is the κ_x resolution due to the very small array aperture; indeed, the actual reduced scattered bandwidth B_{κ_x} is most probably smaller than $0.25k_0$.

Finally, Fig. 1.18(d) and (e) show the eight DORT eigenvalues (see §2.3.3) as a function of frequency for the uncorrected and corrected case, respectively. The correction impact is again on the smoothing of the largest eigenvalue, but also in the increase of the ratio among the two largest ones. Indeed, the first being associated to a sort of target RADAR cross section and the others mainly to the noise power (the antisymmetric relative to this configuration is theoretically much lower), this can be seen as yet another sign of dynamic range improvement.

1.7 Experimental characterization of the antennas

The characterization of the ETS antennas is a necessary step before performing any experiment. In particular, if one wants to numerically simulate the field radiated by the antennas, a mathematical model must be available. By characterization and modeling of

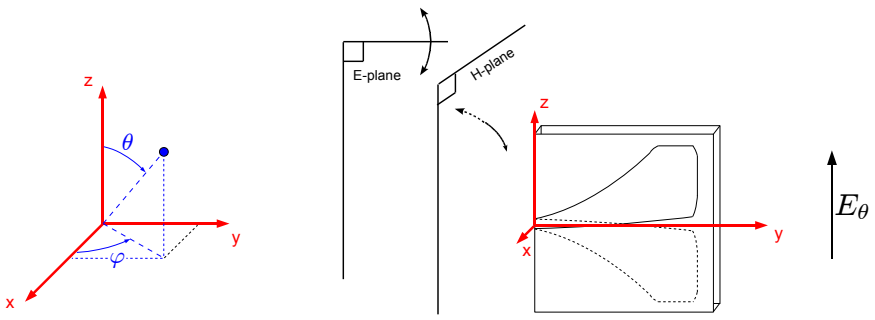

FIGURE 1.19: *Axes and angles convention used for defining the radiation pattern of ETS antennas.*

the antennas it is meant here the knowledge of a) their radiation pattern and b) their time-domain behavior, the latter especially important because of the wide frequency band used.

1.7.1 Far-field, uncoupled antenna

As a first step, one ETS antenna has been characterized at the anechoic chamber of LEAT (much bigger than ours), in Sophia Antipolis. Measurements have been realized in far-field conditions with one single ETS antenna (no coupling effects). The axes and angles convention used here are those in FIG. 1.19. Hence, the antennas being vertically polarized, $E_\theta \triangleq \mathbf{E} \cdot \hat{\boldsymbol{\theta}}$ is the main (or co-) polarization component of the electric field, whereas $E_\varphi \triangleq \mathbf{E} \cdot \hat{\boldsymbol{\varphi}}$ is the cross-polarization. Furthermore, since the experiments are all performed at elevation angle $\theta = 90$ deg (no elevation) and only 2D targets are employed (theoretically infinite along the z-axis), the only pertinent quantity is the electric field in the H-plane, that is, the xOz plane describing the azimuthal behavior of the antennas at $\theta = 90$ deg. With respect to the measured radiation patterns between 2 and 4 GHz shown in FIG. 1.20, some observations can be drawn:

1. concerning E_θ, the antennas are rather isotropic in the vicinity of the broadside direction, namely 60 deg $\leq \varphi \leq$ 120 deg, with amplitude variations equal at most to 3 dB;
2. the cross-polarization rejection, defined as E_θ/E_φ, is almost always beyond 20 dB in the same azimuth range;
3. despite the results in FIG. 1.19 are drawn from far-field measurements, the pattern values at $\varphi = 0, 180$ deg (end-fire direction), give some insights on the behavior of the antennas once they are arranged into an array. For instance, for frequencies up to 2.8 GHz at least, the antennas are prone to couple each other rather strongly, since the co-polarization amplitude at end-fire is around 3 dB, whereas for the highest frequencies much less coupling can be expected.

Finally, the gain curve is shown in FIG. 1.21(a). Although a "strange" negative-gain region can be observed around 2.2 GHz, it can be explained by the "hole" in directivity visible at

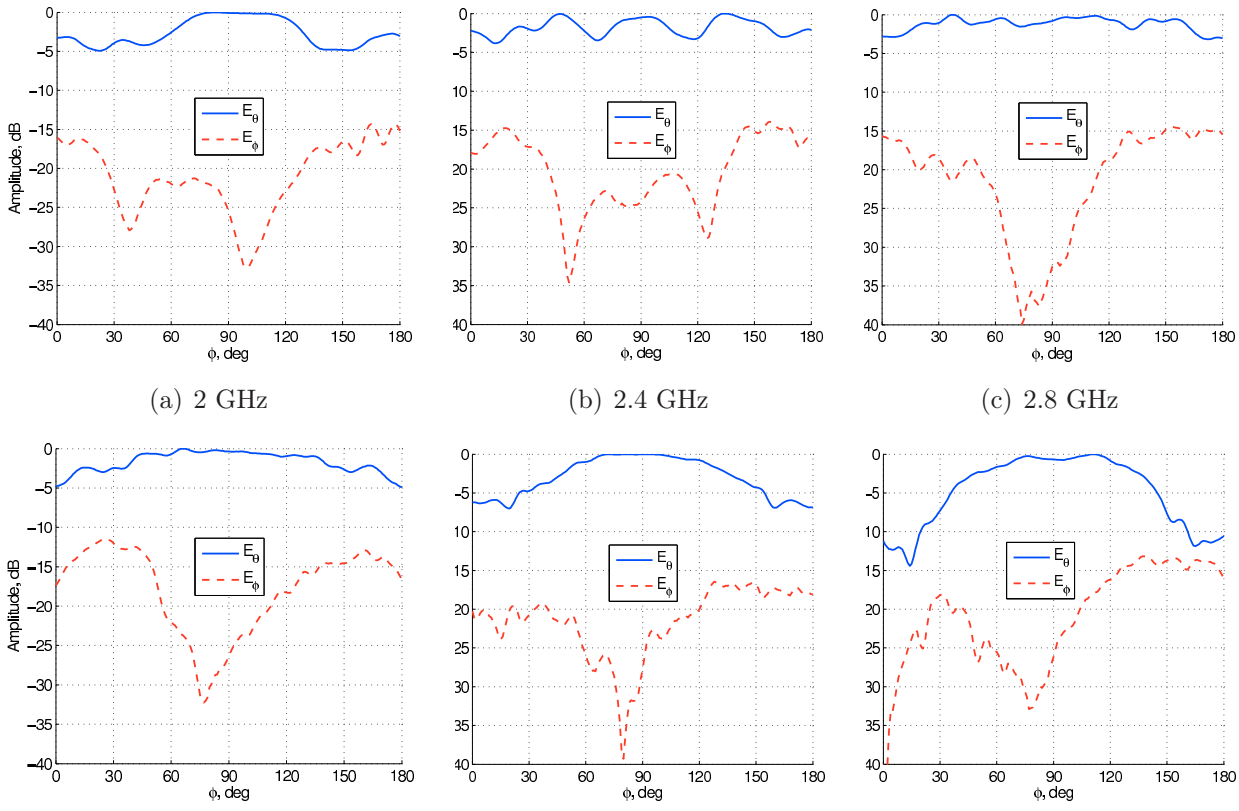

(a) 2 GHz (b) 2.4 GHz (c) 2.8 GHz

(d) 3.2 GHz (e) 3.6 GHz (f) 4 GHz

FIGURE 1.20: *H-plane far-field radiation patterns of the ETS antennas measured at LEAT in Sophia Antipolis.*

broadside in FIG. 1.21(b). Elsewhere in the band, a gain between 7 and 2 dB is measured.

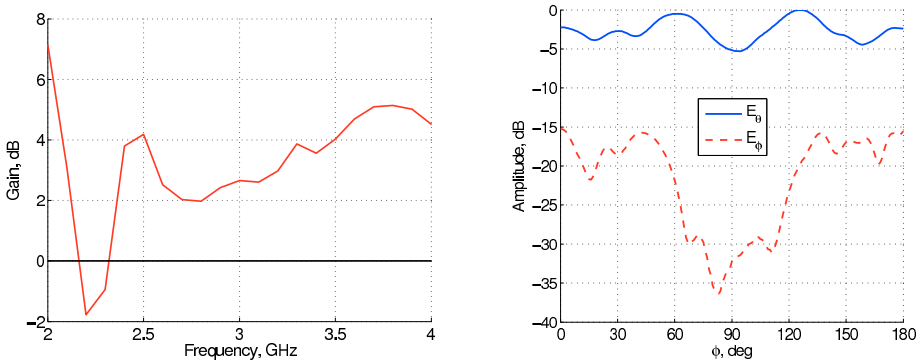

(a) (b)

FIGURE 1.21: *(a) Gain of the ETS antennas and (b) H-plane far-field radiation pattern at 2.2 GHz measured at LEAT in Sophia Antipolis.*

1.7.2 Arrayed antennas

When the antennas are placed into an array their characteristics are altered because of coupling. This has to be taken account in the modeling procedure, and is especially

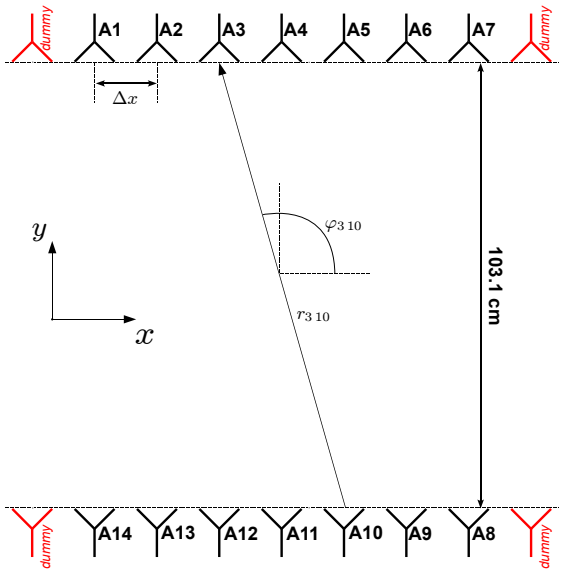

FIGURE 1.22: *Measurement setup for the characterization of the antennas.*

important for quantitative inverse scattering, where a quantitative description of the field radiated by the antennas as well as their radiation pattern at reception is required. It is therefore mandatory to model the antennas starting from data acquired in the very same array configuration used for any of the measurements.

The antenna characterization measurement setup is shown in FIG. 1.22. It is a transmission setup with two arrays made of seven antennas each. Dummy antennas have also been used at the edges of each array, in order to somehow "equalize" the coupling impact on A_1 and A_7 to that on $A_j|_{j=2,6}$ (and analogously for array-2). Two antenna spacings have been tested to further study the impact of coupling: $\Delta x = \{5.3, 6.55\}$ cm.

The first goal is to find a mathematical expression for each measured parameter, S_{jl}^{cal} (*e.g.*, $S_{3\,10}^{\text{cal}}$ in FIG. 1.22), in terms of transmitted (Tx) and received (Rx) electric fields. For this purpose, the *antenna effective length* $\vec{l}_{\text{e}}(\theta, \varphi)$ is introduced. It is defined as "the ratio of the magnitude of the open-circuit voltage developed at the terminals of the antenna to the magnitude of the electric field strength in the direction of the antenna polarization [67]", and is thus a vector with 3 components associated with the spherical coordinate system. For a generic field vector $\vec{E}(\theta, \varphi)$ impinging on a receiving antenna with azimuth and elevation angles θ and φ, respectively, we have then

$$V_{\text{oc}} = \vec{E}(\theta, \varphi) \cdot \vec{l}_{\text{e}}^{\,\text{Rx}}(\theta, \varphi) \ , \tag{1.29}$$

where V_{oc} is indeed the open-circuit voltage at the antenna terminals and $\vec{l}_{\text{e}}^{\,\text{Rx}}$ is the receiving antenna effective length.

Because of reciprocity, the effective length can be used for the Tx radiation pattern as well. Solving the Helmholtz equation and including in the effective length any angular dependency, the radiated field $\vec{E}(\theta, \varphi)$ at a distance r may then be written as

$$\vec{E}(\theta, \varphi) = -i\omega\mu_0 \frac{e^{-ikr}}{4\pi r} I_{\text{in}} \vec{l}_{\text{e}}^{\,\text{Tx}}(\theta, \varphi) \ , \tag{1.30}$$

where I_{in} is the current injected into the emitting antenna. By merging (1.29) and (1.30), we obtain

$$V_{\text{oc}} = -i\omega\mu_0 \frac{e^{-ik_0 r}}{4\pi r} I_{\text{in}} \vec{l}_{\text{e}}^{\,\text{Tx}}(\theta,\varphi) \cdot \vec{l}_{\text{e}}^{\,\text{Rx}}(\theta,\varphi) \ . \tag{1.31}$$

For the present setup, the previous equation can be simplified in virtue of the following remarks:

- since the antennas are vertically polarized, that is, the cross-polarization component of the field can be neglected, both $\vec{l}_{\text{e}}^{\,\text{Rx}}$ and $\vec{l}_{\text{e}}^{\,\text{Tx}}$ can be approximated by scalar quantities;
- neglecting mismatch between antennas due to the fabrication process, it is assumed that $l_{\text{e}}^{\text{Tx}} = l_{\text{e}}^{\text{Rx}} \triangleq l_{\text{e}}$;
- only the azimuthal dependency φ needs to be considered, since, as already stated, the experiments are always performed with the antennas at elevation angle $\theta = 90$ deg and with 2D targets.

In the end, for the measured S_{jl}^{cal} parameter, (1.31) becomes

$$V_{\text{oc}} = -i\omega\mu_0 \frac{e^{-ik_0 r_{jl}}}{4\pi r_{jl}} I_{\text{in}} l_{\text{e}}^2(\varphi_{jl}) \ . \tag{1.32}$$

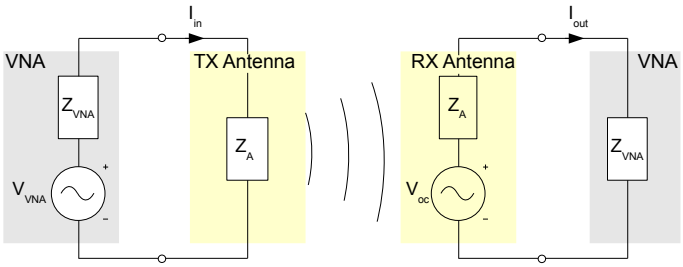

Figure 1.23: *Circuit equivalents of transmitting and receiving antennas.*

Now, the S-parameter measured by the VNA is a current (or voltage) ratio. V_{oc} must then be related to the current I_{out} actually read by the VNA. With respect to the discrete-parameters circuit model in Fig. 1.23, where Z_{VNA} is the input/output impedance of the VNA, assumed to be equal to 50 Ω, and Z_{A} is the input/output impedance of the antenna including the actual radiation impedance (the one responsible of the radiated/received field) and the ohmic lossy part, it follows that

$$I_{\text{out}} = \frac{V_{\text{oc}}}{Z_{\text{A}} + Z_{\text{VNA}}} \triangleq \eta \frac{V_{\text{oc}}}{50} \ , \tag{1.33}$$

where η plays the role of an efficiency factor independent of φ that takes into account, through Z_{A}, the desadaptation of the antennas.

Before carrying on, notice that although the effective length is defined in literature as a far-field quantity, which is confirmed from the modelization in (1.30), the S_{jl}^{cal} are not necessarily measured under far-field conditions. To cope with this, it is sufficient to interprent l_{e} as a generic quantity describing the discrepancy between the field measured at far-field

by an isotropic antenna, represented by the e^{-ik_0r}/r term, and the one actually measured under whatsoever condition. It is then convenient to explicitly add an r_{jl} dependency to l_e, which, putting all the results together, gives

$$S_{jl}^{\mathrm{cal}} = \frac{I_{\mathrm{out}}}{I_{\mathrm{in}}} = -i\eta\frac{\omega\mu_0}{50}\frac{e^{-ik_0r_{jl}}}{4\pi r_{jl}}l_\mathrm{e}^2(r_{jl},\varphi_{jl}) = A\omega\frac{e^{-ik_0r_{jl}}}{r_{jl}}l_\mathrm{e}^2(r_{jl},\varphi_{jl}) \ , \tag{1.34}$$

where A regroups all the constant quantities.

With respect to FIG. 1.22, 49 (7×7) measurements are available, and they can be recast through (1.34) into a set of 49 l_e values. Nevertheless, the sought quantity is the field radiated by an antenna at "any" point in space, that is, a *continuous* description of the co-polarization component of the field, $E_\theta(r,\theta,\varphi)$. Under free-space conditions, this quantity verifies the Helmholtz equation outside the volume of the antenna,

$$\nabla^2 E_\theta(r,\theta,\varphi) + k_0^2 E_\theta(r,\theta,\varphi) = 0 \ , \tag{1.35}$$

where k_0 is the wavenumber of the propagation medium, considered homogeneous. The solution of this equation can be found through the methof of separation of variables. It can then be written as the product of two functions, one with a radial dependency only, r, and another function of the angular variables, (θ,φ). Applying the Sommerfeld condition (or causality condition if expressed in the time-domain) to the result and assuming an $e^{i\omega t}$ time-dependency, the result is

$$E_\theta(r,\theta,\varphi) = \sum_{m=0}^{\infty}\sum_{n=-m}^{m}\gamma_{m,n}h_m^-(k_0r)Y_{m,n}(\theta,\varphi) \ , \tag{1.36}$$

where h_m^- is the spherical Hankel function of order m and second kind ($h_m^- = H_{m+1/2}^-$), $Y_{m,n}$ is the $(m,n)^{\mathrm{th}}$ spherical harmonic, and $\{\gamma_{m,n}\}$ are the set of coefficients whose values depend on the boundary conditions of the problem [68]. The Hankel functions bear the e^{-ik_0r}/r radial dependency, the spherical harmonics describe the multipolar behavior of the field with respect to θ and φ.

To find the coefficients $\gamma_{m,n}$, the retrieved l_e values need to be related to (1.36). This is done by simply equating (1.36) and (1.30). Then, taking into account the fact that every measurement is made at $\theta = \pi/2$, one can write for each $(j,l)^{\mathrm{th}}$ measurement

$$\omega\frac{e^{-ik_0r_{jl}}}{r_{jl}}l_\mathrm{e}(r_{jl},\varphi_{jl}) = \sum_{m=0}^{\infty}\sum_{n=-m}^{m}\gamma_{m,n}h_m^-(k_0r_{jl})Y_{m,n}(\pi/2,\varphi_{jl}) \ , \tag{1.37a}$$

where the constants in (1.30) do not explictly appear and will therefore be contained in the $\gamma_{m,n}$. EQ. (1.37a) can be recast into the linear system

$$\mathbf{l_e} = \mathbf{H}\boldsymbol{\gamma} \ , \tag{1.37b}$$

where $\mathbf{l}_\mathrm{e}$ is the 49-element vector made of the left-side member of (1.37a), $\mathbf{H}$ is a matrix containing the Hankel function-spherical harmonic product, and $\boldsymbol{\gamma}$ is the vector of the unknowns.

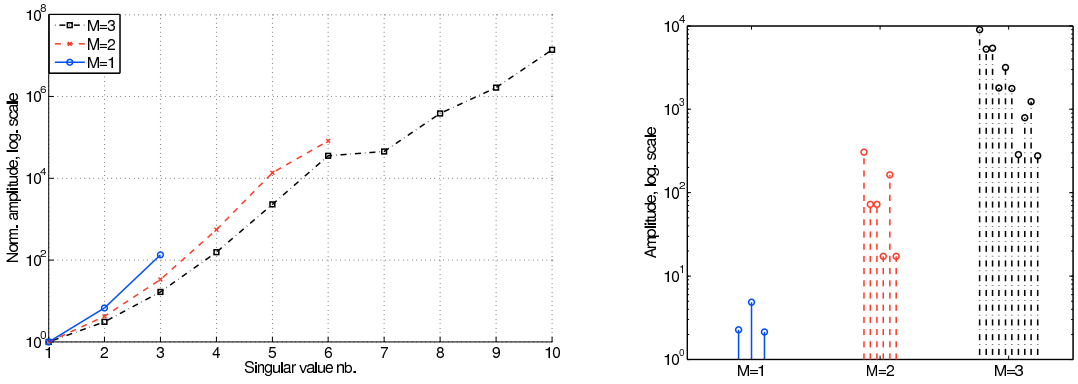

(a) (b)

FIGURE 1.24: *(a) Normalized amplitude of the inverse of the singular values λ_i of the* $\mathbf{H}$ *matrix in (1.37b), and (b) amplitude of the coefficients $\gamma_{m,n}$ for $M = 1, 2, 3$ at 3 GHz. The setup is the one in* FIG. *1.22 with $\Delta x = 6.5$ cm and dummy antennas.*

Of course, the development must be truncated at a finite $M \triangleq \max(m)$, giving $(M+1)^2$ coefficients γ to be retrieved[5]. If this number is smaller than the measurements (here 49), the final linear system is over-determined. It can then be solved in the least squares sense, that is, by minimizing the misfit

$$\mathcal{F}(\boldsymbol{\gamma}) = \|\mathbf{l_e} - \mathbf{H}\boldsymbol{\Lambda}\|_2^2 \ , \tag{1.38}$$

where the subscript 2 indicates the norm-2 operator. The solution can, for instance, be found through the linear Conjugate Gradient method, or by using the Singular Value Decomposition (SVD) of the $\mathbf{H}$ matrix. This writes as

$$\mathbf{H} = \mathbf{U}\boldsymbol{\Lambda}\mathbf{V}^H \ , \tag{1.39}$$

where the columns of the square matrices $\mathbf{U}$ and $\mathbf{V}$ are the left and right singular vectors, respectively, and $\boldsymbol{\Lambda}$ is, in the general case, a rectangular matrix with diagonal elements λ_i, known as singular values and arranged in descending order with respect to their amplitudes, and elements equal to 0 elsewhere. After defining the pseudo-inverse [69] of $\mathbf{H}$ as

$$\mathbf{H}^+ = \mathbf{V}\boldsymbol{\Lambda}^+\mathbf{U}^H \ , \tag{1.40}$$

where $\boldsymbol{\Lambda}^+$ has diagonal elements equal to $1/\lambda_i$ and all the others equal to 0, the solution of (1.37b) is finally

$$\boldsymbol{\gamma} = \mathbf{H}^+\mathbf{l_e} \ . \tag{1.41}$$

The role played by the value of M results can be understood with both mathematical and physical considerations. It can first be noticed that for a large M $\mathbf{H}$ is an ill-conditioned operator, that is, the ratio between the largest and the smallest singular values is very big. As an example, for the setup in FIG. 1.22 with $\Delta x = 6.5$ cm and dummy antennas, the

[5] In fact, since $Y_{l,m}(\pi/2, \varphi) = 0$ if $l+m$ is unpair, the number of unknowns reduces to $(M^2+3M+2)/2$.

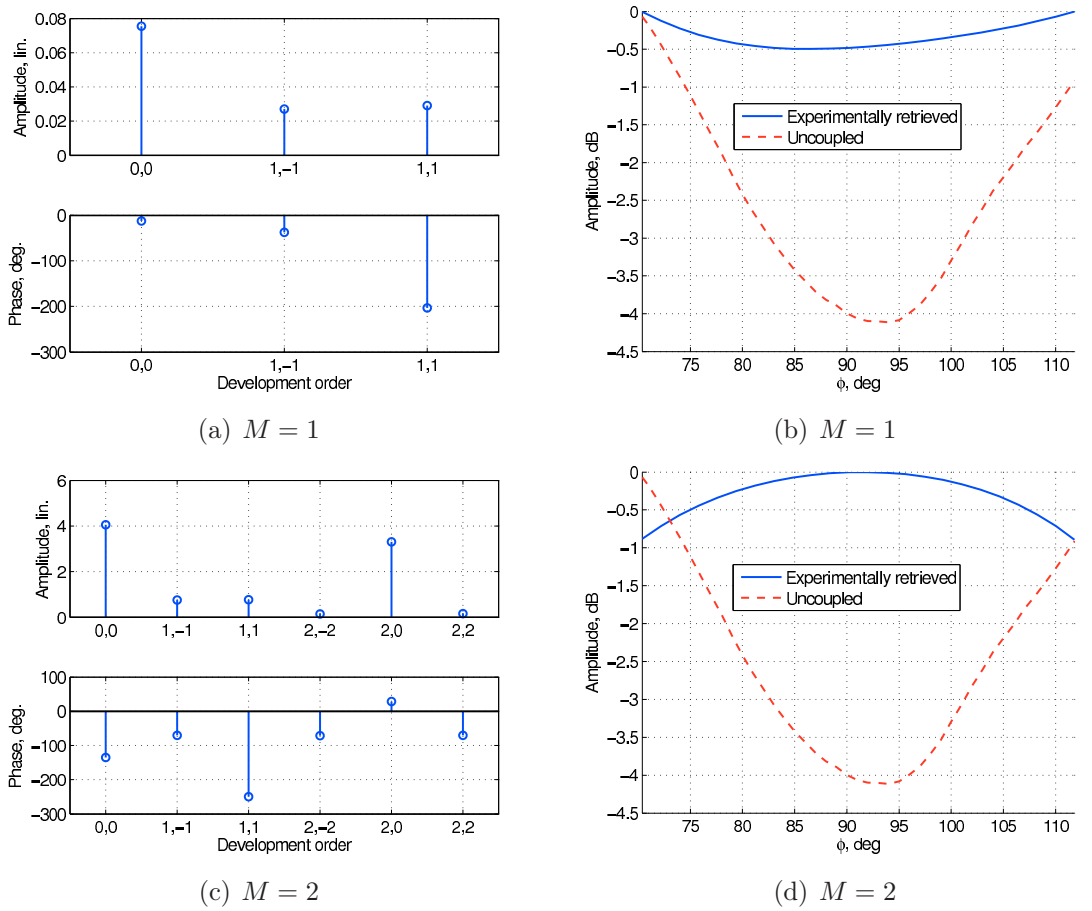

(a) $M = 1$ (b) $M = 1$

(c) $M = 2$ (d) $M = 2$

FIGURE 1.25: *(a,c) Coefficients $\gamma_{m,n}$, and (b,d) reconstructed radiation pattern at 2.2 GHz. Notice that $\gamma_{m,n} = 0$ for $n + m$ unpair since $Y_{m,n}(\pi/2, \varphi_{jl}) = 0$ in (1.37a).*

quantity $|\lambda_1/\lambda_i|$ is plotted in FIG. 1.24(a) with a logarithmic scale for $M = 1, 2, 3$. The ratio increases exponentially, and it is as high as 10^5 for $M = 2$. The result is that $\mathbf{\Lambda}^+$ has very large elements and, since these are multiplied by the measurements vector $\mathbf{l}_e$ in (1.41), the unavoidable presence of noise makes the $\boldsymbol{\gamma}$ elements "explode", corresponding to a non-converging series (1.37a). The values of the $\gamma_{m,n}$ corresponding to FIG. 1.24(a) are given in FIG. 1.24(b): indeed, due to the logarithmic scale, the values increase by a factor 10^2 when increasing M by one.

For a given Signal-to-Noise Ratio (SNR), the series should then be truncated [70] at a value of M as small as possible, which is analogous to the Truncated-SVD approach often used in literature to solve linear inverse problems [71] as the present one. Nonetheless, a *too* small value, that is, the use of only a few spherical harmonics (small m value in (1.36)), corresponds physically to reconstruct a field with slow spatial variations, *i.e.* low spatial frequencies. The result is therefore a too "flat" radiation pattern. To demonstrate such a trade-off, the aforementioned modelization procedure is applied at 2.2 GHz, where the uncoupled, or "ideal", radiation pattern in FIG. 1.21(b) has a hole at broadside. The chosen dataset is the same of FIG. 1.24. The retrieved radiation pattern and the cofficients $\gamma_{m,n}$ are shown in FIG. 1.25 for $M = 1$ and $M = 2$. Concerning the radiation pattern, the

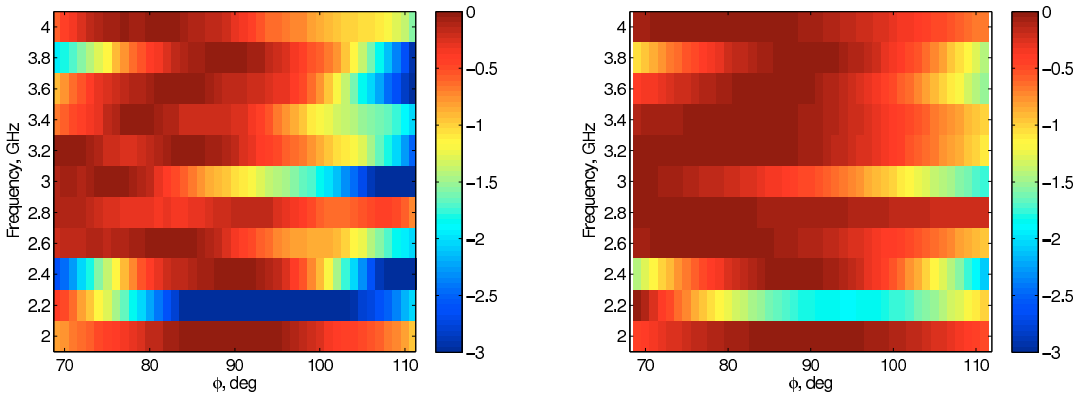

(a) Raw data (b) Multipolar model (1.37a)

FIGURE 1.26: *(a) Raw measurements performed at LEAT (equivalent to E_θ in FIG. 1.20) and (b) radiation pattern retrieved by applying the multipolar model (1.37a) on such raw data. There is no antenna coupling in these data.*

azimuth range is limited to the largest φ_{jl} available in the measurement setup, approximately ± 20 deg. In the case $M = 1$ (FIG. 1.25(b)), the shape of the radiation pattern (blue line) corresponds well to the uncoupled pattern (dashed red line). On the other hand, the amplitude varies much less than in the ideal case, since with $M = 1$ such a rapid variation cannot be recreated by the basis functions of the expansion. On the other hand, for $M = 2$, the coefficients seem to "explode", their values being all larger by a factor 20 at least with respect to those for $M = 1$. As a consequence, the shape of the radiation pattern (FIG. 1.25(d)) does not follow at all the ideal one. This behavior is systematically confirmed at any frequence and for any dataset. From this result and from the "explosion" of the $\gamma_{m,n}$ in FIG. 1.24, the conclusion is that, with arrays made of 7 antennas and separated by a distance of the order of 1 m (*cf.* FIG. 1.22), the antenna spacing/array aperture compromise does not allow to go beyond $M = 1$: this will then be the value used from now on.

FIG. 1.26(a) shows E_θ, extracted from FIG. 1.20, as a function of both frequency and azimuth angle. Applying the multipolar model to this raw set of data, but limiting the azimuth angle φ from roughly 70 to 110 deg, gives the "extrapolated" radiation pattern in FIG. 1.26(b). Although a good matching is obtained, rapid azimuthal variations of the field cannot be tracked with $M = 1$. This result has to be compared with those in in FIG. 1.27, showing the experimental radiation patterns obtained with the same model for the setup in FIG. 1.22 with $\Delta x = \{6.5, 5.2\}$ cm with or without dummy antennas. Concerning the case $\Delta x = 5.2$ cm, since the maximum available azimuth angle is reduced with respect to the setup with $\Delta x = 6.5$ cm, a smaller φ range is plotted. The four figures are different from each other. Consider first the effect of dummy antennas, which for instance allow in FIG. 1.27(b,d) to retrieve the 2.2 GHz directivity hole that is not visible without dummy antennas. Again, especially in the curves with dummy antennas, the increased directivity of the antennas at the high end of the frequency band is confirmed. Overall, a larger antenna spacing Δx in addition to the use of dummy antennas produces a radiation pattern

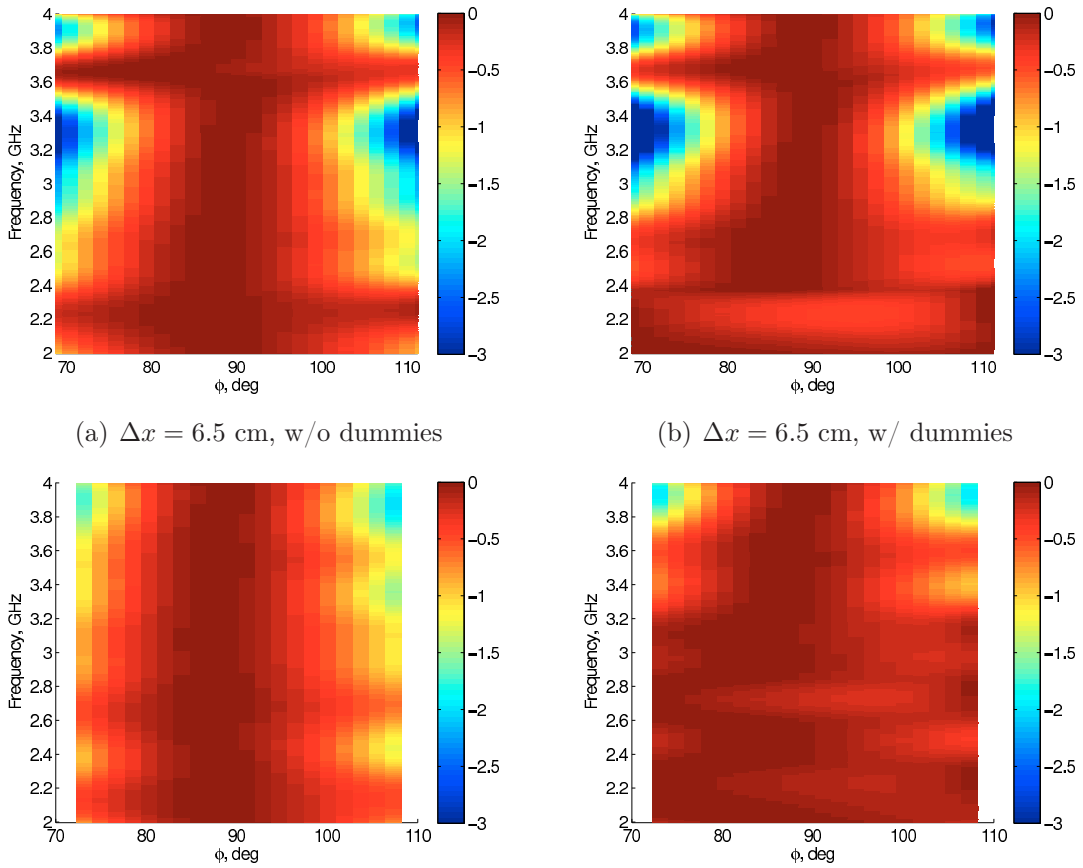

(a) $\Delta x = 6.5$ cm, w/o dummies

(b) $\Delta x = 6.5$ cm, w/ dummies

(c) $\Delta x = 5.2$ cm, w/o dummies

(d) $\Delta x = 5.2$ cm, w/ dummies

FIGURE 1.27: *Experimentally retrieved radiation patterns for the setup in* FIG. *1.22.*

closer to the uncoupled one in FIG. 1.26. Nonetheless, FIG. 1.27(b) and FIG. 1.26(b) still differ sensibly, which confirms that antenna coupling is responsible of an alteration of the radiation mechanism that must be taken into account when inversing scattering data.

It is finally worth to be noted that outside the measured φ range, the radiation patterns retrieved through (1.36) rapidly give aberrant values. Indeed, the extrapolation we implicitly ask to the model makes the series divergent at such unmeasured angles. One must therefore be aware of such limitation and coherently use the methodology developed in this section.

1.7.2.1 Time-domain characterization

The model in (1.36) is applied at all the frequencies between 2 and 4 GHz. This gives an important insight on the UWB (hence time-domain) behavior of the antennas. Before employing it, two ETS antennas, A_1 and A_2, have been placed one in front of each other ($\varphi_{21} = 0$ deg) at a distance $r \approx 1$ m ($10\lambda_0$ at 3 GHz), and the transmission and retrodiffusion coefficients, S_{21} and $S_{jj}|_{j=1,2}$, respectively, have been measured. Their time-domain complex envelopes in dB are shown in FIG. 1.28. For the S_{21} case, the square marker indicating the arrival time is shifted by around 0.33 ns after the free-space arrival time r/c_0, giving a

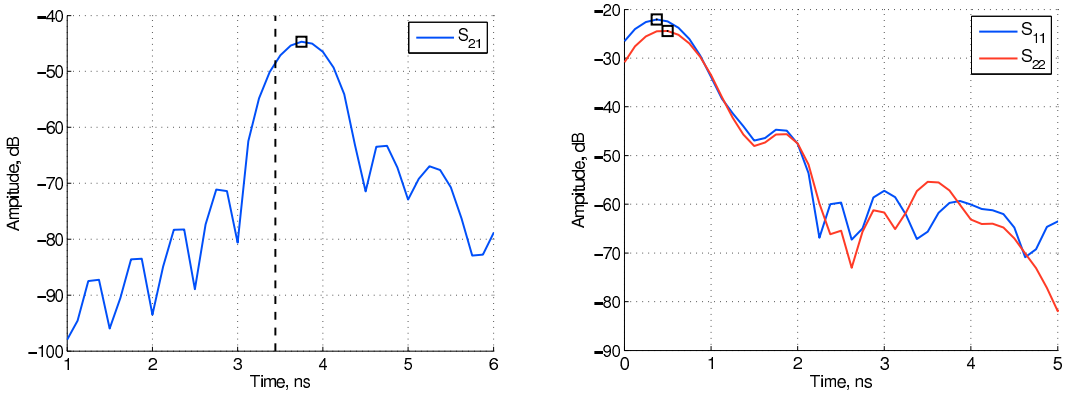

(a) (b)

FIGURE 1.28: *(a) Transmission and (b) retrodiffusion measurements for the setup with two antennas facing each other at a distance of approximatevely 1 m.*

distance of twice 4.98 cm. Also, with respect to the retrodiffusion measurements, the peak of the reflection is not at $t = 0$ ns, corresponding to the antenna connector, but rather between 0.375 and 0.5 ns (the antennas are a bit mismatched), giving a distance between twice 5.6 and 6.5 cm.

These differences with respect to the behavior of a simple dipole antenna are generated by the nature itself of the ETS antennas. They work on the principle of traveling waves, meaning that the radiation does not take place in a single point in space, but all along the antenna length/height. In addition, the substrate is made of duroid, a material with $\varepsilon_r \approx 2.2$. Assuming that the wave speed along the substrate is $c_0/\sqrt{\varepsilon_r}$ (TEM or pseudo-TEM mode), the 4.98 cm correspond to a physical length of 3.36 cm, basically half the length of the metallization of the antenna (*cf.* FIG. 1.19).

It must now be verified that such behavior, at least the one in transmission (the reflection coefficient of the antennas is not modeled), can be retrieved through the model developed so far. Whether antenna coupling influences the time-domain behavior is also to be verified.

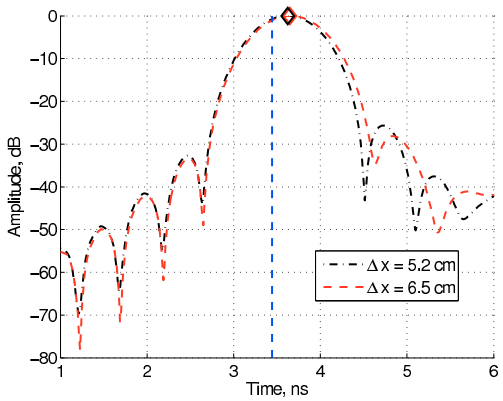

FIGURE 1.29: *Pulse sent by an antenna described by the model in (1.36) at a distance of approximatevely 1 m.*

With respect to the same setup in FIG. 1.22 from which the development coefficients γ are determined, FIG. 1.29 shows the pulse received by an ideal antenna (infinitesimal dipole) placed at the same distance $r \approx 1$ m and at $\varphi = 90$ deg, for the cases with dummy antennas and $\Delta x = \{6.5, 5.2\}$ cm. Such pulse is built performing the IFT from 2 GHz to 4 GHz of the experimentally retrieved electric field, and applying the *lanczos* (or *sinc*) window (1.20). The arrival times (here they must not be divided by 2) are slightly different, and their difference with respect to the free-space arrival time correspond to the distances of 6.2 and 5.45 cm. These values must be compared to the 4.98 cm found for the uncoupled case. The conclusion is that, put aside the limitations of the model, the additional length corresponding to a propagation delay in the substrate of the antennas is well reconstructed through the model in (1.36). In addition, coupling also seems to affect the time-behavior of the antennas, since the two curves in FIG. 1.29 present some differences in the sidelobes after 4 ns.

1.8 Experimental beamforming

As stated in §1.2, the prototype is equipped with a beamforming hardware based on one numerically-controlled A/Φ pair per RF channel. Given a complex steering law $(\tilde{\mathbf{a}}, \tilde{\boldsymbol{\phi}})$ at a given frequency, then, the question of how to implement it in the system arises. Namely, the set of codes $(\tilde{\mathbf{N}}_{\mathrm{A}}, \tilde{\mathbf{N}}_{\Phi})$ to download into the A/Φ pairs corresponding to $(\tilde{\mathbf{a}}, \tilde{\boldsymbol{\phi}})$ need to be found.

The A/Φ transmission characteristics are shown in FIG. 1.30. Despite the fact that both attenuators and phase shifters have rather linear attenuation-in-dB and phase shift curves, respectively, as a function of their input code (FIG. 1.30(a,c)), they also have non-constant phase shift and attenuation laws, respectively (FIG. 1.30(b,d)), which can be seen as defects that must be kept into account.

Let a_{A} and ϕ_{A} be the attenuation-in-dB and phase shift laws - either in rad or s - of the attenuators, and a_{Φ} and ϕ_{Φ} those of the phase shifters. For the j^{th} channel (the index j is omitted for conciseness), in order to obtain the complex coefficient $(\tilde{a}, \tilde{\phi})$, the input codes N_{A} and N_{Φ} must fulfill

$$\begin{cases} \tilde{a} = a_{\mathrm{A}}(N_{\mathrm{A}}) + a_{\Phi}(N_{\Phi}) \\ \tilde{\phi} = \phi_{\mathrm{A}}(N_{\mathrm{A}}) + \phi_{\Phi}(N_{\Phi}) \end{cases} . \tag{1.42}$$

Since the discrete system is perfectly determined, its solution is found iteratively. The initial estimate can be written as

$$\begin{cases} N_{\mathrm{A}}^{0} = a_{\mathrm{A}}^{-1}(\tilde{a} - \bar{a}_{\Phi}) \\ N_{\Phi}^{0} = \phi_{\Phi}^{-1}(\tilde{\phi} - \bar{\phi}_{\mathrm{A}}) \end{cases} , \tag{1.43}$$

where $\bar{a}_{\Phi}$ ($\bar{\phi}_{\mathrm{A}}$) is the mean value of the attenuation of the phase shifter (phase shift of the attenuator), and $a_{\mathrm{A}}^{-1}(\cdot)$ and $\phi_{\Phi}^{-1}(\cdot)$ are the inverse discrete laws. The iterative rule at the

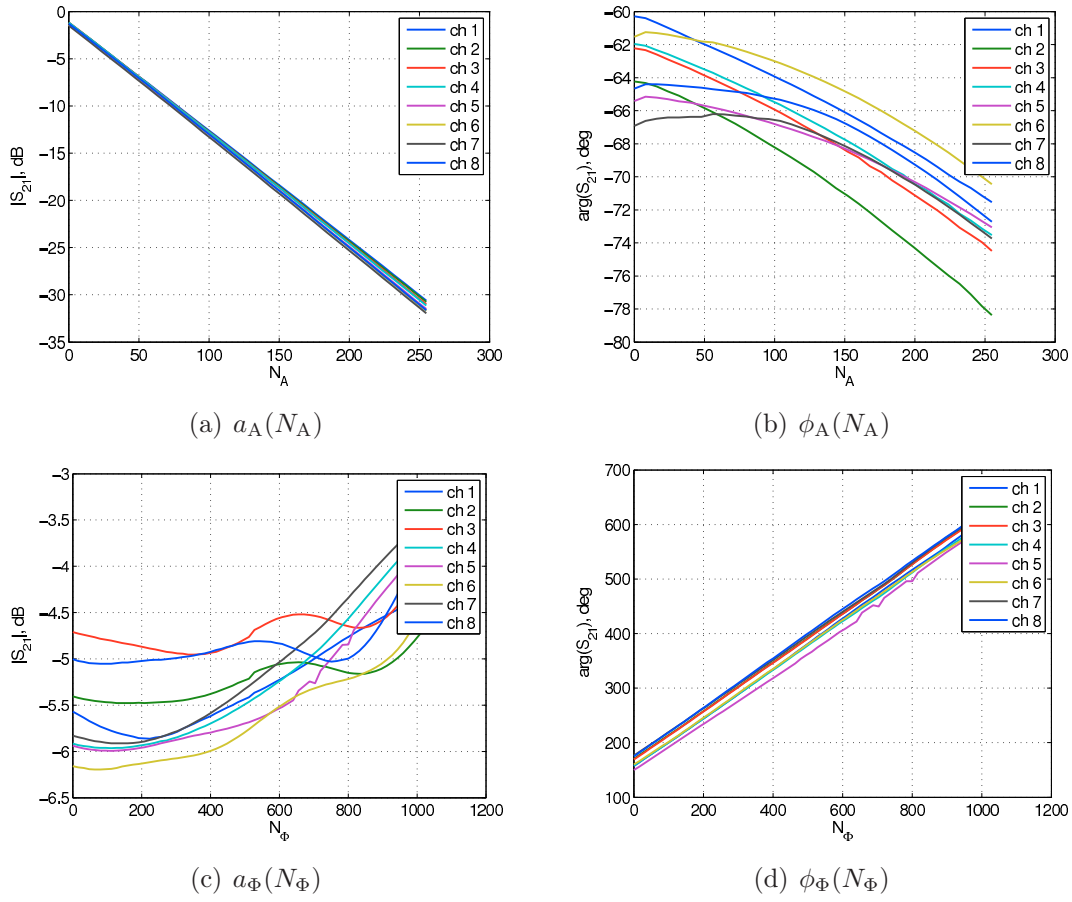

(a) $a_{\mathrm{A}}(N_{\mathrm{A}})$ (b) $\phi_{\mathrm{A}}(N_{\mathrm{A}})$

(c) $a_{\Phi}(N_{\Phi})$ (d) $\phi_{\Phi}(N_{\Phi})$

Figure 1.30: *Amplitude and phase at 3 GHz of attenuators (A) and phase shifters (Φ) as a function of their input code. Each curve stands for a different RF channel.*

i^{th} iteration is then

$$\begin{cases} N_{\mathrm{A}}^{i+1} = a_{\mathrm{A}}^{-1}[\tilde{a} - a_{\Phi}(N_{\Phi}^{i})] \\ N_{\Phi}^{i+1} = \phi_{\Phi}^{-1}[\tilde{\phi} - \phi_{\mathrm{A}}(N_{\mathrm{A}}^{i})] \end{cases}, \tag{1.44}$$

which has to be applied until convergence:

$$\begin{cases} N_{\mathrm{A}}^{i+1} = N_{\mathrm{A}}^{i} \triangleq \tilde{N}_{\mathrm{A}} \\ N_{\Phi}^{i+1} = N_{\Phi}^{i} \triangleq \tilde{N}_{\Phi} \end{cases}. \tag{1.45}$$

The feasibility of a given $(\tilde{\mathbf{a}}, \tilde{\boldsymbol{\phi}})$ set must be guaranteed. The first issue comes from the ratio $\max \tilde{\mathbf{a}} / \min \tilde{\mathbf{a}}$, that has to be smaller than the dynamic range of the attenuators. This is defined as the maximum output amplitude variation with respect to the input code, *e.g.* approximately 30 dB in Fig. 1.30(a). Since the prototype cannot provide any amplification, the first step consists in normalizing the whole set of coefficients with respect to the one with the largest amplitude:

$$\tilde{\mathbf{a}} \leftarrow \tilde{\mathbf{a}} - \max \tilde{\mathbf{a}} \,. \tag{1.46}$$

The phase, on the other hand, is not an issue since it can be wrapped and since up to 4 GHz the phase shifters have a dynamic range of more than 360 deg.

Then, one has to deal with the fact that, as visible in FIG. 1.30, A/Φ couples are rather mismatched from channel to channel. The sought set of coefficients can then be written as

$$\begin{cases} \tilde{\mathbf{a}} \leftarrow \tilde{\mathbf{a}} + \min\left[\mathbf{a}_{\mathrm{A}}(0)\right] + \min \min\limits_{N_\Phi}\left[\mathbf{a}_\Phi(N_\Phi)\right] \\ \tilde{\boldsymbol{\phi}} \leftarrow \tilde{\boldsymbol{\phi}} + \max\left[\boldsymbol{\phi}_\Phi(0)\right] + \max \max\limits_{N_{\mathrm{A}}}\left[\boldsymbol{\phi}_{\mathrm{A}}(N_{\mathrm{A}})\right] \end{cases}, \tag{1.47}$$

where even in the worst mismatch case convergence is assured (this is why min and max values for the attenuation and phase, respectively, are considered).

The drawback of this solution is the loss in attenuation dynamic range resulting from the necessity of covering even the worst mismatch case. For instance, according to (1.47) the smallest attenuation, instead of the 0 dB resulting from (1.46), would be 8.5 dB ($\min\left[\mathbf{a}_{\mathrm{A}}(0)\right] + \min\min_{N_\Phi}\left[\mathbf{a}_\Phi(N_\Phi)\right]$ in FIG. 1.30(a,c)), giving 8.5 dB dynamic range loss. Furthermore, the same quantity must be subtracted from the prototype dynamic range (see §1.4)!

To tackle the issue, once a first set of codes $(\tilde{\mathbf{N}}_{\mathrm{A}}, \tilde{\mathbf{N}}_\Phi)$ is found with (1.47), a new incremented set of values $(\tilde{\mathbf{a}} + 0.5 \text{ dB}, \tilde{\boldsymbol{\phi}})$ is sought, and so on until mismatch actually prevents the algorithm from convergence. At the end, the mismatch will impact the dynamic range by the minimum possible amount, whereas using only (1.47) would result in the most conservative loss.

Chapter 2

Detection/localization with Time Reversal-based methods

In wave imaging, the first difficulty consits in *detecting* the presence of "interesting" objects in the inspected medium, then in *localizing* them. Time Reversal, through the methods inspired from - or related to - it, has proven to be an effective tool to achieve these tasks. This chapter, after presenting the physics beneath TR, presents some of these methods as applied to experimental data collected through the prototype described in §1. Results from a measurement campaign targeting Through-The-Wall (TTW) imaging are also presented [72]. Particular attention is cast into a smart use of the frequency diversity (or degrees of freedom) given by the available UWB.

2.1 Time Reversal theoretical background

The principle of Phase Conjugation (of which Time Reversal is the time-domain counterpart) is employed in electromagnetism since the late 1950's [42] and in optics since the 1980's [73]. The idea consists in illuminating a scatterer with an incident time-harmonic - or narrowband - wave, recording the scattered field, and finally back-propagating its phase conjugated version. The result is a new wave focusing onto the scatterer despite the arbitrariness of the propagation medium (some hypotheses do exist, though, as mentionned later).

In 1989 [2], M. Fink generalized the "old" concept to wideband signals, using a so-called *Time Reversal Mirror* (TRM) in acoustics. At the time, the availability of electronic components (amplifiers, A/D and D/A converters, memories) rapid enough to deal with wideband signals at ultrasonic frequencies (from hundreds of kHz to some MHz) easily allowed to work directly in the time domain; this was of course impossible in electromagnetics and in optics, given carrier frequencies going from hundreds of MHz to hundreds of THz. From then on, accompanied by the overwhelming progress in solid-state electronics, both theoretical studies [23, 74, 75] and experimental results [24, 28, 76–78] have flourished, motivated either

by the quest for focusing beyond the diffraction limit -the so-called *super-resolution* [41] -, or by promising applications in telecommunications [27, 30, 79–83], RADAR [26, 45, 84], biomedicine [85], or geophyisics [86, 87].

Despite a vectorial theory of TR in electromagnetism exists [22, 23], a scalar 2D formulation is preferred here for simplicity. This is motivated by the fact that all the targets used in the experiments performed with the microwave prototype are considered infinite along the polarization direction of the antennas ($E_{//}$ or TM configuration). With reference to FIG. 1.19, the antennas are linearly polarized along the z-axis, resulting in $\vec{e}(x,y,z;t) \approx e_z(x,y;t)\hat{z}$, where $\vec{e}(x,y,z;t)$ is the electric field in the time domain. With $\vec{r} = (x,y)$, the propagation of $e_z(x,y;t)$ is ruled by the d'Alembert equation

$$\nabla^2 e_z(\vec{r};t) - \frac{1}{c^2(\vec{r})}\frac{\partial^2 e_z(\vec{r};t)}{\partial t^2} = 0 \ , \tag{2.1}$$

where $c(\vec{r})$ is the wave speed in the medium, supposed inhomogeneous but non-dispersive. Two operators are therefore applied to the field, a spatial (∇^2) and a temporal one ($\partial^2/\partial t^2$). Since the latter only contains even-order derivatives, both $e_z(\vec{r};t)$ and $e_z(\vec{r};-t)$ are solutions of (2.1), which is known as the *time reversal invariance* property of the field. Dually, in the frequency domain, with $E_z(\vec{r};\omega) = \mathrm{FT}\left[e_z(\vec{r};t)\right](\omega)$, *phase conjugation invariance* results from the Helmholtz equation

$$\nabla^2 E_z(\vec{r};\omega) + k^2(\vec{r})E_z(\vec{r};\omega) = 0 \ , \tag{2.2}$$

where $k^2(\vec{r})$ is the real wavenumber at each point of the propagation medium. Indeed, both $E_z(\vec{r};\omega)$ and $E_z^*(\vec{r};\omega)$ are solutions of (2.2).

Back in the time domain, the consequence of time reversal invariance is that, if $e_z(\vec{r},t)$ is recorded everywhere on a closed surface Γ surrounding the source of the wave (*acquisition* step), and $e_z(\vec{r},-t)$ is transmitted back into the same medium (*back-propagation* step), then the new wave, solution of the same equation, will retrace the life of the initial one in the inverse sense of time, thus converging onto the initial source. Rigorously, the conditions regarding the propagation medium needed by Time Reversal are 1) losslessness (conductivity $\sigma(\vec{r}) = 0$), 2) linearity and isotropy, and 3) stationarity between the acquisition and back-propagation phases. Notice that the hypotheses 2) are the same hypotheses needed for Lorentz's reciprocity.

It is interesting to further study the behavior of the back-propagated wave. Consider a line-source (point-source in 3D) placed in $\vec{r}_S$, and a TRM located at the surface Γ supposed in the far-field of both the source and the medium inhomogenities (if any). In the frequency domain, it has been shown [22] that the back-propagated field $E^{\mathrm{TR}}(\vec{r};\omega)$ is proportional to the imaginary part of the Green function of the medium, $G(\omega;\vec{r},\vec{r}_S)$,

$$E^{\mathrm{TR}}(\vec{r};\omega) \propto \Im\left[G(\omega;\vec{r},\vec{r}_S)\right] \ . \tag{2.3}$$

In free-space, where $G(\omega;\vec{r},\vec{r}_S) = -i/4\ H_0^-(k_0|\vec{r}-\vec{r}_S|)$, this result confirms the classical $\lambda_0/2.6$ ($\lambda_0/2$ in 3D) resolution limit. On the other hand, for an heterogeneous medium with wavenumber fluctuations in proximity of the source, $\Im\left[G(\omega;\vec{r},\vec{r}_S)\right]$ can vary much more rapidly, giving a resolution spot beyond the classical limit as in [41], even with an open measurement line instead of a closed surface surrounding the target. Notice that several other explanations can be given to justify the super-resolution results lately reported, using either evanescent waves (containing higher spatial frequencies) [41], multi-path (which is used constructively creating a sort of virtual array with a larger aperture) [27, 28], or plasmonic modes [88].

Finally, it is important to mention the fundamental difference between Phase Conjugation and Time Reversal in chaotic media [49]. It must be firsts understood that spatial focusing is generated by space diversity at emission. This is why a Phase Conjugation Mirror (PCM) can achieve focusing, since the space diversity comes from the different locations of the array antennas. For the same reason, it is impossible to obtain focusing in free-space with a PCM or TRM made of a single antenna. Nevertheless, in a disordered medium, a one-antenna TRM *can* produce focusing if a sufficiently large bandwidth is available, which cannot be the case with a PCM. The explanation lies in the correlation bandwidth $\delta\omega$ of the medium, that is, in the separation of two frequencies at which the medium response is sufficiently decorrelated. When a single antenna excites the medium with a bandwidth $\Delta\omega > \delta\omega$, Time Reversal is capable of recasting the $\Delta\omega/\delta\omega$ degrees of freedom into space diversity. In other words, the frequency diversity of the medium is "transformed" into space diversity thanks to TR [15,89]. In this sense, the advent of Time Reversal as "improvement" of Phase Conjugation may lead to very interesting experiments and applications.

2.2 Active source case

Time Reversal can be favorably employed in applications where one wants to focus energy onto an active source, *e.g.*, an antenna that sends data and needs to be adressed back in return. One of the first spectacular examples was given in 1998 in underwater acoustics [16]: two vessels several kilometers spaced were able to communicate through a TRM attached to one of them despite the complicated marine waveguide characteristics. Indeed, the telecommunications domain appear as a most receptive one with respect to the use of Time Reversal.

2.2.1 Time Reversal experiments

The effectiveness of Time Reversal for this class of applications is demonstrated here through the microwave prototype. The impact of antenna coupling, due to the arrayed configuration, and of "disorder" added to the propagation medium, is also studied.

2.2.1.1 Details of measurements

The setups of the experiments are shown in FIGS. 2.1-2.4. The distance between the antennas is $\Delta x = 5.3$ cm. In any case, since the prototype works in the frequency domain, the experiment consists of phase-conjugating the field radiated by one array-2 element, A_{12}, over the entire bandwidth. Two steps can be distinguished:

(a) acquisition step. The TRM antennas receive the wave radiated from A_{12}, giving an 8-element vector, $\mathbf{S}^{\mathrm{da}} \triangleq \{S_{j12}\}_{j=1,8}$, at each frequency in the [2-4] GHz band.

(b) back-propagation step. The TRM plays the role of emitter and the array-2 elements that of receivers. The normalized PC steering vector, $\left(\mathbf{S}^{\mathrm{da}}\right)^* / \|\mathbf{S}^{\mathrm{da}}\|$, is implemented in the A/Φ pairs as described in §1.8. The backpropagated signal received by $A_l|_{l=9,\ldots,15}$ is called S^{PC}. To reduce the time needed to cover the whole 2 GHz-wide band, a frequency step of 100 MHz ($N_\omega = 21$ points) is used.

Notice that, differently with respect to what described in §1.6, no signal processing whatsoever is applied to the raw measured data (no time-gating, no drift correction). Signals contain therefore all the ringing through the cables and components of the prototype, and they are time-reversed as well. The only operation performed before step (b) comes from the following consideration. Watching carefully at subfigures (a) and (b) in FIGS. 2.1-2.4, it can be noticed that the RF signal does not follow the same path when the TRM acts (a) as a receiver or (b) as a transmitter. In effect, in the acquisition step it is preferable that the received signal pass through the multiposition switch rather than through the A/Φ channels; since the latter is much more lossy than the former (see TAB. 1.3), the measurement would otherwise suffer from a reduced precision. In order to re-establish the stationarity needed between steps (a) and (b), the chain matrix technique described in §1.5.1 is employed to recast $\mathbf{S}^{\mathrm{da}}$ into a new vector containing the field that would have been measured if the signal passed through the A/Φ pairs.

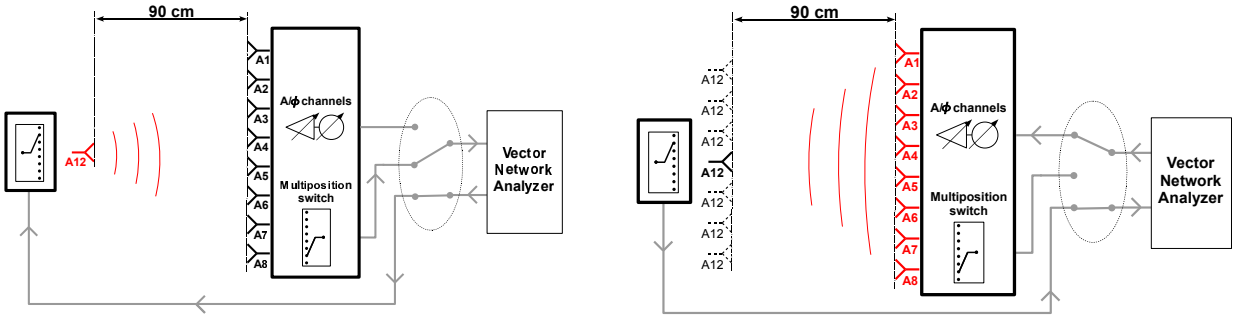

(a) Acqusition (b) Back-propagation

FIGURE 2.1: *Time Reversal experiment setup. One single antenna array-2, A_{12}, is present during both the acquisition (a) and back-propagation (b) steps; during the latter, A_{12} is displaced to study the spatial focusing provided by Time Reversal.*

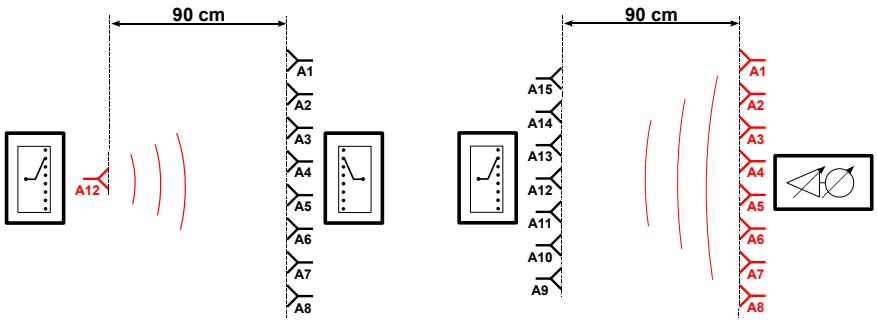

(a) Acqusition (b) Back-propagation

FIGURE 2.2: *Time Reversal experiment setup. Array-2 has one single antenna during the acquisition step (a), whereas in the backpropagation step (b) the entire array-2 is present.*

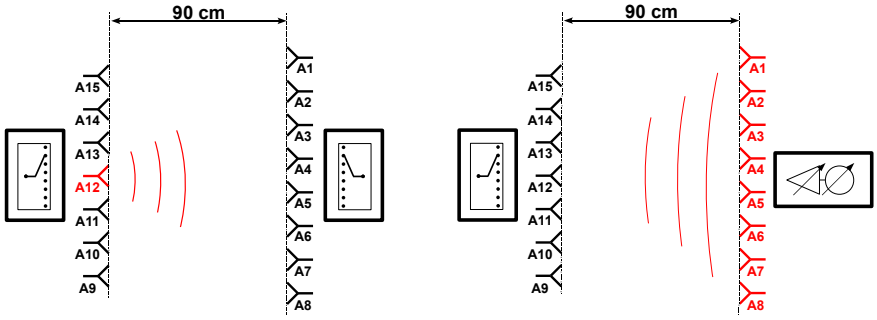

(a) Acqusition (b) Back-propagation

FIGURE 2.3: *Time Reversal experiment setup. The entire array-2 is present during both the acquisition (a) and back-propagation (b) steps.*

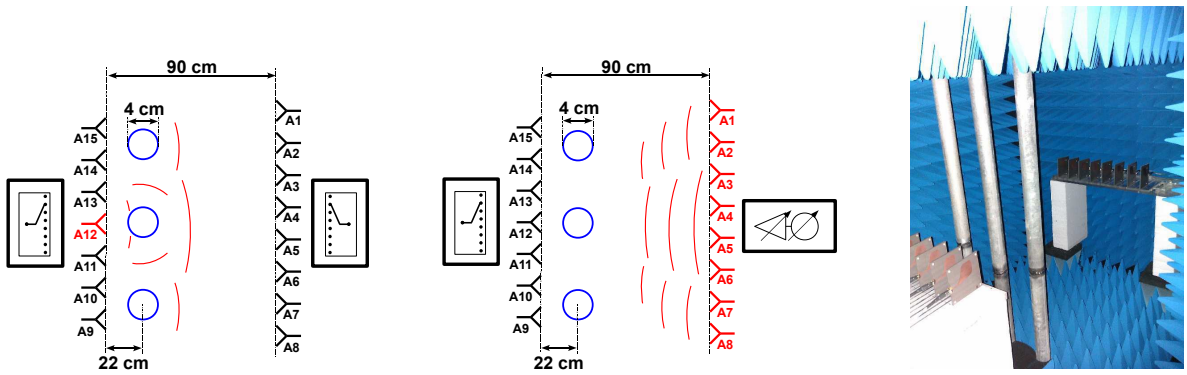

(a) Acqusition (b) Back-propagation (c)

FIGURE 2.4: *Time Reversal experiment setup. With respect to* FIG. *2.3 three metallic cylinders are placed in front of the array-2.*

The three first setups allow to study the impact of antenna coupling in the array-2. While in FIG. 2.1, both in the acquisition and back-propagation steps, only A_{12} is present (it is displaced in step (b) to observe the spatial focusing of the returned field), in FIG. 2.2 the entire array-2 is present during step (b), so that antenna coupling is supposed to alter the

returned signal invalidating the stationarity hypothesis. In FIG. 2.3, on the other hand, the entire array-2 is present in both steps; it can therefore be expected that the coupling present in step (a) be favorably exploited by Time Reversal in step (b). Finally, in FIG. 2.4 three 4 cm-diameter metallic cylinders are placed in front of the array-2 at a distance of 22 cm[1], so to heavily perturbate the signal transmitted by A_{12}. Time Reversal is again expected to take benefit of the disorder introduced in the medium to achieve a better resolution than without the cylinders (FIG. 2.3).

2.2.1.2 Experimental results and discussion

The backpropagated signal measured by A_l can be written as

$$S_l^{\mathrm{PC}} = \frac{\left(\mathbf{S}^{\mathrm{da}}\right)^H}{\|\mathbf{S}^{\mathrm{da}}\|}\mathbf{S}^{\mathrm{bp}} \ , \tag{2.4}$$

where $\mathbf{S}^{\mathrm{bp}} = \{S_{lj}\}_{j=1,8;l=9,15}$ accounts for the propagation between the TRM array element j to A_l. Two cases can be distinguished:

$$\begin{cases} S_l^{\mathrm{PC}} = \|\mathbf{S}^{\mathrm{da}}\| \in \mathbb{R} & A_l = A_{12} \\ S_l^{\mathrm{PC}} \in \mathbb{C} & A_l \neq A_{12} \end{cases} . \tag{2.5}$$

In the first case, the time-reversed signal is measured at the initial position of the array-2 source. The result holds in virtue of reciprocity, which assures that $\mathbf{S}^{\mathrm{da}} = \mathbf{S}^{\mathrm{bp}}$. Physically, the waves emitted by the TRM array elements interfere constructively at A_l. On the other hand, when $A_l \neq A_{12}$, reciprocity does not hold anymore and destructive interference occurs. Notice also that for the setup in FIG. 2.1, although in step (b) the same antenna A_{12} is displaced, each position is still abusively denoted by $l = 9, \ldots, 15$.

Quality of the experimental back-propagation

In order to validate the experimental back-propagation procedure described in §1.8, the first setup (FIG. 2.1) is chosen. For the case $l = 12$, the measured S_l^{PC} is compared against the theoretical quantity $\|\mathbf{S}^{\mathrm{da}}\|$, which can indeed be computed with the acquisition step data only. In the frequency domain, the theoretical phase must be equal to zero; the measurements in FIG. 2.5(a) show a good agreement, with a mean error $\mu = -3.9$ deg and standard deviation $\sigma = 4$ deg. A comparison can also be done in the time domain, by taking the inverse FFT of the measured and theoretical signals without using any FFT window. In FIG. 2.5(b) the two curves match very well. In particular, a quantification of the experimental error can be found in the ratio between the two signals at the time $t = 0$ ns; indeed, naming $s_l^{\mathrm{PC}}(t)$ any of the two time-domain signals,

$$s_l^{\mathrm{PC}}(0) = \sum_{i=1}^{N_\omega} S_l^{\mathrm{PC}}(\omega_i) \ , \tag{2.6}$$

[1]Distances are measured from the antenna connector. Considering the extremity of the ETSA substrate and the cylinder extremity, the distance reduces to 12 cm.

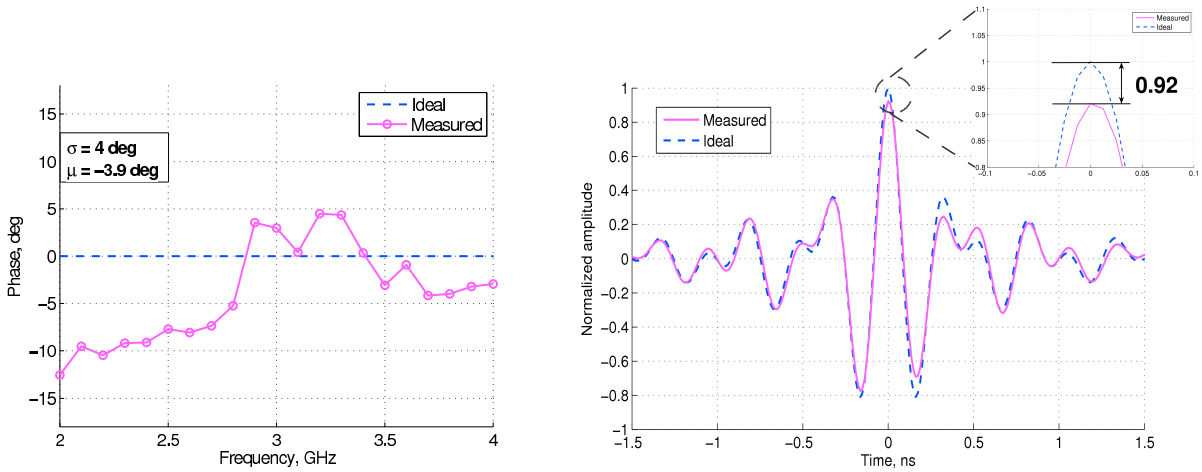

(a) Frequency domain

(b) Time domain

FIGURE 2.5: *Time Reversal experiment for the setup in* FIG. *2.1. For* $l = 12$ *(reciprocity between acquisition and back-propagation steps), ideal (dashed blue line) and measured (full magenta line) signals are compared: (a) in the frequency domain through their phases, and (b) in the time domain.*

that is, a coherent sum of all the frequency components is done. The ratio is as small as 0.92, and its departure from the ideal value 1 is due to the resolution of attenuators and phase shifters (cf. TAB. 1.2), and to the VNA precision impacted by its dynamic range (cf. §1.4).

Similar results are obtained for the stationary configurations in FIG. 2.1 and FIGS. 2.3-2.4. Different considerations hold for the setup in FIG. 2.2, where antenna coupling, present in step (b) but not in step (a), invalidates the time reversal invariance. For $l = 12$, the returned phase curve in the frequency domain (FIG. 2.6(a)) has a mean value $\mu = 6$ deg, more sensibly offset with respect to the ideal 0 deg value than in FIG. 2.5(a). As for the standard deviation, though, its value $\sigma = 5$ deg has hardly changed. The effect of coupling on the $S_l^{\mathrm{PC}}(\omega)$ seems then to be a rather constant phase offset of about 10 deg. The time domain result in FIG. 2.6(b) is somehow surprising, since the error at $t = 0$ ns is even slightly smaller with respect to FIG. 2.5(b)! In the end, coupling seems to have a limited effect in this configuration.

Spatiotemporal focusing

The quality of space-time focusing determined by wave interference is analyzed through the B-scan showing $\{s_l^{\mathrm{PC}}(t)\}_{l=9,\ldots,15}$, and extracting a sort of directivity pattern of the TR array by picking $\max_t \left[s_l^{\mathrm{PC}}(t)\right]$ for each position l. The results are given in FIG. 2.7 for the configurations in FIG. 2.1 and FIGS. 2.3-2.4. The result related to the non-reciprocal configuration in FIG. 2.2, not presented, is very similar to the one in FIG. 2.1 with slightly worse - which is to be expected - focusing resolution.

In both the free-space uncoupled and coupled cases of FIG. 2.1 and FIG. 2.3, respecitvely,

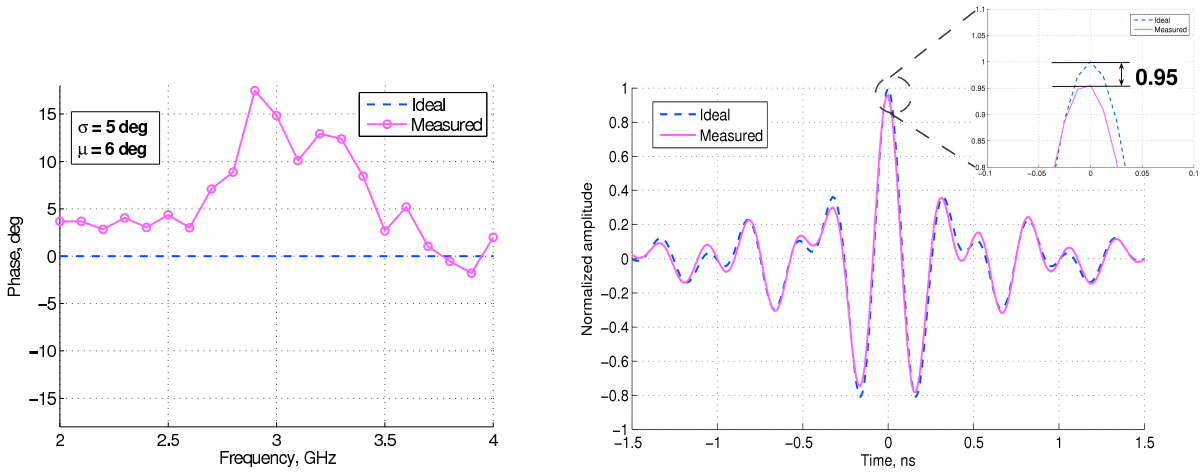

(a) Frequency domain

(b) Time domain

FIGURE 2.6: *Same as* FIG. *2.5 for the setup in* FIG. *2.2.*

the hyperbola constituing the wave front is clearly visible in the B-scan, with very small differences due to antenna coupling. The returned pulse is clean at A_{12} whereas it is damped for all the other positions. The resolution spot size at 3 dB is approximately 18 cm, quite in line with the classical resolution spot formula for a linear array in free-space[2], $\lambda_0 F/D$, where D is the TRM aperture (37.1 cm) and F the distance from the source (90 cm), that gives a value between 36.4 cm (2 GHz) and 18.2 cm (4 GHz).

The result when the cylinders are introduced is presented in FIG. 2.7(c). Notice that the array-2, during back-propagation, in addition to the regular measurement, has also been displaced by $\Delta x/2$ in order to sample more densely the time reversed field, giving a total of 14 positions. The result is quite impressive, since the resolution spot size at 3 dB is 7.5 cm, a factor 2.4 smaller than without cylinders, going therefore far beyond the classical limit. As mentioned, such improvement can be explained with the imaginary-part-of-the-Green-function-theory (see (2.3)), which indeed varies rapidly in proximity of the array-2 due to the presence of the cylinders, or invoking multi-path and the constructive/destructive interference mechanisms already mentioned.

As for temporal resolution, although a widening, or temporal stretching, of the signals away from A_{12} might be expected due to the imperfectly compensated multiple scattering, this can hardly be noticed in any of the results in FIG. 2.7. It can then be concluded that neither the antenna coupling nor the metallic cylinders constitute a "sufficient" degree of disorder to observe such behavior.

[2]Rigorously, this formula gives the distance between the maximum energy point and the first zero of the directivity pattern. Nevertheless, for a sinc-like function, it is almost equivalent to - it slightly overestimates - the 3 dB focusing spot size.

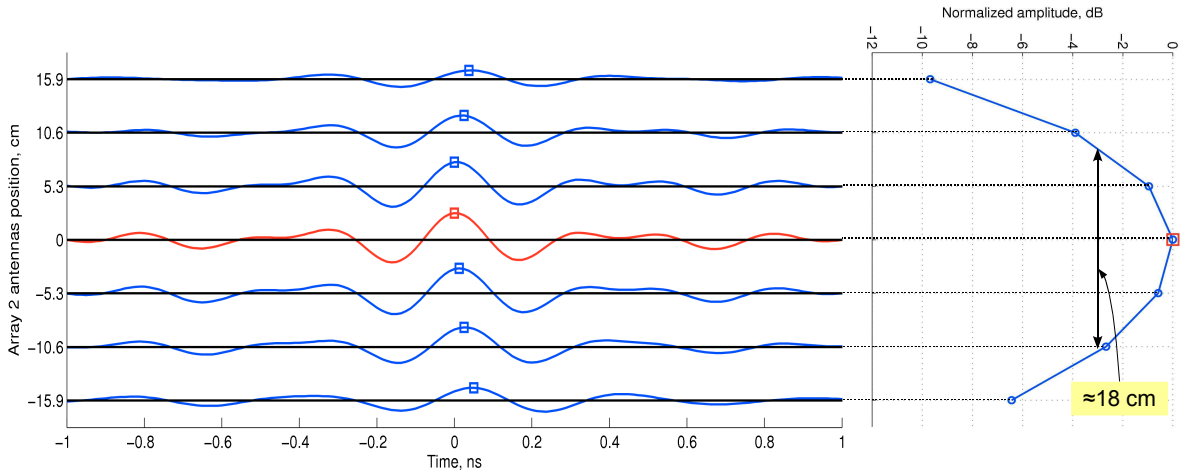

(a) W/o antenna coupling (FIG. 2.1)

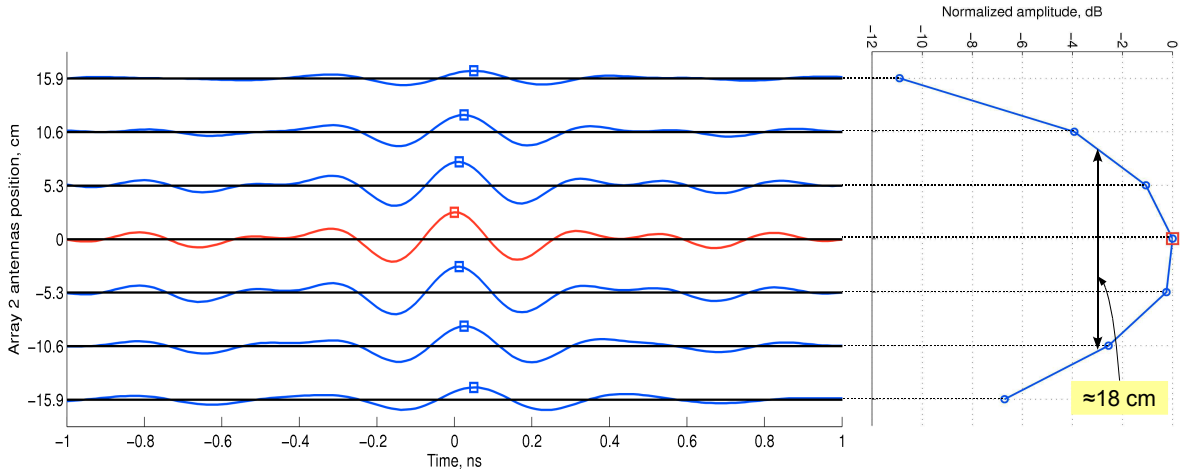

(b) W/ antenna coupling (FIG. 2.3)

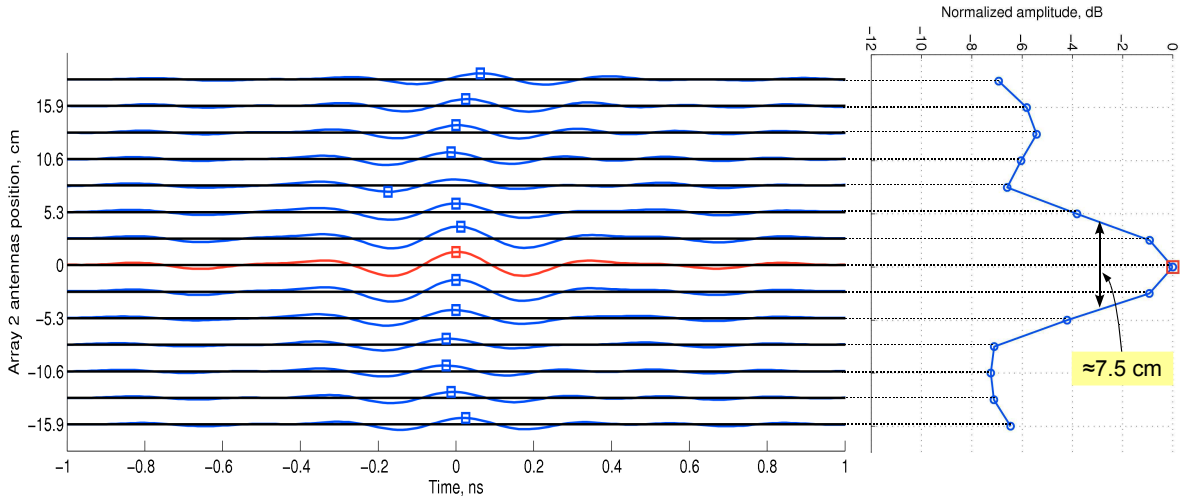

(c) W/ antenna coupling and "disorder" (FIG. 2.4)

FIGURE 2.7

2.3 Scattering case

Scatterers can be assimilated to active sources once they are illuminated by an incident wave. The resulting scattered field can indeed be processed through Time Reversal similarly

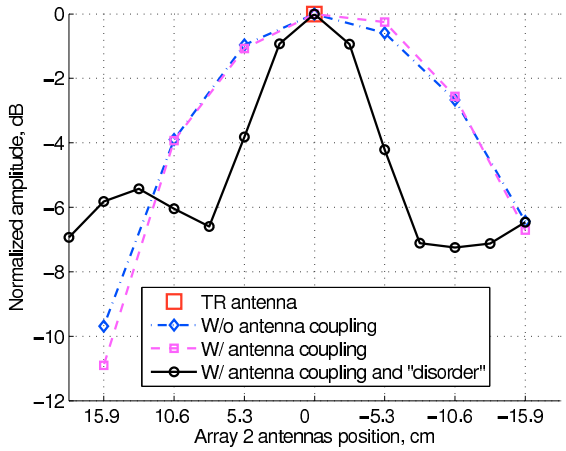

(d)

FIGURE 2.7: *(a-c) B-scans and respective directivity patterns. In (d) the directivity patterns of the configurations without antenna coupling (*FIG. *2.1, dashed-dotted blue line), with antenna coupling (*FIG. *2.3, dashed magenta line), and with antenna coupling and "disorder" (*FIG. *2.4, full black line) are compared.*

to what described until now. In addition, disposing of an array of antennas allows one to record, at each frequency, the so-called *inter-element matrix* (or *multi-static*) $\mathbf{K}(\omega)$, whose $K_{ij}(\omega)$ element corresponds to the response of the medium to a unitary excitation from antenna j measured at antenna i. Working with this matrix, and in particular exploiting its SVD, opens the way to a class of subspace-based methods that can somehow be related to Time Reversal.

An overview of some of these methods is presented next, completed by their application to both numerical and experimental data. In any case, one or two lines of measurements are considered, hence only treating the limited-view case. For synthetic data, generated through the rigourous integral formalism presented in §3.1, a simple line-source model is assumed for the antennas, implying isotropy and absence of coupling. Concerning experimental results, the basic signal processing is the one described in §1.6. In particular, differential measurements are performed, thus retrieving a scattered field inter-element matrix $\mathbf{K}(\omega) \triangleq \mathbf{K}^s(\omega)$. FFT windowing and time-gating are also applied, whereas the drift correction is implemented when applicable. Finally, the antennas are either modeled as infinitesimal dipoles or, if the experimental characterization data is available, using the multipolar model developed in §1.7.

2.3.1 Kirchhoff migration

Kirchhoff migration [90] is a well-established (especially in geophysical prospection) and maybe one of the simplest methods for imaging with antenna arrays. It is based on the concept of arrival time and requires the knowledge of the wave speed in the propagation medium - it applies then in a particularly straightforward manner in free-space. Although

it is not related to Time Reversal, it is presented here as a sort of reference method due to its efficient use of both space (antenna array) and frequency diversity (UWB).

Consider the time-domain version of the inter-element matrix, $\tilde{\mathbf{K}}(t)$. Either the complex envelope or the real signal can be used, the former being preferred here. An image of the scatterer(s) within an investigation domain Ω is sought, $\vec{r}$ being the position within Ω. Due to the 2D configuration, only the section of the scatterer(s) in the plane $z = 0$ is sought. The Kirchhoff migration image $I^{\mathrm{KM}}(\vec{r})$ is built by evaluating $\tilde{\mathbf{K}}(t)$ at the round-trip time $t^{\mathrm{d}}_{jk}(\vec{r})$ associated to the emitting antenna k and the receiving antenna j for the position $\vec{r}$:

$$I^{\mathrm{KM}}(\vec{r}) = \int_{-\delta t}^{\delta t} \left| \sum_{j,k} \tilde{K}_{jk} \left[t^{\mathrm{d}}_{jk}(\vec{r}) + \tau \right] \right|^2 d\tau \ . \tag{2.7}$$

The integration over a $2\delta t$ interval is needed to take into account the finite pulse length, equal to the inverse of the bandwidth (in our case, 1/2 GHz = 0.5 ns). In free-space, the round-trip time writes as

$$t^{\mathrm{d}}_{jk}(\vec{r}) \triangleq t_j + t_k = \frac{d_j(\vec{r})}{c_0} + \frac{d_k(\vec{r})}{c_0} \ , \tag{2.8}$$

with d_j (d_k) being the distance between antenna j (k) and the position $\vec{r}$. The idea behind (2.7) consists then in matching the position-dependent arrival time $t^{\mathrm{d}}_{jk}(\vec{r})$ to the target arrival time contained in $\tilde{K}_{jk}(t)$, which can be written as

$$t^{\mathrm{d}}_{jk}(\vec{r}_{\mathrm{tgt}}) \triangleq \tau_j + \tau_k = \frac{d_j(\vec{r}_{\mathrm{tgt}})}{c_0} + \frac{d_k(\vec{r}_{\mathrm{tgt}})}{c_0} \ . \tag{2.9}$$

Equivalently, Kirchhoff migration can be seen as an algorithm performing time-domain beamforming[3] *both* at emission and at reception for each investigation domain point $\vec{r}$. The points with maximum energy after the beamforming procedure form the image of the target.

Notice also that keeping only the diagonal elements of the $\tilde{\mathbf{K}}$ matrix in (2.7), that is, imposing $j = k$ in the sum, corresponds to the processing usually employed in Synthetic Aperture RADARs (SARs), where a single antenna is displaced and the retrodiffused signal measured [91].

Under far-field conditions ($F \gg D$ and $F \gg \lambda_{\max}$), the resolution[4] performances given by Kirchhoff migration, analytically derived in §B.1, can be summarized as follows.

Down-range The resolution $R^{\mathrm{KM}}_{\mathrm{dn}}$ only depends on the bandwidth of the signal, ω_{bw}, and equals half the corresponding wavelength, $\lambda_{\mathrm{bw}} = 2\pi c_0/\omega_{\mathrm{bw}}$, as in matched-filter processing commonly used in RADAR [92]:

$$R^{\mathrm{KM}}_{\mathrm{dn}} \approx \frac{\lambda_{\mathrm{bw}}}{2} \ . \tag{2.10}$$

[3]While in frequency domain beamforming consists of steering an antenna array with a complex amplitude per channel, in time-domain beamforming is equivalent to using different time delays for each channel.

[4]Given an infinitely long wire (a point in 3D) scatterer in far-field and an image $I(\vec{r})$ of it, the resolution is defined as the distance between the highest-energy spot and the nearest zero.

The array aperture has in practice a negligible impact on $R_{\mathrm{dn}}^{\mathrm{KM}}$.

Cross-range On the other hand, $R_{\mathrm{x}}^{\mathrm{KM}}$ depends also on the central frequency, ω_{c}, and on F and D similarly to Phase Conjugation. When $\omega_{\mathrm{bw}} < \omega_{\mathrm{c}}$, though, the influence of the bandwidth becomes negligible. For the parameters of our system (2 GHz bandwidth and 3 GHz central frequency), only the central frequency determines the cross-range resolution, giving

$$R_{\mathrm{x}}^{\mathrm{KM}} \approx \frac{\lambda_{\mathrm{c}} F}{D} \ . \tag{2.11}$$

For the configurations used in this chapter, with $\omega_{\mathrm{bw}} = 2\pi 3$ GHz, antenna spacing $\Delta x = 5.3$ cm, and $N = 8$ antennas, (2.11) gives $R_{\mathrm{x}}^{\mathrm{KM}} \approx 0.27F$.

Notice that, in general, the resolution spot size at 3 dB can be approximated by the values just mentioned.

Experimental results

The results obtained with the Kirchhoff migration method change considerably under the reflection or transmission configurations. They are therefore presented separately.

Reflection configuration

First, some results pertaining to the reflection configuration, that is, one single array transmitting and receiving (see §1.3), are presented. The simple case of a metallic scatterer with circular section and diameter 4 cm is treated in Fig. 2.8. With synthetic data (Fig. 2.8(b)), one can appreciate a resolution spot with a maximum placed at the point of the cylinder support nearest to the antenna array. The primary reason is that the wave does not penetrate into the object. Furthermore, given the small dimensions of the object and the small array aperture, only a reduced portion of the scattering support is *visible* to the array, so that the scattering phenomenon appears as concentrated into a point. The width of a half of the resolution spot in down-range is approximately equal to $\lambda_{\mathrm{bw}}/2 = 7.5$ cm, in good accordance with the theoretical $R_{\mathrm{dn}}^{\mathrm{KM}}$ value. Concerning the cross-range, a half of the spot size is approximately equal to 11 cm, also in good agreement with the 13 cm found in §B.1. Notice that these values are also affected by the FFT *lanczos* window $W_\omega(\omega)$ introduced in §1.6.2, which unavoidably lowers the effective bandwidth and therefore mainly $R_{\mathrm{dn}}^{\mathrm{KM}}$.

When using experimental data (Fig. 2.8(c)), while the shape of the resolution spot is barely changed, the highest-energy spot is shifted by about 10 cm away from the antenna array. This is due to the time delay introduced by the ETS antennas because of the traveling wave propagation through the duroid substrate. In §1.7.2.1, such delay has been estimated to approximately 5 cm in free-space, giving the observed 10 cm due to both the emitting and receiving antennas.

An alternative strategy to correct for this artefact consists in directly using the experimental antenna radiation pattern to build the migration chart. Once the characterization

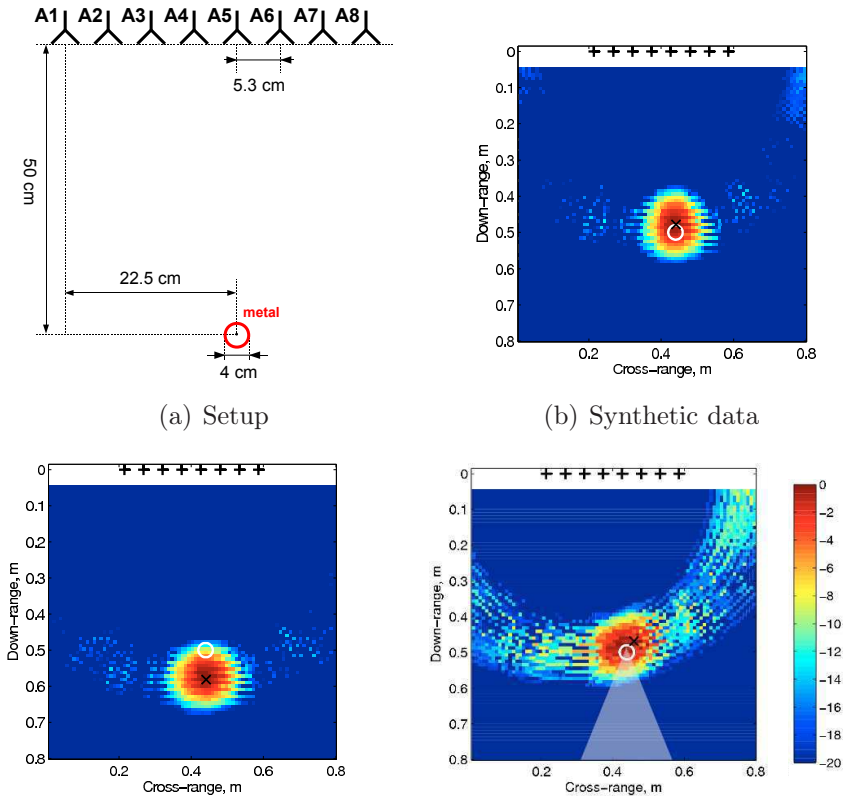

(a) Setup

(b) Synthetic data

(c) Experimental data

(d) Experimental data with antenna pattern correction

FIGURE 2.8: *Kirchhoff migration applied to the reflection setup in (a). In (d), the shaded region identifies the pixels whose azimuth angles with respect to all of the array antennas are within the range measured during the antenna characterization procedure described in §1.7.2. For experimental data, the drift correction is always applied. In all the images, the white circle represents the target support, and the black cross the hottest spot found.*

coefficients have been retrieved as described in §1.7.2, the scattering of a target placed in $\vec{r}$ for the $(j,k)^{\text{th}}$ pair of receiving and emitting antennas, respectively, can be calculated (*cf.* FIG. 1.29). The peak of the retrieved pulse is then the $t^d_{jk}(\vec{r})$ to be used in (2.7). The result is the chart in FIG. 2.8(d), where indeed the "hot" spot is again at the front face of the cylinder. Nevertheless, the result appears globally more perturbated. The reason is that, during the antenna characterization step, the available aperture angle $\Delta\varphi \approx 40$ deg; beyond this value the radiation pattern extrapolation is untrustable. Hence, the region where *all* the antennas are within such range is shaded in FIG. 2.8(d), showing that almost everywhere in the chart an extrapolation is done for at least one antenna, which unavoidably alters the result.

Experimental results pertaining to different targets are shown in FIG. 2.9. Two dielectric (wooden, $\varepsilon_r \approx 2$) targets, one with 1.5 cm-diameter circular section and the other with 10.5×7 cm^2 rectangular section, are first imaged separately; then, a configuration with the

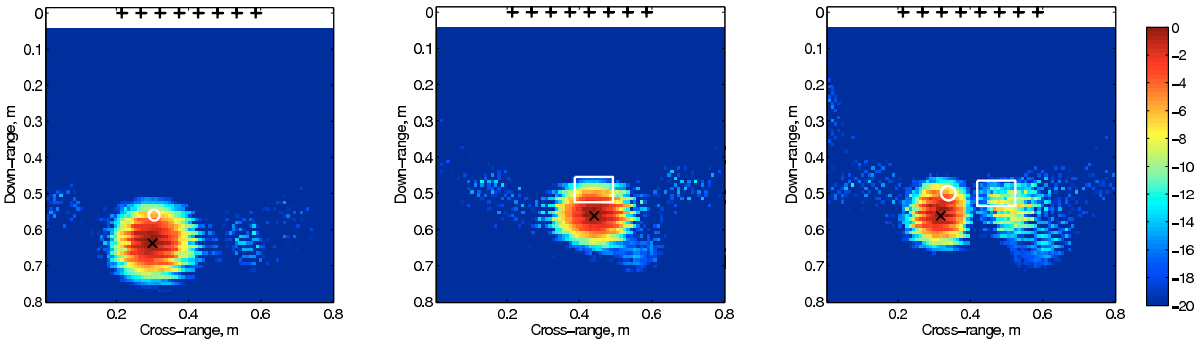

(a) 3 cm-diameter wooden target ($\varepsilon_r \approx 2$) with circular section

(b) 10.5×7 cm^2 wooden target ($\varepsilon_r \approx 2$) with rectangular section

(c) 4 cm diameter metallic target with circular section and 10.5×7 cm^2 wooden target ($\varepsilon_r \approx 2$) with rectangular section

FIGURE 2.9: *Kirchhoff migration applied to several configurations. In all cases, the drift correction is applied whereas the experimental antenna radiation pattern is not used.*

rectangular one and the metallic target of FIG. 2.8 together is studied. The drift correction is applied, whereas the experimental characterization of the antennas is deliberately not used - hence all the spots should be shifted by roughly 10 cm towards the antenna array.

With dielectric targets, Kirchhoff migration behaves slightly differently, due to their penetrability. For instance, comparing FIG. 2.9(a) and FIG. 2.8(c) the dielectric target, although smaller than the metallic one, looks bigger. Nevertheless, in FIGS. 2.9(a)-2.9(b) some indications on the shape of the target can rouglhy be deduced. Finally, even with two targets (FIG. 2.9(c)) a fair image is obtained. Indeed, the center of the targets are 12.5 cm spaced, slightly more than $R_{\mathrm{x}}^{\mathrm{KM}} \approx 12.5$ cm here. Notice also that the metallic target is "hotter" as compared to the wooden one due to its stronger scattering power.

A last result under the reflection configuration aims at tackling the case of a partially unknown propagation medium. In FIG. 2.10, the Kirchhoff migration is applied to two identical two-target configurations, except that in one of them a tile wall and a metallic plate are added laterally with respect to the down-range direction in order to perturbate the propagating medium. Using then the free-space Green function to fetch the arrival times necessary to build $I^{\mathrm{KM}}(\vec{r})$ is erroneous in the sense that the echoes coming from the reflections on the walls are thus ignored. The result is a degradation in the images when comparing FIG. 2.10(c) and FIG. 2.10(d), although the targets can still be detected and localized.

Transmission configuration

Kirchhoff migration behaves differently when used in a limited-aspect transmission configuration as those in FIGS. 2.11(a)-2.12(a). Either with synthetic or experimental data and regardless of the conducting or dielectric nature of the target, the image is elongated

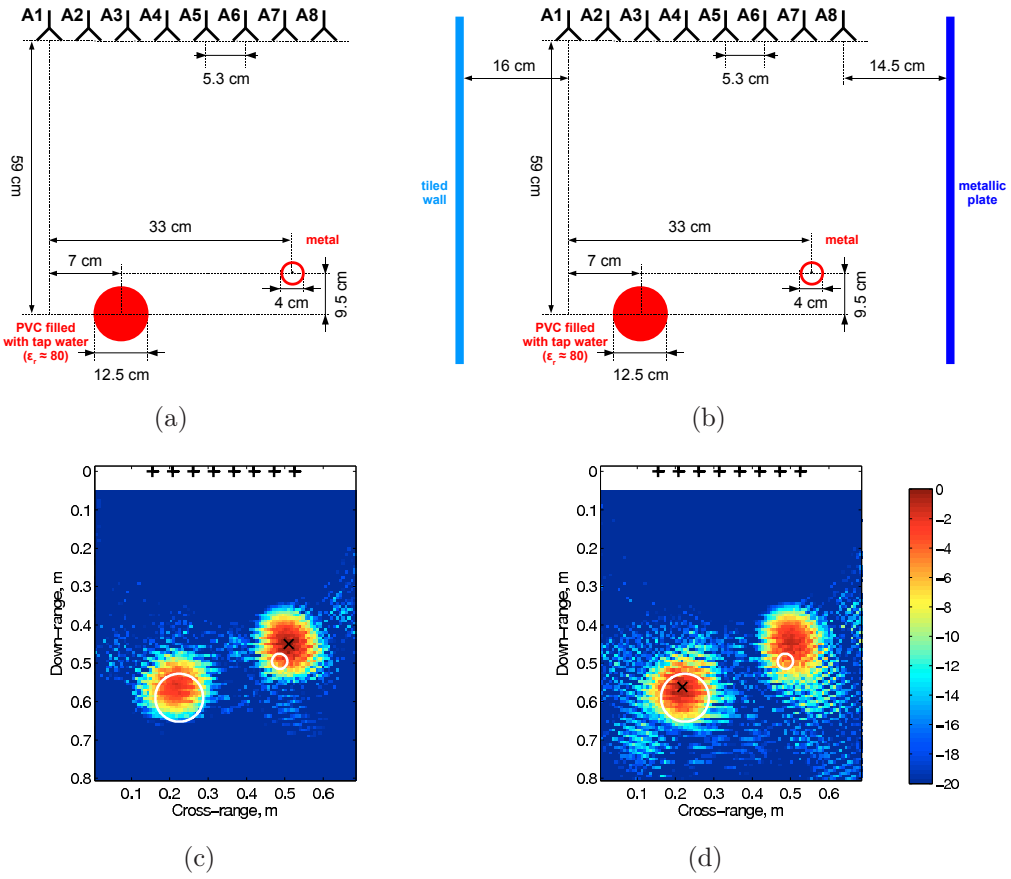

FIGURE 2.10: *Kirchhoff migration applied to the configurations in (a) and (b).*

along the down-range. This is to be expected, since for a given couple (A_k,A_j) of emitting/receiving antennas belonging each to a different array, the arrival time $t^d_{jk}(\vec{r})$ in (2.8) is identical for all the points $\vec{r}$ along the line going from A_j to A_k, and only slightly changes when the point moves away from such line. As a demonstration, elliptical patterns are clearly visible in FIG. 2.11(c).

2.3.1.1 Conclusions

In reflection configurations, Kirchhoff migration behaves very well under free-space assumptions. Care must be taken when imaging dielectric targets, since their penetrability alters the dimensions given by the the Kirchhoff image. In transmission configurations, when the arrays have a limited aperture D, the down-range resolution is on the contrary very rough.

In any case, Kirchhoff migration is deeply affected by a wrong description of the Green function of the medium. In other words, if strong multiple scattering or clutter are present in the medium, the estimation (2.8) of the arrival times becomes wrong and very noisy images must be expected (*cf.* FIG. 2.10(d)).

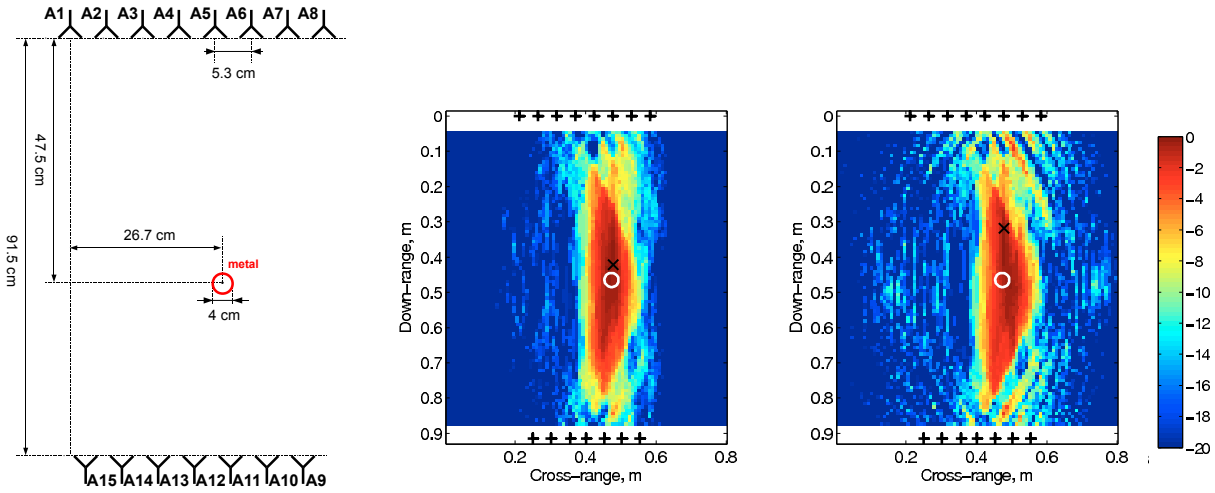

(a) Setup (b) Synthetic data (c) Experimental data

FIGURE 2.11: *Kirchhoff migration applied to the transmission setup in (a). Metallic target.*

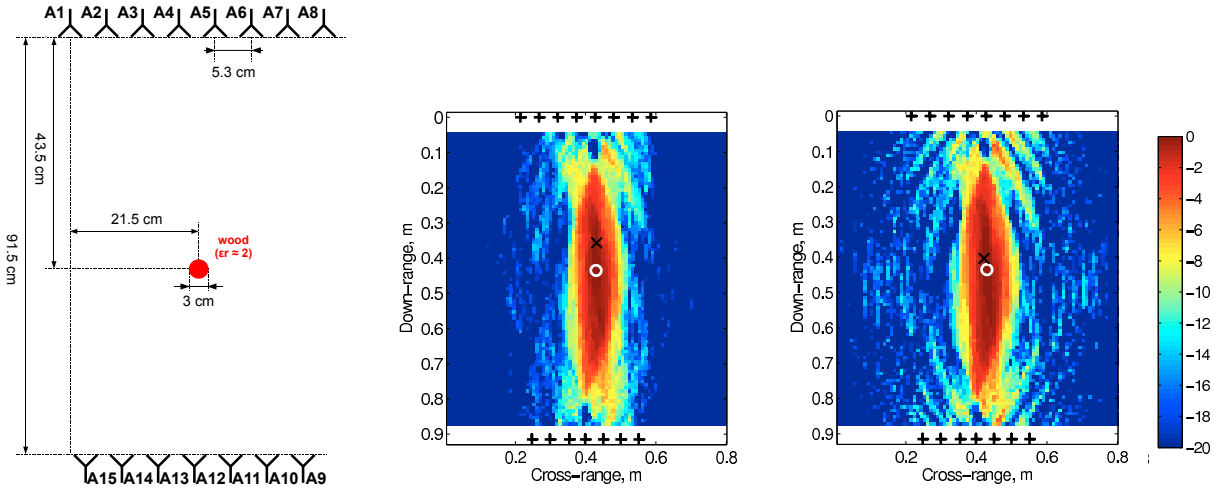

(a) Setup (b) Synthetic data (c) Experimental data

FIGURE 2.12: *Kirchhoff migration applied to the transmission setup in (a). Purely dielectric target.*

2.3.2 Time Reversal

With respect to the active source case described previously in §2.2, it is relatively straightforward to adapt the TR method to the scattering case[5]. The emitting array must illuminate the scene with an incident wave, and the scattered vector - whose components are the scattered signals received by each receiving antenna - must be back-propagated after phase-conjugating each frequency component. The result is a new incident wave focusing onto the scatterer(s) populating the medium. The main difference with the active source case, is that now there is a new scattered wave, which can again be phase-conjugated and back-propagated. An iterative TR procedure [93] can then built up, which, in case of mul-

[5]In acoustics, this configuration is known as *pulse-echo mode*.

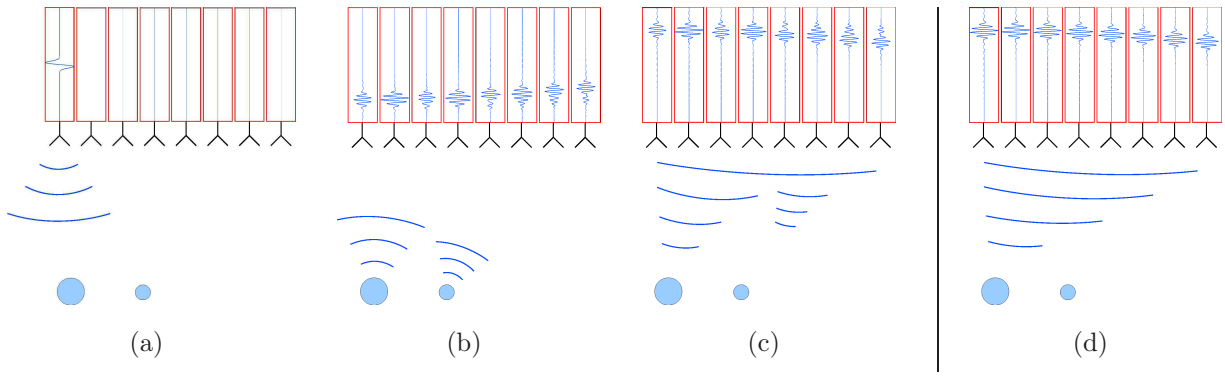

FIGURE 2.13: *Schematization of the iterative TR process. (a) Two targets are illuminated by an incident wave (here a wave emitted by a single array antenna); (b) their scattered field is recorded into a memory by the array antennas; (c) the array antennas retransmit the time-reversed signals, giving a wavefront focusing onto the targets. The process continues iteratively, until (d) the array wavefront focuses only onto the brightest target.*

tiple scatterers, converges to a "final" incident wave focusing onto the brightest scatterer (see FIG. 2.13).

Time Reversal has two main drawbacks:

1. in configurations with a relatively high amount of noise (additive noise on the receiver, clutter in the propagation medium, etc.), the number of iterations needed to reach a sufficient Signal-to-Noise Ratio (SNR) might be sufficiently high to prevent focusing onto targets moving too fast or, rather equivalently, too distant from the array;
2. in presence of multiple targets, TR allows in principle to focus *only* onto the brightest one. Although it is possible to focus onto the others as well by re-starting the iterative process with an incident wave having a null in the direction of the previously detected target(s), the procedure takes even more time and further limits the maximum speed of detectable targets.

Both limitations are elegantly solved by the DORT method, as described next.

2.3.3 DORT

The DORT method, from the french acronym *Décomposition de l'Opérateur de Retournement Temporel*, was first introduced in 1994 by Prada *et al.* [3]. It is issued from the matrix-based analysis of the iterative TR process, and works with monochromatic data just as Phase Conjugation. Although, in order to derive it, the ω depency is removed for conciseness, all the quantities have to be meant as time-harmonic.

Consider two antenna arrays with N_1 and N_2 antennas, that might, but need not, be the same (reflection configuration). At the beginning of the TR iterative process, a steering vector $\mathbf{s}_{\mathrm{Tx}}^{(0)}$ is transmitted into the medium by the first array - this might correspond to a

beamformed wave or simply to a wave emitted by a single antenna. The scattered vector measured at the other array is then

$$\mathbf{s}_{\mathrm{Rx}}^{(0)} = \mathbf{K}\mathbf{s}_{\mathrm{Tx}}^{(0)} \ , \tag{2.12}$$

whereas its phase-conjugated version is back-propagated into the medium:

$$\mathbf{s}_{\mathrm{Tx}}^{(1)} = \mathbf{K}^* \left[\mathbf{s}_{\mathrm{Tx}}^{(0)}\right]^* \ . \tag{2.13}$$

After p iterations of TR, the vector to be back-propagated by the first array is

$$\mathbf{s}_{\mathrm{Tx}}^{(p)} = \left(\mathbf{K}^H\mathbf{K}\right)^{p/2} \mathbf{s}_{\mathrm{Tx}}^{(0)} \ , \tag{2.14}$$

which in practical implementations should be normalized to the wished emitting power level. The eigenvalue decomposition of $\mathbf{K}^H\mathbf{K} = \mathbf{V}\mathbf{\Lambda}^2\mathbf{V}^H$, called Time Reversal Operator (TRO), allows to simplify (2.14). In practice, the same result is more easily obtained using the SVD of $\mathbf{K} = \mathbf{U}\mathbf{\Lambda}\mathbf{V}^H$, where $\mathbf{\Lambda}$ is a diagonal matrix whose elements are the real singular values λ_l arranged in descending order, and $\mathbf{U}$ and $\mathbf{V}$ are unitary matrices[6] whose columns are the left and right singular vectors $\mathbf{u}_l$ and $\mathbf{v}_l$, respectively. Eq. (2.14) becomes then

$$\mathbf{s}_{\mathrm{Tx}}^{(p)} = \sum_{l=1}^{\min(N_1,N_2)} \lambda_l^p \left[\mathbf{v}_l^H \mathbf{s}_{\mathrm{Tx}}^{(0)}\right] \mathbf{v}_l \ . \tag{2.15}$$

Unless $\mathbf{s}_{\mathrm{Tx}}^{(0)}$ is orthogonal to the first singular vector $\mathbf{v}_1$, it is easy to see that as $p \to \infty$, (2.15) reduces to

$$\mathbf{s}_{\mathrm{Tx}}^{(p)} \approx \lambda_1^p \left[\mathbf{v}_1^H \mathbf{s}_{\mathrm{Tx}}^{(0)}\right] \mathbf{v}_1 \ . \tag{2.16}$$

This result shows that, apart from the scalar terms λ_1^p and $\mathbf{v}_1^H\mathbf{s}_{\mathrm{Tx}}^{(0)}$, the iterative TR process converges to a steering vector equal to the first right singular vector of $\mathbf{K}$, $\mathbf{v}_1$. In practical terms, then, there is no need to perform the iterations: provided the $\mathbf{K}$ matrix has been measured, it is sufficient to steer the array with $\mathbf{v}_1$ to obtain the same result.

Imaging through the DORT method consits then in building the field chart associated to the back-propagation of $\mathbf{v}_l$:

$$I_\omega^{\mathrm{DORT}}(\vec{r}; \mathbf{v}_l) = |i\omega\, \mathbf{v}_l^T \hat{\mathbf{G}}(\vec{r})|^2 \ , \tag{2.17}$$

which physically corresponds to an iterative TR process triggered with a vector $\mathbf{s}_{\mathrm{Tx}}^{(0)}$ orthogonal to the $l-1$ first singular vectors $\mathbf{v}_l$. $\hat{\mathbf{G}}(\vec{r})$ is the unit-norm Green function vector whose components are the normalized Green functions between the image pixel $\vec{r}$ and the antennas A_j, $j = 1, N_1$:

$$\hat{\mathbf{G}}(\vec{r}) \triangleq \frac{\mathbf{G}(\vec{r})}{\|\mathbf{G}(\vec{r})\|} \ , \quad \text{with} \quad \mathbf{G}(\vec{r}) = [G(\vec{r},\vec{r}_1)\ G(\vec{r},\vec{r}_2) \cdots G(\vec{r},\vec{r}_N)]^T \ . \tag{2.18}$$

[6] A unitary matrix $\mathbf{A}$ is a matrix such that $\mathbf{A}^H\mathbf{A} = \mathbf{A}\mathbf{A}^H = \mathbf{I}$.

The normalization term $1/\|\mathbf{G}(\vec{r})\|$ helps in nulling the amplitude decrease due to the $1/\sqrt{|\vec{r}|}$ ($1/|\vec{r}|$ in 3D) dependency of the Green function, thus considerably improving the down-range resolution for targets placed far from the array. Also, the $i\omega$ factor comes from the fact that the field chart corresponds to an electric field distribution whereas the antennas are fed in current (see §C for more details).

The field chart can also be built as the back-propagation of the left singular vector $\mathbf{u}_l$ using the second antenna array (A_j, $j = 1, N_2$), giving

$$I_\omega^{\mathrm{DORT}}(\vec{r}; \mathbf{u}_l) = |i\omega\, \mathbf{u}_l^H \hat{\mathbf{G}}(\vec{r})|^2 \ , \tag{2.19}$$

which corresponds to an iterative TR process triggered by the second array. Of course, since in a reflection configuration $\mathbf{K}$ is symmetric in virtue of reciprocity, $\mathbf{u}_l^*$ and $\mathbf{v}_l$ are co-linear, and (2.17) and (2.19) give the same result. On the other hand, in a configuration with two separate arrays, *e.g.* in a transmission configuration, the result is not the same.

Notice also that (2.17) and (2.19) assume ideal dipolar antennas in far-field; on this purpose, a rigorous derivation of the field chart formula is given in §C. Alternatively, the experimentally retrieved antenna radiation pattern, arranged into the unit-norm vector $\hat{\mathbf{RP}}(\vec{r})$, can be utilized in spite of $\hat{\mathbf{G}}(\vec{r})$.

Concerning the resolution given by the DORT method when $\mathbf{v}_l$ focuses onto a target, with reference to §B.2 (although the results are obtained for the time-domain extension of DORT to be studied next), the following results hold.

Down-range For a very small array aperture, DORT gives an infinitely large down-range resolution, since it is here considered as a monochromatic method which is then unable to exploit the arrival time, or range, information:

$$R_{\mathrm{dn}}^{\mathrm{DORT}} \approx \infty \ . \tag{2.20}$$

With a finite array aperture D with respect to the target distance F (see Fig. 2.14), the resolution becomes finite yet very large.

Cross-range As Kirchhoff migration, DORT performs beamforming, even though at a single frequency and at emission (or reception) only. The same resolution is then obtained, that is,

$$R_{\mathrm{x}}^{\mathrm{DORT}} \approx \frac{\lambda F}{D} \ , \tag{2.21}$$

where λ is the wavelength relative to the permittivity of the propagation medium.

2.3.3.1 Extended target in near-field

An analytical study of the DORT method was for the first time carried out in [18] for the complete configuration case (antennas surrounding the propagating medium), and in [20] for the limited-aspect configuration case (measurement line in reflection). The present work is mainly focused on the latter setup. Under this frame, it has been shown through the

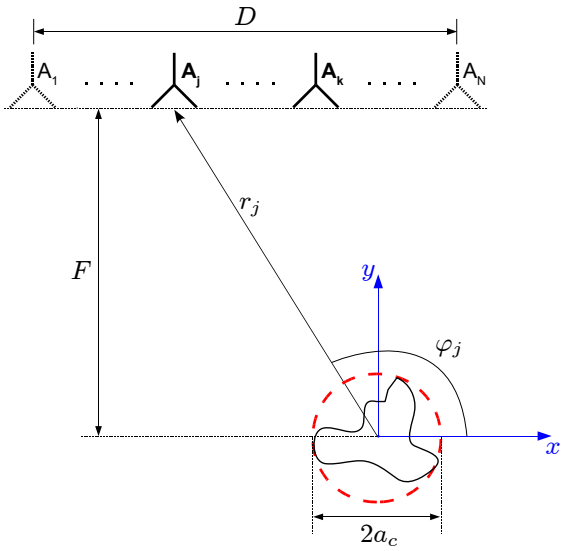

FIGURE 2.14: *Configuration for deriving the properties of the DORT method.*

multipolar expansion of the field scattered by a target, that DORT basically isolates, or extracts, the projection of the multipolar components onto the measurement line [20].

To explain this, with reference to FIG. 2.14 and considering ideal 2D sources/receivers, K_{jk} can be expressed through the use of the Graf's formula [94] and the scattering matrix formalism [95]. The result is

$$K_{jk} = \sum_{m,n} S_{m,n} H_n^-(kr_k) e^{in\varphi_k} H_m^-(kr_j) e^{-im\varphi_j} \ , \tag{2.22}$$

where $S_{m,n}$ is the $(m,n)^{\text{th}}$ element of the scattering matrix and H_n^- is the Hankel function of n^{th} order and second kind[7].

With respect to the dimensions of the target as compared to the wavelength of the background λ, two regimes can be distinguished:

Low-frequency regime

When the dimensions of the target equal at most a fraction of λ, and for targets with a rather regular support, (2.22) is well approximated by considering the scattering matrix as a diagonal matrix[8] with only three non-negligible terms, $S_{-1,-1}$, $S_{0,0}$, and $S_{1,1} = S_{-1,-1}$. Therefore, using the fact that $H_1^- = -H_{-1}^-$,

$$K_{jk} \approx S_{0,0} H_0^-(kr_k) H_0^-(kr_j) + 2S_{1,1} H_1^-(kr_k) H_1^-(kr_j) \cos(\varphi_k - \varphi_j) \ . \tag{2.23}$$

Adding the hypothesis that the target is at least $\lambda/2$ far from the array, Micolau and Saillard [20] have shown that

- one singular space of $\mathbf{K}$ is given by an *anti-symmetric* singular vector $\mathbf{v}^{\text{asym}}$, whose j^{th} component is

$$v_j^{\text{asym}} = H_1^+(kr_j) \cos(\varphi_j) \ , \tag{2.24}$$

[7]The reason why H_n^- is used in spite of H_n^+ is the time dependency convention, here $e^{+i\omega t}$.
[8]This is rigorously true for circular-section targets.

and a singular value λ^{asym} whose amplitude increases with χ^2, where $\chi \propto \varphi_N - \varphi_1$ basically represents the angular aperture of the array;

- two other singular vectors are linear combinations of two *symmetric* vectors described by

$$\begin{cases} H_0^+(kr_j) \\ H_1^+(kr_j)\sin(\varphi_j) \end{cases}, \tag{2.25}$$

whereas for the singular values, $\lambda^{\text{sym},1} \propto \chi^0$ and $\lambda^{\text{sym},2} \propto \chi^2$. In addition, for $\chi \to 0$, that is, for a small aperture, $v_j^{\text{sym},1} \approx H_0^+(kr_j)$.

As long as χ is relatively small, $\lambda^{\text{sym},1}$ is the largest singular value, followed by λ^{asym} and $\lambda^{\text{sym},2}$. The anti-symmetric one, λ^{asym}, tends to become larger than $\lambda^{\text{sym},1}$ when increasing the array aperture and at higher frequencies.

Resonance regime

When removing the low-frequency regime assumption, that is, when the dimensions of the target are comparable to λ, interestingly enough, DORT is still able to separate symmetric and anti-symmetric components of the scattered field, only the amplitude hierarchy of the singular values changes and the largest one is not necessarily that associated with a symmetric field. Also, other anti-symmetric singular vectors with more than one π phase jumps become significant.

Experimental results

By means of an example based on experimental data, it is useful to give an insight into the physical meaning of "symmetric" and "anti-symmetric" vectors. The configuration is shown in Fig. 2.15(a): a 2 cm-radius metallic cylinder is imaged in reflection. The target dimensions do not really fulfill the low-frequency regime hypotheses, especially at the high end of the frequency band. This, in addition to the relatively high aperture angle (around 50 deg), result in Fig. 2.15(d) in an anti-symmetric singular value, λ_2, "only" 20 dB lower than the symmetric one, λ_1. As for the other singular values, they have an irregular, oscillating aspect since they are associated to noise. Although "pure" noise should present a flat behavior - apart from the amplitude damping at the band edges due to the FFT window $W_\omega(\omega)$ - corresponding to the noise floor of the VNA, two factors alter their frequency dependency: 1) the RF signal ringing due to unperfect adaptation of cables and connectors of the prototype, and 2) the thermal drift that pollutes the total/incident field difference and generates a sort of correlated noise (*cf.* §1.4.3).

The complex laws of the singular vectors and the monochromatic field charts at 3 GHz associated to λ_1 and λ_2 are shown in Fig. 2.15(b-c) and Fig. 2.15(e-f), respectively. $\mathbf{v}_1$ is the symmetric singular vector since it corresponds to the isotropic, or monopolar, component of the scattered field: its phase keeps the same sign over the vector elements and the associated field chart focuses in the direction of the target. On the other hand, $\mathbf{v}_2$ is an

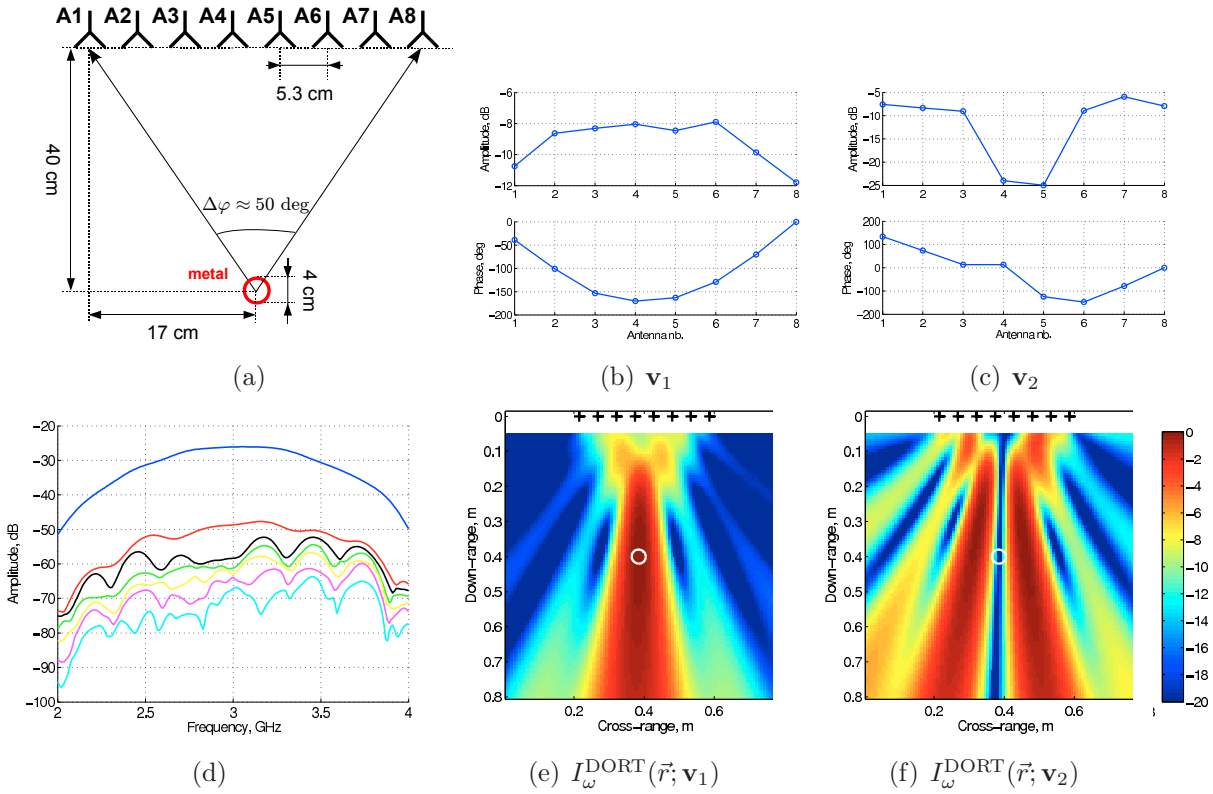

(a) (b) $\mathbf{v}_1$ (c) $\mathbf{v}_2$

(d) (e) $I_\omega^{\mathrm{DORT}}(\vec{r};\mathbf{v}_1)$ (f) $I_\omega^{\mathrm{DORT}}(\vec{r};\mathbf{v}_2)$

FIGURE 2.15: *DORT method applied to the reflection setup in (a). (d)* $\mathbf{K}$ *matrix singular values as a function of frequency. (b-c) and (e-f)* $\mathbf{v}_1$ *and* $\mathbf{v}_2$ *complex laws and corresponding monochromatic field charts at 3 GHz, respectively.*

anti-symmetric singular vector. Its phase has a π jump corresponding to the first order of anistropy, or multipolarity, of the scattered field. As a consequence, it generates a wave with a null at the position of the target. This behavior can somehow be interpreted as well as a focusing property, in the sense that it might favorably exploited in localizing the target, as described for the subspace methods introduced later. As for the other frequencies within the [2-4] GHz band, the respective field charts fully confirm the behavior observed in FIG. 2.15(e-f).

2.3.3.2 Time-domain extension

As opposed to TR, DORT is instrinsicly a time-harmonic method. Extending it to the time-domain is particularly important when using an array with a small aperture angle in reflection. In effect, although this configuration is favorable for well separating symmetric and anti-symmetric singular values/vectors as explained in the previous paragraph, DORT images are very poorly resolved in down-range (*cf.* FIG. 2.15(e)). An efficient exploitation of the available bandwidth can then greatly improve the down-range resolution, as seen for instance with the Kirchhoff migration method (*c.f.* FIGS. 2.8-2.9).

As a starting point, the SVD of $\mathbf{K}(\omega)$ separately at each frequency within the operating band must be performed. For imaging purposes, all the monochromatic field charts in

(2.17) can be either summed incoherently, giving

$$I_{\omega\omega}^{\mathrm{DORT}}(\vec{r};\mathbf{v}_l) = \sum_{\omega=\omega_{\mathrm{m}}}^{\omega_{\mathrm{M}}} \left| i\omega\, \mathbf{v}_l^T(\omega)\hat{\mathbf{G}}(\omega;\vec{r}) \right|^2 , \tag{2.26}$$

or recomposed coherently,

$$I_t^{\mathrm{DORT}}(\vec{r};\mathbf{v}_l) = \mathrm{IFT}\left[i\omega\, \mathbf{v}_l^T(\omega)\hat{\mathbf{G}}(\omega;\vec{r}) \right](t) . \tag{2.27}$$

Physically speaking, (2.27) describes the propagation in time of the electric field produced by an array steered with the time-domain singular vector $\tilde{\mathbf{v}}_l(t) \triangleq \mathrm{IFT}\left[\mathbf{v}_l(\omega)\right](t)$.

Of course, thanks to coherency in frequency, (2.27) allows to greatly improve the down-range resolution performances, very poor in the monochromatic case (2.17) as well as in (2.26). Unfortunately, the singular vectors are mathematically determined up to a complex constant, that is, if $\mathbf{v}_l(\omega)$ is a singular vector, then also $a(\omega)\,\mathbf{v}_l(\omega)$ is one, with $a(\omega) \in \mathbb{C}$, meaning that an infinity of them rigorously exist. Therefore, it is in principle incorrect to directly perform the IFT of the singular vectors, since the coherency in frequency is lost due to the indetermination of the constant $a(\omega)$, and more importantly of its phase $\phi_a(\omega) = \arg[a(\omega)]$.

Some solutions to the construction of coherent temporal singular vectors are reviewed next in §2.3.3.3. Here, it must be stressed that one of the consequences of such phase indetermination is that the time instant at which the back-propagated wave (2.27) focuses onto the target, t^{foc}, is unknown, whereas according to the time-inversion principle of TR it should be equal to 0 s. To form a single image of the scatterer, it is then necessary to "extract" from the "movie" in (2.27) one single frame. Such frame corresponds in principle to t^{foc}, since it is at the target location *and* at the focusing instant that constructive interference takes place. Two approaches can then be used to fetch the "best" image.

- Choose t^{foc} as the instant where the maximum of (2.27) is reached.
- Choose t^{foc} as the instant where the entropy $H(t)$ of the image is minimized [96]. This is motivated by the fact that, at the focusing instant, the back-propagated wave almost corresponds to the wave initially scattered by the target when hit by the field impinging on it. Thus, it should be a "well-ordered" [96] wave, hence its entropy - a measure of the disorder of an image - should be the smallest among all the frames.

The resolution obtained with (2.27) has been analytically studied in §B.2.

Down-range I_t^{DORT} is based on time-domain beamforming *either* at emission with $\mathbf{v}_l$ *or* at reception with $\mathbf{u}_l$. Assuming the focusing instant t^{foc} is well chosen, the down-range resolution is then equal to λ_{bw}, twice the value found for Kirchhoff migration which performes beamforming *both* at emission *and* at reception:

$$R_{\mathrm{dn}}^{\mathrm{DORT}} \approx \lambda_{\mathrm{bw}} . \tag{2.28}$$

Cross-range Assuming $\omega_{\mathrm{bw}}/\omega_{\mathrm{c}} < 1$, the cross-range resolution is basically given by the central frequency monochromatic result, that is,

$$R_{\mathrm{x}}^{\mathrm{DORT}} \approx \frac{\lambda_{\mathrm{c}} F}{D} \ . \tag{2.29}$$

2.3.3.3 Time-domain singular vectors

Back to (2.27), it has already been mentioned that the phase indetermination brought by the SVD of the $\mathbf{K}$ matrix prevents from building coherent time-domain singular vectors. A hint on how to solve this problem might come from the description of the iterative TR process. In effect, it is easy to see that (2.16) actually preserves the frequency coherence, since the $e^{-i\phi_a(\omega)}$ factor appears both in $\mathbf{v}_1$ and, conjugated, in $\mathbf{v}_1^H$.

In this sense, TR and time-domain DORT are strictly equivalent (apart from the absence of iterations and the selective focusing capability given by DORT). But the question to be asked is whether the same spatiotemporal focusing obtained with TR in the *active* source case can be obtained by DORT with a *passive* target. Some possible answers have recently appeared in literature.

Free-space propagation

In free-space, the optimal spatiotemporal focusing is simply obtained by triggering the iterative TR procedure with the emission of a single array antenna, say the j^{th} one. This corresponds to substituting $\mathbf{s}_{\mathrm{Tx}}^{(0)}(\omega) = \mathbf{1}_j$ in (2.16)[9], which gives, in the case of a single target located at $\vec{r}_{\mathrm{tgt}}$, the new steering vector $\hat{\mathbf{v}}_1(\omega)$

$$\begin{aligned} \hat{\mathbf{v}}_1(\omega) &= \lambda_1(\omega) \left[\mathbf{v}_1^H(\omega)\mathbf{1}_j\right] \mathbf{v}_1(\omega) \\ &= \lambda_1(\omega)\mathbf{v}_1(\omega)e^{-i\arg[v_{1,j}(\omega)]} \ . \end{aligned} \tag{2.30}$$

Recalling now §2.3.3.1, in the low-frequency regime and neglecting any amplitude normalization factor, the singular vector given by any SVD routine is of the kind $\mathbf{v}_1(\omega) = \hat{\mathbf{G}}^*(\omega;\vec{r}_{\mathrm{tgt}})e^{i\phi_a(\omega)}$, since in free-space $G(\omega;\vec{r}_j,\vec{r}_{\mathrm{tgt}}) = -iH_0^-(k|\vec{r}_{\mathrm{tgt}} - \vec{r}_j|)/4$. Thus, as

$$\arg\left[v_{1,j}(\omega)\right] = k|\vec{r}_{\mathrm{tgt}} - \vec{r}_j| + \phi_a(\omega) \ , \tag{2.31}$$

(2.30) becomes

$$\hat{\mathbf{v}}_1(\omega) = \lambda_1(\omega)\hat{\mathbf{G}}^*(\omega;\vec{r}_{\mathrm{tgt}})e^{-ik|\vec{r}_{\mathrm{tgt}}-\vec{r}_j|} \ . \tag{2.32}$$

Back-propagating $\hat{\mathbf{v}}_1(\omega)$ at the target location $\vec{r}_{\mathrm{tgt}}$ results in

$$\hat{\mathbf{v}}_1^T(\omega)\hat{\mathbf{G}}(\omega;\vec{r}_{\mathrm{tgt}}) = \lambda_1(\omega)e^{-ik|\vec{r}_{\mathrm{tgt}}-\vec{r}_j|} \ , \tag{2.33}$$

that is, the frequency components of the back-propagated field hit the target with a linear phase dependency with respect to ω. Then, as compared to the "ideal" case

[9] Of course, if a particular pulse shape $\tilde{p}(t)$ is to be emitted, then $\mathbf{1}_j$ needs to be multiplied by its IFT $p(\omega)$.

$\mathbf{v}_1(\omega) = \hat{\mathbf{G}}^*(\omega; \vec{r}_{\text{tgt}})$ that would give the same zero-phase at $\vec{r}_{\text{tgt}}$ at any frequency, this strategy only produces a simple delay equal to $t^{\text{foc}} = |\vec{r}_{\text{tgt}} - \vec{r}_j|/c$, not altering the focusing quality at all. Indeed, (2.27) evaluated at $\vec{r} = \vec{r}_{\text{tgt}}$ gives

$$I_t^{\text{DORT}}(\vec{r}_{\text{tgt}}; \hat{\mathbf{v}}_1) = \text{IFT}\left[i\omega\, \hat{\mathbf{v}}_1^T(\omega)\hat{\mathbf{G}}(\omega; \vec{r}_{\text{tgt}})\right](t) = \frac{\partial \tilde{\lambda}_1\left(t - t^{\text{foc}}\right)}{\partial t}\ , \tag{2.34}$$

where $\tilde{\lambda}_1(t) = \text{IFT}\left[\lambda_1(\omega)\right](t)$.

With this method, there is no need to know *a priori* the target position and if, in case of multiple targets, their separation is assured by DORT, there is no degradation whatsoever of the selective focusing quality. The present analysis is also meaningful to explain experimental results such as those reported in [29] for free-space configurations, since no mathematical justification is given for the very good focusing achieved.

SVP technique

Since in the active source case all the monochromatic back-propagated vectors hit the initial source with the same phase (namely 0 deg, *cf.* FIG. 2.5(a)), it is natural to build a new singular vector $\hat{\mathbf{v}}_l(\omega) = \mathbf{v}_l(\omega)e^{i\phi_{\text{corr}}(\omega)}$, whose correction phase $\phi_{\text{corr}}(\omega)$ has to be determined by imposing that, given the target position $\vec{r}_{\text{tgt}}$, the back-propagated field $\hat{\mathbf{v}}_l^T(\omega)\hat{\mathbf{G}}(\omega; \vec{r}_{\text{tgt}})$ has the same phase at each frequency ω. The method, introduced by Philippe *et al.* [97], has been named SVP from the french acronym *Synchronisation des Vecteurs Propres* (eigenvectors synchronization).

Despite its "elegant" simplicity, this method relies on the *a priori* knowledge of $\vec{r}_{\text{tgt}}$. Although this information can be retrieved through another method (monochromatic DORT, Kirchhoff migration, etc.), the precision of the estimation is resolution-limited. Furthermore, it is not clear where exactly $\vec{r}_{\text{tgt}}$ should be placed in case of an extended target in the resonance regime. Lastly, in complex propagating media whose Green function is not fully known, the estimation of $\vec{r}_{\text{tgt}}$ might even be too erroneous to be used for the correction.

Space-frequency DORT

A totally different approach is followed in [98] by Yavuz *et al.*. It consists in performing the SVD of one big space-frequency matrix (or N smaller ones for each emitter) containing all the measured data: its columns are spanned by the frequency ω and its lines by the emitters/receivers positions. By doing so, there is no more loss of coherency, since one single SVD must be performed to process all the data.

Although a scheme describing how to use the new right and left singular vectors in conjunction with the singular values is proposed, and although some interesting results have been reported, there is no mathematical or physical evidence on why the method should work and be robust to clutter. Also, due to the same lack of mathematical/physical derivation, it is not clear how to choose the number of left and right singular vectors when building the time-domain vectors.

Arrival time estimation

Yet another approach is used by Borcea *et al.* in [99]. As a first step, $k = 1, N$ modified versions of the singular vector $\mathbf{v}_l(\omega)$ are built by projecting onto it the columns of the $\mathbf{K}$ matrix, $\mathbf{K}^{[k]}$, giving

$$\left[\mathbf{v}_l^{[k]}(\omega)\right]^* = \left[\mathbf{v}_l^T(\omega)\mathbf{K}^{[k]}(\omega)\right]\mathbf{v}_l^*(\omega) \ . \tag{2.35}$$

The quantity in (2.35) is coherent in frequency, since both $\mathbf{v}_l$ and its conjugate appear. An IFT can then safely be done. Physically, the k^{th} among the N resulting time-domain signals corresponds to the limit of an iterative TR procedure triggered by the vector $\mathbf{K}^{[k]}(\omega)$ (*cf.* (2.16)). It is then easy to see that the target echo arrival times in the elements of (2.35) are $\tilde{\tau}_k + \tilde{\tau}_j|_{j=1,N}$, the former inherited from $\mathbf{K}^{[k]}$ and the latter from the elements of $\mathbf{v}_l^*$.

Then, the N modified singular vectors (2.35) must be reorganized into the matrix

$$\hat{\mathbf{K}}(\omega) = \left[\left[\mathbf{v}_l^{[1]}(\omega)\right]^* \ \left[\mathbf{v}_l^{[2]}(\omega)\right]^* \ \cdots \ \left[\mathbf{v}_l^{[N]}(\omega)\right]^*\right] , \tag{2.36}$$

which resembles to the orginal $\mathbf{K}$ matrix but is cleaner in the sense that the contribution from the l^{th} target is in principle isolated. By extracting the arrival time from each element of $\hat{\mathbf{K}}(\omega)$ (through a simple peak detection algorithm), an equivalent matrix of arrival times $\tilde{\mathbf{T}}$ such that $\tilde{T}_{jk} = \tilde{\tau}_j + \tilde{\tau}_k$ is built. From this, for instance through the least squares method, the single arrival times $\tilde{\mathbf{t}} \triangleq [\tilde{\tau}_1 \ \tilde{\tau}_2 \ \cdots \tilde{\tau}_N]^T$ are evaluated[10].

Finally, the time-domain singular vector is built by averaging the singular vectors (2.35) after synchronizing them with the respective $\tilde{\tau}_k$:

$$\tilde{\hat{\mathbf{v}}}_l(t) \triangleq \text{IFT}\left[\hat{\mathbf{v}}_l(\omega)\right](t) = \text{IFT}\left[\frac{1}{N}\sum_{k=1}^{N}\mathbf{v}_l^{[k]}(\omega)e^{-i\omega\tilde{\tau}_k}\right](t) = \frac{1}{N}\sum_{k=1}^{N}\tilde{\mathbf{v}}_l^{[k]}(t-\tilde{\tau}_k) \ , \tag{2.37}$$

where $\tilde{\mathbf{v}}_l(t) \triangleq \text{IFT}\left[\mathbf{v}_l(\omega)\right](t)$. When back-propagating the new singular vector, since the arrival times of the elements of $\tilde{\hat{\mathbf{v}}}_l(t)$ are $-\tilde{\tau}_j|_{j=1,N}$, focusing produces at $t^{\text{foc}} = 0$ s, that is, the normal behavior of TR is reestablished. Also, a new and cleaner estimation of the arrival times $\tilde{\tau}_j|_{j=1,N}$ can be done on $\tilde{\hat{\mathbf{v}}}_l(t)$, since, as explained below, the averaging is expected to reduce the effect of noise.

[10]To apply the least squares method, the matrix $\tilde{\mathbf{T}}$ must first be unfolded column-wise into a vector $\mathbf{a}_{\tilde{\mathbf{T}}}$. Then, each of its elements must be linked to the unknown vectors through a coefficients matrix $\mathbf{C}$:

$$\mathbf{a}_{\tilde{\mathbf{T}}} = \mathbf{C}\tilde{\mathbf{t}} \ .$$

Finally, the single arrival times are obtained by minimizing the squared error with respect to $\mathbf{a}_{\tilde{\mathbf{T}}}$, which is mathematically obtained through the pseudoinverse $\mathbf{C}^+$ of $\mathbf{C}$:

$$\tilde{\mathbf{t}} = \mathbf{C}^+\mathbf{a}_{\tilde{\mathbf{T}}} \ .$$

The pseudoinverse $\mathbf{C}^+$ can be calculated by means of the SVD of $\mathbf{C}$ [69].

This solution, necessitating no *a priori* information, can be particularly effective in random propagation media. In effect, provided the single arrival times vector $\tilde{\mathbf{t}}$ is properly estimated, averaging the N modified singular vectors in (2.37) results in smoothing the effect of disorder in the medium while constructively summing the contribution of the target, in principle identical on each $\tilde{\mathbf{v}}_l^{[k]}(t-\tilde{\tau}_k)$. In other words, if the medium response, excluding the target, is well decorrelated when sounding it with different antennas - corresponding to the N versions of $\tilde{\mathbf{v}}_l^{[k]}(t-\tilde{\tau}_k)$ -, then (2.37) sort of averages N realizations of disorder.

It must be noticed that the given method is also rather robust with respect to the coupling of singular vectors in case of multiple targets (see §2.3.3.5). Again, for $l=1$, the averaging in (2.37) reduces the contribution of the other targets, which are not synchronized among the N vectors $\tilde{\mathbf{v}}_1^{[k]}(t-\tilde{\tau}_k^1)$, where $\tilde{\tau}_k^1$ is the estimated arrival time relative to the first target. The same happens for $l=2,N_{\text{tgt}}$, of course. Nonetheless, a necessary condition is that the singular values $\lambda_l(\omega)$ are each associated to the same target at all the frequencies explored [99]. If this is not true, that is, if the singular values cross each other at different frequencies, the coherency in (2.35) is lost, resulting in wrong estimates of the arrival times and in the failure of the synchronization (2.37).

Experimental results

The first experimental configuration is shown in FIG. 2.16(a). The wooden target ($\varepsilon_r \approx 2$) is small and relatively far from the array: the low-frequency approximation conditions hold. Synthetic data for this setup predict a λ_1/λ_2 ratio (symmetric over anti-symmetric singular values) equal to 60 dB. The largest singular value in FIG. 2.16(b) corresponds in effect to λ_1: it is rather smooth over the frequency band, which corresponds well to the theoretical shape of the symmetric singular value of a non-resonant target. Nonetheless, due to the low scattering strength of the target and in spite of the drift correction, the experimental setup has not enough dynamic range to observe λ_2. So, the other singular values in FIG. 2.16(b) are related to noise.

The time-domain images, or frames, built according to (2.27) and using the free-space solution (2.30) are presented in FIG. 2.16(c-l). The experimentally retrieved antenna pattern is used[11]. During the first frames a focusing wave builds up; its amplitude grows, thanks to neater constructive interference among each emitted wave, until it reaches the scatterer at $t=4.25$ ns. Afterwards, the wave diverges and the resolution spot widens. The focusing instant t^{foc} corresponds to the delay that appears in (2.34). Namely, since the N^{th} antenna has been used as triggering antenna, $t^{\text{foc}}=|\vec{r}_{\text{tgt}}^{\,l}-\vec{r}_N|/c=4.15$ ns. This is very well in line

[11]Notice that using the experimental antenna radiation pattern does not blur the field charts as it was the case for Kirchhoff migration in FIG. 2.8(d). Indeed, although only a small region of each chart corresponds to azimuth angles available during the characterization step (*cf.* the grayed area in FIG. 2.8(d)), destructive interference outside this region makes the field sufficiently small despite the erroneous extrapolated antenna pattern.

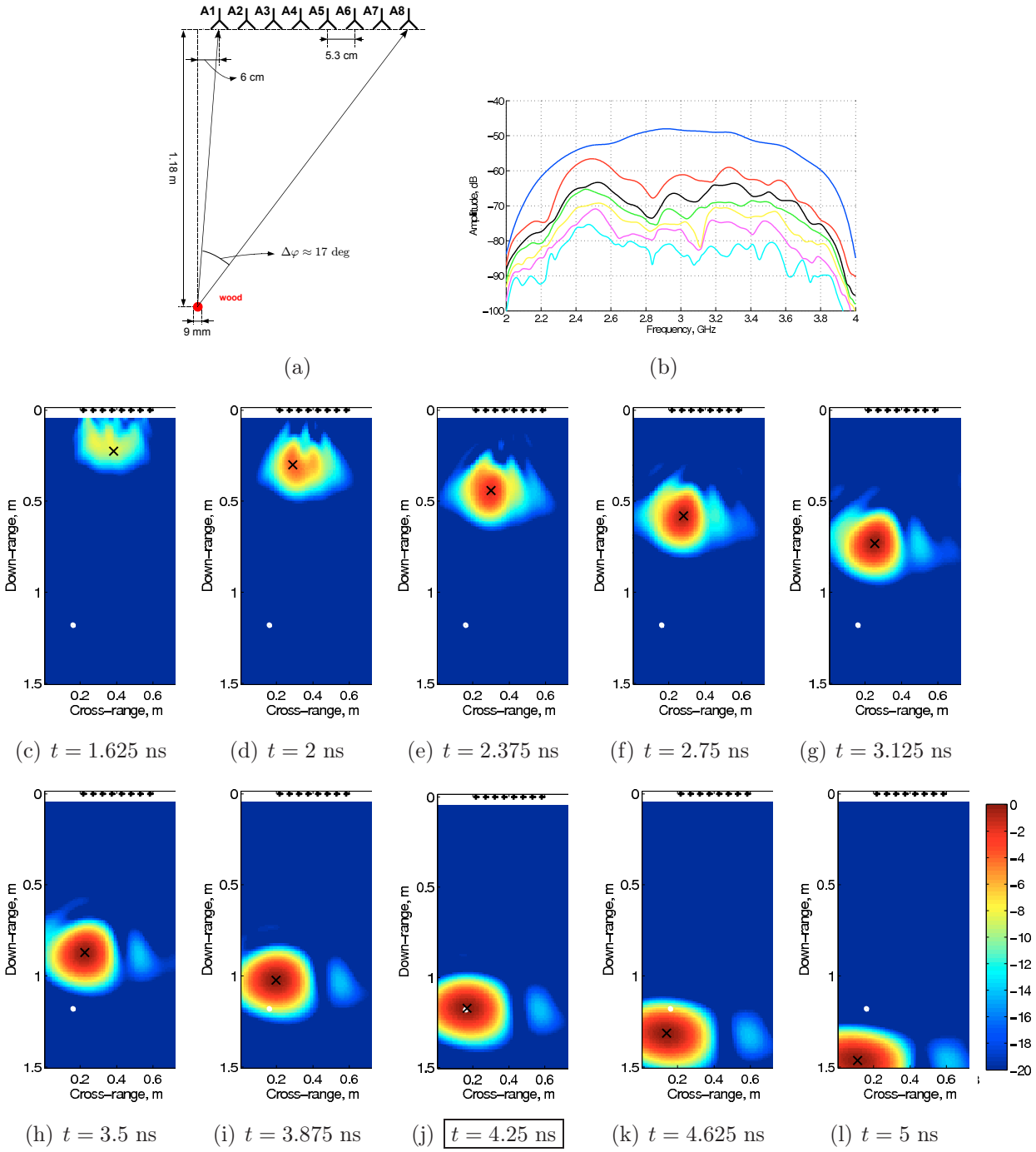

FIGURE 2.16: *DORT method applied to the reflection setup in (a). (b)* $\mathbf{K}$ *matrix singular values. (c-l) Different frames of the time-domain field charts* $I_t^{\mathrm{DORT}}(\vec{r};\mathbf{v}_1)$*. In (j), the back-propagated wave focuses onto the target. Drift and experimental antenna radiation pattern corrections are used.*

with the 4.25 ns experimentally found, with an error of 0.10 ns (3 cm), smaller than the time (space) sampling of the field charts given by $\pi/\omega_{\mathrm{M}} = 0.125$ ns (3.75 cm).

Concerning the way of "automatically" choosing the focusing instant t^{foc}, the maximum of the field charts and their entropy as a function of time are plotted in FIG. 2.17 (a) and (b), respectively. With either method the chosen value does not match $t^{\mathrm{foc}} = 4.25$ ns of

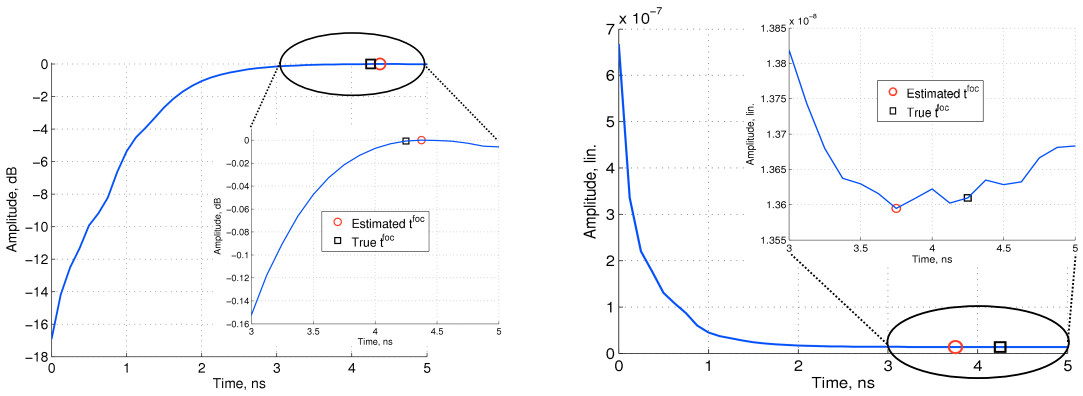

(a) $\max_{\vec{r}} I_t^{\mathrm{DORT}}(\vec{r};\mathbf{v}_1)$ (b) $\min H(t)$

FIGURE 2.17: *Time-domain DORT method applied to the reflection setup in* FIG. *2.16(a). Evolution of the field chart (a) maximum value, and (b) entropy as a function of time.*

FIG. 2.16(j), although especially for the former method the error is as small as 0.125 ns. In fact, the entropy-based method systematically anticipates the focusing instant when the target is far from the array, even with synthetic data, since for larger distances F the focusing spot widens as $\lambda_c F/D$, and the entropy value starts to grow. On the other hand, the maximum-based strategy seems more robust (the Green function normalization is mandatory here); in this case, for instance, the error corresponds to the time resolution, it is then minimum.

Another example is given in FIG. 2.18. A large PVC cylinder filled with tap water is imaged in reflection in the anechoic chamber first (FIG. 2.18), then in a reverberating medium (FIG. 2.19). While two singular values clearly emerge from noise in FIG. 2.18(b) - symmetric and anti-symmetric - reverberation alters them and seemingly adds new singular values in FIG. 2.19(b), probably associated to the scattering from the metallic plate and/or the tiled wall. The time-domain field charts $I_t^{\mathrm{DORT}}(\vec{r};\mathbf{v}_1)$ are built either with the free space method (2.27) (FIG. 2.18(c) and FIG. 2.19(c)) coupled with the maximum-based approach for picking the right t^{foc}, or with the arrival time estimation-based method (2.35)-(2.37) (FIG. 2.18(d) and FIG. 2.19(d)). In the anechoic case, both approaches give a very clean image at the instant of focusing. As for the choise of t^{foc} in FIG. 2.18(c), the entropy-based method (not shown) is again in advance by 0.125 ns with respect to the maximum-based criterion, but both give a focusing instant preceeding the one found in FIG. 2.18(d).

The reverberating case is more intriguing. Applying the free-space method gives a noisy field chart, regardless of the choice of t^{foc} (both maximum- and entropy-based approaches give here the same t^{foc} value). Indeed, a second focusing wave temporally following the stronger one plus some "warm" spots all around appear. The reason for this lies in the mismatch between time-domain Green functions of the medium and of free-space. The former comprises the effect of the reflecting surfaces, similarly to what observed when

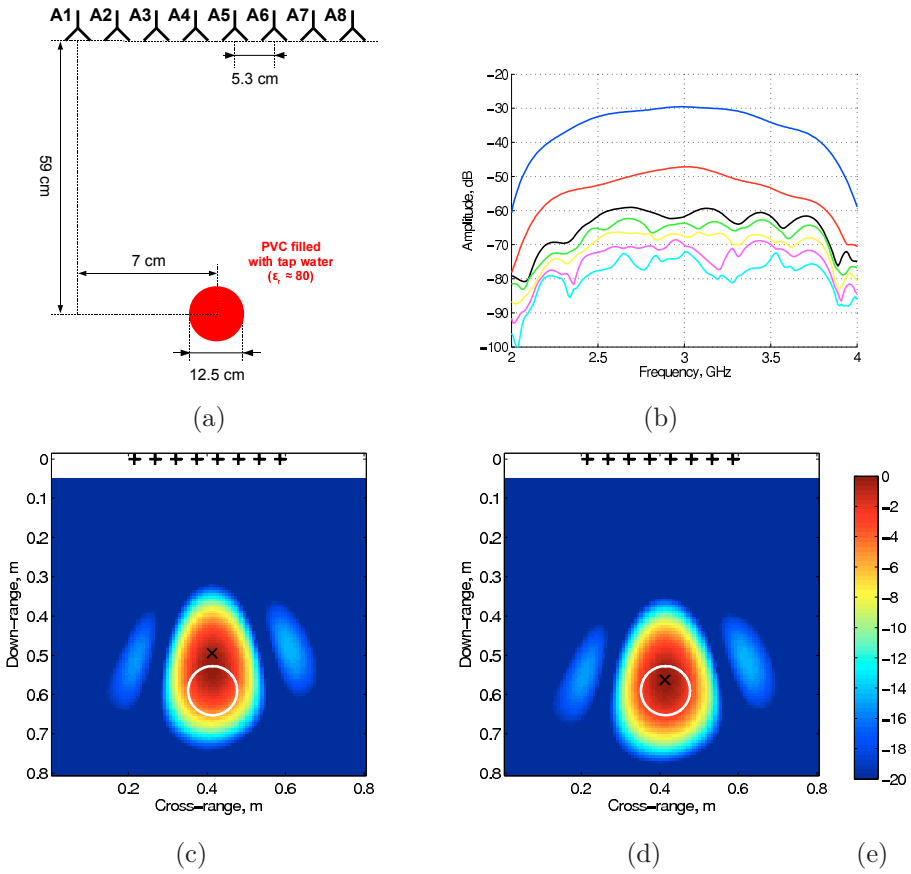

FIGURE 2.18: *DORT method applied to the reflection setup (a) in the anechoic chamber. (b) Singular values distribution over frequency. (c,d) Time-domain DORT field charts* $I_t^{\mathrm{DORT}}(\vec{r};\mathbf{v}_1)$. *In (c), the focusing instant* t^{foc} *is retrieved through the maximum-based approach; in (d), the arrival times estimation method (2.35)-(2.37) is used, so that* $t^{\mathrm{foc}} = 0$ *s.*

applying DORT in waveguides [100, 101]; the latter is the one intrinsically used during back-propagation. On the other hand, the arrival time estimation-based method results in a great improvement, so that almost the same chart FIG. 2.18(d) found in free space is retrieved here. As explained, it is the averaging of the synchronized singular vectors (2.37) that reduces the effect of reverberation, which behaves on each version of the singular vectors (2.35) as a different stochastic realization of the medium.

2.3.3.4 Different Tx and Rx arrays

An issue somehow similar to the one of building time-domain singular vectors appears when dealing with a configuration with two separate arrays, *e.g.* the transmission configuration. In effect, since two different field charts can be obtained at a given frequency by using the right and left singular vectors $\mathbf{v}_l$ and $\mathbf{u}_l$, respectively (see (2.17) and (2.19)), it seems natural to recombine them coherently, that is, summing them, in order to improve the resolution of the images. Hence, the similarity with the time-domain DORT method

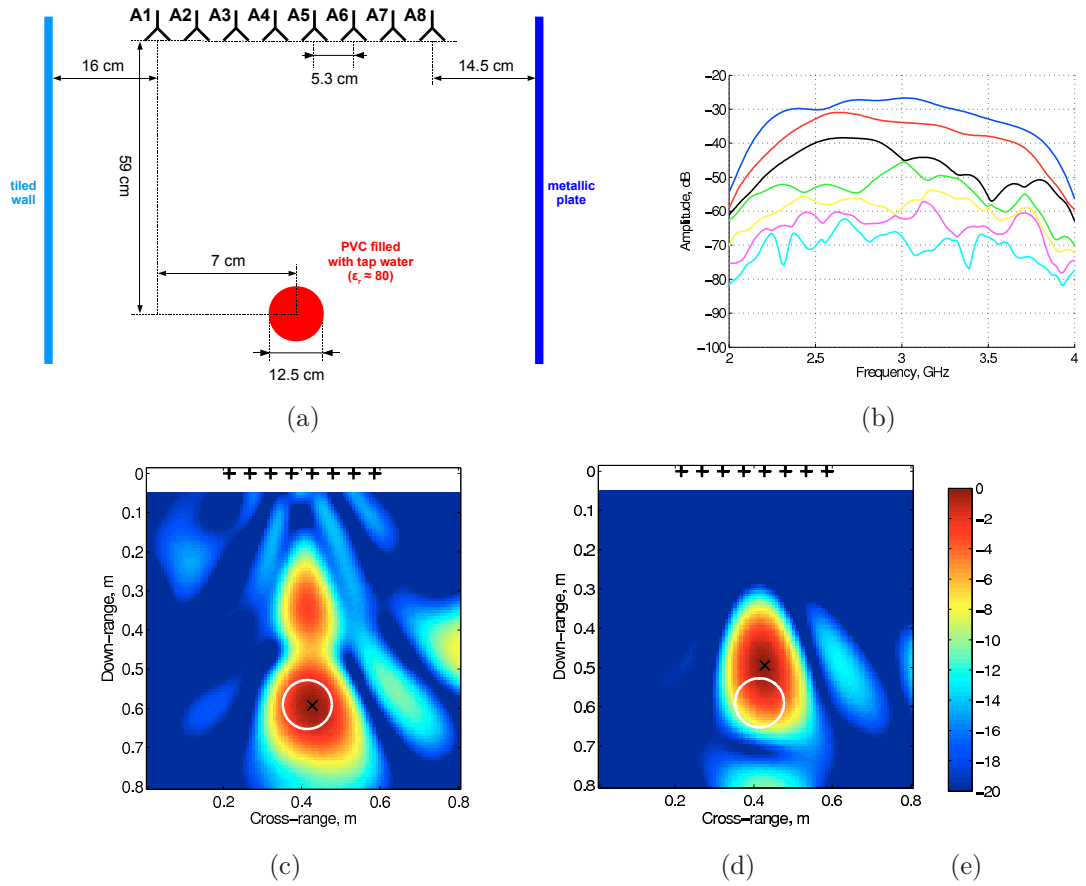

FIGURE 2.19: *DORT method applied to the reflection setup (a) in a reverberating medium. (b) Singular values distribution over frequency. (c,d) Time-domain DORT field charts* $I_t^{\mathrm{DORT}}(\vec{r};\mathbf{v}_1)$. *In (c), the focusing instant* t^{foc} *is retrieved through the maximum-based approach; in (d), the arrival times estimation method (2.35)-(2.37) is used, so that* $t^{\mathrm{foc}} = 0$ *s.*

consisting of coherently recombining all the monochromatic field charts.

Unfortunately, exactly the same phase indetermination issue forbids the coherent recombination, since from the SVD of $\mathbf{K}(\omega)$ it can be seen that

$$\begin{cases} \mathbf{v}_l \propto e^{i\phi_b} \\ \mathbf{u}_l \propto e^{i\phi_b} \end{cases}, \tag{2.38}$$

where ϕ_b is the undetermined phase, and the two field charts are built using $\mathbf{v}_l$ and $\mathbf{u}_l^*$.

Some of the methods developed for the time-domain approach can therefore be applied to remove this indetermination. Namely, a sort of SVP technique setting the phase of both field charts to a same value at the target location would be effective in recombining them, although under the same constraints mentioned in §2.3.3.2 [102]. Alternatively, the arrival times estimation method (2.35)-(2.37) can be applied to estimate the first and second array arrival times, $\tilde{\tau}_j^1|_{j=1,N_1}$ and $\tilde{\tau}_k^2|_{k=1,N_2}$, respectively[12]. Then, the separate synchronization

[12]For a two-arrays configuration, the method described in §2.3.3.2 must be slighlty modified. Given an

(2.37) of right and left singular vectors assures that both field charts focus at $t^{\text{foc}} = 0$ s, thus allowing their coherent recombination.

Experimental results

The test case is the configuration already used with Kirchhoff migration in FIG. 2.11(a). A metallic target is imaged in transmission by two separate arrays. In FIG. 2.20(a), the arrival times retrieved with the singular vector-based method in (2.35)-(2.37) are first shown. They correspond well to the distances of the respective antennas, and they are used to build, in FIG. 2.20(b,c), the time-domain DORT field charts $I_t^{\text{DORT}}(\vec{r};\mathbf{v}_1)$ and $I_t^{\text{DORT}}(\vec{r};\mathbf{u}_1)$, respectively. Such charts show how focusing is first obtained *separately* by each array at $t^{\text{foc}} = 0$ s. Then, the two charts are summed coherently thanks to the synchronization (2.37): the plotted frames in FIG. 2.20(d-h) depict the formation of both focusing waves at $t < 0$ s, then the focusing instant $t = t^{\text{foc}} = 0$ s at which they both converge onto the target, and finally their respective departure from the focusing position at $t > 0$ s.

Notice that for a transmission configuration, the only improvement given by the coherent use of right and left singular vectors consists in an enhanced temporal focusing, that is, the amplitude of the focusing waves decreases more rapidly at $t \neq 0$ s with respect to either $I_t^{\text{DORT}}(\vec{r};\mathbf{v}_1)$ or $I_t^{\text{DORT}}(\vec{r};\mathbf{u}_1)$. For an improved spatial resolution, different configurations are needed, for instance two interleaved or side-by-side arrays.

2.3.3.5 Multiple targets case

The second drawback of TR, the impossibility of separately imaging two targets, can under certain conditions also be overcome with DORT. As initial assumptions, the targets, located at $\vec{r}_{\text{tgt}}^{\,1}$ and $\vec{r}_{\text{tgt}}^{\,2}$, must be in the low-frequency regime and their cross-range distance must be larger than the resolution limit $\lambda F/D$.

Using synthetic data, in FIG. 2.21 two identical small metallic targets placed at 60 cm and 70 cm from the array are imaged. FIG. 2.21(b) compares the two largest singular values of $\mathbf{K}$, λ_1 and λ_2, to the largest singular values obtained when either one or the other target are present, $\bar{\lambda}_1^1$ and $\bar{\lambda}_1^2$. It appears that the new singular values "oscillate" around the single-target ones, hence the mutual presence of the targets alters the result. First Tortel *et al.* in 1999 [18], and later Minonzio *et al.* in 2006 [103] who added multiple scattering to the mathematical derivation, have indeed shown that:

$N_2 \times N_1$ $\mathbf{K}$ matrix, the $k = 1, N_1$ versions of the left singular vector are

$$\mathbf{u}_l^{[k]}(\omega) = \left[\mathbf{u}_l^H(\omega)\mathbf{K}^{[k]}(\omega)\right]\mathbf{u}_l(\omega) \ ,$$

where $\mathbf{K}^{[k]}$ is now the k^{th} line of $\mathbf{K}$. Then, the $N_2 \times N_1$ arrival times matrix $\tilde{\mathbf{T}}$ is built identically. Nonetheless, since $\tilde{T}_{jk} = \tilde{\tau}_k^1 + \tilde{\tau}_j^2$, where $\tilde{\tau}^1$ and $\tilde{\tau}^2$ are the estimated arrival times pertaining to the first and second arrays, respectively, the extraction of the single arrival times $\tilde{\mathbf{t}}^1$ and $\tilde{\mathbf{t}}^2$ must be modified accordingly.

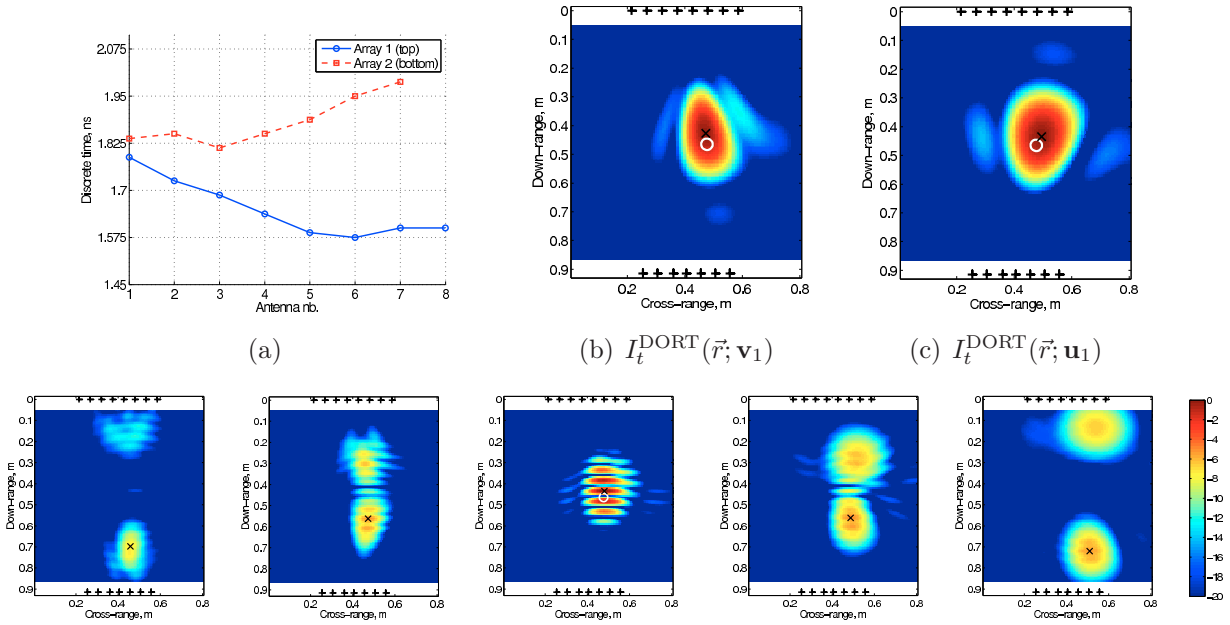

(a) (b) $I_t^{\mathrm{DORT}}(\vec{r};\mathbf{v}_1)$ (c) $I_t^{\mathrm{DORT}}(\vec{r};\mathbf{u}_1)$

(d) $t=-1$ ns (e) $t=-0.5$ ns (f) $t=0$ ns (g) $t=0.5$ ns (h) $t=1$ ns

FIGURE 2.20: *Time domain DORT method applied to the transmission setup in* FIG. *2.11(a). The arrival times estimation method (2.35)-(2.37) is applied. (a) Arrival times for each array. (b,c) Time domain DORT field charts for the right and left singular vectors* $\mathbf{v}_1$ *and* $\mathbf{u}_1$*, respectively. (d-h) Different frames of the movie resulting from the coherent back-propagation of both* $\mathbf{v}_1$ *and* $\mathbf{u}_1$*.*

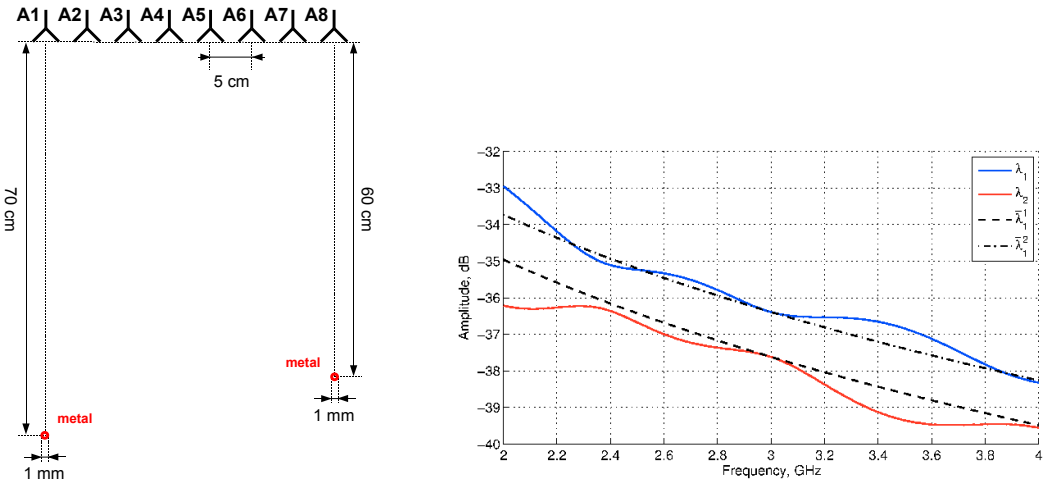

(a) (b)

FIGURE 2.21: *Synthetic data with two small metallic targets. (a) Setup and (b) DORT singular values as a function of frequency (blue and red curves) compared to the largest singular values obtained with one single target in place for each of the targets (black dashed and dotted-dashed curves).*

- The quadratic nature of the SVD operator, even without multiple scattering between targets, is responsible of such behavior. The key factor is the scalar product $(\bar{\mathbf{v}}_1^1)^H \bar{\mathbf{v}}_1^2$

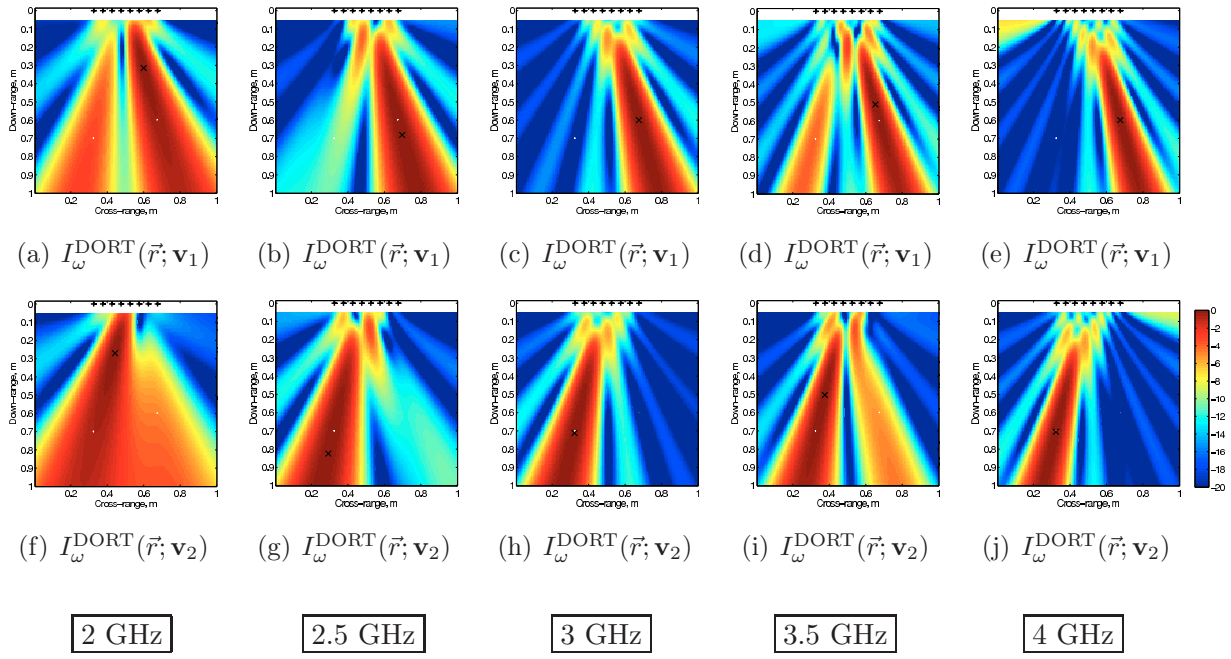

(a) $I_\omega^{\mathrm{DORT}}(\vec{r};\mathbf{v}_1)$ (b) $I_\omega^{\mathrm{DORT}}(\vec{r};\mathbf{v}_1)$ (c) $I_\omega^{\mathrm{DORT}}(\vec{r};\mathbf{v}_1)$ (d) $I_\omega^{\mathrm{DORT}}(\vec{r};\mathbf{v}_1)$ (e) $I_\omega^{\mathrm{DORT}}(\vec{r};\mathbf{v}_1)$

(f) $I_\omega^{\mathrm{DORT}}(\vec{r};\mathbf{v}_2)$ (g) $I_\omega^{\mathrm{DORT}}(\vec{r};\mathbf{v}_2)$ (h) $I_\omega^{\mathrm{DORT}}(\vec{r};\mathbf{v}_2)$ (i) $I_\omega^{\mathrm{DORT}}(\vec{r};\mathbf{v}_2)$ (j) $I_\omega^{\mathrm{DORT}}(\vec{r};\mathbf{v}_2)$

2 GHz | 2.5 GHz | 3 GHz | 3.5 GHz | 4 GHz

FIGURE 2.22: *DORT images from 2 GHz to 4 GHz associated to the (a-e) first and (f-j) second singular values of the* $\mathbf{K}$ *matrix relative to the configuration in* FIG. *2.21.*

between the unperturbated singular vectors

$$\left(\bar{\mathbf{v}}_1^1\right)^H \bar{\mathbf{v}}_1^2 \approx \sum_j H_0^-(k|\vec{r}_j - \vec{r}_{\mathrm{tgt}}^1|) H_0^+(k|\vec{r}_j - \vec{r}_{\mathrm{tgt}}^2|) \ , \tag{2.39}$$

that strongly affects λ_1 and λ_2. Although it can been shown, for example through the use of the Graf's formula for each Hankel function, that in the complete configuration $\left(\bar{\mathbf{v}}_1^1\right)^H \bar{\mathbf{v}}_1^2 \propto J_0(k|\vec{r}_{\mathrm{tgt}}^2 - \vec{r}_{\mathrm{tgt}}^1|) = \Im\left[G(\omega;\vec{r}_{\mathrm{tgt}}^1,\vec{r}_{\mathrm{tgt}}^2)\right]$ [18], in the case of a measurement line no such simple result holds. Nevertheless, an oscillating behavior can be expected, exactly as in FIG. 2.21(b), where the period of the oscillations of λ_1 and λ_2 around $\bar{\lambda}_1^1$ and $\bar{\lambda}_1^2$ is in a range between 600 MHz and 800 MHz, close to $c/|\vec{r}_{\mathrm{tgt}}^2 - \vec{r}_{\mathrm{tgt}}^1| \approx 800$ MHz.

- In presence of multiple scattering, yet another term oscillating with $k|\vec{r}_{\mathrm{tgt}}^2 - \vec{r}_{\mathrm{tgt}}^1|$ appears [103].
- As for the singular vectors $\mathbf{v}_1$ and $\mathbf{v}_2$, they are linear combinations of $\bar{\mathbf{v}}_1^1$ and $\bar{\mathbf{v}}_1^2$, and this again regardless of multiple scattering. This generates a *coupling* that is responsible of parasite focusing in the direction of the "wrong" target.

The effect of the presence of two targets onto the singular vectors is clearly shown in FIG. 2.22, where the field charts corresponding to $\mathbf{v}_1$ and $\mathbf{v}_2$ between 2 GHz and 4 GHz are plotted with a step of 500 MHz. At those frequencies where, in FIG. 2.21(b), the singular values are unmodified, *e.g.* 3 GHz and 4 GHz, the field charts show clean focusing beams in the directions of either target. On the other hand, when the singular values are altered, *e.g.* at 2 GHz and 3.5 GHz, the beams couple, although more energy is always sent in the direction of the "right" target.

It must be noticed that the nice selective focusing achieved in FIG. 2.22 is not always ensured. In [103], for the case of two identical targets placed symmetrically with respect to the array axis, it is shown that $\mathbf{v}_1$ and $\mathbf{v}_2$ are proportional to $\bar{\mathbf{v}}_1^1 \pm \bar{\mathbf{v}}_1^2$, which implies that both of them focus onto both of the targets, although with different phases. On the other hand, if the targets have different scattering power and/or are placed at different distances with respect to the array, some degree of selective focusing can be obtained as in FIG. 2.22.

In the general case, there exists no solution to the best of our knowledge to the problem of retrieving $\bar{\mathbf{v}}_1^1$ and $\bar{\mathbf{v}}_1^2$ given the coupled $\mathbf{v}_1$ and $\mathbf{v}_2$. Nonetheless, the availability of a large bandwidth is somehow helpful in this sense. In effect, if $f_{\text{bw}} > 2c/|\vec{r}_{\text{tgt}}^2 - \vec{r}_{\text{tgt}}^1|$, according to (2.39), there is at least one frequency where $\left(\bar{\mathbf{v}}_1^1\right)^H \bar{\mathbf{v}}_1^2$ nulls, that is, a minimum amount of coupling affects the singular vectors and true selective focusing is obtained. Furthermore, using all the monochromatic charts, one for each frequency, as previously explained in §2.3.3.2, helps in increasing the quality of target separation with respect to the single-frequency case.

Experimental results

The experimental result proposed here is relative to a transmission configuration. As described in §1.3, the transmission configuration is experimentally particularly interesting because of a far larger dynamic range than in the reflection configuration. In the frame of DORT, the same behavior observed in reflection must be expected. In effect, (2.3.3.1) is formally unchanged, so that all the subsequent derivations hold as well provided the geometric hypotheses (low-frequency regime and so-on) are verified for both the antenna arrays.

In FIG. 2.23 the results of a two-target setup are presented. The imaged objects are placed at the same distance from the array, rather symmetrically with respect to its axis, but they have different scattering strengths, the first being metallic and the second wooden ($\varepsilon_r \approx 2$) and slightly smaller. Thanks to the large dynamic range, at least four singular values emerge neatly from noise. As shown by the time-domain field charts associated to the three largest singular values, a symmetric component per target and an anti-symmetric one - a sort of "common" anti-symmetric for both targets - are extracted. The arrival times estimation method (2.35)-(2.37) has been applied to plot the field charts, so that $t^{\text{foc}} = 0$ s[13]. Coupling between $\mathbf{v}_1$ and $\mathbf{v}_2$ is at the origin of the parasite focusing onto the wooden target,

[13]For a two-arrays configuration, the method described in §2.3.3.2 must be slighlty modified. Given an $N_2 \times N_1$ $\mathbf{K}$ matrix, the $k = 1, N_1$ versions of the left singular vector are

$$\mathbf{u}_l^{[k]}(\omega) = \left[\mathbf{u}_l^H(\omega)\mathbf{K}^{[k]}(\omega)\right]\mathbf{u}_l(\omega) \ ,$$

where $\mathbf{K}^{[k]}$ is now the k^{th} line of $\mathbf{K}$. Then, the $N_2 \times N_1$ arrival times matrix $\tilde{\mathbf{T}}$ is built identically. Nonetheless, since $\tilde{T}_{jk} = \tilde{\tau}_k^1 + \tilde{\tau}_j^2$, where $\tilde{\tau}^1$ and $\tilde{\tau}^2$ are the estimated arrival times pertaining to the first and second arrays, respectively, the extraction of the single arrival times $\tilde{\mathbf{t}}^1$ and $\tilde{\mathbf{t}}^2$ must be modified accordingly.

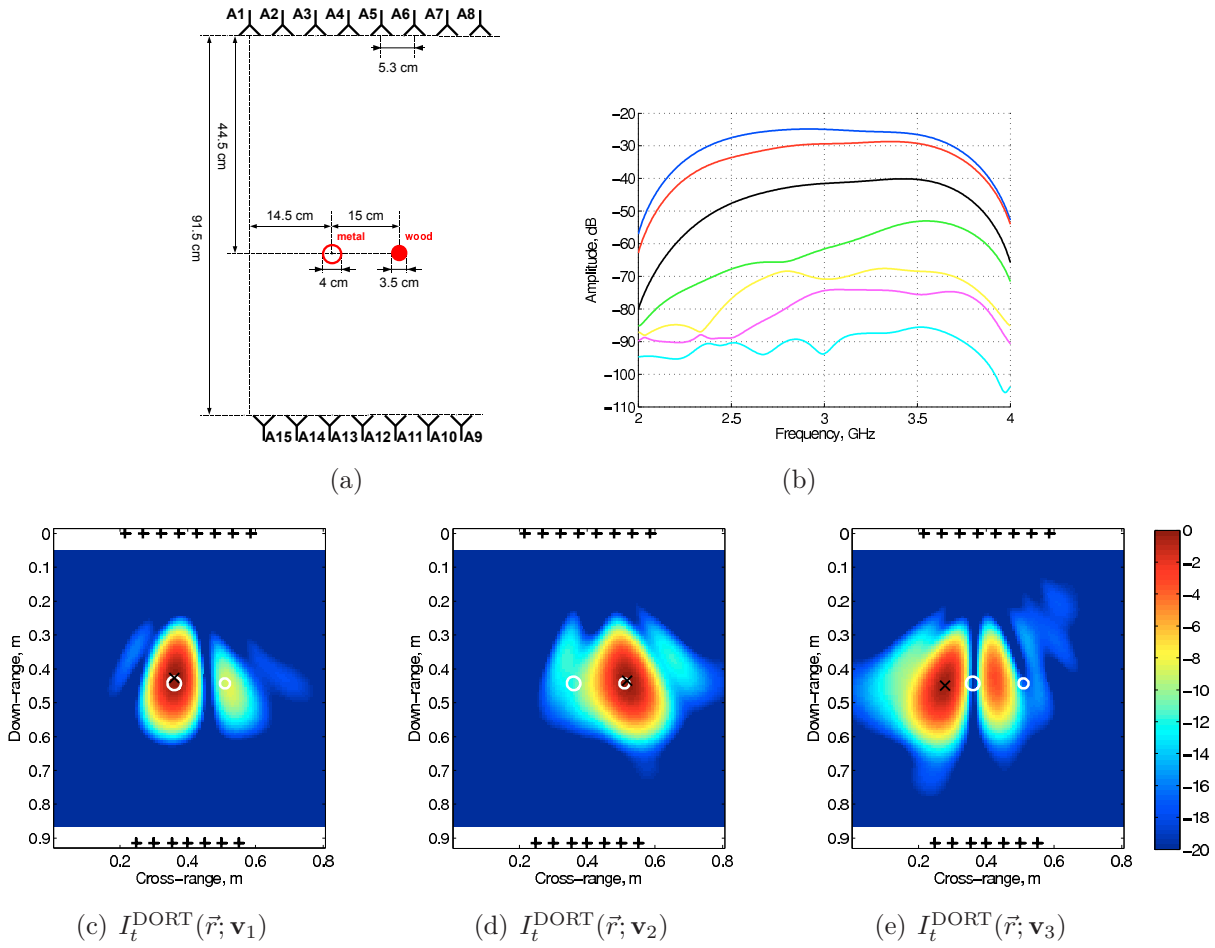

(a) (b)

(c) $I_t^{\mathrm{DORT}}(\vec{r};\mathbf{v}_1)$ (d) $I_t^{\mathrm{DORT}}(\vec{r};\mathbf{v}_2)$ (e) $I_t^{\mathrm{DORT}}(\vec{r};\mathbf{v}_3)$

Figure 2.23: *DORT method applied to the transmission setup in (a). (b)* $\mathbf{K}$ *matrix singular values as a function of frequency. (b-d) Time-domain field charts associated to the right singular vectors* $\mathbf{v}_l|_{l=1,2,3}$ *built using the arrival times estimation method (2.35)-(2.37). The experimentally retrieved antenna pattern is used.*

normally associated to $\mathbf{v}_2$, when plotting $I_t^{\mathrm{DORT}}(\vec{r};\mathbf{v}_1)$, and vice versa. Nonetheless, using a temporal approach over a so large bandwidth helps in improving the rejection of the wrong target: with respect to those frequencies where coupling is considerably higher (*e.g.* only 3-5 dB rejection, *cf.* Fig. 2.22), the rejection is increased, without any frequency selection procedure, up to around 8-10 dB. Notice also that the field charts are built using the experimentally retrieved antenna pattern. Indeed, the maximum point (black cross) of the focusing charts well corresponds to the target position, and in particular for the metallic case to the side nearest to the emitting array.

2.3.3.6 Acquisition of the K matrix

The advantages given by the DORT method, namely the immediate availability of the focusing vector (without TR iterations) and the selective focusing capability, necessitate the knowledge of the inter-element matrix $\mathbf{K}$. Given an array of N antennas, the most straightforward way of recording $\mathbf{K}$ consists in illuminating the medium with the first

antenna and measuring the response over the entire array, then switching to the second, and so on until the N^{th}. The steering vectors are then $\mathbf{s}_1 = \mathbf{1}_1^T$, $\mathbf{s}_2 = \mathbf{1}_2^T$, up to $\mathbf{s}_N = \mathbf{1}_N^T$, and the corresponding measurements are the columns of $\mathbf{K}$. As compared to TR, which necessitates the acquisition of only one column of $\mathbf{K}$, this procedure takes at least N times more time, ultimately limiting the detection range or, equivalently, the target speed or "degree of unstationarity" of the medium under which detection is still ensured. This is the price to pay when using DORT in practical applications.

Nevertheless, at least two alternative strategies aimed at reducing the acquisition time can be considered.

- In [104], the authors propose to sound the medium with N orthogonal vectors $\{\mathbf{s}_l\}_{l=1,N}$ each involving all the antennas and not simply "turning on" one single antenna per emission. The idea consists in improving the SNR in the received signals, since each emitted beam is now more energetic whereas the receiver noise is unchanged. Building a matrix $\mathbf{S} = [\mathbf{s}_1\ \mathbf{s}_2 \cdots \mathbf{s}_N]$, the measured matrix is simply $\mathbf{KS}$. Naming $\hat{\lambda}_l$ and $\hat{\mathbf{v}}_l$ the new l^{th} singular value and vector, respectively, it is easy to see that $\hat{\lambda}_l = \lambda_l$ and $\hat{\mathbf{v}}_l = \mathbf{S}^H \mathbf{v}_l$, where λ_l and $\mathbf{v}_l$ are the l^{th} singular value and vector of $\mathbf{K}$. The latter, which is the actual sought steering vector, can finally be retrieved as $\mathbf{S}\hat{\mathbf{v}}_l$.
  Folégot *et al.* have proposed in [105] to reduce to $M < N$ the number of orthogonal sounding vectors, which indeed reduces by a factor N/M the acquisition time. Although the measured matrix $\mathbf{KS}$ is now a $[N \times M]$ matrix, if M is sufficiently larger than the number of targets (especially if in the low-frequency regime), the SVD of the new matrix gives exactly the same informations obtainable with $\mathbf{K}$.
- A different approach, requiring wideband signals, consists in sounding the medium again with all the antennas transmitting at the same time, but each sending a pulse belonging to an orthognal set. At reception, through deconvolution at each receiver, the orthogonality in the time domain is recast into the space domain, allowing to retrieve the impulse response of the medium to each emitting antenna. After IFT, one element of the $\mathbf{K}(\omega)$ matrix is thus measured. Of course ideal codes having *both* impulsive auto-correlation and zero cross-correlation do not exist (unless infinite sequences, or emission time, are considered!). Hence, the $\mathbf{K}$ matrix measured through this technique suffers from a reduced SNR, ultimately limiting the precision of the DORT method (or any other method based on the use of $\mathbf{K}$). In [106], a study on how to build efficient codes for a given application is carried out.

2.3.3.7 Conclusions

The DORT method can be favorably exploited in an experimental multi-static, multi-frequency setup. Detection and localization work well in free-space. For a single-target in reflection, though, the down-range resolution is poorer than with Kirchhoff migration, as visible for instance when comparing Fig. 2.8(c) and Fig. 2.16(j). As for cross-range, the

resolutions are comparable.

In transmission, on the other hand, while Kirchhoff migration suffers from the limited array aperture and is extremely sensitive to the estimation of the arrival times, DORT achieves the same good results observed in reflection. This happens because DORT does not rely on a round-trip estimation as Kirchhoff migration, it rather extracts the feeding vectors of each array separately throught the SVD of the **K** matrix.

One very interesting feature offered by the DORT method concerns selective focusing. Indeed, apart from the selective imaging capability (*cf.* FIG. 2.23), it is possible to naturally retrieve, *via* the SVD of the multi-static matrix, the focusing law that, as for TR, can be used to experimentally transmit a focusing wave. Although coupling between singular vectors, present even in absence of multiple scattering, prevents from perfect selective focusing, more than 10 dB "wrong" target rejection is observed for targets in far-field and sufficiently separated.

The time-domain extension of DORT, leading to coherent temporal singular vectors, is feasible especially through the arrival times-based method (2.35)-(2.37). This technique does not necessitate any *a priori* information and seems rather robust with respect to clutter. The only requirement is that the pertinent singular value be always associated to the same target within the frequency band employed. Indeed, in configurations with very small or even negative-in-dB SNR, it might be impossible or very hard to track over frequency the singular values associated to the targets of interest, resulting in wrong arrival times estimations and singular vectors synchronization. An example of such a delicate case is given in §2.3.5 for an experimental through-the-wall configuration.

Finally, a "side-effect" of the SVD at the heart of the DORT method is the possibility of classifying the singular values as belonging to the signal or noise subspaces. This distinction casts the basis of a category of localization methods, among which the TR- (or DORT-) MUSIC is probably the most representative and is therefore presented next.

2.3.4 TR-MUSIC

TR-MUSIC as a method for detecting targets with a multi-static system was proposed in 2000 by Lev-Ari and Devaney [4] and formalized in 2003 by Prada and Thomas [5] by merging the non-linear MUSIC estimator principle [107, 108] with the Time Reversal and, more explicitly, DORT methods. The idea consists in borrowing the statistical concepts of *signal* and *noise subspaces* and in applying them to the deterministic frame of DORT, and namely to the SVD of the multi-static matrix **K**. These subspaces are the $(\lambda_m; \mathbf{u}_m, \mathbf{v}_m)$ singular spaces into which **K** is decomposed: the signal subspace contains those associated to the target(s) - for instance symmetric and anti-symmetric spaces in the case of a measurement line; the noise subspace all the others. The assumption that the $m = 1, M$ first singular spaces form the signal subspace is usually done for defining the TR-MUSIC method.

Now, due to the orthogonality of the singular vectors, it can be expected that those belonging to the noise subspace do not focus onto the target(s), whereas the signal subspace ones do. Therefore, inspired by the "classical" MUSIC method, the measure of the distance between the signal subspace $\{\mathbf{v}_m\}_{m=1,M}$ and the normalized Green function vector $\hat{\mathbf{G}}(\vec{r})$ gives an indication on whether the point $\vec{r}$ belongs or not to the focusing region of the target. For instance, since for a point target located at $\vec{r}_{\text{tgt}}$ DORT gives $\mathbf{v}_1 = e^{i\phi_a}\hat{\mathbf{G}}^*(\vec{r}_{\text{tgt}})$, the aforementioned distance, $1 - \left|\mathbf{v}_1^T\hat{\mathbf{G}}(\vec{r})\right|^2$ equals 0 at $\vec{r} = \vec{r}_{\text{tgt}}$, that is, it is minimized. Finally then, the TR-MUSIC image can be obtained as

$$I_\omega^{\text{TR-MUSIC}}(\vec{r}; M) = \left[1 - \sum_{m=1}^{M}\left|\mathbf{v}_m^T\hat{\mathbf{G}}(\vec{r})\right|^2\right]^{-1} = \left[\sum_{m=M+1}^{\min(N_1,N_2)}\left|\mathbf{v}_m^T\hat{\mathbf{G}}(\vec{r})\right|^2\right]^{-1}, \tag{2.40}$$

which is supposed to be maximum at the target location.

Concerning the achievable resolution, it must be noticed that in absence of noise, since as just stated the signal subspace-Green function distance is null for $\vec{r} = \vec{r}_{\text{tgt}}$, (2.40) diverges. Therefore, the image reduces to a point and the resolution is infinitely small! The presence of noise brings back the resolution to a finite value that depends on the SNR. As an example, the case of a measurement line with a large number of antennas imaging two very close point targets (distance $d < \lambda/2$) has been analytically studied by Davy in [109] assuming gaussian noise decorrelated over the antennas.

Of course, the main difficulty in (2.40) consists in choosing the correct signal subspace dimension M. On this purpose, thresholding mechanisms as those employed in RADAR signal processing to achieve a constant false-alarm rate (CFAR) [92] in conjunction with the use of random matrix theory to estimate the distribution of noise singular values [110] might be useful.

What is interesting here, is the role of the anti-symmetric singular vectors in the case of extended targets. Indeed, although they rigourously belong to the signal subspace - they cannot exist in absence of targets - the field charts associated to them have a null in the direction of the target (*cf.* Fig. 2.15(f)). Thus, it seems advisable to rather classify them as part of the noise subspace, which is supposed to further improve the quality of the TR-MUSIC image. In Fig. 2.24, a numerical example based on the setup in Fig. 2.18 is presented. For the PVC cylinder filled with tap water $\varepsilon_r = 80$ has been chosen for the numerical resolution. The results show that setting $M = 1$ indeed gives almost a single point with infinite resolution, which is limited here only by the pixel dimensions in the field chart. Notice that the position of this point does not correspond to the center of the circle mainly because the array aperture angle $\Delta\varphi$ is not infinitely small (*c.f.* §2.3.3.1). Adding also the first anti-symmetric singular space to the signal subspace ($M = 2$) brings the resolution to a finite, although very small, value. This can be explained since the symmetric singular value corresponds to an isotropic field and hence to a point target, which is indeed retrieved in Fig. 2.24(b). On the other hand, adding anti-symmetric singular values means imaging an extended target, justifying the finite-dimension spot in Fig. 2.24(c). This is also why

further increasing M gives results very similar to the $M = 2$ case.

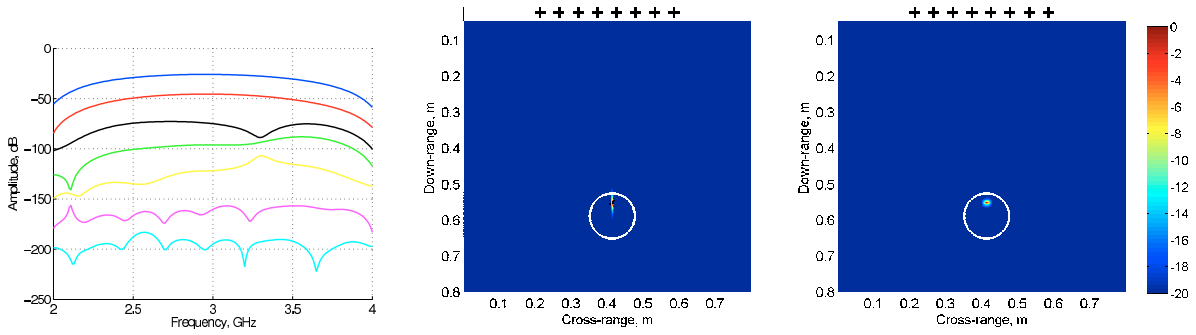

(a) (b) $I_\omega^{\mathrm{TR-MUSIC}}(\vec{r}; 1)$ (c) $I_\omega^{\mathrm{TR-MUSIC}}(\vec{r}; 2)$

FIGURE 2.24: *Synthetica data relative to the configuration in* FIG. *2.18. (a) Singular values distribution, and (b-c) TR-MUSIC images at 3 GHz with signal subspace dimension $M = 1$ and $M = 2$, respectively.*

Experimental results

The absorbing and reverberating configurations presented in FIG. 2.18(a) and FIG. 2.19(a), respectively, are tested in FIG. 2.25. Concerning the former (top row), for which the symmetric and anti-symmetric singular values were clearly distinguished from noise in FIG. 2.18(b), the down-range resolution is severely impacted with respect to the synthetic results just studied. Switching to $M = 2$ degrades even more the cross-range resolution.

The results related to the reverberating configuration (bottom row) globally show reduced resolution and image contrast, or rejection, in cross-range, especially in the case $M = 1$. This is due to the perturbation of the propagating medium with respect to free-space, which alters the complex amplitude laws of the singular vectors. It is interesting to notice how using $M = 2, 3$ adds additional spots in the direction of the metallic plate (on the left of the array) and of the tiled wall, whereas the cross-range rejection is improved. The additional spots are due to the fact that $\mathbf{v}_m|_{m=2,3}$ generate themselves additional beams in their directions. The improved cross-range rejection, on the other hand, comes from the coupling between $\mathbf{v}_m|_{m=2,3}$ and $\mathbf{v}_1$ due to their small amplitude separation in FIG. 2.19(b). In other words, $\mathbf{v}_m|_{m=2,3}$ contain a part of the signal scattering contribution as well and it makes thus sense to include them within the signal subspace.

2.3.4.1 Time-domain extension

As DORT or Phase Conjugation, TR-MUSIC deals with time-harmonic signals. Nevertheless, as already discussed in the case of DORT, extending the method to time-domain can be advantageous under several aspects.

As done for DORT in (2.26), summing all the frequencies already improves the result.

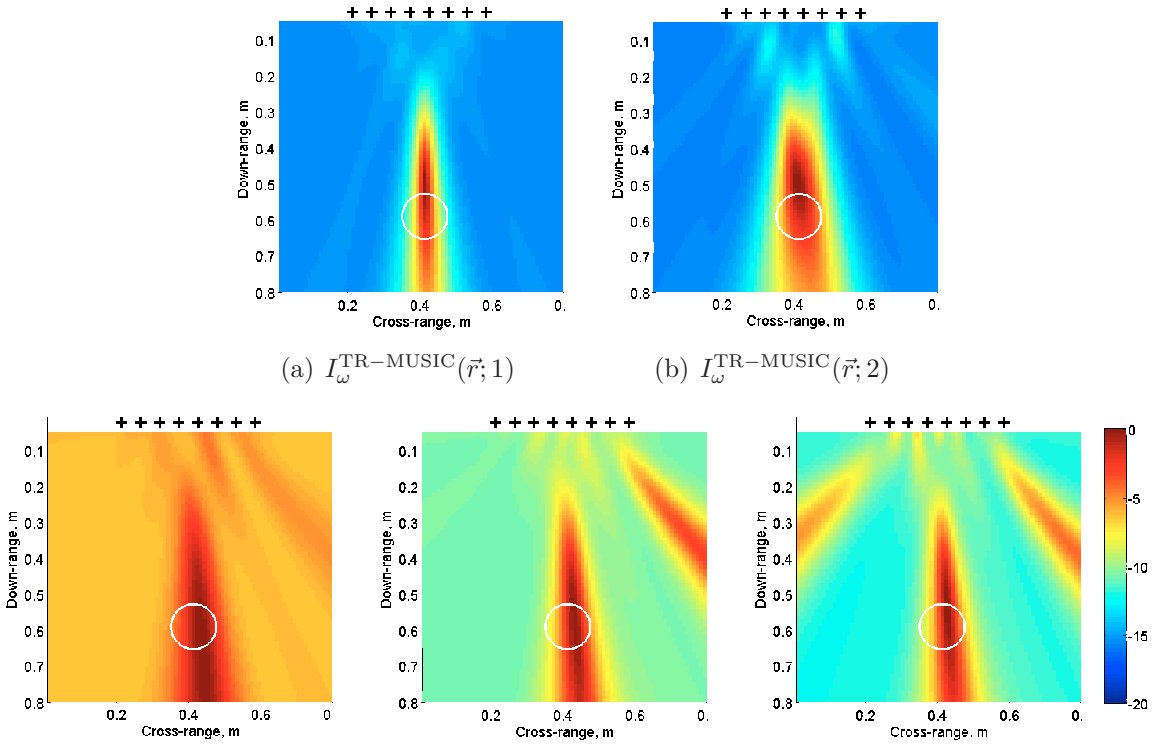

(a) $I_{\omega}^{\mathrm{TR-MUSIC}}(\vec{r};1)$ (b) $I_{\omega}^{\mathrm{TR-MUSIC}}(\vec{r};2)$

(c) $I_{\omega}^{\mathrm{TR-MUSIC}}(\vec{r};1)$ (d) $I_{\omega}^{\mathrm{TR-MUSIC}}(\vec{r};2)$ (e) $I_{\omega}^{\mathrm{TR-MUSIC}}(\vec{r};3)$

FIGURE 2.25: *TR-MUSIC at 3 GHz applied to the configurations (a,b) in the absorbing chamber of* FIG. *2.18(a), and (c-e) in the reverberating medium of* FIG. *2.19(a).*

Two possible ways of doing so exist:

$$I_{\omega\omega}^{\mathrm{TR-MUSIC}}(\vec{r};M)=\begin{cases}\left[\displaystyle\sum_{\omega_{\mathrm{m}}}^{\omega_{\mathrm{M}}}\sum_{m=M+1}^{\min(N_1,N_2)}\left|\mathbf{v}_m^T(\omega)\hat{\mathbf{G}}(\omega;\vec{r})\right|^2\right]^{-1} & \textit{type 1}\\ \displaystyle\sum_{\omega_{\mathrm{m}}}^{\omega_{\mathrm{M}}}\left[\sum_{m=M+1}^{\min(N_1,N_2)}\left|\mathbf{v}_m^T(\omega)\hat{\mathbf{G}}(\omega;\vec{r})\right|^2\right]^{-1} & \textit{type 2}\end{cases}. \tag{2.41}$$

Nonetheless, either solution does not exploit frequency coherency.

In [99], Borcea *et al.* have proposed an interesting frequency-coherent approach. As a first step, the following time-domain vector must be built:

$$\mathcal{A}(t;\vec{r};M)=\mathrm{IFT}\left\{\sum_{m=M+1}^{\min(N_1,N_2)}\left[\mathbf{v}_m^T(\omega)\hat{\mathbf{G}}(\omega;\vec{r})\right]\mathbf{v}_m^*(\omega)\right\}(t)\ . \tag{2.42}$$

It represents a sort of time-domain back-propagated noise subspace not suffering from the phase indetermination issue due to the SVD (thanks to the presence of both $\mathbf{v}_m$ and $\mathbf{v}_m^*$). The image is finally obtained by recombining the components of the vector $\mathcal{A}(t;\vec{r};M)$ after evaluating them at the antenna-investigation point arrival time $t_j^{\mathrm{d}}(\vec{r})$:

$$I_t^{\mathrm{TR-MUSIC}}(\vec{r};M)=\left\{\int_{-\delta t}^{\delta t}\left|\sum_{j=1}^{N_1}\mathcal{A}_j\left[t_j^{\mathrm{d}}(\vec{r})+\tau;\vec{r};M\right]\right|^2 d\tau\right\}^{-1}, \tag{2.43}$$

where the integration over a $2\delta t$ interval is needed to take into account the finite probing pulse length. The arrival time is simply

$$t_j^{\mathrm{d}}(\vec{r}) \triangleq t_j = \frac{d_j(\vec{r})}{c_0} \ . \tag{2.44}$$

Notice that this solution could in principle be applied to the signal subspace of the $\mathbf{K}$ matrix, with no need for the $(\cdot)^{-1}$ in (2.43). A coherent time-domain DORT image would then be obtained. Nonetheless, it would suffer from reduced resolution performances with respect to TR-MUSIC, both in cross- and in down-range.

As already described in the case of DORT (see §2.3.3.4), the coherent recombination of the images built with the right and left singular vectors is possible with TR-MUSIC. But, while for DORT a sort of synchronization of the two charts were needed by extracting the arrival times from the target to each antenna, (2.42) assures coherency between right and left singular vectors just as it does in time. Therefore, two time-domain vectors can be defined:

$$\mathcal{A}_1(t;\vec{r};M) = \mathrm{IFT}\left\{ \sum_{m=M+1}^{\min(N_1,N_2)} \left[\mathbf{v}_m^T(\omega)\hat{\mathbf{G}}_1(\omega;\vec{r})\right] \mathbf{v}_m^*(\omega) \right\}(t) \tag{2.45a}$$

and

$$\mathcal{A}_2(t;\vec{r};M) = \mathrm{IFT}\left\{ \sum_{m=M+1}^{\min(N_1,N_2)} \left[\mathbf{u}_m^H(\omega)\hat{\mathbf{G}}_2(\omega;\vec{r})\right] \mathbf{u}_m(\omega) \right\}(t) \ , \tag{2.45b}$$

where $\hat{\mathbf{G}}_1$ and $\hat{\mathbf{G}}_2$ are the normalized Green function vectors pertaining to the first and second arrays, respectively. Finally, the TR-MUSIC image can be built as

$$I_t^{\mathrm{TR-MUSIC}}(\vec{r};M) = \left\{ \int_{-\delta t}^{\delta t} \left| \sum_{j=1}^{N_1} \mathcal{A}_{1;\,j}\left[t_{1;\,j}^{\mathrm{d}}(\vec{r}) + \tau;\vec{r};M\right] + \right. \right.$$
$$\left. \left. + \sum_{k=1}^{N_2} \mathcal{A}_{2;\,k}\left[t_{2;\,k}^{\mathrm{d}}(\vec{r}) + \tau;\vec{r};M\right] \right|^2 d\tau \right\}^{-1} \ , \tag{2.46}$$

where the arrival times $t_{1;\,j}^{\mathrm{d}}(\vec{r})$ and $t_{2;\,k}^{\mathrm{d}}(\vec{r})$ have to be calculated with respect to the position of the antennas of the first and second arrays, respectively. It is easy to see in (2.45) that by evaluating the elements of $\mathcal{A}_1$ and $\mathcal{A}_2$ at the corresponding arrival times, the contributions of the two arrays sum up constructively and, depending on the geometry of the setup, an improvement in the DORT image can be obtained.

Experimental results

As a first step, the same reflection configurations studied in Fig. 2.25 are tested here. Fig. 2.26 corresponds to the absorbing chamber setup. With respect to the monochromatic result in Fig. 2.25(a,b), using $I_{\omega\omega}^{\mathrm{TR-MUSIC}}$ gives an overall cleaner image than in Fig. 2.25(a),

in the sense that eventual side lobes are averaged out by the incoherent frequency sum. Apart from this, the cross-range rejection is barely changed. As for the difference between the two solutions in (2.41), almost none can be appreciated. On the other hand, the coherent time-domain approach $I_t^{\mathrm{TR-MUSIC}}$ in (2.42)-(2.43) drastically improves cross-range resolution and rejection.

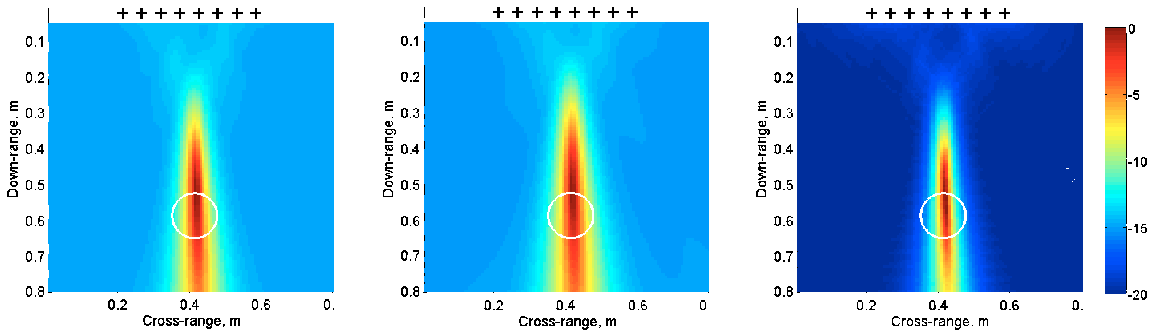

(a) $I_{\omega\omega}^{\mathrm{TR-MUSIC}}(\vec{r};1)$, type 1 (b) $I_{\omega\omega}^{\mathrm{TR-MUSIC}}(\vec{r};1)$, type 2 (c) $I_t^{\mathrm{TR-MUSIC}}(\vec{r};1)$

FIGURE 2.26: *Time-domain extensions of TR-MUSIC applied to the reflection configuration in the absorbing chamber of* FIG. *2.18(a).*

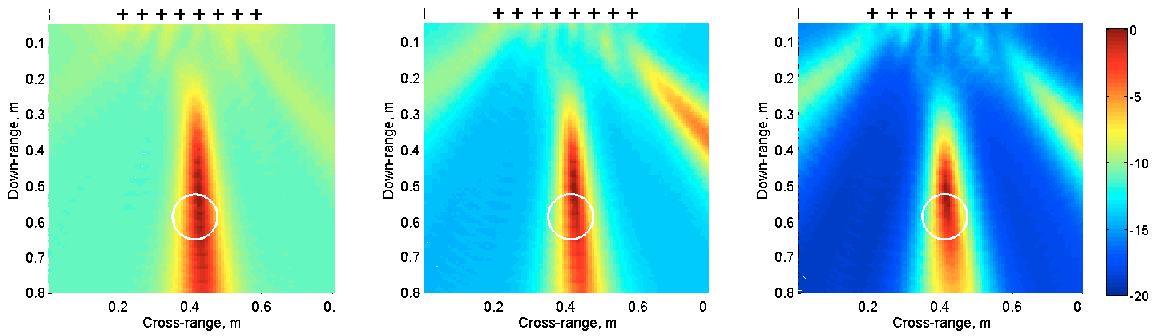

(a) $I_t^{\mathrm{TR-MUSIC}}(\vec{r};1)$ (b) $I_t^{\mathrm{TR-MUSIC}}(\vec{r};2)$ (c) $I_t^{\mathrm{TR-MUSIC}}(\vec{r};3)$

FIGURE 2.27: *Time-domain extension of TR-MUSIC applied to the reflection configuration in the reverberating medium of* FIG. *2.19(a).*

As for the reverberating case in FIG. 2.27, only $I_t^{\mathrm{TR-MUSIC}}$ has been used by varying M from 1 to 3. The monochromatic results are confirmed: using $M = 2$ and $M = 3$ improves the quality of the image in cross-range. In addition, with respect to FIG. 2.27, the frequency coherency of this method helps in reducing the energy of the "lobes" directed towards the sides of the chamber.

A final example concerns the transmission setup already shown in FIG. 2.23(a) with two targets, a metallic and a wooden cylinder 15 cm spaced (from center to center). Given the singular values distribution in FIG. 2.23(b), and since $\lambda_m|_{m=1,2}$ are each associated to a target, M is set to 2. The results in FIG. 2.28 again show the better cross-range rejection given by the coherent time-domain approach and, remarkably, the improved quality of the image obtained when coherently merging the charts of the two arrays (EQ. (2.46)).

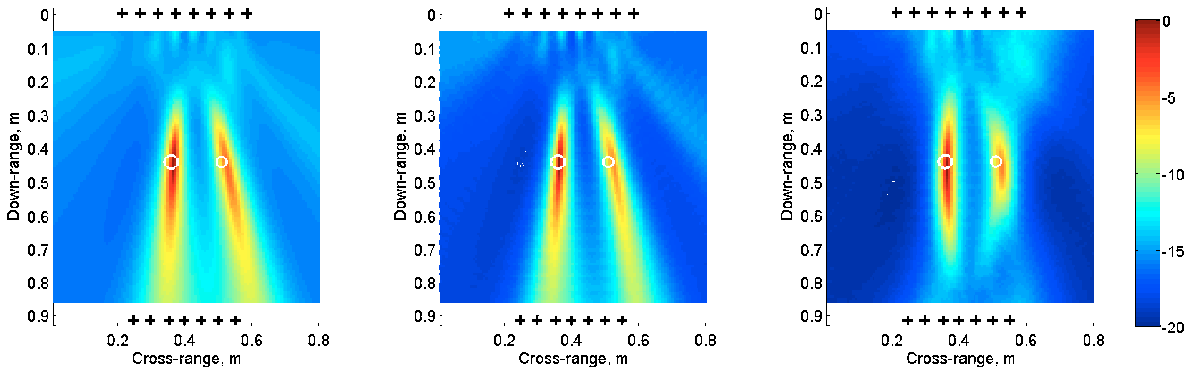

(a) $I_{\omega\omega}^{\mathrm{TR-MUSIC}}(\vec{r};3)$ (b) $I_{t}^{\mathrm{TR-MUSIC}}(\vec{r};3)$ - (2.43) (c) $I_{t}^{\mathrm{TR-MUSIC}}(\vec{r};3)$ - (2.46)

FIGURE 2.28: *Time-domain extensions of TR-MUSIC applied to the transmission configuration in* FIG. *2.23(a). The experimentally retrieved antenna pattern is used.*

2.3.4.2 Arrival time regularization

From the experimental results just presented it is clear that while TR-MUSIC has a very good cross-range resolution because of its non-linear nature, its performances in down-range are rather poor. In §B.2, under the frame of DORT, that is, using the signal subspace instead of the noise one in (2.42)-(2.43), it is shown that the theoretical down-range resolution is indeed infinitely large, becoming finite but yet very poor if considering the effect of the array aperture. This happens because in (2.42)-(2.43) the image is formed by trying to null the discrepancy between the following *differences*

$$\left[t_k^{\mathrm{d}}(\vec{r}) - t_j^{\mathrm{d}}(\vec{r})\right] \; - \; (\tau_k - \tau_j) \; , \tag{2.47}$$

where, with reference to (2.42)-(2.43), the antenna-target arrival times $\tau_j - \tau_k$ are contained in $\mathbf{v}_m^*$ and $\mathbf{v}_m$, respectively, and the pixel-dependent arrival times $t_j^{\mathrm{d}}(\vec{r}) - t_k^{\mathrm{d}}(\vec{r})$ are brought by the Green function and by the evaluation of (2.42) at $t_j^{\mathrm{d}}(\vec{r})$. Indeed, under the paraxial approximation, that is, for $F \gg D$, it is easy to see that when moving in down-range the two differences are approximately equal, resulting in a lack of down-range resolution. Although employing the noise singular vectors provides some more down-range resolving power, almost the same behavior has to be expected with TR-MUSIC.

The key for obtaining a satisfying down-range resolution lies in a proper estimation of the antenna-target arrival times $\tilde{\tau}_j|_{j=1,N}$. A possible way of retrieving them based on the synchronization of the singular vectors (2.35)-(2.37) has already been discussed in §2.3.3.2. Once they are known, again inspired by [99] and considering the case of a single array for simplicity, it is possible to include them for imaging as a regularizing term,

$$I_t^{\mathrm{TR-MUSIC-AT}}(\vec{r};M) = \left\{ \int_{-\delta t}^{\delta t} \left| \sum_{j=1}^{N} \mathcal{A}_j \left[t_j^{\mathrm{d}}(\vec{r}) + \tau; \vec{r}; M\right] \left| t_j^{\mathrm{d}}(\vec{r}) - \tilde{\tau}_j + \tau \right| \right|^2 d\tau \right\}^{-1} . \tag{2.48}$$

Here, the regularizing term is based on the difference between *single* arrival times, the antenna-pixel arrival time, $t_j^{\mathrm{d}}(\vec{r})$, and the estimated antenna-target one, $\tilde{\tau}_j$. With respect

to (2.47) where the difference between *differential* arrival times appears, the image is now much better resolved in down-range.

In case of multiple targets, say N_{tgt}, it easy to adapt (2.48) as

$$I_t^{\text{TR-MUSIC-AT}}(\vec{r};\{M_n\}_{n=1,N_{\text{tgt}}}) = \sum_{n=1}^{N_{\text{tgt}}} \left\{ \int_{-\delta t}^{\delta t} \left| \sum_{j=1}^{N} \mathcal{A}_j \left[t_j^{\text{d}}(\vec{r}) + \tau; \vec{r}; M_n \right] \left| t_j^{\text{d}}(\vec{r}) - \tilde{\tau}_j^n + \tau \right| \right|^2 d\tau \right\}^{-1}, \quad (2.49)$$

where M_n and $\tilde{\tau}_j^n$ are the signal subspace dimension and the estimated arrival time pertaining to the n^{th} target, respectively.

Experimental results

The arrival time regularization has been tested against the experimental configurations already studied in §2.3.4.1. For both the anechoic and reverberating configurations in Fig. 2.26 and Fig. 2.27, the arrival times extracted from the raw **K** matrix or through the singular vector-based method (2.35)-(2.37) are also shown in Fig. 2.29(a,d). While in the anechoic case both methods give roughly the same values, a significant difference is observed in the reverberating configuration. Again, through the use of the singular vectors and their averaging, the reduction of the effect of reverberation produces a significant improvement in the estimates, since the **K** matrix-based values differ from 0.25 ns to 0.5 ns, corresponding to a down-range error of 7.5 cm to 15 cm. As expected, a great improvement in the down-range resolution is obtained in Fig. 2.29(c) and Fig. 2.29(f), which merge the TR-MUSIC results of Fig. 2.26(c) and Fig. 2.27(c) with the arrival time regularizations shown in Fig. 2.29(b) and Fig. 2.29(e), respectively.

A similar improvement is also observed in Fig. 2.30 for the transmission two-target configuration already studied in Fig. 2.28, where the multiple target approach (2.49) has been used in addition to the conjoint use of both arrays (2.46).

2.3.4.3 Conclusions

The importance of TR-MUSIC lies mainly in the improved - theoretically infinitely small - cross-range resolution with respect to linear methods such as DORT or Kirchhoff migration. This is confirmed even with realistic values of SNR. Its extension to time-domain further enhances the achievable resolution, and proves to be rather effective in cluttered media to reduce the blurring of the images.

The drawback of TR-MUSIC is clearly its poor down-range resolution in the case of a small measurement line. Nonetheless, an image regularization based on the estimation of the antenna-target arrival times can considerably improve the results. Here, it has been validated through experimental results.

The main difficulty, as for DORT, is hidden in the classification of the singular spaces issued from the SVD of the **K** matrix. A clarifying example is given in the next paragraph,

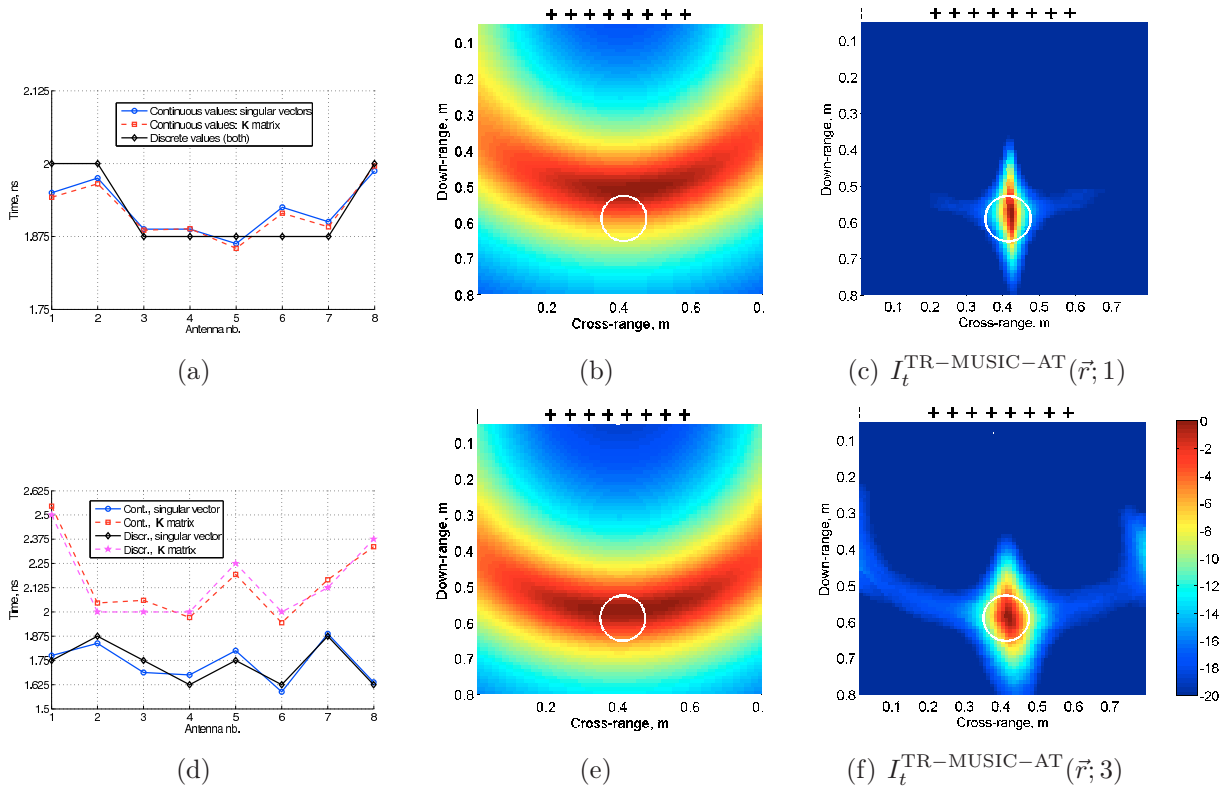

(a) (b) (c) $I_t^{\mathrm{TR-MUSIC-AT}}(\vec{r};1)$

(d) (e) (f) $I_t^{\mathrm{TR-MUSIC-AT}}(\vec{r};3)$

FIGURE 2.29: *Arrival time regularization applied to TR-MUSIC for the anechoic (top) and reverberating (bottom) configurations in* FIG. *2.26(c) and* FIG. *2.27(c), respectively. (a,d) Extracted arrival times - from the raw* $\mathbf{K}$ *matrix or through the singular vector-based method (2.35)-(2.37). (b,e) Chart of the regularization term only based on the arrival times. (c,f) Regularized TR-MUSIC chart.*

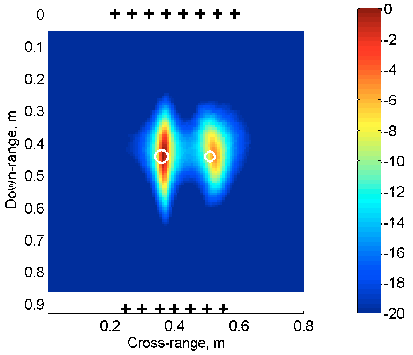

FIGURE 2.30: *Arrival time regularization applied to TR-MUSIC,* $I_t^{\mathrm{TR-MUSIC-AT}}(\vec{r};2,2)$*, for the transmission configuration in* FIG. *2.28(c).*

where a low SNR makes it hard to separate signal an noise subspaces. An additional degree of difficulty comes from the necessity of tracking the singular spaces over frequency, since it is mandatory - especially for the estimation of the arrival times - that a signal subspace be associated to the (same) target at all the frequencies within the band. In this sense, Kirchhoff migration appears as a more robust method for imaging purposes, since no classification whatsoever is required. If high resolving power is needed and a low SNR

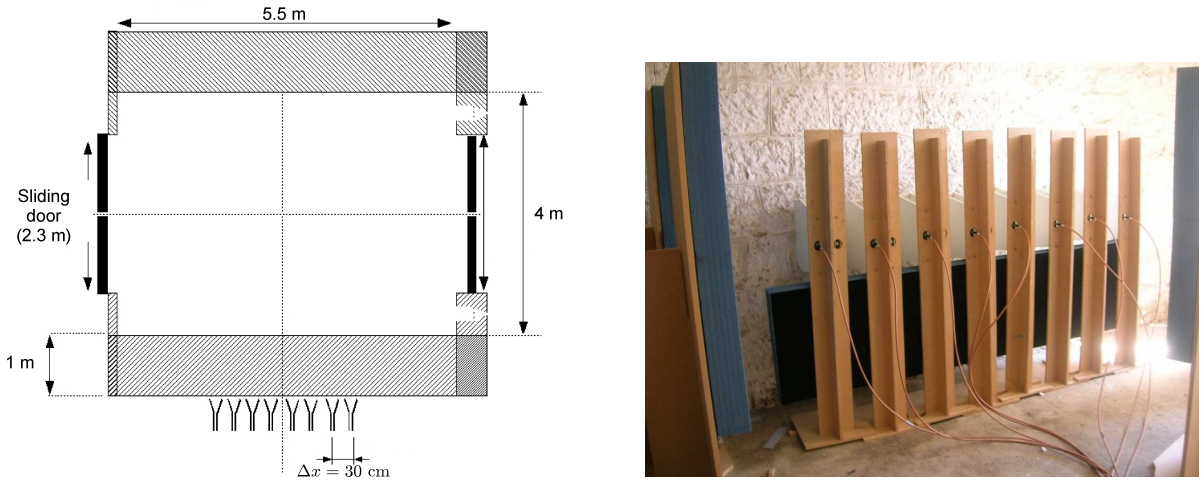

(a) (b)

Figure 2.31: *(a) Schematization of the room sounded with the antennas shown in (b) and placed behind the wall.*

is available, though, algorithms capable of classifying and tracking the singular spaces are required for TR-MUSIC to work properly.

2.3.5 An experimental case study: the Through-The-Wall measurement campaign

During the PhD period, the LSEET participated to a national project financed by the French Ministry of Defence (REI / 2008 34 0022). It consisted in exploring the potentialities of Time Reversal-based processing for detection of human targets in a room sounded from behind a wall. This kind of topic is known in literature as Through-The-Wall (TTW) imaging. Other partners of the project were the Laboratoire d'Électronique, Antennes et Télécommunications (LEAT) in Nice-Sophia Antipolis, responsible for the experimental workpackages, the Institut Langevin in Paris, exploiting the data just as the LSEET, and the Office National d'Études et Recherches Aérospatiales (ONERA) as coordinating entity.

Two measurement campaigns, resulting into two experimental databases, were held in november 2009 and july 2010, respectively, in an old fort located at La Turbie, France[14]. Some of the details concerning the configuration explored here are listed next:

- the room where the targets are placed has a surface of 4×5.5 m^2, and is separated from the antennas by a 1 m-deep wall built with limestone rocks (see Fig. 2.31(a));
- the wall thickness and permittivity, d^{w} and $\varepsilon_r^{\mathrm{w}}$ respectively, are experimentally estimated to $d^{\mathrm{w}} = 1$ m and $\varepsilon_r^{\mathrm{w}} \approx 11.8$;
- the room is furnished, and the target is a human being located at one of the positions in Fig. 2.32;

[14]LSEET also participated to the first campaign in support of the leading group from LEAT

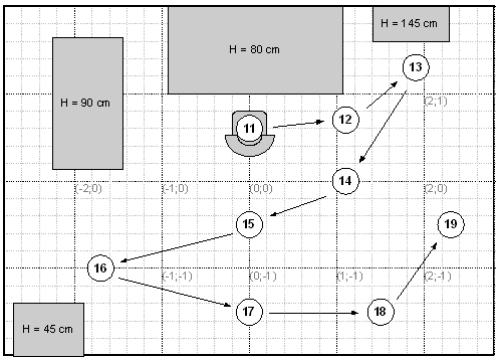

(a)

(b) P11

(c) P12

(d) P17

(e) P18

FIGURE 2.32: *(a) Measurement positions of a human target moving in the furnished room of* FIG. *2.31(a). The antennas are behind the wall (not shown) at the bottom of the figure. (b-e) Pictures of the positions 11, 12, 17, and 18, which are used later as test cases.*

- an array made of 8 ETS antennas[15] separated by $\Delta x = 30$ cm is used in a multi-static configuration;
- the **K** matrices, with and without targets, are measured with an 8-port VNA in a frequency band going from 0.45 to 5 GHz with a step of 5 MHz and 100 Hz IF filter bandwidth; the **K** matrix acquisition time is approximately 75 s;
- the antennas are placed right against the wall (see FIG. 2.31(b)), since it has experimentally been found that this assures a better dynamic range than a configuration with the antennas away from the wall. Also, the antennas are surrounded (in the back) by absorbing panels that avoid the propagation of the signal reflected from the wall in the room where the antennas are placed.

Some of the results have been published in [72].

Concerning the signal processing adapted for this kind of experiments, most of the methods developed in §1.6 are used here. For instance, as shown in FIG. 2.33(a), each element of the **K** matrix is time-gated in the time domain in order to extract only the contribution of the targets within the room. Particular attention must be cast into the choice of the FFT window, $W_\omega(\omega)$. For any retrodiffusion element K_{jj}, it must indeed be avoided that the echo of the front side of the wall, stronger than the antenna reflection coefficient (see

[15] Although based on the same design, these ETS antennas are larger than those used at LSEET, resulting in a bandwidth shifted towards the low frequencies.

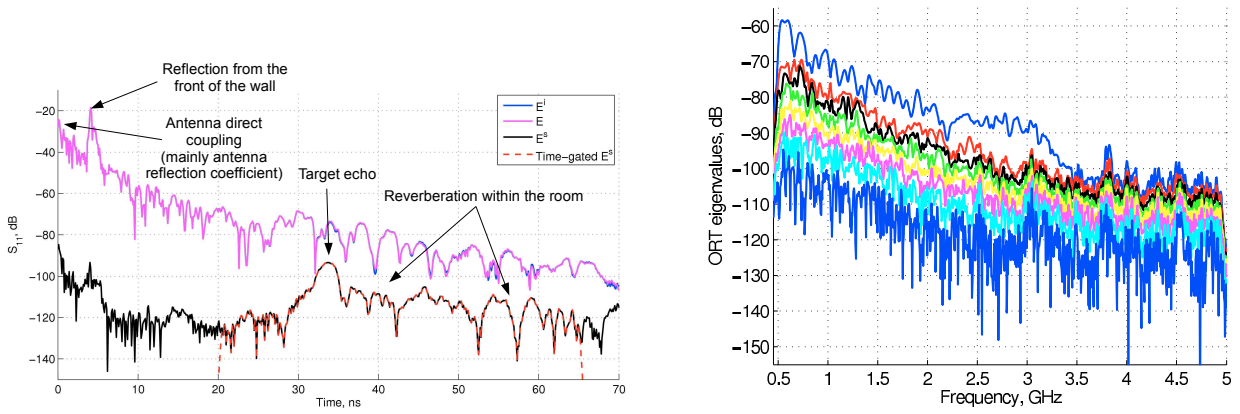

(a) (b)

FIGURE 2.33: *(a) Time domain retrodiffusion measurement (incident, total, and scattered S_{11}). (b) Singular values distribution as a function of frequency for the position P12 in* FIG. *2.32.*

FIG. 2.33(a)), does not alias upon the target echo after windowing. Although the differential approach reduces here by more than 70 dB this contribution, and although the target echo is rather "far" in time due to the long propagation of the signal through the wall, still a window other than the rectangular function must be employed. The choice has fallen onto a *tukey* window (*cf.* §1.6.2) with a tapering of 100 MHz at both edges of the frequency band.

Propagation through the wall must properly be taken into account when plotting field charts or evaluating arrival times. Although a formal, exact derivation (at least in the case of a wall infinitely large in the cross-range with respect to the antenna array) is feasible, the approximation in [111] is simply employed here. It consists in describing the signal propagation as a single path from one side to the other of the wall, hence neglecting the multiple reflections within its width. With respect to the rigorous expression, it is computationally extremely faster, while the results are hardly affected due to the relatively high conductivity value of the wall, σ^{w}, which determines a rapid attenuation of the signal rebounding within its width. The parameters of such a model are d^{w} and $\varepsilon_r^{\mathrm{w}}$. As for the lateral and rear walls of the room in FIG. 2.31(a), they are not taken into account at all.

The singular values of the $\mathbf{K}$ matrix as a function of frequency for the configuration P11 in FIG. 2.32 are plotted in FIG. 2.33(b). As a first remark, the amplitude of the largest one decreases rapidly as the frequency grows. Up to 3.5 GHz, the decrease is rather linear in dB, that is, exponential in natural units, which corresponds to the attenuation within the wall due to the non-zero σ^{w} value. For larger frequencies, it is possible to state that any signal is completely overruled by noise. In practice, for any method utilizing the SVD of $\mathbf{K}$, only the frequency band [0.45-1.5] GHz is exploited.

The results presented next aim at comparing the performances of the Kirchhoff migration method (§2.3.1) against those relative to the time-domain TR-MUSIC method combined

with the arrival time regularization (§2.3.4.2). In Fig. 2.34, this is done for the four positions shown in Fig. 2.32 and using the differential **K** matrix calculated, as usual, as the difference between the matrices relative to the room with and without target(s). On the other hand, Fig. 2.35 gives the results when the **K** matrices related to two configurations are subtracted, namely P12-P11 in Fig. 2.35(a-c) and P18-P17 in Fig. 2.35(d-f). Doing so, there is no need for the measurement of the empty room, which might be problematic in real applications. As for the resulting signals, they are equivalent to those that would be measured if two targets were present in the room, apart from the multiple scattering between them that cannot be recreated. Notice that the color scale in both figures has been set to 0 to -10 dB, that is, a 10 dB-smaller range than for all the other results of the chapter. Although purely for visual inspection of the results, this is needed in order to counteract the effect of a much lower SNR - due to the reduced dynamic range induced by the attenuation of the wall - in the present TTW setup.

Both methods give globally satisfactory results. For the positions farther from the array side of the room, namely P11 and P12, the proximity of the wall alters the images: for instance, with Kirchhoff migration two hot spots appear, whereas TR-MUSIC gives a single, worse-resolved region in-between such spots for P11. As for the multiple targets results, in the P18-P17 case TR-MUSIC fails in detecting both of them.

The general conclusion is that Kirchhoff migration is a very robust method. If d^{w} and $\varepsilon_r^{\mathrm{w}}$ are properly estimated, there is no choice whatsoever to be made when building the image of the targets. Due to its fine down-range resolution, the effect of a wall in the room placed in the down-range direction creates sort of replicas of the target image, probably due to the reflection of the wall and its interference with the direct echo from the target.

On the other hand, while these artefacts are apparently reduced because of a lower obtainable down-range resolution, TR-MUSIC is very sensitive to the repartition of the **K** matrix singular spaces. Indeed, for the choice of the signal subspace dimension M, it is necessary that the singular value(s) associated to the target(s) do not cross in frequency with noise-related ones. This happens clearly in Fig. 2.34(a) at 660 MHz, 1.025 GHz, and 1.375 GHz, in Fig. 2.34(d) at 720 MHz, to mention only a few. Hence, only configurations with a large SNR can really beneficiate from these SVD-based methods.

Nonetheless, in multiple targets scenarii, even if a high SNR is available, it may happen that the singular values associated to the targets cross. The effects are then similar to those just mentioned for crossings with nose-related singular values, becoming especially critical if the arrival times estimation based on the singular vector averaging (2.35)-(2.37) is used.

It finally seems that only when additional algorithms capable of tracking the nature of the singular spaces will be available it will be possible to fully - and safely - rely on any of these subspace-based methods.

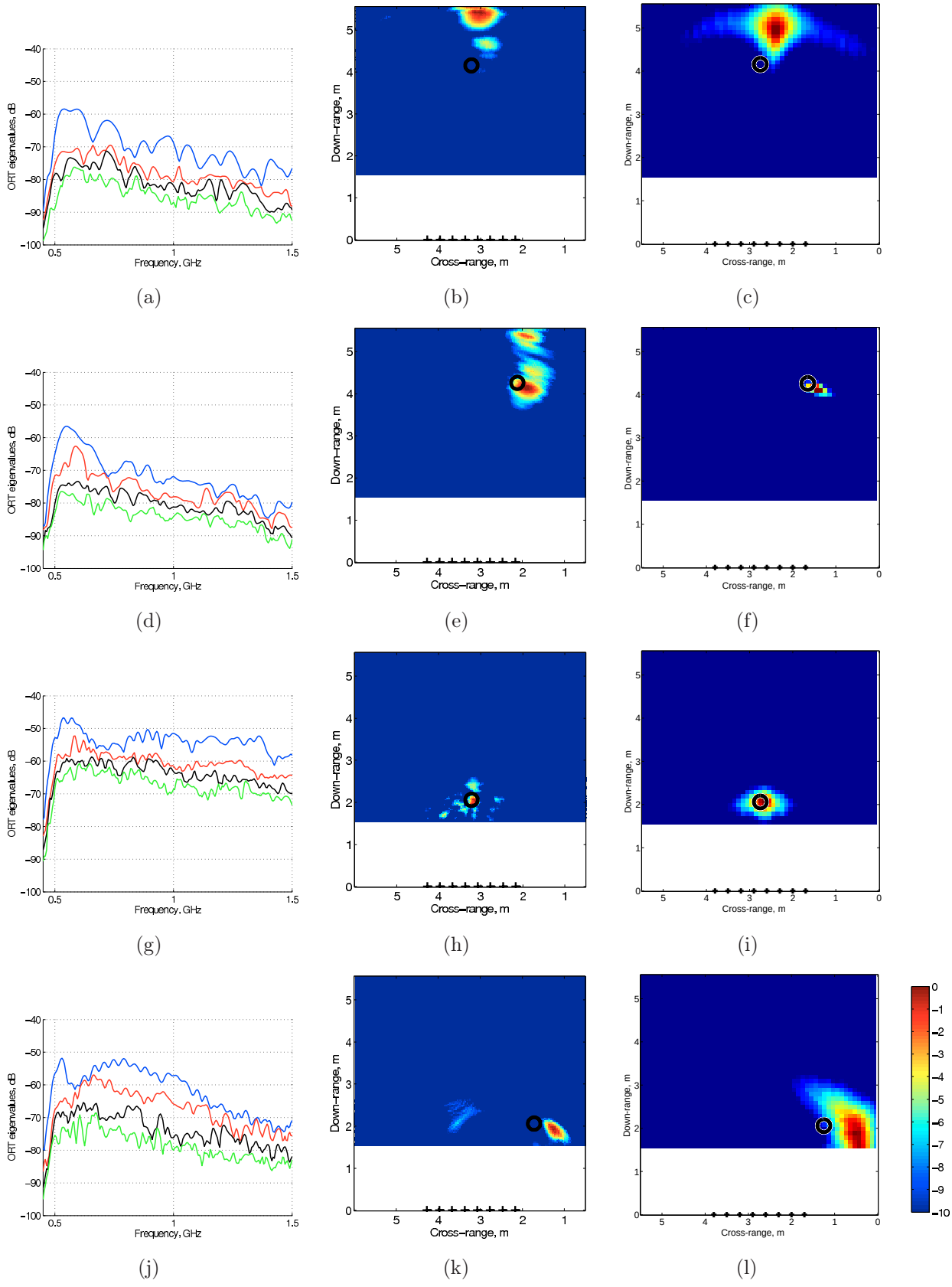

FIGURE 2.34: *(left) Four largest singular values as a function of frequency. (center) and (right) Kirchhoff migration and TR-MUSIC with arrival time regularization methods, respectively. From top to bottom, the tested positions are P11, P12, P17, and P18 in* FIG. *2.32.*

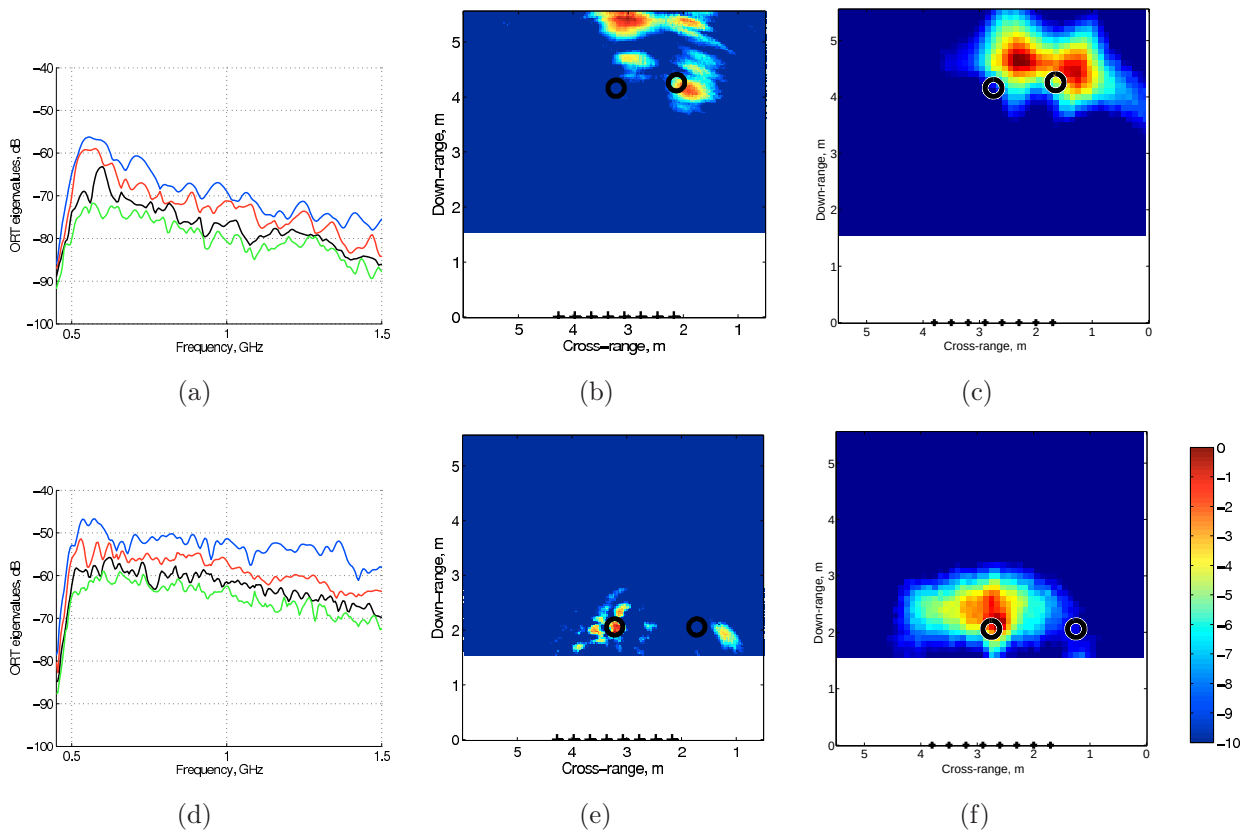

FIGURE 2.35: *As* FIG. *2.34, but the tested configurations are P12-P11 and P18-P17 in* FIG. *2.32.*

Chapter 3

Quantitative inverse scattering

Depending on the applications, detection/localization of targets is not sufficient. Informations on the shape and/or on the nature of a scatterer are for instance mandatory in medical applications, or in geophysical prospection, just to mention a few. In addition, non-destructive or non-invasive techniques are often needed to retrieve them. In this sense, electromagnetic inverse scattering appears as a good candidate for solving the problem. In effect, it consists of measuring the electromagnetic field scattered from a medium - which is a non-desctructive process as long as the power emitted to sound the medium is relatively low - and to retrieve a full, quantitative description of the scatterers.

From the mathematical point of view, the general problem is a very difficult one. Although it can, in some cases, be simplified if a priori informations about the scatterers are available (*e.g.* its shape or its nature - dielectric or purely metallic), this chapter concentrates on the unsimplified problem.

The rigourous physical description of the scattering process is contained in the Maxwell's equation. The problem of solving, or *inverting*, these equations is first mathematically formulated and studied. Then, a short and unexaustive overview of the existing inversion methods is given, with emphasis on the algorithm chosen for the present work, the Modified^2 Gradient Method [12]. Finally, the adaptation of such algorithm to the experimental setup presented in §1 is described, completed by a collection of experimental results.

3.1 Problem formulation

The section in the xOy plane of the general setup is shown in Fig. 3.1. Time-harmonic fields with a $e^{i\omega t}$ dependency are considered in the following. An emitting antenna generates a so-called incident wave associated to the incident field $\vec{E}^{\mathrm{i}}(\omega;\vec{r})$. The interaction of the wave with an object, whose support is $\mathcal{D}$, generates the total field, $\vec{E}(\omega;\vec{r})$, which is measured by a receiving antenna. The difference between the two aforementioned quantities is introduced under the name of scattered field, $\vec{E}^{\mathrm{s}}(\omega;\vec{r}) \triangleq \vec{E}(\omega;\vec{r}) - \vec{E}^{\mathrm{i}}(\omega;\vec{r})$. The propagation medium is free-space (ε_0), whereas the permittivity and conductivity of the scatterer

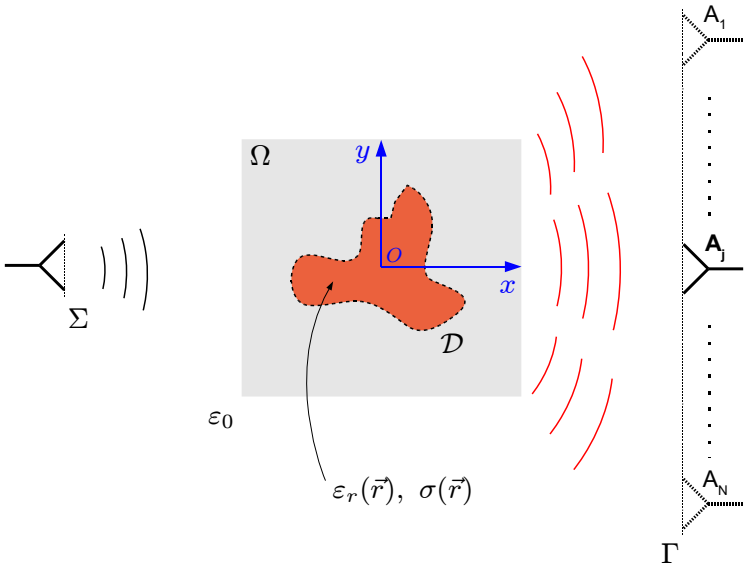

FIGURE 3.1: *General setup for the inverse problem.*

are $\varepsilon_r(\vec{r})$ and $\sigma(\vec{r})$, respectively, both real quantities. Both the propagation medium and the scatterer are considered as non-magnetic ($\mu(\vec{r}) = \mu_0$); the former is in addition supposed stationary, linear, isotropic and charge-free.

As already stated, Maxwell's equation describe the whole process. Omitting the ω dependency for conciseness, they can be re-arranged to obtain the propagation equation for the complex amplitude

$$\vec{\nabla} \times \vec{\nabla} \times \vec{E}(\vec{r}) - k_0^2 \vec{E}(\vec{r}) = k_0^2 \chi(\vec{r}) \vec{E}(\vec{r}) - i\omega\mu_0 \vec{J}_0(\vec{r}) \ , \tag{3.1}$$

where $\chi(\vec{r})$ is the contrast function defined as

$$\chi(\vec{r}) = \epsilon_r(\vec{r}) - i\frac{\sigma}{\omega\epsilon_0} - 1 \ , \tag{3.2}$$

and $\vec{J}_0(\vec{r})$ is the current distribution within the source antenna, whose surface is indicated with Σ in FIG. 3.1. All the properties of the scatterer (position, shape, nature) are contained in $\chi(\vec{r})$, which constitutes then the unknown of the inverse problem.

For the experiments performed within this manuscript, (3.1) can be restricted to a scalar field. This is possible since 1) in virtue of the good cross-polarization rejection of the antennas, a single polarization oriented in the z-direction can be considered for the electic field, and 2) the scatterers are ideally infinite along z. The propagation equation becomes then

$$\nabla^2 E(\vec{r}) + k_0^2 E(\vec{r}) = -k_0^2 \chi(\vec{r}) E(\vec{r}) + i\omega\mu_0 J_0(\vec{r}) \ . \tag{3.3}$$

Invoking the Green function

$$G(\vec{r}, \vec{r'}) = -\frac{i}{4} H_0^-(k_0 |\vec{r} - \vec{r'}|) \ , \tag{3.4}$$

solution of

$$\nabla^2 G(\vec{r}, \vec{r'}) + k_0^2 G(\vec{r}, \vec{r'}) = -\delta(\vec{r} - \vec{r'}) \tag{3.5}$$

combined with Sommerfeld's radiation condition [68], the solution of (3.3) becomes

$$\begin{aligned} E(\vec{r}) &= G(\vec{r},\vec{r'}) * \left[k_0^2 \chi(\vec{r}) E(\vec{r}) - i\omega\mu_0 J_0(\vec{r})\right] \\ &= k_0^2 \int_{\mathcal{D}} G(\vec{r},\vec{r'}) \chi(\vec{r'}) E(\vec{r'}) d\vec{r'} + E^{\mathrm{i}}(\vec{r}) \ , \end{aligned} \tag{3.6}$$

with

$$E^{\mathrm{i}}(\vec{r}) \triangleq -i\omega\mu_0 \int_{\Sigma} G(\vec{r},\vec{r'}) J_0(\vec{r'}) d\vec{r'} \ . \tag{3.7}$$

Hence, at any given location $\vec{r}$, the total field is the sum of two contributions: the incident field E^{i}, that is, the field generated by the primary sources with support Σ that would be measured in absence of scatterers, and the scattered field generated by the induced sources χE with support $\mathcal{D}$. The product χE is also known as *contrast-source* since it plays the role of an induced current, hence a source, within $\mathcal{D}$.

The inverse problem consists in retrieving $\chi(\vec{r})$ within a pre-determined investigation region Ω, given the knowledge of the total field $E|_\Gamma$ on the measurement line Γ (see FIG. 3.1). In many cases, it is also possible to measure the incident field $E^{\mathrm{i}}|_\Gamma$ in absence of scatterers. Then, the data of the problem are rather the scattered field measurements, $E^{\mathrm{s}}|_\Gamma \triangleq E|_\Gamma - E^{\mathrm{i}}|_\Gamma$, which fits well the differential measurement approach adopted in this work and described in the previous chapters. The equation relating them to the unknown $\chi(\vec{r})$, known as *data equation*, is derived from (3.6) when the evaluation position $\vec{r} \in \Gamma$:

$$E^{\mathrm{s}}(\vec{r}) = k_0^2 \int_{\Omega} G(\vec{r},\vec{r'}) \chi(\vec{r'}) E(\vec{r'}) d\vec{r'} \ , \quad \vec{r} \in \Gamma \ , \tag{3.8}$$

where the integral is now performed over the entire investigation region Ω since $\chi(\vec{r}) = 0$ if $\vec{r} \in \Omega - \mathcal{D}$. In order to invert (3.8), though, the total field $E|_\Omega$ over the region Ω is needed. This can be obtained from (3.6) evaluated at $\vec{r} \in \Omega$, resulting in the *state equation*

$$E(\vec{r}) = E^{\mathrm{i}}(\vec{r}) + k_0^2 \int_{\Omega} G(\vec{r},\vec{r'}) \chi(\vec{r'}) E(\vec{r'}) d\vec{r'} \ , \quad \vec{r} \in \Omega \ . \tag{3.9}$$

3.1.1 Non-linearity and ill-posedness

The data and state equations can be re-written in the following concise way:

$$E^{\mathrm{s}} = \mathcal{G}^{\Gamma}(\chi E) \tag{3.10}$$

$$E = E^{\mathrm{i}} + \mathcal{G}^{\Omega}(\chi E) \ . \tag{3.11}$$

$\mathcal{G}^{\Gamma}$ and $\mathcal{G}^{\Omega}$ are two linear integral operators both mapping the contrast-source χE to a scattered field. Nonetheless, it is important to stress the fact that $\mathcal{G}^{\Gamma}$ has values in Γ, and is therefore sometimes called the *far-field radiation operator* (although Γ is not necessarily in far-field with respect to Ω), whereas $\mathcal{G}^{\Omega}$ has values in Ω itself, hence its name of *near-field radiation operator*:

$$\begin{aligned} \mathcal{G}^{\Gamma} &: \Omega \to \Gamma \\ \mathcal{G}^{\Omega} &: \Omega \to \Omega \ . \end{aligned} \tag{3.12}$$

In a slightly abusive manner, (3.11) can be solved for E, which, substituted in (3.10), produces a unique equation. In formulae:

$$E = \left(\mathcal{I} - \mathcal{G}^{\Omega}\chi\right)^{-1} E^{\mathrm{i}} \quad \Rightarrow \quad E^{\mathrm{s}} = \mathcal{G}^{\Gamma}\left[\chi\left(\mathcal{I} - \mathcal{G}^{\Omega}\chi\right)^{-1} E^{\mathrm{i}}\right] , \tag{3.13}$$

where $\mathcal{I}$ is the identity operator. These results are particularly meaningful. From the left equation, it can be observed that the relation between total and incident fields is linear. On the other hand, the data of the problem, E^{s}, depend non-linearly on the unknown χ: the inverse problem is therefore a non-linear problem.

Furthermore, since it can be shown that the operator $\mathcal{G}^{\Gamma}$ has an analytical kernel[1], it is a compact operator. Mathematically, the inverse of a compact operator cannot be continuous [112]. The conclusion is that, since $\mathcal{G}^{\Gamma}$ needs to be inverted in (3.13) in order to find χ, its lack of continuity can make the solution diverge if the data are affected by noise - which is unavoidable in practice. Hence, according to Hadamard's definition, the problem is ill-posed [1].

These two properties (non-linearity and ill-posedness) make particularly hard the resolution of the inverse problem. They are at the origin of a wide litterature of algorithms, methods, regularization schemes that alleviate these issues trading-off execution speed and/or precision of the solution. Some of them are briefly presented next.

3.2 Overview of inversion methods

From a mathematical point of view, the solution of the inverse problem consisting in finding the contrast $\chi(\vec{r})$ given the scattered field $E^{\mathrm{s}}|_{\Gamma}$ is recast into an optimization problem which, in most cases, is solved in the least-squares (or norm L_2) sense. Under this frame, two errors can be defined: one with respect to the data equation,

$$e^{\Gamma} \triangleq \|E^{\mathrm{s;meas}} - \mathcal{G}^{\Gamma}(\chi E)\|_{\Gamma}^2 , \tag{3.14}$$

where $E^{\mathrm{s;meas}}$ are the measured scattered field data, and one to the state equation,

$$e^{\Omega} \triangleq \|E - E^{\mathrm{i}} - \mathcal{G}^{\Omega}(\chi E)\|_{\Omega}^2 . \tag{3.15}$$

The $\|\cdot\|$ symbol stands for L_2 norm, and the indexes Γ and Ω indicate their domain of validity. Then, a cost, or misfit, function that evaluates the overall error can be built:

$$\mathcal{F}(\chi) = w^{\Gamma} e^{\Gamma} + w^{\Omega} e^{\Omega} , \tag{3.16}$$

where w^{Γ} and w^{Ω} are two weights to be set (although the only relevant tuning parameter is their ratio). Notice that the true data estimation misfit is given by the first term of

[1]The kernel of an operator $\mathcal{L}$ is the set of all operands v such that $\mathcal{L}(v) = 0$. From a physical point of view, it is well known that there exist values of χE, the so-called non-radiating sources, such that $\mathcal{G}^{\Gamma}(\chi E) = 0$, hence the kernel of $\mathcal{G}^{\Gamma}$ is not empty. Finally, a kernel is said analytic if it can be expressed in an analytic form, which is the case for $\mathcal{G}^{\Gamma}$.

(3.16); the second one, related to the state, or auxiliary, variable E, plays the role of a regularization in a constrained optimization problem.

Starting from this formulation, a first distinction among the approaches to solve the inverse problem is between global and local optimization schemes. In the first case, the global minimum $\bar{\chi}$ of the cost function is searched exhaustively, for instance using the concept of neural network [113–115]. It is easy to see the drawback of this approach: when the number of unknowns increases (*e.g.* for large investigation domains Ω and/or in 3D problems), the computational burden becomes too heavy. For this reason, they are not considered in this manuscript and are not detailed further. Local optimization schemes, on the other hand, try to find a local minimum $\hat{\chi}$ of (3.16) in an iterative fashion starting from an initial estimation. The computation burden is obviously reduced, at the price of the risk of converging to a local minimum of $\mathcal{F}(\chi)$.

Among the local optimization methods, further categories can be distinguished. A first one concerns the role of the state equation. In many cases, it is indeed preferred to remove it from the minimization procedure by considering a simplified cost function with only the state equation term. Then, given the estimate χ_n at the n^{th} iteration, $\tilde{E}_n$ is found by directly solving the state equation (3.9) (which is linear in E), and a new estimate χ_{n+1} is retrieved from the minimization of the cost function. This way, an unconstrained minimization of the data equation is realized, and the problem is as a matter of fact linearized. The minimization of the cost function can at least be done in two ways: 1) through Newton-based approaches, as in the well-known Newton-Kantorovich Method [116–119] or in the equivalent [120] Distorted Wave Born Method [121, 122], or 2) through the use of the standard Polak-Ribière conjugate gradient (CG) procedure, as in the Born Method [123] or in the Modified Born Method (MBM) [124].

On the other hand, the auxiliary unknown E can be sought conjunctly with χ by minimizing the whole cost function (3.16). The problem is again non-linear. In this case, the CG minimization is always preferred to Newton-based methods, since the latter require a higher complexity that must be added to the already increased complexity of the problem. The resulting approach is called Modified Gradient Method (MGM) [118, 125–127]. To this category also belong two other methods based on a different yet equivalent mathematical formulation of the problem aimed at decreasing its degree of non-linearity. They are the Contrast Source Inversion (CSI) method [128], where both sides of the state equation are multipled by χ so that the contrast-source χE replaces E as state variable, and the Contrast Source-Extended Born (CS-EB) Method [129–131]. Today, the first is probably the most employed inversion method for electromagnetic problems [11, 132–135].

As opposed to these deterministic inversion techniques, the Bayesian framework has recently been adopted to solve the inverse scattering problem [136–140]. While a rigorous mathematical formulation is still adopted to describe the problem, it is here a functional based on an a posteriori probability density function that is maximized (as opposed to the cost function minimization carried out in the deterministic approaches). Since this work

focuses on the experimental approach and not on an investigation about optimal inversion methods, such stochastic approaches are not dealt with in this manuscript.

3.3 M^{2}GM inversion algorithm

The category of inversion methods selected for this thesis is the MGM. Its mathematical formulation is the following. The investigation domain Ω is discretized through an equispaced grid along x and y, with a pixel area of $\Delta_x\Delta_y \triangleq d_{\text{pix}}^2$ and a total of $N_xN_y \triangleq N_{\text{pix}}$ points. Both the unknown χ and the state variable E are defined, at n^{th} iteration of the minimization algorithm, through the piecewise bilinear expansions

$$\chi_n = \sum_{i=1}^{N_{\text{pix}}} \chi_{n,i}\psi_i \tag{3.17}$$

$$E_n = \sum_{i=1}^{N_{\text{pix}}} E_{n,i}\psi_i \ , \tag{3.18}$$

whose basis functions are [141]

$$\psi_i = \Lambda(x - x_i)\Lambda(y - y_i) \ , \tag{3.19}$$

with (x_i, y_i) being the coordinates of the i^{th} pixel, and $\Lambda(\tau)$ the triangular function

$$\Lambda(\tau) = \begin{cases} 1 - |\tau|/h & \text{if } |\tau| < h \\ 0 & \text{otherwise} \end{cases} \ . \tag{3.20}$$

Thus, at each iteration, the values of the expansions coefficients $\chi_{n,i}$ and $E_{n,i}$ become the actual sought quantities, represented through the vectors $\boldsymbol{\chi}_n$ and $\mathbf{E}_n$.

The Method of Moments (MoM) is used to discretize the equations. To stress this, the far- and near-field operators are from now on indicated through the matricial notations $\mathbf{G}^\Gamma$ and $\mathbf{G}^\Omega$, respectively, so that the cost function can be written as

$$\mathcal{F}(\chi; E) = w^\Gamma \|E^{\text{s;meas}} - \mathbf{G}^\Gamma \chi E\|_\Gamma^2 + w^\Omega \|E - E^{\text{i}} - \mathbf{G}^\Omega \chi E\|_\Omega^2 \ . \tag{3.21}$$

The weights are set to "physical" values meant to equilibrate the impact of each of the two terms on the minimization procedure, namely

$$w^\Gamma = \|E^{\text{s;meas}}\|_\Gamma^{-2} \tag{3.22}$$

$$w^\Omega = \|E^{\text{i}}\|_\Omega^{-2} \ . \tag{3.23}$$

As it can be seen, their values only depend on the data of the problem, hence they do not change during the iterations. This choice differs from that employed, for instance, in the CSI scheme [128], where w^Ω is a function of χ and thus evolves at each iteration. Although there is no evidence that the values used here are optimal in any mathematical sense, they

have proven to lead to senseful results and they indeed have a physical meaning. Very interesting remarks on the choice of the weights can be found in [135].

The constrast is actually split into two unknowns, its real and imaginary parts. Furthermore, a positivity constraint, or a priori information, is added through the use of squared variables. The result is

$$\boldsymbol{\chi}_n = 1 + \boldsymbol{\xi}_n^2 - \varepsilon_{r;\mathrm{b}} - i\frac{\boldsymbol{\eta}_n^2 - \sigma_\mathrm{b}}{\omega\epsilon_0} \ , \tag{3.24}$$

where $\varepsilon_{r;\mathrm{b}}$ and σ_b are the (known) background permittivity and conductivity, respectively. In all the experiments performed herein $\varepsilon_{r;\mathrm{b}} = 1$ and $\sigma_\mathrm{b} = 0$, that is, free-space propagation conditions are considered. This justifies completely the positivity assumption. The update rules are

$$\boldsymbol{\xi}_{n+1} = \boldsymbol{\xi}_n + \beta_n^\xi \mathbf{d}_{n+1}^\xi \tag{3.25}$$

$$\boldsymbol{\eta}_{n+1} = \boldsymbol{\eta}_n + \beta_n^\eta \mathbf{d}_{n+1}^\eta \ , \tag{3.26}$$

where $\beta_n^\xi, \beta_n^\eta \in \mathbb{R}$ are the steps minimizing $\mathcal{F}_{n+1}$, and $\mathbf{d}_{n+1}^\xi, \mathbf{d}_{n+1}^\eta$ are the standard Polak-Ribière CG descent directions. These are defined as

$$\mathbf{d}_{n+1}^\xi = -\mathbf{g}_{n+1}^\xi + \zeta_{n+1}^\xi \mathbf{d}_n^\xi \tag{3.27}$$

$$\mathbf{d}_{n+1}^\eta = -\mathbf{g}_{n+1}^\eta + \zeta_{n+1}^\eta \mathbf{d}_n^\eta \ , \tag{3.28}$$

where $\mathbf{g}_{n+1}^\xi, \mathbf{g}_{n+1}^\eta$ are the gradients of $\mathcal{F}_n$ with respect to $\boldsymbol{\xi}_n$ and $\boldsymbol{\eta}_n$, respectively, and

$$\zeta_{n+1}^\xi = \frac{\left(\mathbf{g}_{n+1}^\xi - \mathbf{g}_n^\xi\right)^T \mathbf{g}_n^\xi}{\|\mathbf{g}_n^\xi\|^2} \tag{3.29}$$

$$\zeta_{n+1}^\eta = \frac{\left(\mathbf{g}_{n+1}^\eta - \mathbf{g}_n^\eta\right)^T \mathbf{g}_n^\eta}{\|\mathbf{g}_n^\eta\|^2} \ . \tag{3.30}$$

Notice that descent directions, gradients, and $\zeta_{n+1}^\xi, \zeta_{n+1}^\eta$ are all real quantities. As for the expressions of the gradients, they are given later in §3.3.1 for the more generic case of a multi-view multi-frequency inversion scheme.

For the electric field, a similar approach is followed. Nonetheless, the choice of employing a modified version of the MGM is done here, consisting in the update rule

$$\mathbf{E}_{n+1} = \mathbf{E}_n + \alpha_n \mathbf{d}_{n+1}^E + \gamma_n \left(\tilde{\mathbf{E}}_n - \mathbf{E}_n\right) \ , \tag{3.31}$$

where $\tilde{\mathbf{E}}_n$ is the solution of the state equation (3.9) given $\boldsymbol{\chi}_n$. The last term in (3.31), representing the modification to the standard MGM, can be called *Born term* since in the MBM this is the only term used for updating the total field (that is, α_n is set to 0). The modified MGM resulting from this new term has been introduced by Belkebir *et al.* in [12,31] and has been named Modified² Gradient Method (M²GM). As it will be detailed later, it can be seen as a "hybrid" method blending the benefits of solving the forward

problem for E at each iteration to the frame of the MGM. As for the CG descent direction, it writes as

$$\mathbf{d}_{n+1}^E = -\mathbf{g}_{n+1}^E + \zeta_{n+1}^E \mathbf{d}_n^E \ , \tag{3.32}$$

where $\mathbf{g}_{n+1}^E$ is the gradient of $\mathcal{F}_n$ with respect to $\mathbf{E}_n^*$, and

$$\zeta_{n+1}^E = \frac{\Re\left\{\left(\mathbf{g}_{n+1}^E - \mathbf{g}_n^E\right)^H \mathbf{g}_n^E\right\}}{\|\mathbf{g}_n^E\|^2} \ . \tag{3.33}$$

Notice that here, since the total field is a complex quantity, the gradient and the descent direction are complex quantities, whereas the Polak-Ribière factor ζ_{n+1}^E must be real.

Some comments are now in order. As just stated, the only difference with a standard MGM method lies in the update rule (3.31) for the total field, where, in addition to the standard conjugate-gradient term, the solution $\tilde{\mathbf{E}}_n$ of the state equation is taken into account. The first benefit of this correction comes from a considerably decreased number of iterations necessary to reach convergency (given a required precision value) with respect to the classic MGM (or CSI) [12]. Unfortunately, this does not necessarily imply a reduced execution time, since the price to pay at each iteration is the resolution of the state equation for E, which is not required in the MGM. Nevertheless, a considerable reduction is effectively reached thanks to the very powerful direct solver used. This has two main features: first, it solves the state equation through a linear CG method relying on an FFT (CG-FFT) to compute the spatial convolution $\mathcal{G}^\Omega(\chi E)$. Then, it employs a so-called "marching on in frequency and source" strategy to generate the initial estimate for the CG based on the solutions found for previous sources and at previous frequencies, reducing in turn the number of linear CG iterations needed to reach convergency [141]. See also [142] for further implementation details on the CG-FFT method.

In addition, the degree of non-linearity of the problem is reduced. This can be understood by acknowledging that, without the $\tilde{\mathbf{E}}_n$ correction, the value of $\mathbf{E}_n$ might be far from the $\tilde{\mathbf{E}}_n$ solution of the state equation. Mathematically, such a discrepancy can be produced by the convergency of the algorithm into a local minimum of the cost function; physically, by the influence of the so-called non-radiating sources [143, 144], that is χE values such that $\mathcal{G}^\Gamma(\chi E) = 0$ whereas $\mathcal{G}^\Omega(\chi E) \neq 0$. Motivated by the same reasoning, a different way of taking into account $\tilde{\mathbf{E}}_n$ had already been introduced by Lambert *et al.* in [127], who once every I iterations used, instead of the MGM update rule, simply $\mathbf{E}_{n+1} = \tilde{\mathbf{E}}_n$. Nevertheless, this approach caused a jump in the value of $\mathcal{F}_{n+1}$ and needed an empirical value for I, whereas here a rather proper minimization is carried on.

It is also worth mentioning that the implementation (3.24) of the positivity constraint on χ, if recast into (3.13), undoubtedly increases the non-linearity of the problem. Yet, as compared to a harsh thresholding of the $\boldsymbol{\chi}_n$ values, it seems to be a safer solution from a numerical point of view.

Finally, notice that playing with the values of α_n and γ_n in (3.31) some of the previously mentioned methods can be obtained (see Tab. 3.1).

	Born	**Modified Born**	**Modified Gradient**
α_n	0	0	$\times$
γ_n	1	$\times$	0

TABLE 3.1: *Values of α_n and γ_n parameters transforming the M^{2}GM into a Born, Modified Born, or Modified Gradient method. The symbol '$\times$' means that the parameter is left to be optimized.*

3.3.1 Multi-view multi-frequency inversion

The M^{2}GM described so far applies to single-view single-frequency data. When many sources and/or many frequencies are available, they increase the information content, or available information, of the data. Thus, it is of crucial importance to add them to the inversion machinery. Concerning frequencies (but the same approach could in principle be applied for sources), the so-called frequency-hopping approach has been succesfully applied in many cases [141, 145–147]. It consists in starting from inverting monochromatic data at the lower frequency, that is, where the problem is less non-linear, then in using the result as initial estimate for the successive frequency, and so on. Nonetheless, it is has been shown [147] that incorporating all the data into a unique cost function results into a scheme more robust to noise. This cost function can be written as

$$\begin{aligned}\mathcal{F}(\chi_p; E_{j,p}) = w^{\Gamma} \sum_{p=1}^{P} \sum_{j=1}^{J} \| E_{j,p}^{\mathrm{s;meas}} - \mathbf{G}_p^{\Gamma} \chi_p E_{j,p} \|_{\Gamma}^2 + \\ w^{\Omega} \sum_{p=1}^{P} \sum_{j=1}^{J} \| E_{j,p} - E_{j,p}^{\mathrm{i}} - \mathbf{G}_p^{\Omega} \chi_p E_{j,p} \|_{\Omega}^2 \ ,\end{aligned} \tag{3.34}$$

whose weights are

$$w^{\Gamma} = \left(\sum_{p=1}^{P} \sum_{j=1}^{J} \| E_{j,p}^{\mathrm{s;meas}} \|_{\Gamma}^2 \right)^{-1} \quad \text{and} \quad w^{\Omega} = \left(\sum_{p=1}^{P} \sum_{j=1}^{J} \| E_{j,p}^{\mathrm{i}} \|_{\Omega}^2 \right)^{-1} \ . \tag{3.35}$$

The j index stands for the sources and p for the frequencies.

Notice that as the number of unknowns describing the contrast, namely $\boldsymbol{\xi}_n$ and $\boldsymbol{\eta}_n$ is unchanged, the number of auxiliary variables $\mathbf{E}_{n;j,p}$ is multiplied by JP. Indeed, there is now one total field per source and per frequency. As a consequence, there are also JP steps

α_n and γ_n. Finally, keeping this into account, the expressions of the gradients are

$$\mathbf{g}^{\xi} \triangleq \nabla_{\xi}\mathcal{F} = -4\xi \left\{ w^{\Gamma} \sum_{j,p} \Re\left[\left(\mathbf{G}_p^{\Gamma} E_{j,p}\right)^H e_{j,p}^{\Gamma} \right] + w^{\Omega} \sum_{j,p} \Re\left[\left(\mathbf{G}_p^{\Omega} E_{j,p}\right)^H e_{j,p}^{\Omega} \right] \right\} \tag{3.36}$$

$$\begin{aligned} \mathbf{g}^{\eta} \triangleq \nabla_{\eta}\mathcal{F} = 4\frac{\eta}{\varepsilon_0} \Bigg\{ & w^{\Gamma} \sum_{j,p} \Im\left[\left(\frac{1}{\omega} \mathbf{G}_p^{\Gamma} E_{j,p} \right)^H e_{j,p}^{\Gamma} \right] + \\ & + w^{\Omega} \sum_{j,p} \Im\left[\left(\frac{1}{\omega} \mathbf{G}_p^{\Omega} E_{j,p} \right)^H e_{j,p}^{\Omega} \right] \Bigg\} \end{aligned} \tag{3.37}$$

$$\mathbf{g}_{j,p}^{E} \triangleq \nabla_{E_{j,p}^*}\mathcal{F} = -w^{\Gamma} \left(\mathbf{G}_p^{\Gamma}\chi_p\right)^H e_{j,p}^{\Gamma} + w^{\Omega} \left(I - \mathbf{G}_p^{\Omega}\chi_p\right)^H e_{j,p}^{\Omega} \ , \tag{3.38}$$

where the iteration dependency has been omitted for conciseness of the notations. Concerning the latter, the definition of gradient of a complex variable has been adopted [148, 149]. This consists in evaluating the partial derivative of $\mathcal{F}$ with respect to E^* while considering E and E^* as independent variables.

The role played by the terms of $\mathcal{F}$ at different frequencies deserves more consideration. As anticipated, as the frequency grows the non-linearity of the inverse problem increases. Inversely, the obtainable resolution is better at higher frequencies. Therefore, it is advised to penalize higher frequencies with respect to the lower ones, but not too much in order not to waste the fine resolution given by them [122]. Dubois *et al.* have shown [146] that dividing each term of each sum in (3.34) by $1/\omega^2$ is an effective strategy to improve the results. In practice, this is accomplished by symply modifying the incident and measured scattered fields, before the iterative procedure starts, as follows:

$$\begin{aligned} E_{j,p}^{\mathrm{i}} &\leftarrow E_{j,p}^{\mathrm{i}}/\omega \\ E_{j,p}^{\mathrm{s;meas}} &\leftarrow E_{j,p}^{\mathrm{s;meas}}/\omega \ . \end{aligned} \tag{3.39}$$

3.3.2 Line search and stop criterion

At each iteration n of the CG scheme just described, the following $(2JP+2)$-element vector comprising all the steps can be constructed:

$$\mathbf{s}_n \triangleq \left[\beta_n^{\xi} \quad \beta_n^{\eta} \quad \alpha_{n;1,1} \ldots \alpha_{n;1,P} \ldots \alpha_{n;J,P} \quad \gamma_{n;1,1} \ldots \gamma_{n;1,P} \ldots \gamma_{n;J,P} \right]^T \ . \tag{3.40}$$

The value of $\mathbf{s}_n$ that minimizes $\mathcal{F}_{n+1}$ must then be determined. This minimization procedure is called *line search*. Differently from classical CG schemes, the line search is here multi-dimensional, since $2JP+2$ steps are actually sought instead of a single one.

In order to recast this problem into a classical scalar line search problem, a nested CG is applied on the steps vector. The update rule for the steps is then

$$\mathbf{s}_{n;k+1} = \mathbf{s}_{n;k} + \lambda_k \mathbf{d}_{k+1}^{s} \ , \tag{3.41}$$

where k indicates the iterations of such nested CG routine, and $\mathbf{d}_{k+1}^{s}$ is the Polak-Ribiére CG descent direction with respect to $\mathbf{s}$. The resulting scalar line search consisting in

finding the λ_k that minimizes $\mathcal{F}(\mathbf{s}_{n;k+1})$ is implemented through the derivative-based Brent's method [150].

stopped at the simultaneous fulfillment of Wolfe's conditions [151] (see §D for a description of these conditions).

As for the line search stop conditions, the nested CG uses Wolfe's conditions [151] (see §D for a description). For the main CG, multi-dimensional Wolfe's conditions should be derived given the fact that different steps - the elements of $\mathbf{s}_n$ - for the different variables of the problem - $\boldsymbol{\xi}_n$, $\boldsymbol{\eta}_n$, and $\mathbf{E}_n$ - exist. Nevertheless, as underlined in §D, this would require the computation of additional gradients of $\mathcal{F}$ with respect to each variable. It is then preferred to use a user-defined precision-based stop condition[2], since, because of the additional computation, no appreciable gain in execution time would be obtained by using Wolfe's conditions.

The flow of the minimization procedure might be schematized as follows.

- ▶ Method: $\underline{\text{CG}_1}$
  - Update rules:
$$\begin{cases} \boldsymbol{\xi}_{n+1} = \boldsymbol{\xi}_n + \beta^{\xi}_n \mathbf{d}^{\xi}_{n+1} \\ \boldsymbol{\eta}_{n+1} = \boldsymbol{\eta}_n + \beta^{\eta}_n \mathbf{d}^{\eta}_{n+1} \\ \mathbf{E}_{n+1;j,p} = \mathbf{E}_{n;j,p} \begin{array}{l} + \alpha_{n;j,p} \mathbf{d}^{E}_{n+1;j,p} \\ + \gamma_{n;j,p} \left(\tilde{\mathbf{E}}_{n;j,p} - \mathbf{E}_{n;j,p} \right) \end{array} \end{cases} \qquad j = 1 \dots J,\ p = 1 \dots P$$
  - Line search (multi-dimensional)
    - Step: $\mathbf{s}_n \triangleq \left[\beta^{\xi}_n \ \beta^{\eta}_n \ \{\alpha_{n;j,p}\} \ \{\gamma_{n;j,p}\} \right]^T$
    - Stop condition: user-defined precision
    - Method: $\underline{\text{CG}_2}$
      - Update rule: $\mathbf{s}_{n;k+1} = \mathbf{s}_{n;k} + \lambda_k \mathbf{d}^{s}_{k+1}$
      - Line search (scalar)
        - Step: λ_k
        - Stop condition: Wolfe's conditions
        - Method: derivative-based Brent's

This implementation strategy differs profoundly from the one commonly used for CSI (see for instance [132]). In effect, while in CSI alternate CG iterations are performed on the auxiliary variables (χE) first, and on the unknowns (χ) then, a unique CG on both the auxiliary variables and unknowns is applied here. As a consequence, while scalar line

[2]The condition is the following:
$$\frac{|\mathcal{F}_{n+1} - \mathcal{F}_n|}{|\mathcal{F}_{n+1}| + |\mathcal{F}_n| + \varepsilon} \leq \texttt{tol} \ ,$$
where `tol` is a precision set be the user. Empirically, it has been found that the value `tol`$= 10^{-4}$ gives a good trade-off between precision of the solution and execution time.

searches are needed in CSI at each alternate iteration, a nested CG is needed here. For interesting comments on the minimization procedure, see [152].

3.3.3 Initial estimate

In any iterative method used to solve an inverse problem (whether it be linear or not), an initial estimate of the unknown(s) is needed to trigger the inversion procedure. In the case of the inverse scattering problem, the quantity $\boldsymbol{\chi}_0$ is sought.

Back-propagation is a method very often used in the inverse scattering community to rapidly provide a "good-enough" initial estimate [12, 126, 128, 153]. The basic idea consists in inverting the data equation for the contrast-source χE using the adjoint operator of $\mathbf{G}^\Gamma$. Physically, this is equivalent to back-propagating $E^{\mathrm{s;meas}}$ within Ω. The whole algorithm can be resumed as follows.

1. For each frequency and source antenna, retrieve the contrast-source as

$$\Phi_{j,p} \triangleq \chi_p E_{j,p} = \kappa_{j,p} \left(\mathbf{G}_p^\Gamma\right)^H E_{j,p}^{\mathrm{s;meas}} \qquad \forall j,p \ , \tag{3.42}$$

   where $\kappa_{j,p}$ is the minimizer of the error

$$\| E_{j,p}^{\mathrm{s;meas}} - \mathbf{G}_p^\Gamma \Phi_{j,p} \|_\Gamma^2 \ , \tag{3.43}$$

   which gives

$$\kappa_{j,p} = \frac{\| \left(\mathbf{G}_p^\Gamma\right)^H E_{j,p}^{\mathrm{s;meas}} \|_\Omega^2}{\| \mathbf{G}_p^\Gamma \left(\mathbf{G}_p^\Gamma\right)^H E_{j,p}^{\mathrm{s;meas}} \|_\Gamma^2} \ . \tag{3.44}$$

   Notice that in the original formulation [126], one coefficient κ_j per frequency is retrieved by minimizing the data equation error (3.43) summed over all the sources. It is not clear which between this solution and the one adopted here gives better results. At any rate, they give definitely comparable results for all the configurations studied in this manuscript.
2. Find the total field from the state equation

$$E_{j,p} = E_{j,p}^{\mathrm{i}} + k_0^2 \mathbf{G}_p^\Omega \Phi_{j,p} \ . \tag{3.45}$$

3. Since, using (3.24), it holds that

$$\begin{cases} W_{j,p}^R \triangleq \Re\left(\Phi_{j,p} E_{j,p}^*\right) = \left(1 + \xi^2 - \varepsilon_{r;\mathrm{b}}\right) |E_{j,p}|^2 \\ W_{j,p}^I \triangleq \Im\left(\Phi_{j,p} E_{j,p}^*\right) = -\dfrac{\eta^2 - \sigma_{\mathrm{b}}}{\omega_p \varepsilon_0} |E_{j,p}|^2 \end{cases} , \tag{3.46}$$

the unknowns ξ_0 and η_0 can be found by minimizing the following cost functions

$$\begin{cases} \mathcal{F}_\xi = \displaystyle\sum_{j,p} \left[\frac{W^R_{j,p} - (1+\xi^2-\varepsilon_{r;\mathrm{b}})\,|E_{j,p}|^2}{\sqrt{1+\xi^2-\varepsilon_{r;\mathrm{b}}}\,|E_{j,p}|} \right]^2 \\ \mathcal{F}_\eta = \displaystyle\sum_{j,p} \left[\frac{W^I_{j,p} + \dfrac{\eta^2-\sigma_\mathrm{b}}{\omega_p\varepsilon_0}|E_{j,p}|^2}{\sqrt{\dfrac{\eta^2-\sigma_\mathrm{b}}{\omega_p\varepsilon_0}}\,|E_{j,p}|} \right]^2 \end{cases}, \tag{3.47}$$

which can be done analytically and gives

$$\begin{cases} \xi_0^2 = \sqrt{\dfrac{\displaystyle\sum_{j,p}\frac{(W^R_{j,p})^2}{|E_{j,p}|^2}}{\displaystyle\sum_{j,p}|E_{j,p}|^2}} - 1 + \varepsilon_{r;\mathrm{b}} \\ \eta_0^2 = \sqrt{\dfrac{\displaystyle\sum_{j,p}\frac{\omega_p\varepsilon_0(W^I_{j,p})^2}{|E_{j,p}|^2}}{\displaystyle\sum_{j,p}\frac{|E_{j,p}|^2}{\omega_p\varepsilon_0}}} + \sigma_\mathrm{b} \end{cases}. \tag{3.48}$$

Notice the expression of the denominator of the cost functions in (3.47). In fact, at least two other choices are possible: no denominator at all, or the square of the one used in (3.47) (giving dimensionless $\mathcal{F}_\xi$ and $\mathcal{F}_\eta$). In both cases, though, the ξ_0^2 and η_0^2 values found after minimization can take negative values, whereas this is not the case in (3.48) due to the presence of squared-only quantities under the square root sign (and retaining the positive solution of the square root). So, to cope with the positivity constraint of the contrast χ, the only acceptable solution is the one in (3.47).

The approach in (3.42) reminds of the Phase Conjugation/Time Reversal methods described in §2.3, since by back-propagation it is meant here the propagation of $E^{\mathrm{s;meas}}$ back in space through the use of the phase-conjugated far-field Green function. This is exactly the conjugated of a Phase Conjugation or DORT time-harmonic field chart (*cf.* for instance Fig. 2.15(e) or Fig. 2.22(c))! Based on this, some features of the back-propagation method can be foreseen. In particular, in the case of a small line, all the energy scattered by the target is, when backpropagated, smeared over a large region, very poorly resolved in down-range and $2\lambda_0 F/D$ wide in cross-range (D is the array width and f the array-target distance). Then, while the integral of all this energy equals the one received by the array, that actually covering the support of the target is very small, hence low Φ values within Ω when applying (3.42) are to be expected. As a consequence, the small-scattering assumption of the Born approximation holds, so that $E \approx E^\mathrm{i}$ in (3.45), and, as a further consequence, ε_r and σ take low values typical of the Born approximation. This will be often shown in the experimental results section (§3.6.4), and differs considerably from the very

nice initial estimates retrieved in the case of complete or almost-complete configurations ([6, 7, 126] just to mention a few).

As a final note, it is worth mentioning that other linear methods exist for inverting the data equation and rapidly obtaining an initial estimate for the iterative inversion algorithm. For instance, recalling the compactness of the far-field operator, its truncated SVD could be employed for evaluating its pseudo-inverse $\left(\mathbf{G}^{\Gamma}\right)^{+}$, so that

$$\Phi_{j,p} = \left(\mathbf{G}_p^{\Gamma}\right)^{+} E_{j,p}^{\text{s;meas}} \ . \tag{3.49}$$

This approach is for instance at the heart of the so-called Subspace-based Optimization Method (SOM) [154–156], where, as for any truncated SVD-based procedure, the choice of the best truncation order is difficult yet of crucial importance. Nonetheless, despite its increased complexity with respect to back-propagation, the results obtained with the truncated-SVD are impressively similar to those issued from the back-propagation method, at least for the configurations tested in this manuscript.

3.4 Available information and Ewald's circle

A fundamental question concerning inverse scattering problems is related to the maximum amount of information that is contained in the data and that it is therefore possible to extract. Then, whether this information is actually extracted or not, depends on the choice of the inversion algorithm and is not of concern in this section.

Bucci and co-authors have long worked on this subject. Some of the conclusions are profoundly related to the principle of band-limitedness of the scattered field that is behind the drift correction algorithm described in detail in §1.6.3. First of all, it has been mentioned that the far-field operator $\mathcal{G}^{\Gamma}$ is a compact operator, that is, it has M non-null singular values and the remaining ones equal to 0. The value of M is linked to the effective bandwidth of the reduced scattered field (see §1.6.3), $k_0 a_c$, where a_c is the radius of the smallest circle containing the support of the scatterer [63]. In practice, $M \approx 2k_0 a_c$ for 2D problems ($(k_0 a_c)^2$ in 3D) [1]. Consequently [112],

$$E^{\text{s;meas}} = \mathcal{G}^{\Gamma}(\chi E) \approx \sum_{n=1}^{M} \lambda_n u_n v_n^*(\chi E) \ , \tag{3.50}$$

where u_n and v_n are the left and right singular functions, respectively, and the operatorial notation $v_n^*(\chi E)$ means

$$v_n^*(\chi E) = \int_{\Omega} v_n^*(\vec{r'}) \chi(\vec{r'}) E(\vec{r'}) d\vec{r'} \ . \tag{3.51}$$

Exploiting the orthogonality of left (u_n) and right (v_n) singular functions, this equation can be inverted, giving

$$\chi E \approx \sum_{n=1}^{M} \lambda_n^{-1} v_n u_n^*(E^{\text{s;meas}}) \triangleq \sum_{n=1}^{M} (\chi E)_n \ , \tag{3.52}$$

where

$$u_n^*(E^{\mathrm{s;meas}}) = \int_\Gamma u_n^*(\vec{r}) E^{\mathrm{s;meas}}(\vec{r}) d\vec{r} \; . \tag{3.53}$$

This result shows that the contrast-source, and so the contrast, can be represented, within any specified accuracy, through the linear combination of M sub-components $(\chi E)_n$. In this sense, a representation of the unknowns as the one in (3.17) matches well with the limited-amount-of-retrievable-information point of view. In fact, it represents an implicit regularization of the inverse problem. Notice, though, that the same concepts do not hold for the auxiliary variables, since they are physically determined by a different equation - the state equation - whose operator, $\mathcal{G}^\Omega$, is not compact. Notice also that the present derivation has been carried on in a single-view case. Adding views and frequencies helps in increasing the number M of retrievable parameters, as long as the corresponding scattered fields are sufficiently decorrelated from each other.

A totally different approach to have a grasp of the concept of retrievable information is given by the so-called *Ewald's circle* (sphere in 3D) theory. The framework is the diffraction tomography one, where the plane wave approximation is used for the incident field, that is,

$$E^{\mathrm{i}} \approx e^{-i\vec{k}^{\mathrm{i}} \cdot \vec{r}} \; , \tag{3.54}$$

and the Born approximation is applied, that is, the total field within the support $\mathcal{D}$ of the scatterer is well approximated by the incident field:

$$E(\vec{r}) \approx E^{\mathrm{i}}(\vec{r}) \quad \forall \vec{r} \in \mathcal{D} \; . \tag{3.55}$$

Under these approximations, it is easy to see that the spatial Fourier Transform of the state equation gives

$$\hat{E}^{\mathrm{s}}(\vec{k}^{\mathrm{s}}) \approx k_0^2 \, \hat{\mathcal{G}}^\Gamma(\vec{k}^{\mathrm{s}}) \, \hat{\chi}(\vec{k}^{\mathrm{s}} - \vec{k}^{\mathrm{i}}) \; , \tag{3.56}$$

where $\vec{k}^{\mathrm{s}}$ is the wavenumber associated to the scattered wave, and the $\hat{}$ symbol indicates the spatial Fourier transform. Eq. (3.56) states that among all the wavenumbers, or spatial frequencies, that describe the contrast, only those equal to $\vec{k}^{\mathrm{s}} - \vec{k}^{\mathrm{i}}$ are available in the measured scattered field and can therefore be retrieved.

A graphic schematization is given in Fig. 3.2. In Fig. 3.2(a), for a reflection configuration with a theoretical receiving array aperture angle of 90 deg, the measured wavenumbers lie in the outer half of a circle in the $\vec{k} = \vec{k}^{\mathrm{s}} - \vec{k}^{\mathrm{i}}$ plane. Although not shown, for the case of a transmission configuration with the same incident field it is rather the inner half of the circle to be sampled. The meaning of this is that the reflection configuration gives access to higher spatial frequencies (outer half-circle) in the down-range direction y, that is, finer details of the target can be retrieved. As a conterpart, the convergence of the inversion algorithm to the appropriate minimum of the cost function might be more difficult, since as already stated higher frequencies - both spatial and temporal - enhance the non-linearity of the inverse problem.

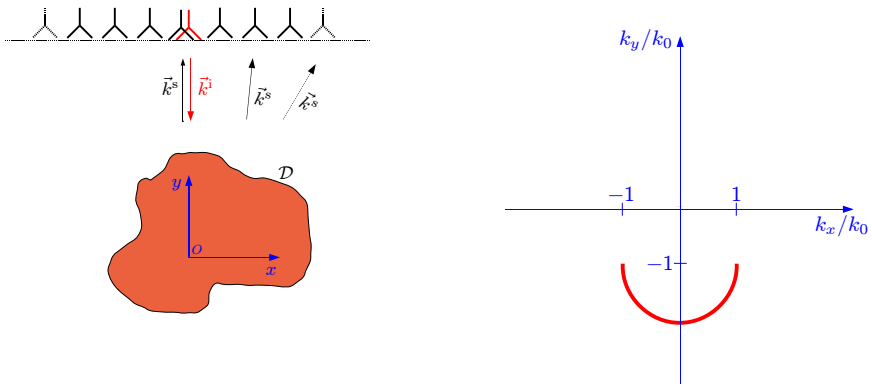

(a) Reflection configuration

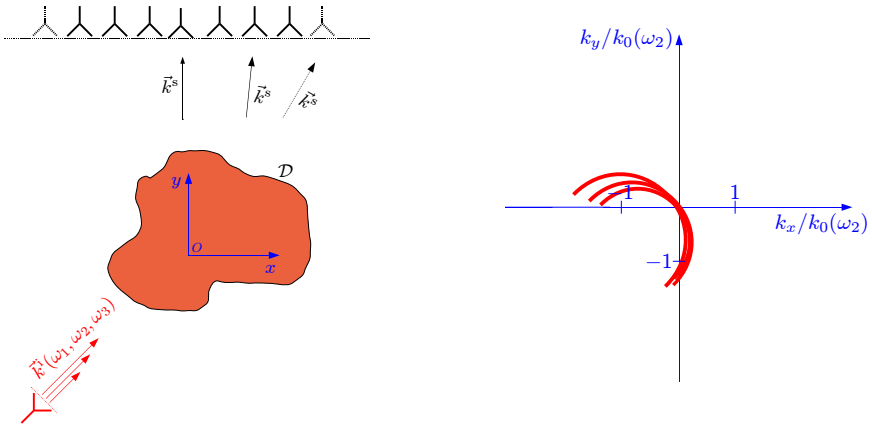

(b) Transmission configuration + multi-frequency

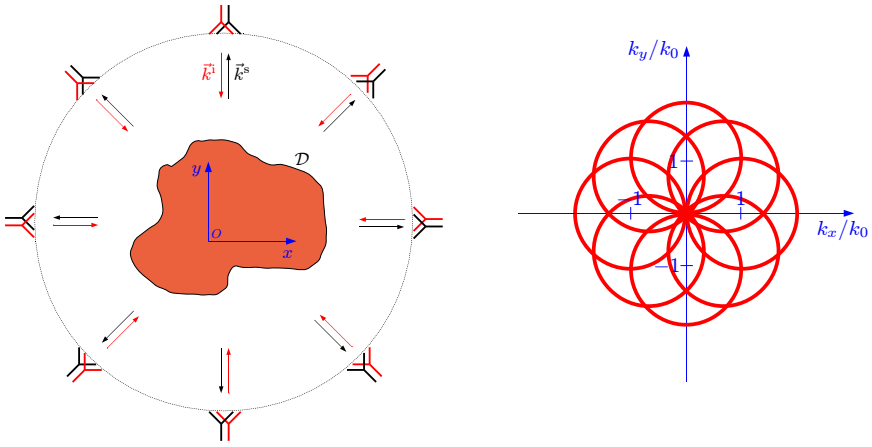

(c) Complete configuration

Figure 3.2: *Ewald's circle representation. (left) Measurement setups and (right) corresponding sampled wavenumbers in the spatial Fourier domain.*

In Fig. 3.2(b), for a transmission configuration, the effect of a different direction of the incident wave results in a rotation around the origin of the center of the half-circle. Furthermore, exploiting multiple frequencies leads to multiple half-circles, each with a displaced center and different radius. This shows why the available information increases when using multi-frequency data. Finally, for a monochromatic wave, the sampling of the Fourier plane

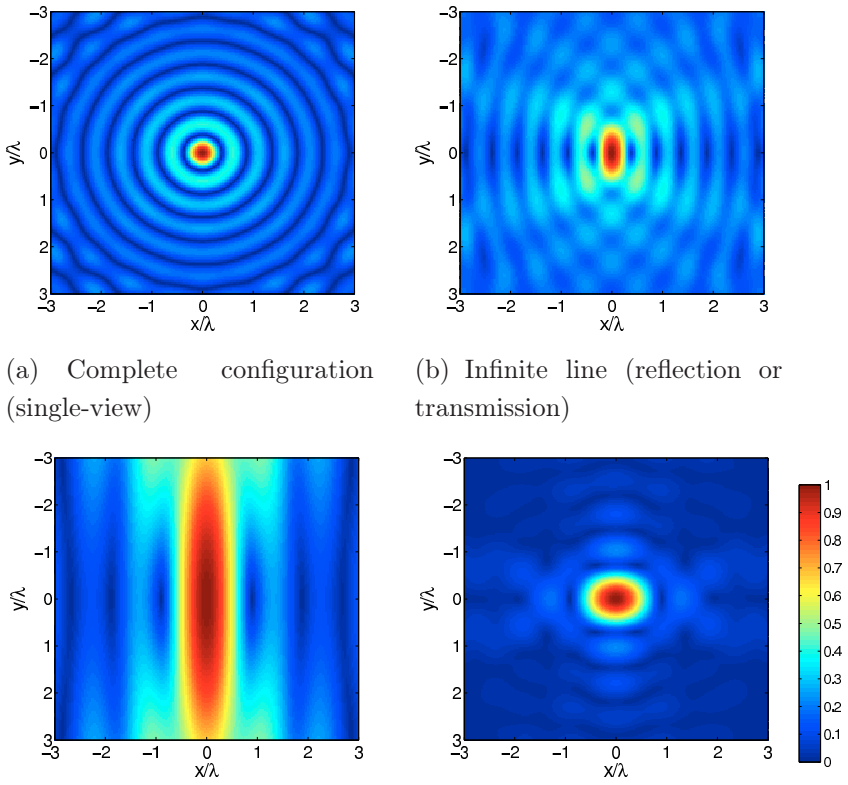

(a) Complete configuration (single-view)

(b) Infinite line (reflection or transmission)

(c) Small line (reflection or transmission)

(d) Small line, multi-frequency (reflection or transmission)

FIGURE 3.3: *Resolution patterns issued from the Ewald's circle formalism. All the configurations are single view, and the amplitude scale is linear. x and y axes are normalized with respect to the wavelength (in (d) it is the one corresponding to the central frequency, λ_c).*

in a multi-view multi-static configuration is shown in FIG. 3.2(c). A dense sampling of the plane can be appreciated, resulting in a large quantity of available information.

The same analysis casts light on the theoretical achievable resolution of an inverse scattering system. In line with the definition of resolution, consider a point target placed at the origin of a coordinate system. Then, $\chi(\vec{r}) = \delta(\vec{r})$ and $\hat{\chi}(\vec{k}) = 1$, that is, the spatial support of the scatterer is infinite over the $\vec{k}$ plane. Nonetheless, only those frequencies satisfying $\vec{k} = \vec{k}^{\mathrm{s}} - \vec{k}^{\mathrm{i}}$ can be measured according to (3.56), that is, the measured $\hat{\chi}$ is $\hat{\chi}^{\mathrm{meas}} = \delta[\vec{k} - (\vec{k}^{\mathrm{s}} - \vec{k}^{\mathrm{i}})]$. Its IFT, $\mathcal{F}^{-1}[\hat{\chi}^{\mathrm{meas}}](\vec{r})$, gives then the image of the target as it is "seen" by the system, that is, it gives the resolution pattern shown in FIG. 3.3 for four different geometric configurations (the amplitude scale is linear).

FIG. 3.3(a) The first subfigure is for the single-view complete configuration, which corresponds in the Fourier plane to only one circle among those in FIG. 3.2(c). The resolution along x and y is the same, and the half-width (along either axis) of the resolution spot is $\lambda/2.6$, where 2.6 is the first zero of $J_0(x)$ divided by 2π (for a 3D configuration the spot size would have been $\lambda/2$).

Fig. 3.3(b) If an infinitely long line is considered with a single incidence (as in Fig. 3.2(a)) either in reflection or in transmission, the resolution pattern becomes asymetric. While the cross-range (y) resolution is barely changed, the down-range profile (x) is strongly degraded.

Fig. 3.3(c) The array aperture angle is reduced to ± 30 deg, a small line is thus considered. The loss in resolution is dramatic in down-range.

Fig. 3.3(d) For the same small array, a frequency bandwdith of an octave is considered (*cf.* Fig. 3.2(b)). As expected, the down-range resolution is improved, and it indeed equals the theoretical value $c_0/2f_{\text{bw}}$ (in this case it was $f_{\text{bw}} = 2$ GHz as in all the experiments of this manuscript).

As mentioned, the achievable resolution patterns shown in Fig. 3.3 hold under the Born and incident wave approximations. The first one is particularly important. In fact, it is a single-scattering approximation, so that it holds for small and/or low-valued-χ scatterers. If this is not the case, multiple scattering taking place either within the scatterer itself - expressed mathematically by the convolution product in the state equation - or among separated scatterers allows in principle to retrieve finer details than those in Fig. 3.3. This is why a rigourous method such as the M^{2}GM has been chosen instead of one of the linearized methods: despite its complexity, it can in principle retrieve such finer details of the imaged scatterers.

3.5 Experimental inversion: the calibration issue

From the state equation (3.9), the incident field $E^{\text{i}}|_\Omega$, that is, inside the investigation domain Ω, is considered as a known quantity within the inverse problem. In fact, it is an absolute incident field that is required, not a normalized one as for detection methods, which are indeed qualitative methods and do not try to match an absolute scattered field to the result of a model. Hence, since it is impossible to measure E^{i} everywhere within Ω, at least in a non-destructive way, it must be extrapolated from a model and, if available, from suitable experimental data. In this sense, the procedure consisting in matching the true E^{i} with the one issued from a model is known in the inverse scattering community as *incident field calibration*.

An analytical model for the incident field was already developed in §1.7.2. The co-polarization component of the electric field was modeled through a multipolar expansion whose coefficients were retrieved from measurements performed in addition to the scattering experiment. Nevertheless, while the *sources* (antennas) radiate a 3D, or spherical, field ($1/r$ dependency instead of the $1/\sqrt{r}$ dependency of a wire antenna), the *targets* may be considered as two-dimensional since their direction of invariance is parallel to the co-polarization axis of the antennas. Hence, the scattered field has a cylindrical front, that is, it has a 2D nature. According to the definition often encountered in literature, this is known as a 2.5D configuration.

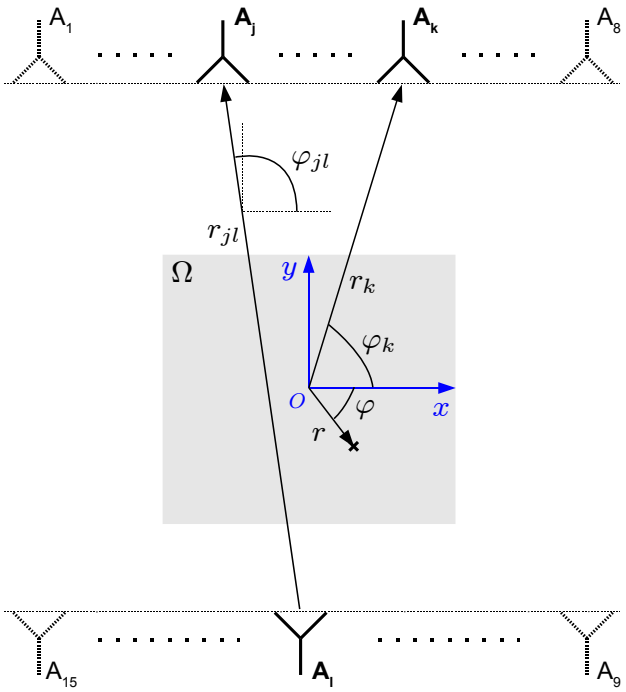

FIGURE 3.4: *Configuration for the incident field and Green function modeling.*

Of course, because of the requirement on the absolute knowledge of $E^{\mathrm{i}}|_{\Omega}$, this has to be properly accounted for in the inversion process. Two possible solutions exist: developing a 2.5D code, which would include the dependency of the electric field on the vertical (z) axis, or adapting the incident field model to a 2D frame. Since a 2D code was available, and the development of a 2.5D one would have been (at least!) time-consuming, the second option has been retained. A similar choice has been made, for instance, in [10].

3.5.1 2D incident field and Green function models

The modeling procedure is applied separately at each frequency within the used band. For conciseness, the ω dependency is omitted here. Considering the k^{th} antenna as source, the 2D incident field is modeled as

$$E_k^{\mathrm{i}} = \sum_{m=-M}^{M} \gamma_m^{\mathrm{tx}} H_n^-(k_0|\vec{r}-\vec{r}_k|)e^{-im(\varphi-\varphi_k)} \ , \tag{3.57}$$

where the geometric quantities are shown in FIG. 3.4, H_n^- is the Hankel function of second kind and n^{th} order, and $\{\gamma_m^{\mathrm{tx}}\}_{m=-M\ldots M}$ are the coefficients to be determined.

Similarly, the far-field Green function $\mathcal{G}^{\Gamma}$ has to somehow model the radiation pattern of the *receiving* antennas. Then, for the j^{th} receiving antenna,

$$\mathcal{G}_j^{\Gamma} = \sum_{m=-M}^{M} \gamma_m^{\mathrm{rx}} H_n^-(k_0|\vec{r}-\vec{r}_j|)e^{-im(\varphi-\varphi_j)} \ , \tag{3.58}$$

where different coefficients $\{\gamma_m^{\mathrm{rx}}\}_{m=-M\ldots M}$ need to be determined as explained next.

As in §1.7.2, the measurements from where the model coefficients must be extracted are the incident fields recorded from the array-1 antennas when either one or all the array-2 antennas transmit. The generic measurement is indicated by S_{jl}^{cal} (see FIG. 3.4), and it is worth recalling its expression from §1.7.2:

$$S_{jl}^{\text{cal}} = A\omega \frac{e^{-ik_0 r_{jl}}}{r_{jl}} l_{\text{e}}^2(r_{jl}, \varphi_{jl}) \ , \tag{3.59}$$

where A is a constant. Here, $\omega e^{-ik_0 r_{jl}} l_{\text{e}}(r_{jl}, \varphi_{jl})/r_{jl}$ represents the incident field radiated by A_l and impinging on A_j. The latter, in turn, applies its receiving pattern modeled by its effective length $l_{\text{e}}(r_{jl}, \varphi_{jl})$ and measures S_{jl}^{cal}. From (3.59), then, one value of $l_{\text{e}}(r_{jl}, \varphi_{jl})$ per measurement can be retrieved[3].

Now, these effective lengths must be related to the unknwown model coefficients γ_m^{tx} and γ_m^{rx}. Different procedures are followed for the incident field and the Green function.

Incident field

It must be first noticed that although (3.57) is a 2D model that suits a 2D inversion code, it is erroneous in the sense that the $1/\sqrt{r}$ dependency of the Hankel functions does not match the experimental $1/r$ dependency of the field. This is the consequence for having chosen a 2D code despite the 2.5D experimental configuration, and cannot be avoided. On the other hand, for relatively small investigation regions Ω, this amplitude error should be small enough to hardly impact the inversion results.

Nevertheless, it can be imposed that at the center of Ω, that is, at $\vec{r} = \vec{0}$, the measured and modeled incident fields are perfectly matched. To do so, the γ_m^{tx} are retrieved through the hybrid relation (*cf.* (1.37a))

$$\omega \frac{e^{-ik_0 r_{jl}}}{r_{jl}} l_{\text{e}}(r_{jl}, \varphi_{jl}) = \sum_{m=-M}^{M} \gamma_m^{\text{tx}} H_n^-(k_0 r_{jl}) e^{-in\varphi_{jl}} \ , \tag{3.60}$$

which results in $\gamma_m^{\text{tx}} \propto 1/\sqrt{r_{jl}}$. Then, a set of coefficients per transmitting antenna A_k are evaluated through

$$\gamma_m^{k;\text{tx}} \triangleq \gamma_m^{\text{tx}} \sqrt{\frac{\bar{r}_{jl}}{r_k}} \ , \tag{3.61}$$

where $\bar{r}_{jl}$ is the mean among all the r_{jl} distances in the incident field calibration setup. These coefficients replace the γ_m^{tx} in (3.57). As a result, $\gamma_m^{k;\text{tx}} \propto 1/\sqrt{r_k}$ which, combined with the $1/\sqrt{|\vec{r} - \vec{r}_k|}$ dependency of H_n^- in (3.57), gives the sought $1/r_k$ dependency at $\vec{r} = \vec{0}$.

[3]When taking the square root to obtain l_{e} particular attention must be paid to the correct definition of its phase. Indeed, since any complex number is defined up to a $e^{in2\pi}$ factor, then the l_{e} for different (j, l) pairs and/or at different frequencies may have $n\pi$ jumps between them resulting in wrong values. To avoid this, an unwrap (that is, a modulo 2π reduction) must be applied to the l_{e}^2 over (j, l) pairs and over frequencies before taking the square root.

Far-field Green function

The receiver coefficients are more simply given by

$$H_0^-(k_0 r_{jl}) l_\mathrm{e}(r_{jl}, \varphi_{jl}) = \sum_{m=-M}^{M} \gamma_m^\mathrm{rx} H_n^-(k_0 r_{jl}) e^{-in\varphi_{jl}} \ , \tag{3.62}$$

since as already stated the scattered field measured at the receivers truly is (at least as long as the scatterers can be considered infinitely long along z) a 2D field.

Finally, to retrieve the model coefficients from (3.60) and (3.62), the same approach detailed in §1.7.2 can be followed. Eq. (3.60) and (3.62) are first written in the matricial form

$$\mathbf{l}_\mathrm{e} = \mathbf{H}\boldsymbol{\gamma} \ , \tag{3.63}$$

where $\mathbf{l}_\mathrm{e}$ is the vector containing the left hand-side terms in (3.60) and (3.62) for all the measured (j, l) pairs, $\mathbf{H}$ is the matrix filled with the values of the expansion basis functions $H_n^-(k_0 r_{jl}) e^{-in\varphi_{jl}}$, and $\boldsymbol{\gamma}$ is the vector of the unknowns (γ_m^tx or γ_m^rx). Then, $\mathbf{H}$ is inverted through a truncated-SVD, so that the final result is

$$\boldsymbol{\gamma} = \mathbf{H}^+ \mathbf{l}_\mathrm{e} \ , \tag{3.64}$$

where $\mathbf{H}^+$ is the pseudo-inverse of $\mathbf{H}$. The maximum expansion order is set to $M = 1$ as explained in §1.7.2.

A final word about the originality of this approach is dued. In most experimental contributions, it is the monopolar approach that is preferred, leading to the determination of one single coefficient. This is sufficient when rather isotropic antennas are available [10], or in circular-scanner configurations where the azimuth angle φ varies of only a few degrees around the broadside direction [7, 11].

Less frequent is the adoption of a multipolar expansion of the fields. Yet, modeling the *receiving* antenna pattern in addition to the transmitting one has - at the best of our knowledge - never been reported in the inverse scattering community. In [70], for instance, a similar multipolar expansion is used to model the incident field, but $\mathcal{G}^\Gamma$ is not modified at all. Furthermore, the γ_m^tx are retrieved directly from the S_{jl}^cal in (3.59) without any square root. They are thus proportional to the square of l_e, and both the directivities of TX and RX antennas are modeled at the emission side through (3.57). As shown next in §3.6.2, this can generate important errors in the matching between measured and simulated scattered fields, with important repercussions on the inversion results. Finally, remark that the model is also valid in near-field conditions, since no far-field simplification has been applied.

3.5.1.1 Phase center correction

The model developed so far does not take into account the localization of the phase center of the antennas, which is defined as the center of the circle (sphere in 3D) that best

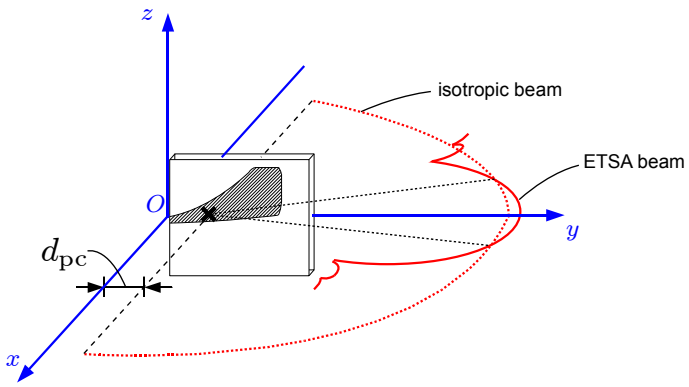

FIGURE 3.5: *Illustration of the definition of phase center in the case of an ETS antenna.*

approximates the main lobe of the antenna radiation pattern (see FIG. 3.5). Although its position can vary with frequency and/or polarization, the concept of phase center is in any case associated to cylindrical (spherical in 3D) wavefronts, which are exactly those modeled through the Hankel functions in (3.57) and (3.58). Hence, these expressions implicitly assume that the position $\vec{r}_k$ of the k^{th} antenna is taken with respect to its phase center, and not with respect to the antenna connector as assumed until now. The correction that must be applied and that is described next, then, is meant to achieve a better matching between actual and modeled antenna patterns.

It is relatively easy to retrieve the exact position of the phase center by simulation. This is for instance very useful to improve the design of an antenna, since in the case of an UWB antenna it is expected that the position of the phase center doest not vary much over frequency. On the other hand, how to directly measure the exact position of the phase center is a sort of open problem in literature. Yet, as for the radiation patterns, it is mandatory to characterize the phase center while the antennas are in their operational environment rather than in an anechoic chamber. Namely, the effect of coupling - in the case of an antenna array - might influence the phase center position.

Following this reasoning, two main assumptions on the location of the phase center are made:

- it is stable over the [2-4] GHz frequency band, which can be justified in virtue of the UWB behavior of the ETS antennas (SWR < 2 in the [2-18] GHz band);
- it is related to the traveling wave behavior of the ETS antennas propagation, and more specifically to the propagation of the RF signal within the duroid substrate.

According to this, it is guessed that the phase center is located, independently of the frequency, at the distance d_{pc} corresponding to the additional delay τ measured in §1.7.2.1 when two ETS antennas are put one in front of the other. Such distance, keeping into account the slower propagation through the duroid substrate, had been estimated to $d_{\text{pc}} = 3.36$ cm. Stated differently, since the time delay exists and is due to the propagation within the duroid substrate, one may assume that the signal has practically not started to radiate until having reached the distance corresponding to τ. Hence, the wavefronts will appear as

if they were centered at this "delayed" point, leading to identify $d_{\rm pc} = \tau c_0/\sqrt{2.2}$, where 2.2 is the permittivity of duroid. To validate this guess, an experimental verification is given in §3.6.2.

Whatever its value, to keep into account $d_{\rm pc}$ within the model, it is sufficient to proceed as if the antennas were shifted, with respect to the position of their connector, by $d_{\rm pc}$ along their axis. Then, with reference to FIG. 3.4,

$$\begin{cases} \vec{r}_k \leftarrow \vec{r}_k - d_{\rm pc}\hat{y} & \text{if } \mathrm{A}_k \in \text{array-1} \\ \vec{r}_k \leftarrow \vec{r}_k + d_{\rm pc}\hat{y} & \text{if } \mathrm{A}_k \in \text{array-2} \end{cases} , \tag{3.65}$$

where $\hat{y}$ is the unitary vector oriented along the y direction.

In order to show that this correction does not undermine the correctness of the model developed in the previous paragraph, consider (3.59). The measured $S_{jl}^{\rm cal}$ can better be written as

$$S_{jl}^{\rm cal} = A'\omega \frac{e^{-ik_0 r_{jl}}}{r_{jl}} b^2(d_{\rm pc}) e^{-2ik_{\rm drd} d_{\rm pc}} , \tag{3.66}$$

where A' is a constant also containing the directivity value at φ_{jl}, and r_{jl} must be calculated after the correction (3.65). This equation models the effect of the phase center position through an amplitude term, $b(d_{\rm pc})$, and a phase term, $e^{-ik_{\rm drd} d_{\rm pc}}$, where $k_{\rm drd}$ is the wavenumber associated to the duroid substrate, that is, $k_0\sqrt{2.2}$. Both terms are squared to keep into account the effect of both transmitting and receiving antennas. If the same equation (3.59) is used to retrieve the effective lengths, it is easy to see that

$$l_{\rm e}(r_{jl}, \varphi_{jl}) \propto b(d_{\rm pc}) e^{-ik_{\rm drd} d_{\rm pc}} , \tag{3.67}$$

which substituted in both (3.60) and (3.62) gives

$$\gamma_m^{\rm tx}, \gamma_m^{\rm rx} \propto b(d_{\rm pc}) e^{-ik_{\rm drd} d_{\rm pc}} . \tag{3.68}$$

Finally, according to (3.57) and (3.58), $E^{\rm i}$ and $\mathcal{G}^{\Gamma}$ also end up being proportional to the $b(d_{\rm pc})e^{-ik_{\rm drd} d_{\rm pc}}$ factor, which represents the correct correction. In addition, the retrieved radiation patterns are improved thanks to the proper handling of the phase center position.

3.5.1.2 Elevation radiation pattern correction

Utilizing a 2D code in spite of a 2.5D one leads to another systematic modeling error. In 2D, no dependency whatsoever on the elevation angle θ, or on the vertical direction z, is ever considered. As a consequence, the antennas are implicitly considered isotropic along θ, whereas they are not in reality - at least in the case of the ETS antennas.

To cope with this problem, a workaround has been implemented. Given the maximum height z_M of the targets[4], the idea consists in correcting both the TX and RX radiation patterns by a simple, scalar, factor given by the ratio of the integrals between $\pm z_M$ of the

[4]Basically, the height of the anechoic chamber.

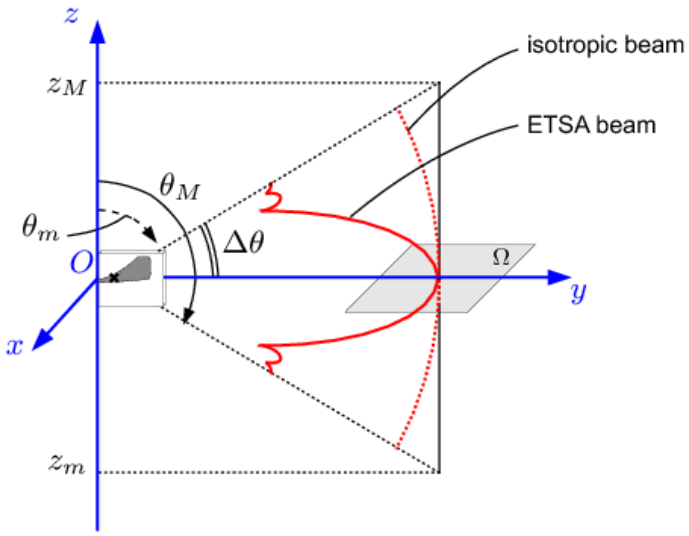

FIGURE 3.6: *Illustration of the elevation radiation pattern correction.*

fields radiated by an isotropic and an ETS antenna. In detail, with respect to FIG. 3.6, the following quantities are introduced:

$$\Delta\theta = \tan^{-1}\left(\frac{z_M}{r}\right) \quad \Rightarrow \quad \begin{pmatrix}\theta_M \\ \theta_m\end{pmatrix} = \frac{\pi}{2}\begin{pmatrix}+ \\ -\end{pmatrix}\Delta\theta,$$

where $\vec{r}$ describes the position over the xOy plane.

The procedure, which must be repeated at each frequency, is:

1. for each pixel in Ω, evaluate the integral of the isotropic field:

$$\hat{E}_{\text{iso}}(\vec{r}) = \int_{\theta_m}^{\theta_M} E_{\text{iso}}(\vec{r},\theta)d\theta = \frac{1}{\sqrt{r}}2\Delta\theta \ . \tag{3.69}$$

2. for each pixel in Ω, evaluate the integral of the directive field pertaining to the ETS antennas. For this purpose, the elevation radiation patterns characterized in the anechoic chamber of LEAT in Nice-Sophia Antipolis are used. Such radiation patterns are interpolated by an N-degree polynomial $p_N(\theta)$ in order to have the following closed form for the integration

$$\hat{E}_{\text{dir}}(\vec{r}) = \int_{\theta_m}^{\theta_M} E_{\text{dir}}(\vec{r},\theta)d\theta = \frac{1}{\sqrt{r}}\int_{\theta_m}^{\theta_M} p(\theta)d\theta = \frac{1}{\sqrt{r}}\sum_{n=0}^{N}\frac{a_n}{n+1}(\theta_M^{n+1}-\theta_m^{n+1}) \ , \tag{3.70}$$

   where $\{a_n\}_{n=0,\ldots,N}$ are the coefficients of $p_N(\theta)$.

3. for each pixel in Ω, the ratio of the two quantites gives the sought factor

$$f_{\text{dir}}(\vec{r}) \triangleq \frac{\hat{E}_{\text{dir}}(\vec{r})}{\hat{E}_{\text{iso}}(\vec{r})} \ . \tag{3.71}$$

4. for each pixel in Ω and for each trasnmitting antenna, correct the incident field

$$E^{\text{i}}(\vec{r}) \leftarrow E^{\text{i}}(\vec{r}) f_{\text{dir}}(\vec{r}) \ . \tag{3.72}$$

5. for each pixel in Ω and for each receiving antenna, correct the far-field Green function

$$G^{\Gamma}(\vec{r}) \leftarrow G^{\Gamma}(\vec{r}) f_{\mathrm{dir}}(\vec{r}) \ . \tag{3.73}$$

3.6 Experimental results

3.6.1 Data preparation

In this section, the experimental scattered field data, $E^{\mathrm{s;meas}}|_{\Gamma}$, are systematically compared against synthetic data. In virtue of the calibration procedure described previously, the former are simply given by the S parameters measured by the VNA (see §1.3). As for the synthetic data, they are obtained through the so-called *direct problem* consisting in solving for $E^{\mathrm{s}}|_{\Gamma}$ the system made of data and state equations given χ and $E^{\mathrm{i}}|_{\Omega}$. As already discussed, the incident field $E^{\mathrm{i}}|_{\Omega}$ relies on a given antenna model, so that for synthetic data a further distinction can be made:

- the antenna model is the simplest one: isotropic wire antennas. The resulting data, called $\tilde{E}^{\mathrm{s}}|_{\Gamma}$, are used in §3.6.4 as an ideal reference against which the experimental results are compared.
- the antenna model is the one used for the experimental data and described in §3.5.1. The resulting data are indicated by $E^{\mathrm{s}}|_{\Gamma}$ and are used in §3.6.2 to validate the calibration procedure.

In order to perform "fair" comparisons, the same signal processing operations must be applied to both experimental and synthetic data sets. Namely, the former undergo the signal processing operations described in §1.6: data is frequency windowed - or weighted - with a $W_{\omega}(\omega)$ function, then time-gated with a $w_t(t)$ signal. Frequency windowing is especially important. In §1.6, the choice of the *lanczos* window had been made to cope with the sidelobe attenuation needed to avoid the aliasing of the very first time instants of the signal onto the portion containing the scattered field.

When using the incident field data needed for calibration reasons (the S_{jl}^{cal} in (3.59)), the latter must as well be windowed with the same $W_{\omega}(\omega)$. By doing so, the weight "propagates" as in the following:

$$S_{jl}^{\mathrm{cal}} W_{\omega} \quad \Rightarrow \quad \gamma_m^{\mathrm{tx}}, \gamma_m^{\mathrm{rx}} \propto \sqrt{W_{\omega}} \quad \Rightarrow \quad E^{\mathrm{i}}, \mathcal{G}^{\Gamma} \propto \sqrt{W_{\omega}} \quad \Rightarrow \quad E \propto \sqrt{W_{\omega}} \quad \Rightarrow \quad E^{\mathrm{s}} \propto W_{\omega} \, ,$$

which in the end allows to compare the results from both $\tilde{E}^{\mathrm{s}}|_{\Gamma}$ and $E^{\mathrm{s}}|_{\Gamma}$ against the measured ones.

3.6.2 Direct problem: validation of the calibration procedure

In order to validate the antenna modeling procedure developed so far, the test case in Fig. 3.7 is studied. The scattered field $E^{s;meas}$ is measured in reflection for all the

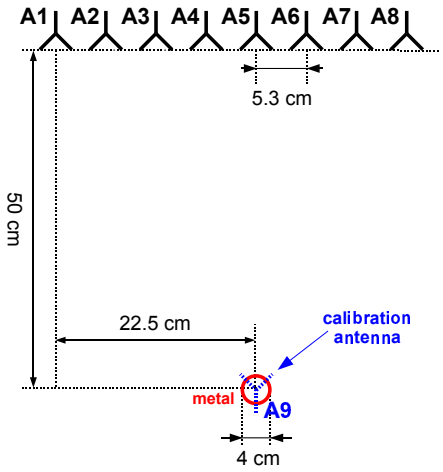

FIGURE 3.7: *Incident field modeling procedure. Setup of the experiment.*

sources and receivers. In addition, the $S_{j9}^{\text{cal}}|_{j=1,\dots,8}$ are measured in order to retrieve the effective lengths and the calibration coefficients $\gamma_m^{k;\text{tx}}$ and γ_m^{rx}. The calibration antenna A_9 is placed almost at the same location as the target (the target is of course removed during the calibration measurements). This is definitely favorable in terms of aperture angle $\Delta\varphi$, since the $\Delta\varphi$ of the calibration measurements almost corresponds to the one of the scattering experiment. As a result, there is no need for extrapolating the experimentally retrieved antenna patterns beyond the calibration aperture angle $\Delta\varphi$. Nonetheless, it must not be forgotten that placing the calibration antenna at the same location of the target is impossible in many applications, *e.g.* in non-destructive testing. In these cases, A_9 can only be placed farther from the array, resulting in a smaller $\Delta\varphi$ and in the need for an extrapolation.

The measured scattered fields $E^{\text{s;meas}}|_\Gamma$ are now compared to those retrieved by the solution of the direct problem, $E^{\text{s}}|_\Gamma$. They differ because of the following contributions:

- $E^{\text{s;meas}}|_\Gamma$ contains measurement noise, n, mainly related to the VNA (noise floor, thermal drift) and to the parasite reflections in the cables of the prototype;
- being extrapolated from noisy measurements - the S_{jl}^{cal} -, $E^{\text{s}}|_\Gamma$ contains itself a noise contribution, n_{cal};
- the modeling procedure introduces an error into $E^{\text{s}}|_\Gamma$, ϵ_{model}, namely because of the necessary truncation in the multipolar expansions (3.57) and (3.58);
- the antennas are in practice mismatched; yet, there is not any mismatch in $E^{\text{s}}|_\Gamma$, whose impact can be indicated with m and must not be considered as a noise contribution.

Thus:

$$\begin{cases} E^{\text{s;meas}}|_\Gamma = \tilde{E}^{\text{s}}|_\Gamma + n \\ E^{\text{s}}|_\Gamma = \tilde{E}^{\text{s}}|_\Gamma + \epsilon_{\text{model}} + n_{\text{cal}} + m \end{cases}, \tag{3.74}$$

where $\tilde{E}^{\text{s}}|_\Gamma$ is the ideal scattered field in absence of noise and *including* antenna mismatch.

A first comparison is carried out in FIG. 3.8 for the complete model described in §3.5.1: both the incident field and far-field green functions are modeled through the multipolar

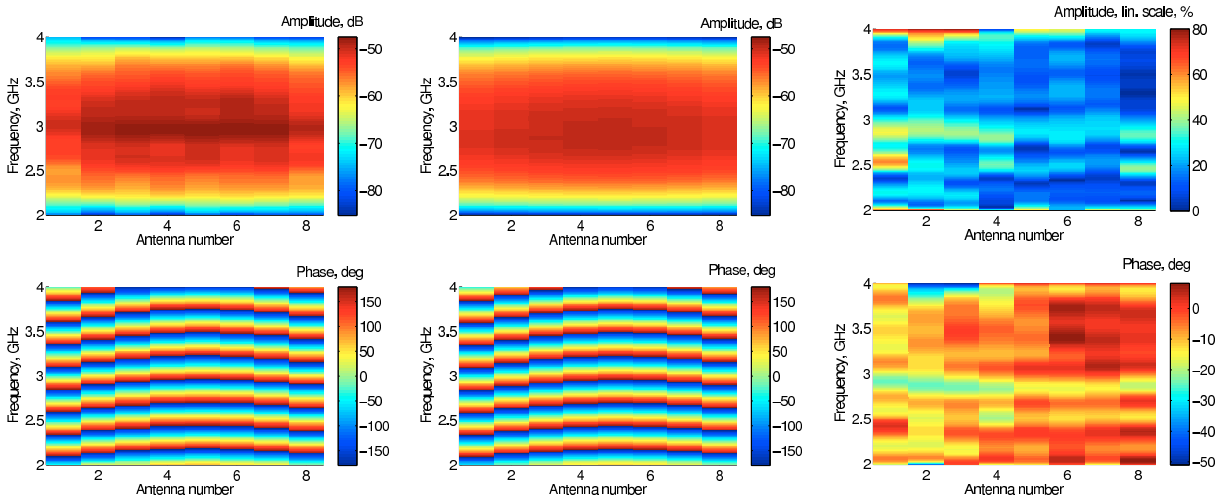

(a) Measurement (b) Model (with calibration) (c) Error

FIGURE 3.8: *Comparison of (a) the measured data $E^{\mathrm{s;meas}}|_\Gamma$ against (b) the synthetic data $E^{\mathrm{s}}|_\Gamma$ including the incident field and green function calibration model. The transmitting antenna is A_1. In (c), the errors defined in (3.75) are also shown (top, $\epsilon^A_{j,p}|_\Gamma$; bottom, $\epsilon^P_{j,p}|_\Gamma$). The overall error in (3.76) is $\epsilon = 23.7$ %*

expansion with $M = 1$, and both the phase center ($d_{\mathrm{pc}} = 3.36$ cm) and elevation corrections are applied. One antenna, A_1, is used as emitter, and the amplitude and phase of the scattered field is observed as a function of both receiving antenna and frequency. The measurement is shown in FIG. 3.8(a), whereas the simulation result is in FIG. 3.8(b). To quantify their difference, the following quantities are defined

$$\begin{cases} \epsilon^A_{j,p}|_\Gamma = \left| \dfrac{E^{\mathrm{s;meas}}_{j,p}|_\Gamma - E^{\mathrm{s}}_{j,p}|_\Gamma}{E^{\mathrm{s;meas}}_{j,p}|_\Gamma} \right| = \left| 1 - \dfrac{E^{\mathrm{s}}_{j,p}|_\Gamma}{E^{\mathrm{s;meas}}_{j,p}|_\Gamma} \right| \\ \epsilon^P_{j,p}|_\Gamma = \arg\left(\dfrac{E^{\mathrm{s}}_{j,p}|_\Gamma}{E^{\mathrm{s;meas}}_{j,p}|_\Gamma} \right) = \arg\left(E^{\mathrm{s}}_{j,p}|_\Gamma \right) - \arg\left(E^{\mathrm{s;meas}}_{j,p}|_\Gamma \right) \end{cases}, \tag{3.75}$$

where the first one is an overall indicator for each receiver, transmitter, and frequency, whereas the second one only observes the phase. They are both plotted in FIG. 3.8(c). In addition, an overall indicator comprising all sources, receivers, and frequencies can be classically defined as

$$\epsilon = \sqrt{\frac{\sum_{j,p} \| E^{\mathrm{s;meas}}_{j,p} - E^{\mathrm{s}}_{j,p} \|^2_\Gamma}{\sum_{j,p} \| E^{\mathrm{s;meas}}_{j,p} \|^2_\Gamma}} \,. \tag{3.76}$$

Noitce that these quantities, in virtue of (3.74), do not quantify only the error introduced by the antenna modeling strategy, but also include the contribution of experimental noise and antenna mismatch.

For FIG. 3.8(c), the matching between measurements and simulation is globally good. The phase error $\epsilon^P_{1,p}|_\Gamma$ is for most receivers and frequencies between ± 10 deg, whereas the overall error $\epsilon^A_{1,p}|_\Gamma$ stays below 20 %. It is on the edges of the frequency band and for $\mathrm{A}_j|_{j=1,2,3}$ that higher values are reached (*e.g.* $\epsilon^P_{1,4\ GHz}|_{j=2,3} \approx -50$ deg and $\epsilon^A_{1,4\ GHz}|_{j=1,2,3} \approx$

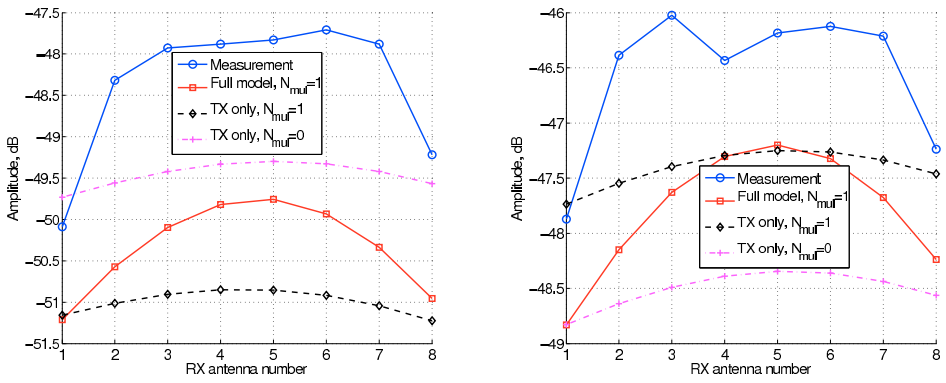

(a) TX antenna: A_1 (b) TX antenna: A_5

FIGURE 3.9: *Comparison of the amplitude of the measured data against the result of the direct problem for three different models at 3 GHz and for two different emitting antennas.*

80 %). The overall error (including all the sources) is $\epsilon = 23.7$ %. Notice also how the amplitude decrease at the frequency band edges due to the *lanczos* window is properly retrieved in the simulated field.

In order to investigate the effect of each "ingredient" of the model, two emitting antennas, A_1 and A_5, are first selected, and the frequency 3 GHz is selected. In FIG. 3.9 the corresponding amplitude patterns are shown in the case of: 1) measurement, 2) full model, 3) incident field model but no modification of $\mathcal{G}^{\Gamma}$, and 4) as in 3) but with the expansion order $M = 0$. Notice that 3) corresponds to the method proposed in [70], where the receiving antenna pattern is not modeled, whereas 4) results in an isotropic model, as the one used for instance in [146] where, due to the geometric configuration of the experiment (a circular vitual array), the antennas always worked practically at broadside. From this comparison the benefit of using a full model, including both the radiation and receiving antenna patterns through a multipolar expansion, is clear. Indeed, it is only with the full model that the dynamics of the amplitude (1.5 dB for A_1 and 2 dB for A_5) approaches that of the measurement, whereas for 3) and 4) the variation hardly reaches 0.5 dB. Confirming this, the overall errors are $\epsilon = 23.7$ %, 25.1 %, and 28.2 % for 2), 3), and 4), respectively.

Back to the full model, the 1 to 2 dB amplitude underestimation observed in FIG. 3.8(b) with respect to FIG. 3.8(a) (and also visible in FIG. 3.9) can be attributed to the systematic error due to directivity of the antennas in the elevation direction. The workaround described in §3.5.1.2 can indeed only partially recover such error, whereas only a full 2.5D code could eliminate it. In order to quantify the impact of the correction term f_{dir} in (3.71), its value is plotted in FIG. 3.10 for A_5 and at the target center. The variations are due to the frequency-dependency of the antenna directivity. In FIG. 3.9(b), the value at 3 GHz, $f_{\text{dir}} \approx -1.5$ dB is applied to the red, full-line curve. Without the correction, the latter would be shifted by around +3 dB (twice the f_{dir} value), giving now an overestimation by 1 to 2 dB ! While at other frequencies and for other antennas the correction actually improves

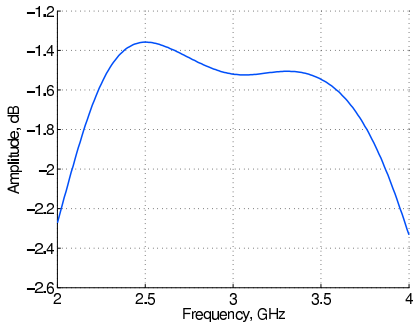

FIGURE 3.10: *Value of f_{dir} as a function of frequency for the antenna A_5 and at the target center.*

the measurement/reconstruction matching, this example proves the systematic nature of the error and the impossibility to rigourously solve it.

Another interesting parameter of the model is the phase center offset with respect to the connector of the antennas, d_{pc}. Under the hypothesis that d_{pc} does not vary with frequency, different values have been tested within the full model framework. For each of them, ϵ has been computed according to (3.76), and the results are plotted in FIG. 3.11(a). The blue, circle-marker curve shows surprisingly that the value giving the smallest ϵ is $d_{\text{pc}} = -1$ cm! To further understand the effect of the phase center correction, the error for two emitting antennas, A_1 and A_5, is also plotted. The results are again surprising, since for A_1 the smallest ϵ is found for $d_{\text{pc}} = 2.5$ cm, whereas for A_5 and practically all the other antennas (not shown) d_{pc} tends to be even smaller than -1 cm. Finally, since as a matter of fact $d_{\text{pc}} = -1.5$ cm gives the smallest error, it will be used for all the inverse problems in the following.

Two possible explanations of the negative value found in FIG. 3.11(a) can be given. First, it must not seem awkward that d_{pc} is negative: the phase center being a rather

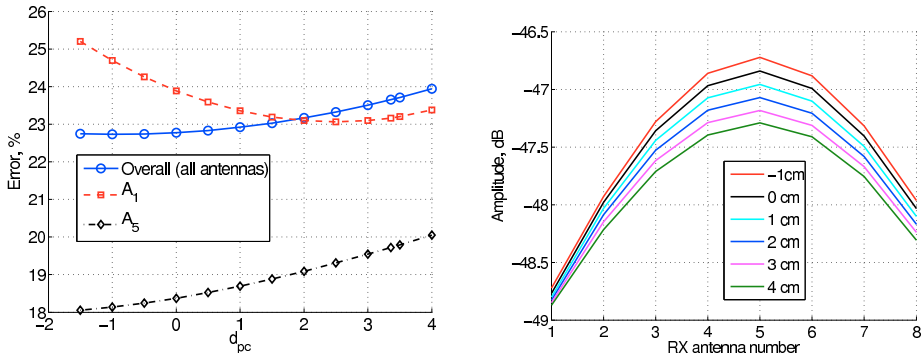

(a) (b)

FIGURE 3.11: *(a) Overall error ϵ and errors for A_1 and A_5 as emitters as a function of d_{pc}. (b) Reconstructed amplitude radiation pattern at 3 GHz for A_5 as emitter and for different values of d_{pc}.*

arbitrary parameter, it simply means that the radiation of the ETS antennas appears as centered in a point that lies before the antenna connector, which might in fact be the case depending on the particular antenna design. The results in FIG. 3.11(b) tend to confirm this explanation. It is shown the retrieved scattered field amplitude pattern at 3 GHz in the case of A_5 as source and as a function of receiving antenna. Different $d_{\rm pc}$ values are tested; for smaller ones, the reconstructed directivity increases, in the sense that the excursion of the amplitude is wider. This is to be expected, since a smaller $d_{\rm pc}$ means that the same measured amplitude pattern, $|S_{jl}^{\rm cal}|$, is associated to smaller azimuth angles φ_{jl} and to a reduced aperture angle $\Delta\varphi$. Summarizing, two contrasting behaviors appear when reducing $d_{\rm pc}$: on the one side, an improved directivity, better matching the measured one, is obtained; on the other side, for $d_{\rm pc}$ values smaller than the hypothetical 3.36 cm, the fitting of the theoretical cylindrical wavefronts is probably worse. Indeed, the two tendencies seem to overall balance themselves for $d_{\rm pc} = -1$ cm.

3.6.3 SNR definition

As for any experimental study, defining a Signal-to-Noise-Ratio (SNR) is an important step to properly analyze the results. $E^{\rm s}|_\Gamma$, the synthetic field built through the calibration procedure just described and validated, is the only signal that can help in quantifying the noise contribution. Yet, several other contributions affect it as shown in the discussion preceding (3.74).

Therefore, although the classical SNR expression

$$\mathrm{SNR} \triangleq \frac{\sum_{j,p} \left\| E_{j,p}^{\rm s} \right\|_\Gamma^2}{\sum_{j,p} \left\| E_{j,p}^{\rm s;meas} - E_{j,p}^{\rm s} \right\|_\Gamma^2} \,, \tag{3.77}$$

where all the norms are L_2-norms, can be evaluated, antenna mismatch and modeling limitations are also included.

3.6.4 Inverse problem

The analysis of the inversion results involves a large number of parameters: number of frequencies and bandwidth, number of sources/receivers, geometric configuration of the setup, type of the initial estimate, just to number a few. First of all, a main distinction is applied in the following over the different types of geometric configurations, that is, reflection, transmission, and full setups (see §1.3). In all cases, relatively small arrays are considered in order to investigate the effect of a small aperture on the inverstion results. Whether using a large bandwidth might compensate such a limited view is also investigated.

Unless otherwise specified, the inversion algorithm is run with the parameters in TAB. 3.2. The top table concerns the actual inversion parameters, which apply then to both experimental and synthetic data sets. The bottom one, dealing with the incident field and far-field Green function calibration, only applies to the experimental case. As for the number of

inversion algorithm	frequency bandwidth	nb. of frequencies	frequency weighting	pixel size
M^{2}GM	[2-4] GHz	$N_p = 21$	$1/\omega^2$	$\leq \lambda_0/10$ @ 3 GHz

multipolar development	phase center correction	elevation correction
$M = 1$	$d_{\text{pc}} = -1$ cm	active

TABLE 3.2: *Main characteristics and parameters of the inversion algorithm (above) and of the incident field and far-field green function calibration (below).*

frequencies, although a step $\Delta f = 5$ MHz ($N_p = 401$) is available, the value $\Delta f = 100$ MHz ($N_p = 21$) has been chosen since for a smaller step hardly any improvement in the results can be observed whereas the execution time is of course considerably reduced. The size $\Delta_x = \Delta_y \triangleq d_{\text{pix}}$ of the pixels discretizing the investigation domain Ω is always set to a value smaller or equal to $\lambda_0/10$ @ 3 GHz, that is, 1 cm. When synthetica data are generated for a comparison between experimental/theoretical results, care is taken not fall into the *inverse crime* [157] consisting of choosing a step for the inversion equal to (or smaller than) the one used for the generation of the data.

3.6.4.1 Frequency weighting

As explained in §3.3.1, the terms of the cost function at different frequencies are multiplied by a $1/\omega^2$ weight whose role is to better condition the data in order to trade-off between convergency and resolution. Due to the use of the FFT *lanczos* window $W_\omega(\omega)$ necessary to reduce the aliasing of time domain echos (see §1.6), an additional weight affects the data. This happens because, neglecting the effect of the time-domain gate $w_t(t)$ (which gives a convolution in the frequency domain and sort of mixes all the frequencies), the cost function can be written as

$$\mathcal{F}(\chi_p; E_{j,p}) \approx \sum_{p=1}^{P} W_\omega^2(\omega_p) \sum_{j=1}^{J} \left(w^\Gamma e_{j,p}^\Gamma + w^\Omega e_{j,p}^\Omega \right) \ , \tag{3.78}$$

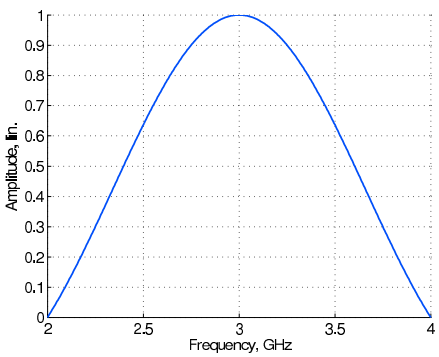

FIGURE 3.12: *Amplitude of the lanczos window $W_\omega(\omega)$ as a function of the frequency.*

where $e^{\Gamma}_{j,p}$ and $e^{\Omega}_{j,p}$ are the errors on the data and state equations, respectively, for the j^{th} source and at the p^{th} frequency. Given then the shape of the *lanczos* window in FIG. 3.12, the weight of the lower and higher frequencies in the [2-4] GHz band is considerably reduced with respect to the one of the central frequencies. As a consequence, the inversion result will only partially be influenced by the additional information provided by them. Such information must therefore be efficiently included back, especially because the lower frequencies improve convergency and robustness of the algorithm while the higher ones allow to reconstruct finer details of the scatterers.

One could first think of replacing the *lanczos* window by a different window, possibly asymmetric in order to enhance the weight of the lower frequencies and reducing that of the higher ones. Such a window is nonetheless hard to find in our case, where the requirements on the sidelobe suppression are very strict (*cf.* §1.6).

The easiest, and probably safest, way to solve this problem consists instead in multiplying both the incident and the measured scattered fields, E^{i} and $E^{;\text{meas}}$, respectively, by $1/W_\omega(\omega)$ at each frequency, so to compensate exactly (apart again from the effect of the time-gating) the profile of the *lanczos* window.

Notice also that applying the inverse of the window does not invalidate the anti-aliasing role originally played by $W_\omega(\omega)$. In fact, while the first application of the window is a coherent one, in the sense that it is necessary to retrieve a clean-enough time-domain signal to be time-gated, here the processing is *incoherent* with respect to the available frequencies. As a matter of fact, the cost function is made of a sum of norms, and for the gradients in §3.3.1 the frequency components are summed through either their real or imaginary part.

Unless otherwise stated, the frequency window compensation is always applied to the data. An example of the impressive improvement given by this strategy is given in FIG. 3.18.

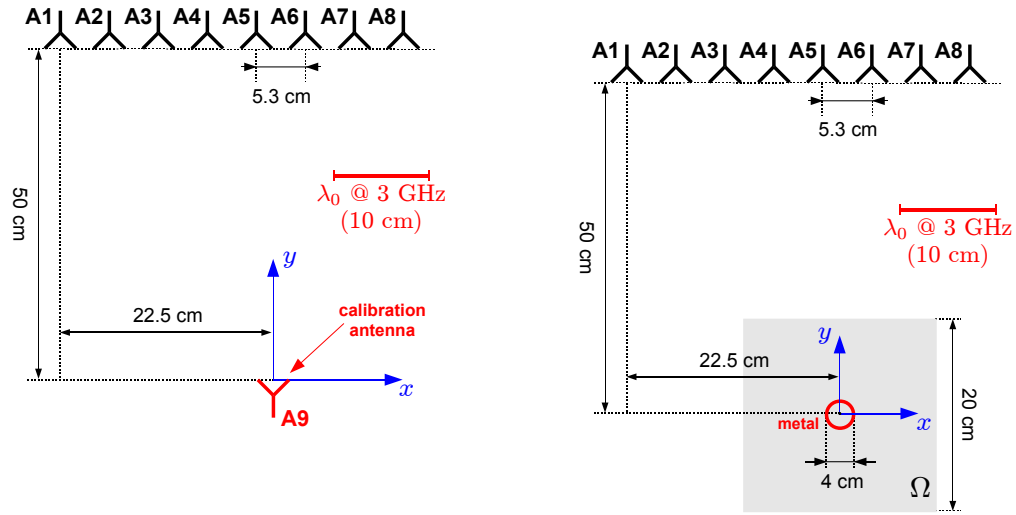

(a) Calibration (b) Scattering

FIGURE 3.13: *Inversion setup. Metallic cylinder in reflection.*

3.6.4.2 Reflection configuration

Metallic targets

The setup of the first example is the one in FIG. 3.13, already used in §3.6.2 for the calibration methodology validation. A metallic cylinder with 2 cm radius is imaged with 8 antennas. Although it is empty, the metallic width is much larger than the skin depth at 2 GHz (lowest frequency), so that the hypothesis of perfect conductor is fully verified. The target-line distance is 50 cm, and the aperture angle is $\Delta\varphi \approx 40$ deg. The investigation region is square with a side of 20 cm ($2\lambda_0$ @ 3 GHz). The SNR evaluated through (3.77) is equal to 17.7 dB.

In FIG. 3.14 the initial estimates obtained with the back-propagation method for both synthetic ($\tilde{E}^{\mathrm{s}}$) and experimental ($E^{\mathrm{s;meas}}$) data are presented. The results, showing from left to right the real part of the permittivity, ε_r, the conductivity σ, and the modulus of the contrast χ at 3 GHz, hardly present any difference between synthetic and experimental data. As a first remark, it appears that while $|\chi|$ shows a hot spot at the visible face of the metallic cylinder (the one facing the antenna array), ε_r and σ are rather complementary. In other words, the back-propagation algorithm fails in distinguishing the purely conductive features of the object. Nonetheless a good localization is obtained. The very low values of ε_r and σ confirm what was claimed at the end of §3.3.3.

The final results are shown in FIG. 3.15. They are final in the sense that the iterative

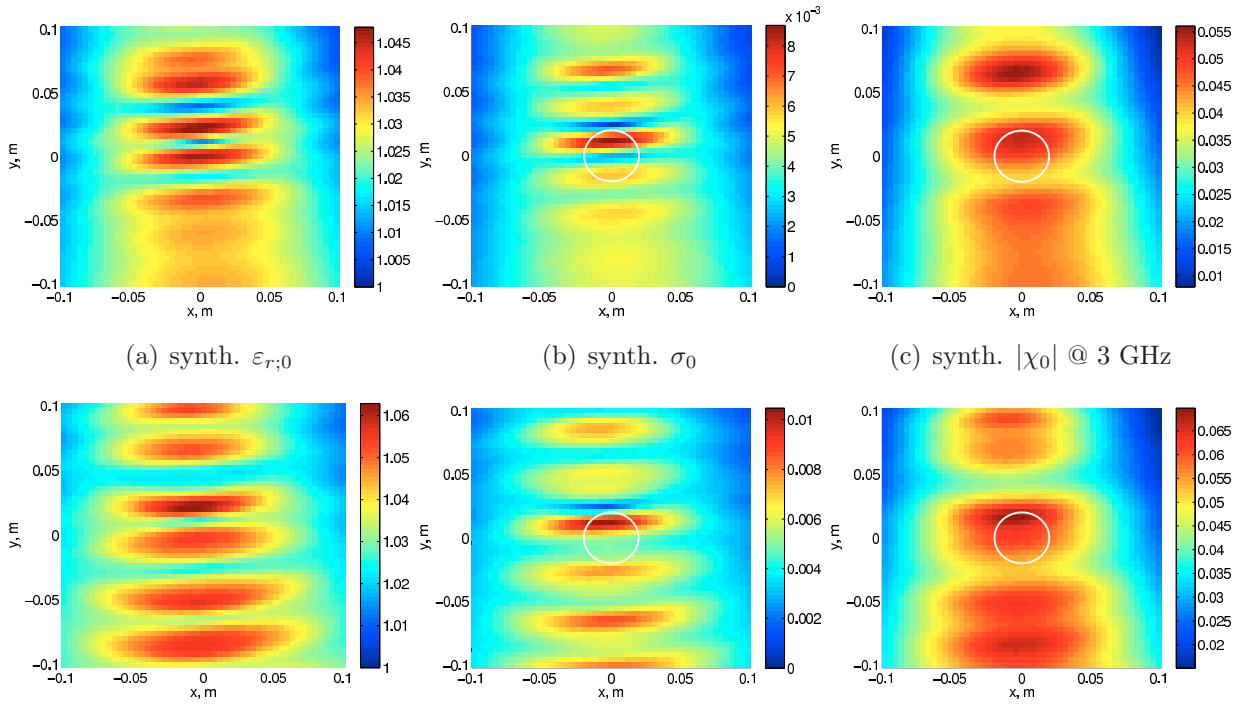

(a) synth. $\varepsilon_{r;0}$ (b) synth. σ_0 (c) synth. $|\chi_0|$ @ 3 GHz

(d) exp. $\varepsilon_{r;0}$ (e) exp. σ_0 (f) exp. $|\chi_0|$ @ 3 GHz

FIGURE 3.14: *Inversion of the configuration in* FIG. *3.13. Initial estimate. Comparison between (above) synthetic data and (below) experimental results.*

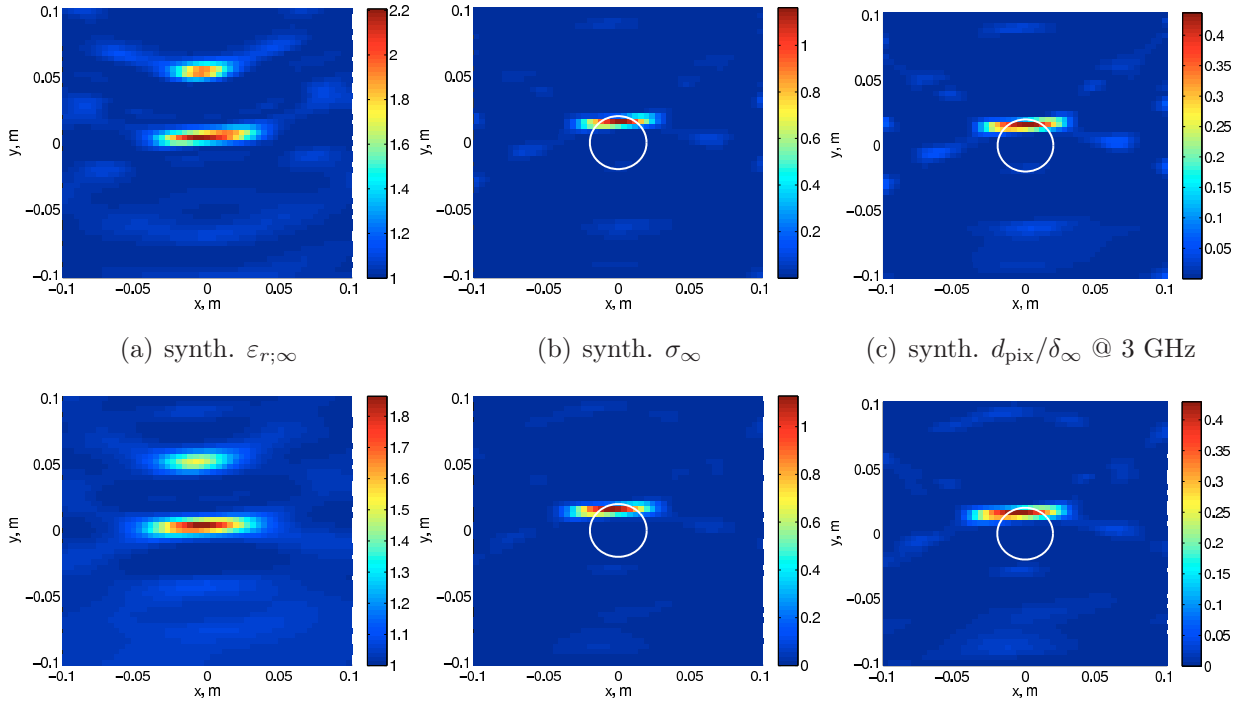

(a) synth. $\varepsilon_{r;\infty}$ (b) synth. σ_∞ (c) synth. $d_{\text{pix}}/\delta_\infty$ @ 3 GHz

(d) exp. $\varepsilon_{r;\infty}$ (e) exp. σ_∞ (f) exp. $d_{\text{pix}}/\delta_\infty$ @ 3 GHz

FIGURE 3.15: *Inversion of the configuration in* FIG. *3.13. Final results. Comparison between (above) synthetic data and (below) experimental results.*

algorithm does not manage to further refine the reconstructed profiles with additional CG iterations. Again the difference between experimental and synthetic results is hardly visible, proving that the SNR for this experiment is high enough (indeed, the cylinder has a high scattering power due to its dimensions and metallic nature).

In FIG. 3.15(c,f) the ratio of pixel size d_{pix} and skin depth δ at 3 GHz, instead of $|\chi|$, is plotted. The skin depth is defined as

$$\delta \triangleq \{x \mid e^{-ikx} = e^{-1}\} \quad \Leftrightarrow \quad \delta = -\frac{1}{\Im\{k\}},\ k = k_0\sqrt{1+\chi}\ , \tag{3.79}$$

and it will systematically be shown when perfect conductors will be imaged. The reason comes from their impenetrability coupled with the use of an inversion algorithm based on an integral formalism. In effect, what such an algorithm reconstructs is a total field E equal to 0 within the support of purely metallic targets, which is practically the case if $\delta(\sigma) \leq d_{\text{pix}}$. Values of $\delta(\sigma)$ below this limit only hardly alter E, already almost zero, and will therefore not be retrieved from the algorithm. The maximum values around 0.4 in FIG. 3.15(c,f) are therefore a bit low to trustfully affirm that the target is a conductor, but they at least let it suppose. As a demonstration, the amplitude of the total field E (at 3 GHz and for A_5 as emitter) over Ω is presented in FIG. 3.16: within the support of the target E has indeed a small value with respect to those in front of it. As for the two hot "stains" in the ε_r profiles, they are artifacts of the algorithm. The one nearer to the array is an error, since there is no dielectric target in that region. The other one can be neglected

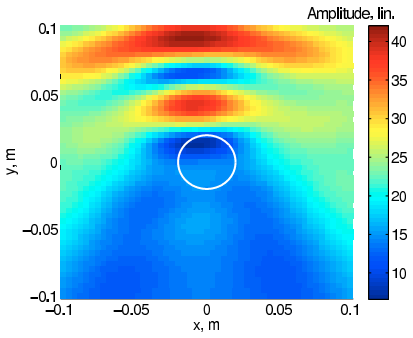

FIGURE 3.16: *Inversion of the configuration in* FIG. *3.13. Amplitude of the total field E at 3 GHz and for A_5 as emitter at the convergence of the algorithm with experimental data.*

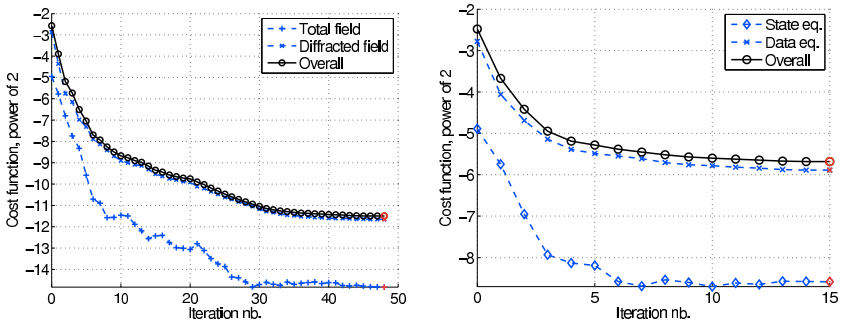

(a) synth. (b) exp.

FIGURE 3.17: *Inversion of the configuration in* FIG. *3.13. Cost functions as a function of the CG iteration number. Comparison between (a) synthetic and (b) experimental data.*

since placed behind the reconstructed portion of the target perimeter, where E is as just explained very small. The information available in the data combined with the M^{2}GM as inversion algorithm is therefore not sufficient yet for clearly distinguishing a dielectric from a metallic target, although these results appear as very encouraging.

Finally, the evolution of the cost function $\mathcal{F}$ as a function of the CG iteration number is shown in FIG. 3.17. The full line with circle markers represents the whole $\mathcal{F}$, wheareas the two other lines stand for the state and data equation terms, $\mathcal{F}^\Omega \triangleq w^\Omega e^\Omega$ and $\mathcal{F}^\Gamma \triangleq w^\Gamma e^\Gamma$ in (3.16). In the synthetica data case, the absence of noise allows the algorithm to run for many more iterations before reaching the precision of the stop condition as compared to the experimental case (see §3.3.2). Notice indeed how the final value of $\mathcal{F}$ is much lower in the former case, meaning that although the additional iterations reduce considerably the value of $\mathcal{F}$ the δ/d_{pix} profile is barely improved. Notice also that the larger contribution in the overall $\mathcal{F}$ is given by $\mathcal{F}^\Gamma$.

In order to prove the effectiveness of the frequency weighting strategy presented in §3.6.4.1, the same data set has also been inversed without applying the *lanczos* window

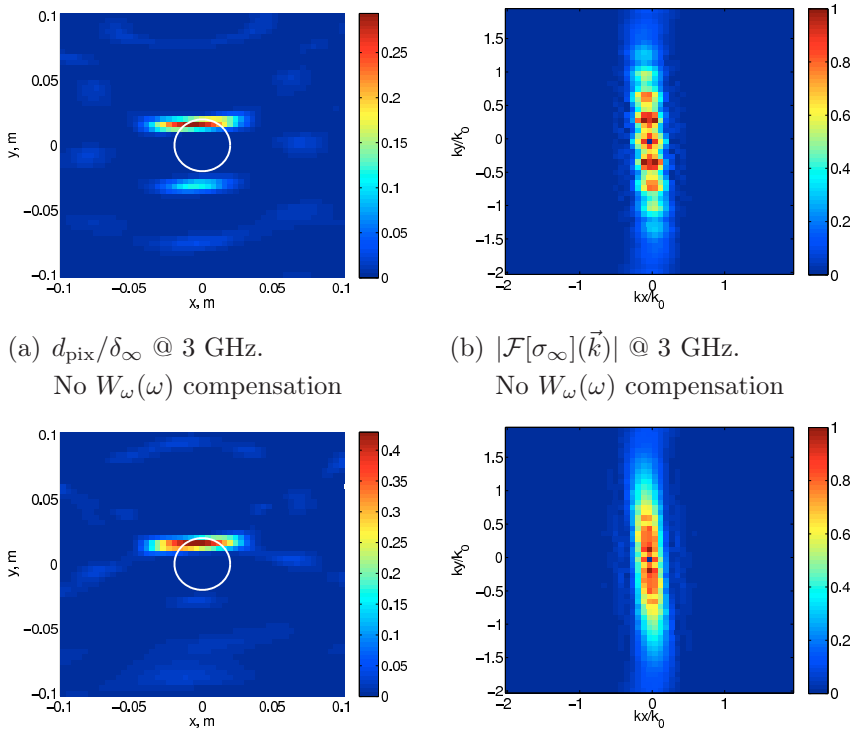

(a) $d_{\text{pix}}/\delta_\infty$ @ 3 GHz. No $W_\omega(\omega)$ compensation

(b) $|\mathcal{F}[\sigma_\infty](\vec{k})|$ @ 3 GHz. No $W_\omega(\omega)$ compensation

(c) $d_{\text{pix}}/\delta_\infty$ @ 3 GHz. $W_\omega(\omega)$ compensation.

(d) $|\mathcal{F}[\sigma_\infty](\vec{k})|$ @ 3 GHz. $W_\omega(\omega)$ compensation.

Figure 3.18: *Inversion of the configuration in* Fig. *3.13. Experimental data. Final results (top row) without and (bottom row) with the lanczos window compensation. For the spatial spectra (right column), the amplitude of the 0-frequency bin has been set to 0 in order to better appreciate the dynamics of the other components.*

compensation but leaving the $1/\omega^2$ ponderation. The results are presented in Fig. 3.18, where, besides the normalized skin depth δ_∞ at the end of the iterative process, the amplitude of the spatial Fourier Transform of the retrieved conductivity σ_∞ at 3 GHz is shown. From the skin depth profile in Fig. 3.18(a), it is immediately clear how without the compensation the inversion result is affected by periodic patterns at a period approximately equal to $\lambda_0/2$ at 3 GHz, giving an almost discrete spectrum in Fig. 3.18(b) with spots at $nk_0/2,\ n = 1, 2, \ldots$. In other words, the spatial content of the retrieved image is discretly linked to $\lambda_0/2$. This is then essentialy due to the frequency weighting, which almost acts as if time-harmonic data at 3 GHz where available instead of a rather continuous spectrum between 2 and 4 GHz. The proof is that, when the spectrum-equalizing compensation is applied, the spatial frequency content is much smoother, with no particular frequency being privileged.

A different test consists in applying the MBM and the MGM to the data set. In fact, as alrady observed in literature (see *e.g.* Fig. 9 in [146]), the former is known to retrieve higher σ - hence δ - values in the case of perfect conducting targets. This is indeed verified in Fig. 3.19, where the MBM is employed and the δ/d_{pix} ratio grows up to more than

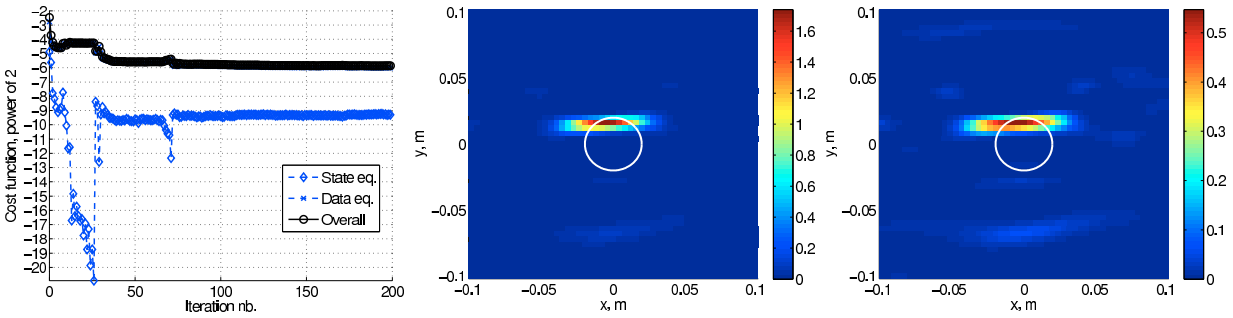

(a) exp. $\mathcal{F}$ (b) exp. σ_∞ (c) exp. $d_{\text{pix}}/\delta_\infty$ @ 3 GHz

FIGURE 3.19: *Inversion of the configuration in* FIG. *3.13. Final results. The MBM is used instead of the M²GM (see §3.3).*

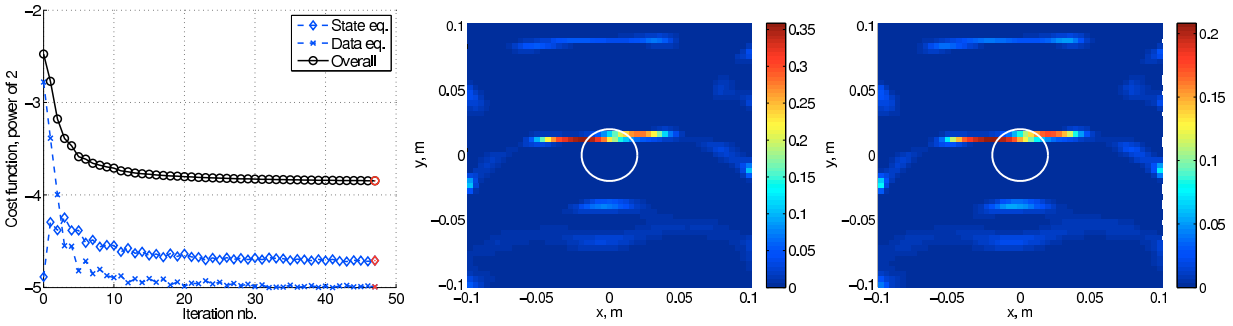

(a) exp. $\mathcal{F}$ (b) exp. σ_∞ (c) exp. $d_{\text{pix}}/\delta_\infty$ @ 3 GHz

FIGURE 3.20: *Inversion of the configuration in* FIG. *3.13. Final results. The Modified Gradient Method (MGM) is used instead of the M²GM (see §3.3).*

0.5. The price to pay is a much larger number of iterations. Indeed, in FIG. 3.19(a) 200 CG iterations have been performed and convergency is not even reached, resulting in a proportionally larger execution time. Also, it can be seen that $\mathcal{F}$ is not a monotonically decreasing function anymore, since the update of the total field is now done exclusively with a value issued from the resolution of a direct problem (the so-called Born term) and not with a classical conjugate gradient direction.

Inversely, if the Born term is removed from the total field update rule, that is, if the MGM is used, the inversion results in FIG. 3.20 appear dramatically degraded with respect to both the M²GM and the MBM. The regularizing effect of using a direct solver is thus confirmed. Notice also how the equilibrium of the components of $\mathcal{F}$ are altered, since now $\mathcal{F}^\Gamma$ and $\mathcal{F}^\Omega$ have rather similar values (the latter is even larger now).

Back to the M²GM method, it is instructive to observe the evolution of the gradients of $\mathcal{F}$ during the CG iterations. With reference to the notations in §3.3, and given the fact that all the gradients are vectors (one component per point $\vec{r} \in \Omega$), the following quantities

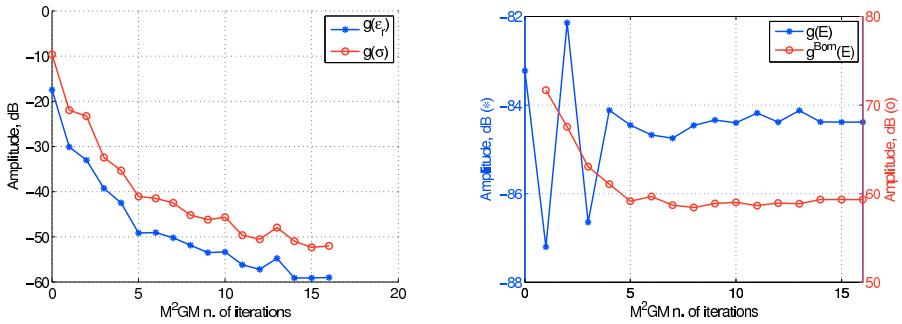

(a) $g(\varepsilon_r), g(\sigma)$ (b) $g(E), g^{\mathrm{Born}}(E)$

FIGURE 3.21: *Inversion of the configuration in* FIG. *3.13. Evolution of the norm of the gradients in (3.80) as a function of the CG iteration number.*

are observed:

$$\left\{\begin{array}{l} \left.\begin{array}{l} \varepsilon_r \rightarrow g(\varepsilon_r) \triangleq \|\mathbf{g}^{\xi}\|_{\Omega}^2 \\ \sigma \rightarrow g(\sigma) \triangleq \|\mathbf{g}^{\eta}\|_{\Omega}^2 \end{array}\right\} \chi - \text{gradients} \\ \left.\begin{array}{l} E \rightarrow g(E) \triangleq \sum\limits_{j,p} \|\mathbf{g}_{j,p}^{E}\|_{\Omega}^2 \\ \text{Born term} \rightarrow g^{\mathrm{Born}}(E) \triangleq \sum\limits_{j,p} \|\tilde{\mathbf{E}}_{j,p} - \mathbf{E}_{j,p}\|_{\Omega}^2 \end{array}\right\} E - \text{gradients} \end{array}\right. . \tag{3.80}$$

The results from the experimental inversion are presented in FIG. 3.21. The χ-gradients have a nicely decreasing shape with a dynamics of about 45 dB. Hence, a true minimization over χ of the cost function is performed, and convergency is reached when the gradients reach a plateau. The behavior is not as effective for the E-gradients in FIG. 3.21(b). As for $g(E)$, it basically oscillates with a larger excursion in the first 4 iterations (5 dB) and a smaller then (1 dB) without really being minimized. The first conclusion is that the much smaller excursion with respect to the χ-gradients means that $\mathcal{F}$ is much less sensitive to the E profile than to the χ one. In addition, while the update of E made in the first iterations alters its norm, the minimization "work" achieved in the following ones basically concerns only χ. As a further proof, $g^{\mathrm{Born}}(E)$ almost stabilizes after iteration 5, demonstrating that the following χ refinements almost do not affect both E_n and $\tilde{E}_n$.

The conclutions issued from this testcase are mainly two. First of all, the experimental data are fairly suitable for a quantitative inverse scattering problem, at least in the case of a rather big perfect conductor. The experimental results are indeed very similar to the synthetic ones, showing that the inversion algorithm is robust with respect to noise, at least down to the SNR value of 12.7 dB estimated for this configuration. Concerning the available information and the effectiveness in extracting it, it appears that in the case of a perfect conductor and of a small Tx/Rx line in reflection only the image of the front side of the scatterer support can be retrieved[5]. Despite the frequency diversity available,

[5]This is actually true only in the $E_{//}$ polarization case treated here. Inversely, if $H_{//}$ polarized waves

though, the value of the conductivity is slightly underestimated, even when using synthetic data. Additional information, hence data, is needed for an unambiguous and quantitatively trustful inversion.

Dielectric targets

Dealing with dielectric targets leads to very different results. The configuration under test is equivalent to the one in FIG. 3.13, only a dielectric cylinder with circular section is used instead of the metallic one. Only synthetic data are used to test the inversion algorithm.

First, for a given relatively low permittivity value, *e.g.* $\varepsilon_r = 2$, the radius of the object has been shrinked from $\lambda_0/5$ to $\lambda_0/20$ at 3 GHz. FIG. 3.22 shows the corresponding retrieved ε_r profiles (except for FIG. 3.22(a), whose $|\chi|$ at 3 GHz is shown in FIG. 3.23(d), σ is

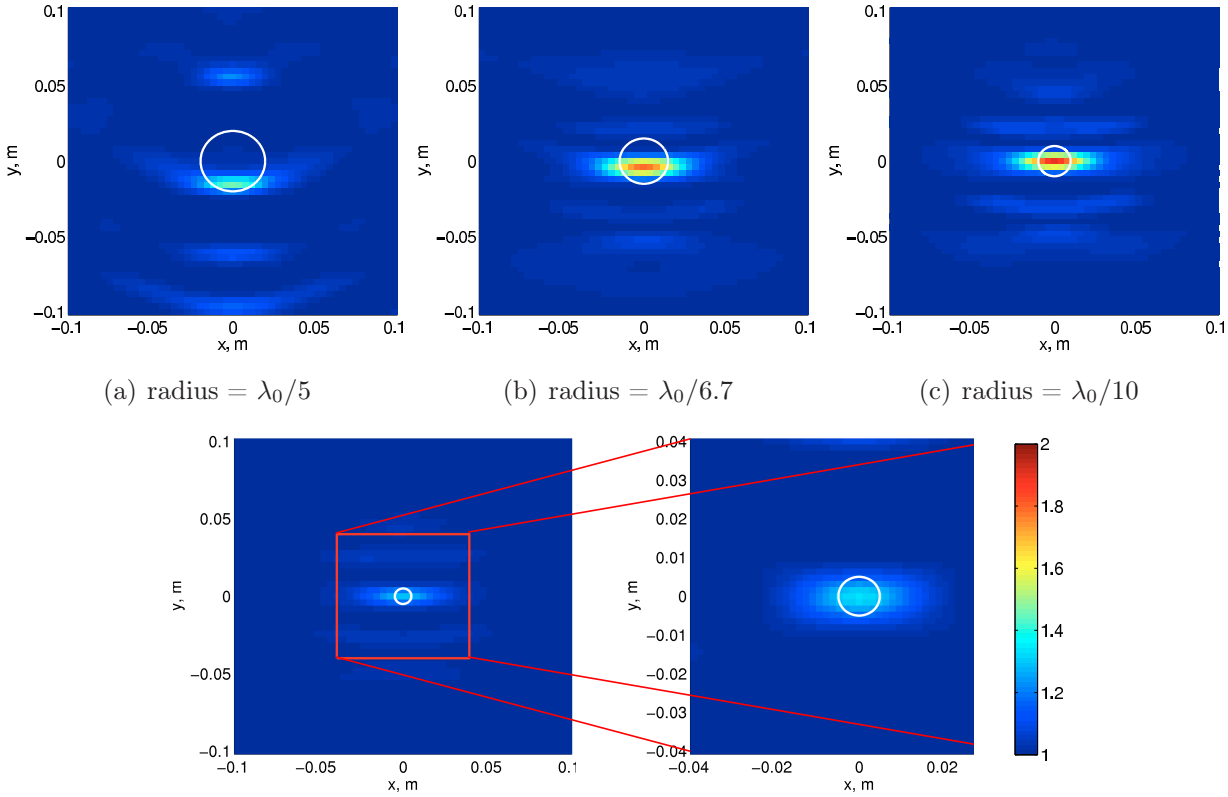

(a) radius = $\lambda_0/5$ (b) radius = $\lambda_0/6.7$ (c) radius = $\lambda_0/10$

(d) radius = $\lambda_0/20$

FIGURE 3.22: *Synthetic data inversion of a dielectric cylinder with $\varepsilon_r = 2$ and four different radii. Only the ε_r profile is shown. The configuration is equivalent to the one in* FIG. *3.13. In (d), two inversions have been run with two different Ω sizes (hence different pixel sizes) to prove that the low ε_r values found with a large Ω (left) are not due to the large pixel size-target dimensions ratio.*

are used, the creeping waves propagating along the perimeter of the scatterer support re-radiate back in the direction of the array after one or more complete tours, thus carrying informations also on the "dark side" of the support.

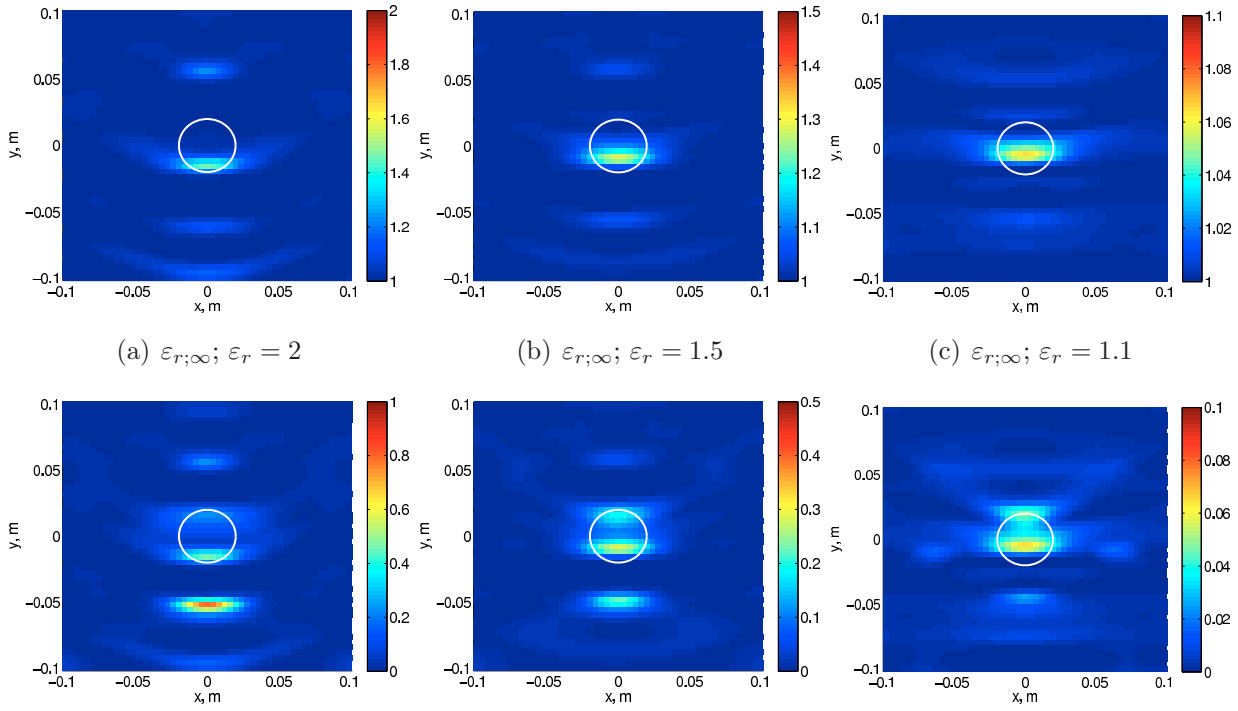

(a) $\varepsilon_{r;\infty}$; $\varepsilon_r = 2$ (b) $\varepsilon_{r;\infty}$; $\varepsilon_r = 1.5$ (c) $\varepsilon_{r;\infty}$; $\varepsilon_r = 1.1$

(d) $|\chi_\infty|$ at 3 GHz; $\varepsilon_r = 2$ (e) $|\chi_\infty|$ at 3 GHz; $\varepsilon_r = 1.5$ (f) $|\chi_\infty|$ at 3 GHz; $\varepsilon_r = 1.1$

FIGURE 3.23: *Synthetic data inversion of a dielectric cylinder with radius* $= \lambda_0/5$ *and three different permittivity values. The configuration is equivalent to the one in* FIG. *3.13. (above)* ε_r *profiles, and (below)* $|\chi|$ *at 3 GHz.*

not shown because it takes very small values). A finding common to all the figures is the systematic underestimation of the value of ε_r. Nonetheless, quite different behaviors appear in the large and small target cases. In FIG. 3.22(a), a sort of "focusing effect" takes place, so that instead of imaging all the target support just a spot is found at its rear side. Actually, as shown in FIG. 3.23(d), there is a similar focusing on the σ profile, which is not negligible with respect to ε_r. This "focusing" phenomenon was already shown in [147] (see *e.g.* FIG. 4(b)), where two spots where found on two sides of the support due to the fact that a complete configuration was used, leading to conclude that this effect is typical of multi-frequency inversions, since a rather different shape was found in [147] when using a frequency hopping approach. As the dimensions lower, the hot spot coincides more with the center of the target. The ε_r value increases up to 1.8 in FIG. 3.22(c), but decreases to 1.4 for the smallest target in FIG. 3.22(d). Two conclusions can be drawn:

- when the dimensions of the target decrease, a better estimation has to be expected, both in terms of shape and permittivity value;
- nonetheless, for very small targets with respect to the frequencies used, the resolution given by the geometry of the configuration systematically leads to an underestimation of ε_r, since the actual value is smeared over a larger region whose size depends indeed on the available resolution.

On the other hand, fixing the radius of the target to 2 cm and testing ε_r values from 2

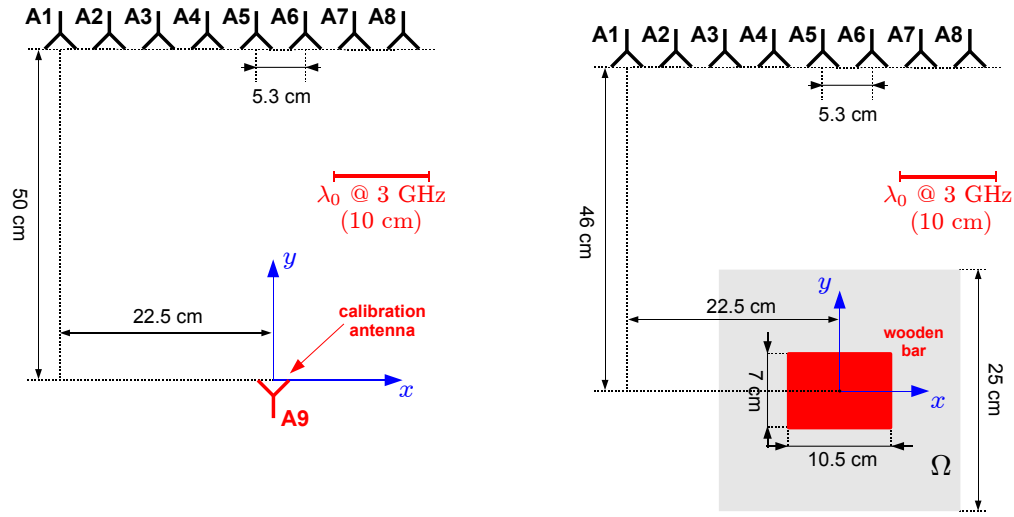

(a) Calibration (b) Scattering

FIGURE 3.24: *Inversion setup. Wooden bar in reflection.*

to 1.1 gives the results in FIG. 3.23. Both the ε_r and $|\chi|$ at 3 GHz profiles are shown, since as anticipated the conductivity values are not negligible. In fact, not even when $\varepsilon_r = 1.1$, corresponding to an electrically very small target, the permittivity profile is clean; σ is somehow complementary and systematically brings a focusing onto the rear face of the object.

From the comparison of FIGS. 3.22-3.23 it can finally be concluded that although the RADAR cross section of a dielectric target depends, at least under the Born approximation, on the $r^2\epsilon_r$ product, which might lead to state that dividing by $\sqrt{2}$ the radius r gives the same result as dividing by 2 the permittivity, quite different behaviors appear when changing r or ε_r, mainly due to the resolution limit attained by the algorithm.

Despite the previous results show that for targets electrically (very) large it is impossible to obtain accurate reconstructions, it is nonetheless very interesting to investigate the behavior of the inverse problem in such cases. In the experimental setup in FIG. 3.24 a wooden rectangular-section bar whose sides are of the order of λ_0 at 3 GHz is imaged. Based on experimental informations found in literature, the value of ε_r should be between 2 and 3. The resonance pattern found in FIG. 3.25(b) at about 2.4 GHz seems indeed to be matched by the one given by a wooden bar with $\varepsilon_r = 3$ whose scattered field for A_4 as transmitting antenna is shown in FIG. 3.24(a). The corresponding SNR is 3.2 dB.

The inversion of the experimental data gives the results in FIG. 3.26. Concerning the ε_r profile, two spots corresponding to the faces of the bar parallel to the array are clearly found. The permittivity value is, as expected, underestimated. Within the bar, $\varepsilon_r \approx 0$. As for the σ profile, one spot appears within the support of the bar. As a result, the contrast at 3 GHz (FIG. 3.26(f)) fills the support better than ε_r or σ alone, although the conductivity profile is dominant. Replacing the back-propagation initial estimate by a flat profile (*i.e.*

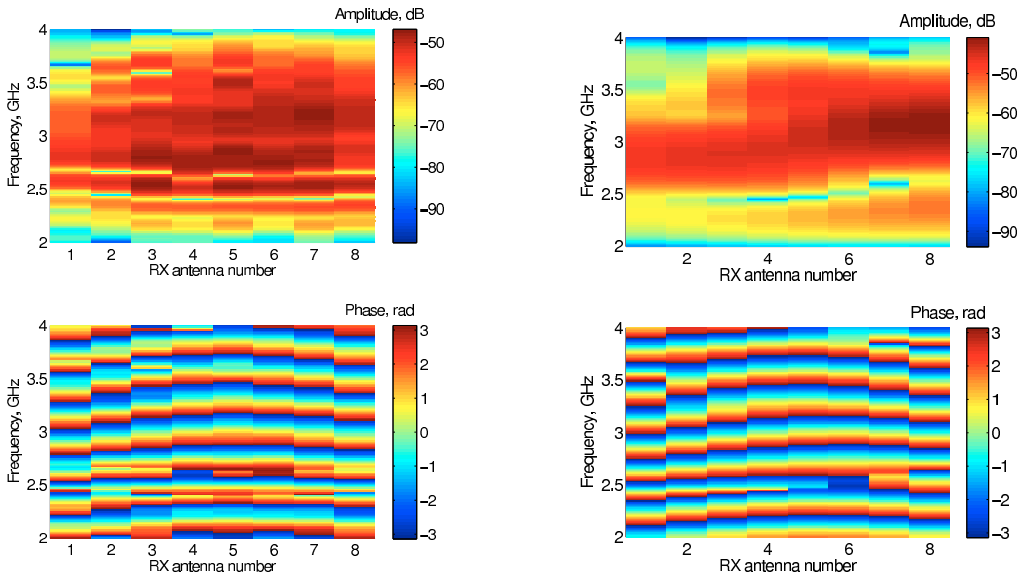

(a) Measurement (b) Model (with calibration), $\varepsilon_r = 3$

FIGURE 3.25: *(a) Measured and (b) modeled scattered fields for A_4 as transmitting antenna and as a function of receiving antenna and frequency.*

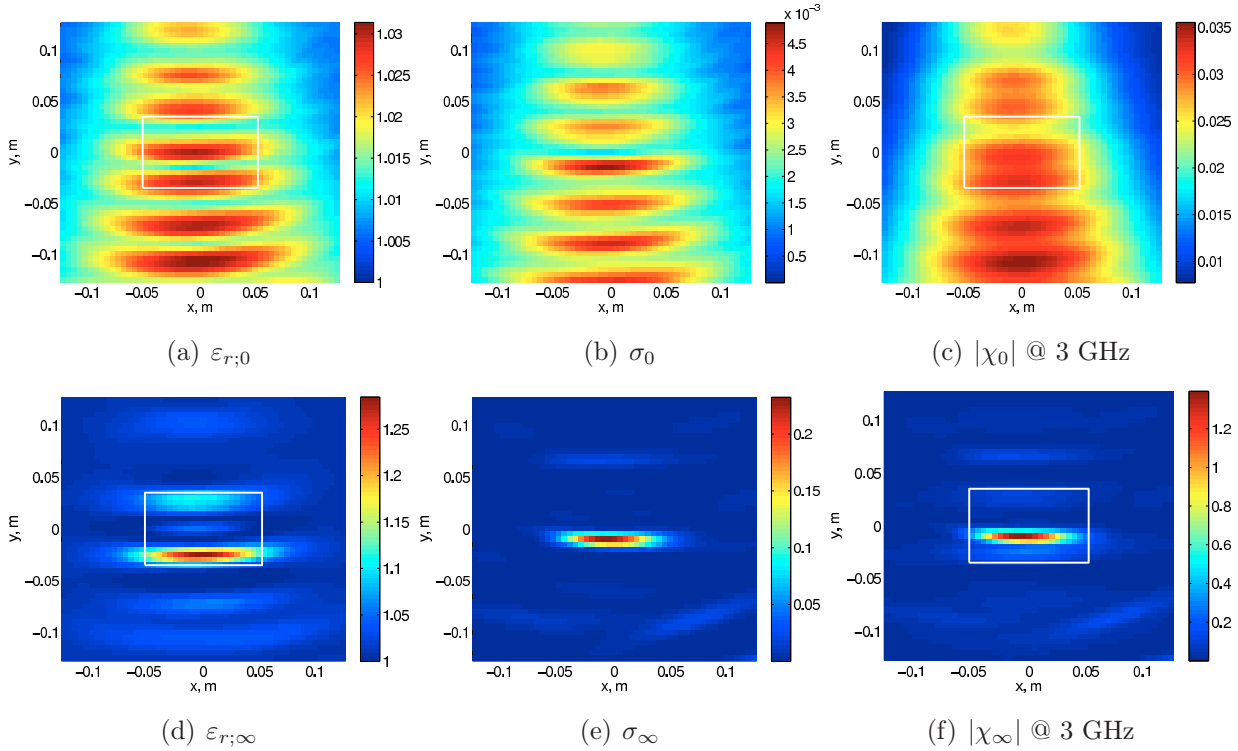

(a) $\varepsilon_{r;0}$ (b) σ_0 (c) $|\chi_0|$ @ 3 GHz

(d) $\varepsilon_{r;\infty}$ (e) σ_∞ (f) $|\chi_\infty|$ @ 3 GHz

FIGURE 3.26: *Inversion of the configuration in* FIG. *3.24. Experimental results. (top) Back-propagation, (bottom) final results.*

$\varepsilon_{r;0} = 1.01$ and $\sigma_0 = 0.01$ $\forall \vec{r} \in \Omega$) can in some cases be advantageous. Here (not shown), it only slightly improves the results, namely the ε_r values rise to 1.4 and becomes dominant over the imaginary part.

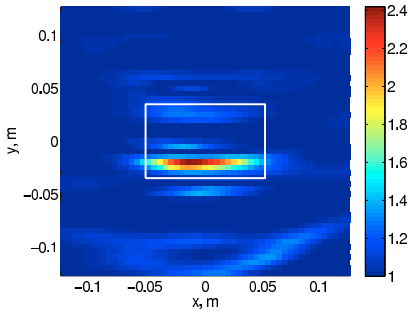

FIGURE 3.27: *Same as* FIG. *3.26, but the target is forced to be purely dielectric. Final result* $(\varepsilon_{r;\infty})$.

The conclusion is then that the inversion scheme seems to possess not enough information to distinguish between a conducting and a dielectric object. This is why it is interesting to force the algorithm to search for a purely dielectric target[6], that is, exploiting the a priori information that the target is a purely dielectric one. The resulting ε_r profile is in FIG. 3.27, much cleaner and quantitatively less underestimated than the one in FIG. 3.26. As for the results with synthetic data, not shown, they are very similar to the experimental ones and do not present any sensible improvement.

It is also instructive to observe the behavior of the cost function and of the norms of

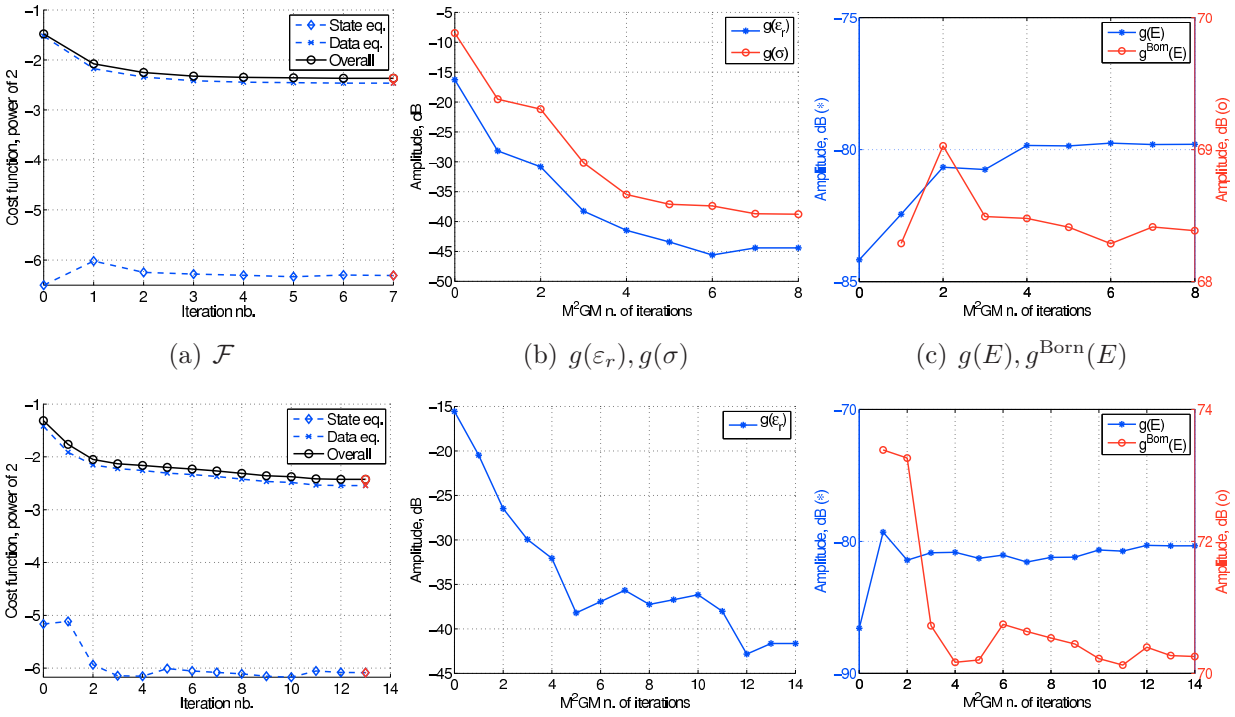

(a) $\mathcal{F}$ (b) $g(\varepsilon_r), g(\sigma)$ (c) $g(E), g^{\mathrm{Born}}(E)$

(d) forced dielectric, $\mathcal{F}$ (e) forced dielectric, $g(\varepsilon_r)$ (f) forced dielectric, $g(E), g^{\mathrm{Born}}(E)$

FIGURE 3.28: *Inversion of the configuration in* FIG. *3.24. Experimental results. Evolution of the gradients as a function of the CG iteration number.*

[6]Within the algorithm, this is simply done by switching off the minimization of $\mathcal{F}$ with respect to η setting $\beta_n^\eta = 0$ in (3.26), and by imposing a σ profile equal to 0 everywhere within Ω.

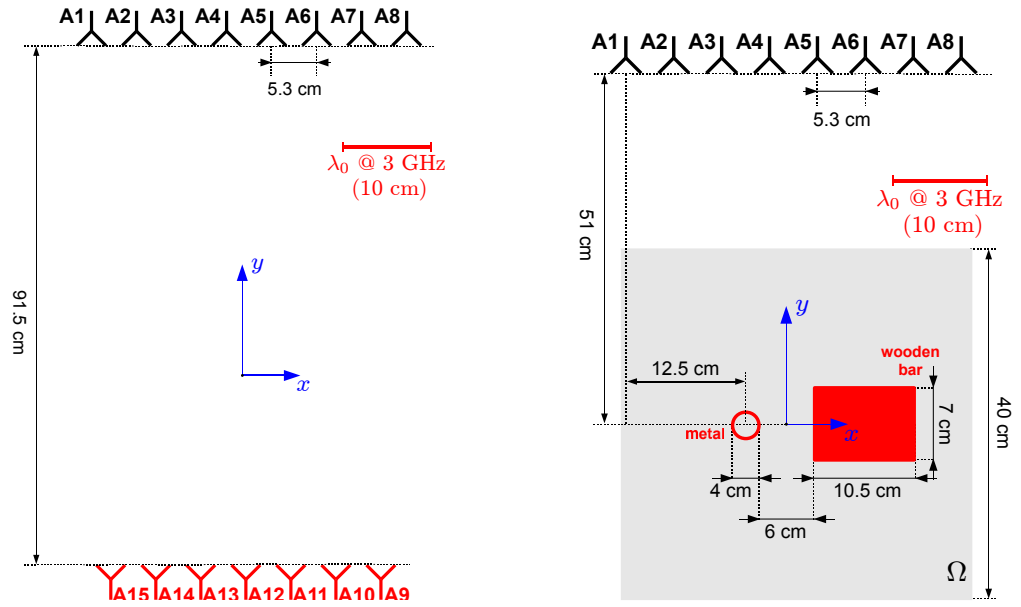

(a) Calibration (b) Scattering

FIGURE 3.29: *Inversion setup. Metllic cylinder and wooden bar in reflection.*

the gradients as a function of the iterations of the algorithm. From the results in FIG. 3.28, showing also the pure dielectric case just mentioned, it appears that the components of the cost function $\mathcal{F}^\Gamma$ and $\mathcal{F}^\Omega$ are even more unbalanced here than in the example of the metallic target (*cf.* FIG. 3.17(b)). In addition, in FIG. 3.28(c,f), the gradient $g(E)$ grows instead of decreasing, meaning that E is less and less a minimizer of $\mathcal{F}$.

Metallic and dielectric targets

As a final test case, the setup in FIG. 3.29 has been tested. Both the metallic cylinder and the wooden bar are present, with an edge-to-edge distance of 7.5 cm ($3/4\lambda_0$ at 3 GHz).

The results are presented in FIG. 3.30. The first remark is that, despite the smaller area, the metallic target has a much higher scattering power, resulting in an initial estimate which has barely any trace of the wooden bar (see *e.g.* the difference in the values of χ_0 at the location of the targets in FIG. 3.30(c)). The algorithm is nonetheless capable of reducing this imbalance, at least up to the conducting/dielectric resolving power already pointed out for the two targets alone. Indeed, the final result for the metallic cylinder strongly resembles the one observed in FIG. 3.15: a hot σ spot at the front side with respect to the array, and two ε_r parasite regions in front and inside of it. It might nevertheless be pointed out that the σ spot is now split into two parts; the right one is in fact absent in FIG. 3.15, which might lead to the conclusion that its presence is caused by the proximity of the dielectric target, which is partially imaged too: a first demonstration that multiple scattering is taken into account in the inversion process could possibly show here. As for the wooden bar, as just said the image is not clear; still, some of the elongated spots observed in FIG. 3.26 are retrieved.

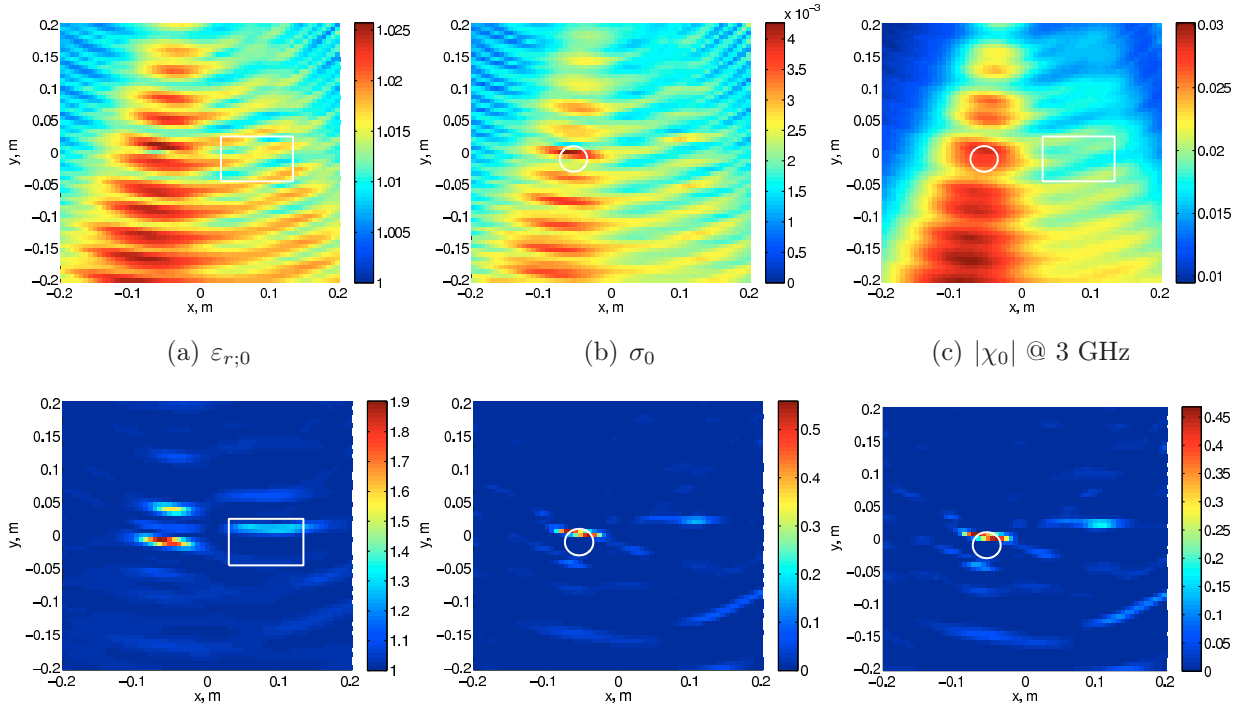

(a) $\varepsilon_{r;0}$ (b) σ_0 (c) $|\chi_0|$ @ 3 GHz

(d) $\varepsilon_{r;\infty}$ (e) σ_∞ (f) $d_{\text{pix}}/\delta_\infty$ @ 3 GHz

FIGURE 3.30: *Inversion of the configuration in* FIG. *3.29. Experimental results.*

3.6.4.3 Transmission configuration

Two configurations have been tested in the case of a transmission setup. Both the antenna arrays are used giving a 7×8 scattered field matrix with only transmission data $(S_{jl}|_{j=1,\ldots,8;\,9,\ldots,15})$. The first test case (FIG. 3.31(b)) deals with a metallic cylinder, the second (FIG. 3.31(c)) with a wooden one ($\varepsilon_r \approx 2$), their radii being equal to $\lambda_0/5$ and

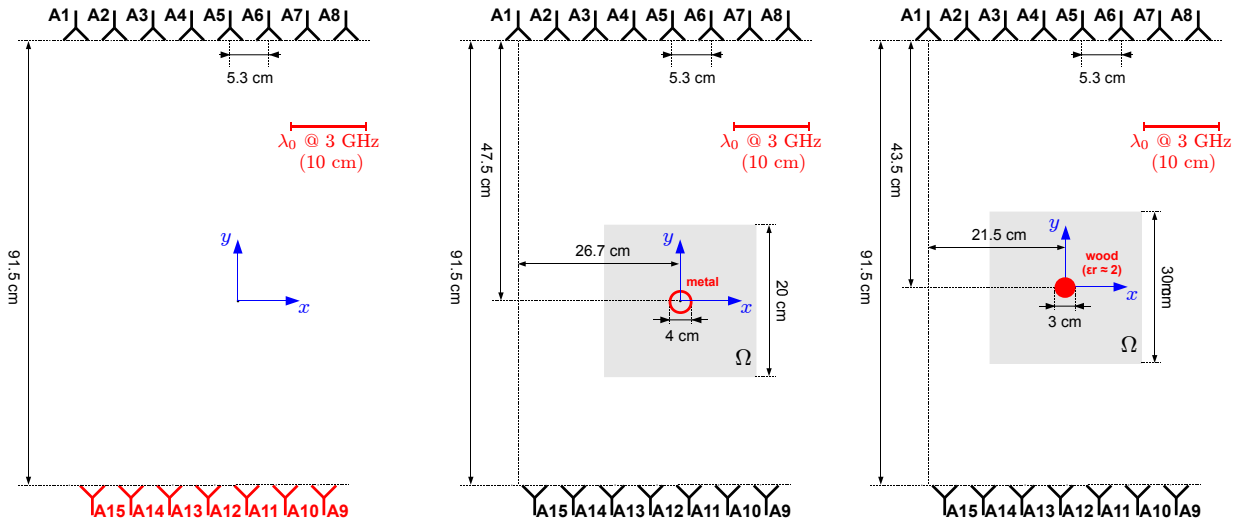

(a) Calibration (b) Scattering (metallic) (c) Scattering (dielectric)

FIGURE 3.31: *Inversion setup. (a) Metllic and (b) dielectric cylinder in transmission.*

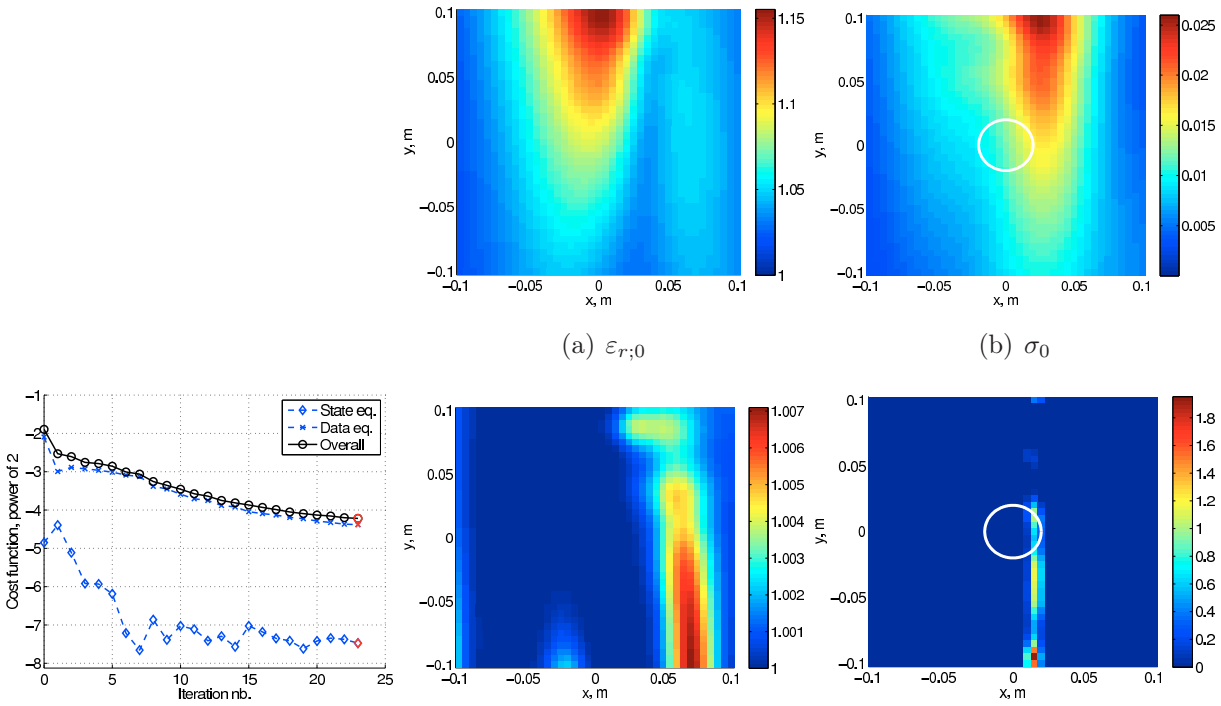

(a) $\varepsilon_{r;0}$ (b) σ_0

(c) $\mathcal{F}$ (d) $\varepsilon_{r;\infty}$ (e) σ_∞

FIGURE 3.32: *Inversion of the transmission configuration in* FIG. *3.31(b). Experimental results.*

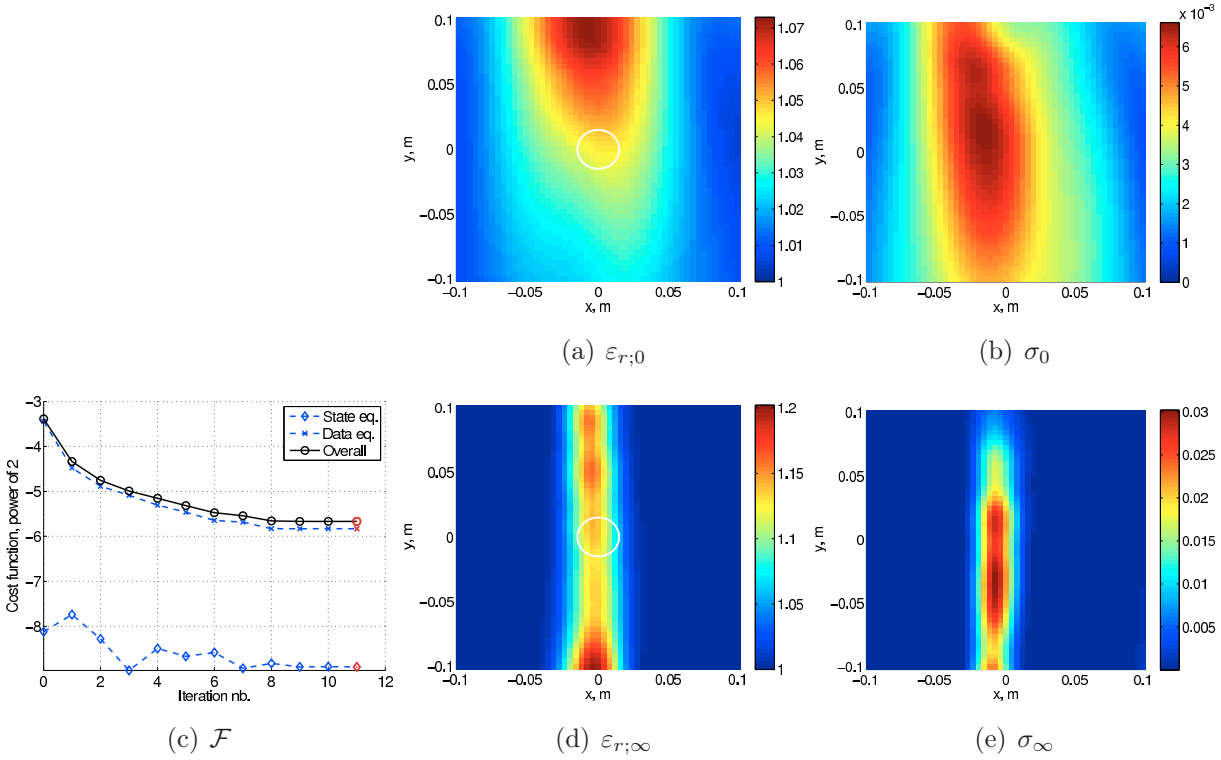

(a) $\varepsilon_{r;0}$ (b) σ_0

(c) $\mathcal{F}$ (d) $\varepsilon_{r;\infty}$ (e) σ_∞

FIGURE 3.33: *Inversion of the transmission configuration in* FIG. *3.31(c). Experimental results.*

$\lambda_0/6.7$, respectively, at 3 GHz.

For both the metallic and dielectric target cases, the results in FIG. 3.32 and FIG. 3.33,

respectively, show that using only transmission data with a small array aperture is insufficient for properly localizing the scatterer in down-range. This phenomenon was already observed with the Kirchhoff migration method in FIGS. 2.11-2.12, where the same configurations where actually used. Indeed, not even the coherent time-domain approach intrinsic to the Kirchhoff migration - supposedly more efficient for down-range localization than the multi-frequency incoherent approach of the inverse problem - led to a proper localization of the targets.

The results do not even change when a flat initial profile is used for the contrast, meaning that the lack of localization is not just in the initial estimate but rather in the information content of the transmission data. Nevertheless, as demonstrated in the next paragraph, the information available in the transmission data considerably enhances the inversion results when combined with the one in reflection.

3.6.4.4 Full configuration

While the two array-configuration, such as the one in FIG. 3.31, is still used here, the measurements to be inverted comprise all the retrodiffusion coefficients $S_{jj}|_{j=1,8}$ and $S_{ll}|_{l=9,\dots,15}$ in addition to the transmission data S_{jl}. In matrix form, this becomes

$$\mathbf{K}^{\text{full}} = \left[\begin{array}{cccc|cccc} S_{11} & \circ & \cdots & \circ & S_{19} & S_{1\,10} & \cdots & S_{1\,15} \\ \circ & S_{22} & \ddots & & S_{29} & S_{2\,10} & & S_{2\,15} \\ \vdots & & \ddots & \vdots & \vdots & & \ddots & \vdots \\ \circ & \cdots & \circ & S_{88} & S_{89} & S_{8\,10} & \cdots & S_{8\,15} \\ \hline S_{91} & S_{92} & \cdots & S_{98} & S_{99} & \circ & \cdots & \circ \\ S_{10\,1} & S_{10\,2} & & S_{10\,8} & \circ & S_{10\,10} & & \circ \\ \vdots & & \ddots & \vdots & \vdots & & \ddots & \vdots \\ S_{15\,1} & S_{15\,2} & \cdots & S_{15\,8} & \circ & \circ & \cdots & S_{15\,15} \end{array}\right] . \tag{3.81}$$

Although additional data, namely the $S_{jk}|_{j,k=1,\dots,8}$ can also be measured, they are not included here. This is due, on the one side, to their small added value in terms of information content with respect to the retrodiffusion data, and on the other to the fact that measuring them requires a different experimental configuration (the reflection one - see §1.3).

Metallic targets

The first configuration is the one already presented in FIG. 3.31(b). First, all the retrodiffusion coefficients are used for the inversion (that is, the diagonal elements of the matrix in (3.81)), ignoring the transmission data. The results in FIG. 3.34 show that two sides of the cylinder support are retrieved, those facing the arrays. Nonetheless, they appear elongated in the direction parallel to the arrays, while a strong ε_r spot is found within the support. This basically confirms the results found with the reflection configuration (*cf.* FIG. 3.15), although two main differences hold in this case: 1) here *two* arrays, each in reflection, illu-

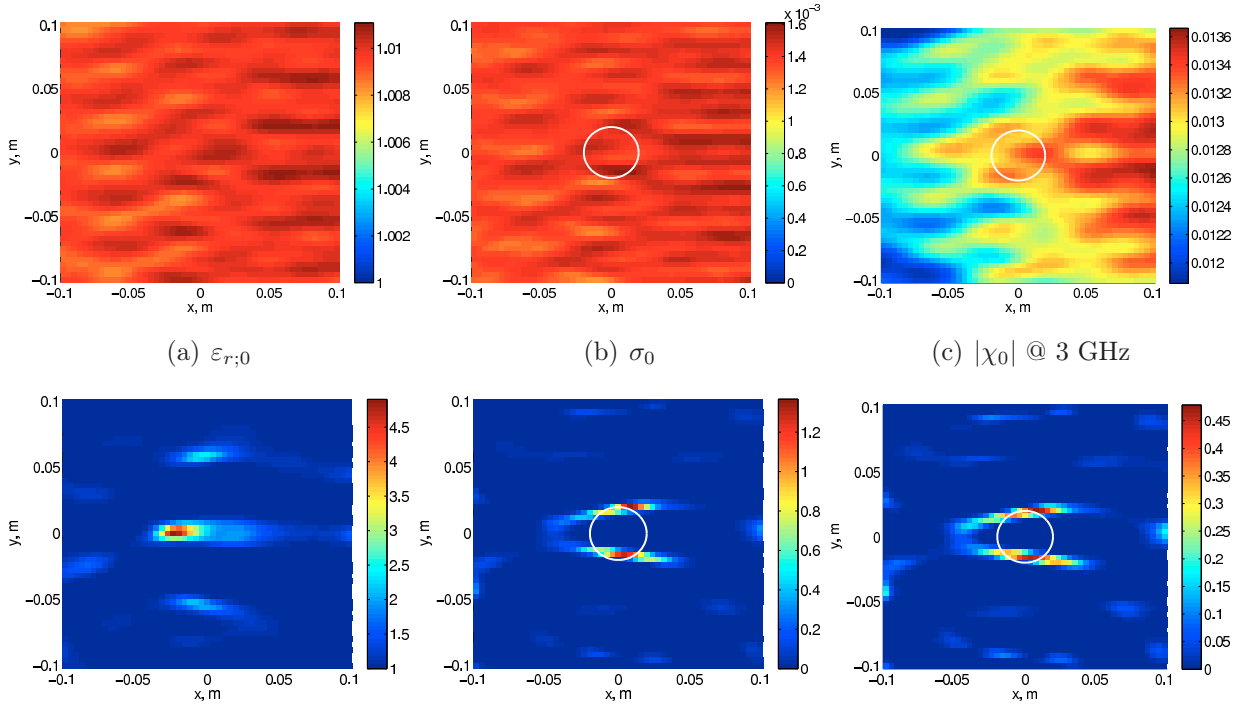

(a) $\varepsilon_{r;0}$ (b) σ_0 (c) $|\chi_0|$ @ 3 GHz

(d) $\varepsilon_{r;\infty}$ (e) σ_∞ (f) $d_{\text{pix}}/\delta_\infty$ @ 3 GHz

FIGURE 3.34: *Inversion of the configuration in* FIG. *3.31(b). Retrodiffusion data only. Experimental results.*

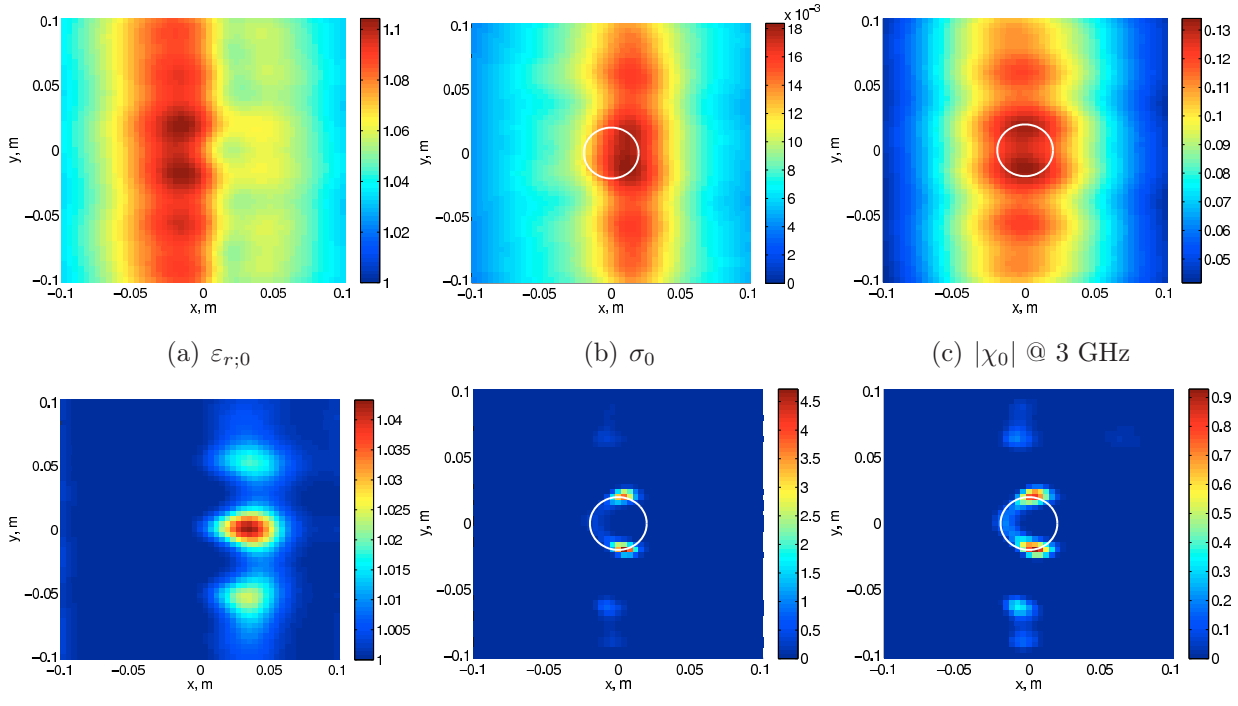

(a) $\varepsilon_{r;0}$ (b) σ_0 (c) $|\chi_0|$ @ 3 GHz

(d) $\varepsilon_{r;\infty}$ (e) σ_∞ (f) $d_{\text{pix}}/\delta_\infty$ @ 3 GHz

FIGURE 3.35: *Inversion of the configuration in* FIG. *3.31(b). Full data. Experimental results.*

minate the target, and 2) the data used here are only the retrodiffusion coefficients and not

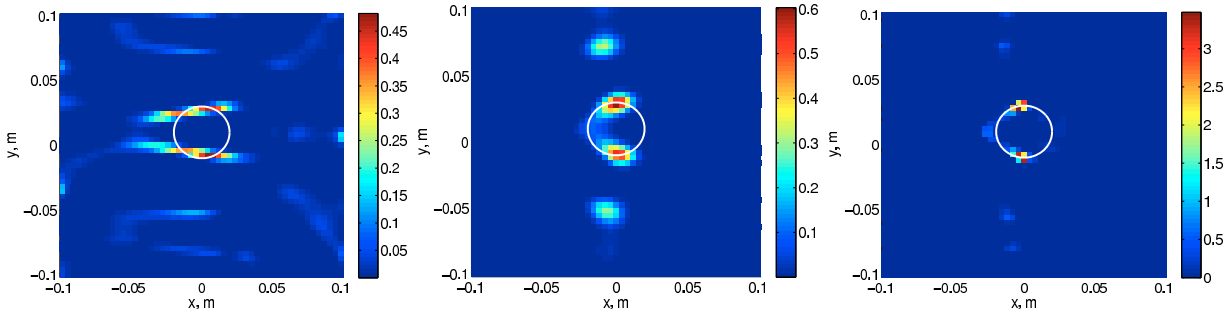

(a) Retrodif. config. (b) Full config., iteration 12 (c) Full config., final result

FIGURE 3.36: *Inversion results with synthetic data.* $d_{\text{pix}}/\delta_\infty$ *@ 3 GHz.*

the whole reflection matrix $(S_{jk}|_{j,k=1,\dots,8})$. The result with synthetic data in FIG. 3.36(a), very similar to the experimental one, confirms this remark.

A drastic improvement is obtained when the full data matrix (3.81) is used. The real part of the contrast is now practically zero, whereas σ has three hot spots, two at the front sides with respect to the arrays - much hotter than in FIG. 3.34(f) - and one laterally as well. Two more spots appear above and below the target, although much less strong. This is again confirmed with synthetic data in FIG. 3.36(b-c): after 12 iterations - approximately the same number of iterations needed in the experimental case to reach convergency - the skin depth profile (FIG. 3.36(b)) resembles very much the experimental one. Only, the absence of noise allows the algorithm to iterate much longer (more than 50 iterations) and to sharpen

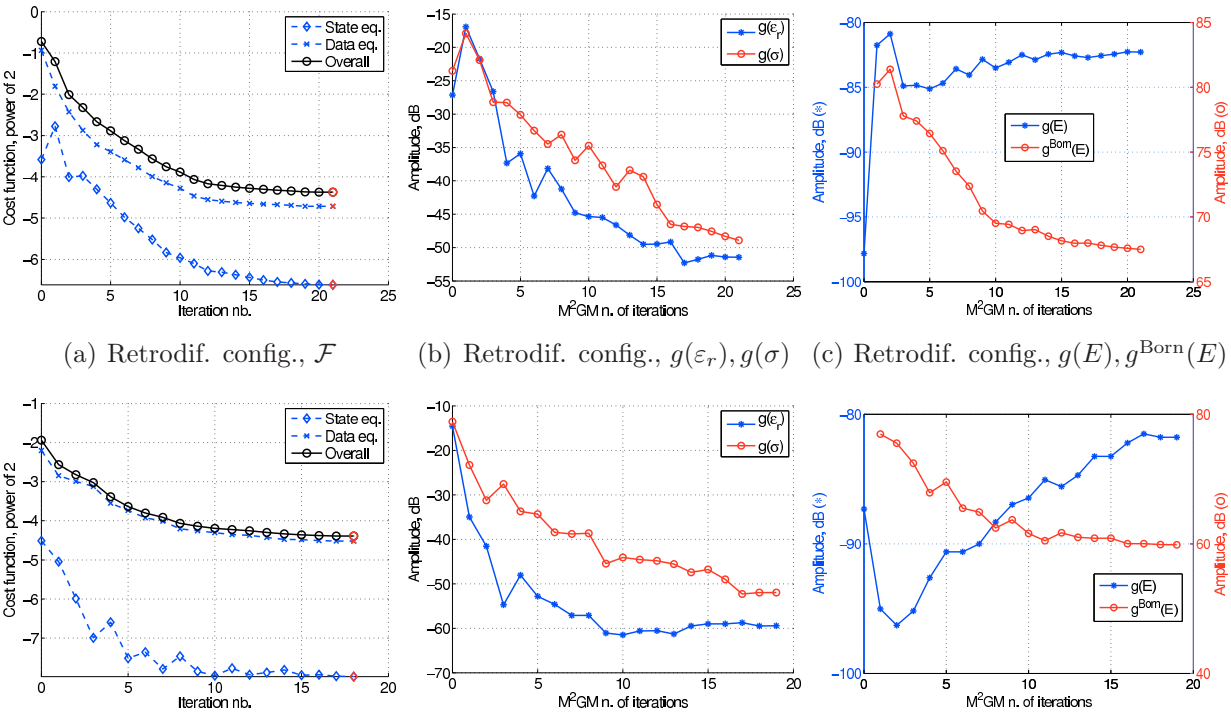

(a) Retrodif. config., $\mathcal{F}$ (b) Retrodif. config., $g(\varepsilon_r), g(\sigma)$ (c) Retrodif. config., $g(E), g^{\text{Born}}(E)$

(d) Full config., $\mathcal{F}$ (e) Full config., $g(\varepsilon_r), g(\sigma)$ (f) Full config., $g(E), g^{\text{Born}}(E)$

FIGURE 3.37: *Inversion of the configuration in* FIG. *3.31(b). Experimental results.*

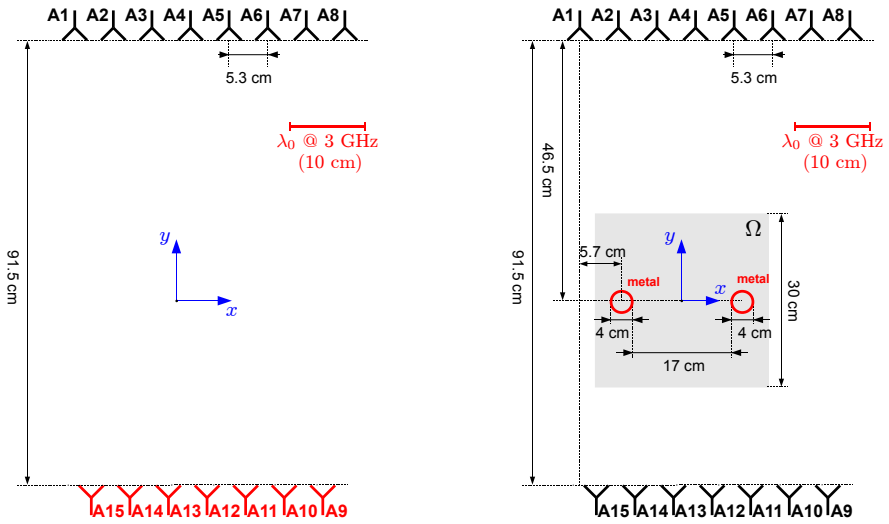

(a) Calibration (b) Scattering

FIGURE 3.38: *Inversion setup. Two metllic cylinders in full configuration.*

the three hot spots up to the result in FIG. 3.36(c). Although not under the scope of this work, notice that these spots would probably be avoided including in the cost function a regularization term that would limit the spatial gradient of the retrieved contrast (see for instance [132]), resulting in a smoother final profile.

As for the cost function and the gradients, shown in FIG. 3.37 for both the retrodiffusion and full configurations, it can first be remarked that $\mathcal{F}^{\Gamma}$ and $\mathcal{F}^{\Omega}$ are more unbalanced in the full case. Nonetheless, as seen before, the result is much better in this case, and the decrease of the gradients $g(\varepsilon_r)$ and $g(\sigma)$ overcomes by more than 10 dB the one in the retrodiffusion case. The behavior of $g(E)$ is somehow strange. For the retrodiffusion configuration, it undergoes a big +15 dB jump after the initial iteration, then it decreases by 4 dB at iteration 3, and finally slowly grows until convergency of the algorithm. On the other hand, for the full configuration $g(E)$ decreases by more than 5 dB after the first iteration and then rises by 10 dB approximatively until convergency. It is hard to explain why the latter behavior gives better results than the former. For the full configuration case, it might be that $\mathcal{F}(E)$ points to a local minimum after the first iteration, but then makes it to change direction toward another local minimum such that $g(E_2) > g(E_1)$, E_2 and E_1 being the values of E for the initial and final local minima, respectively. That is, the algorithm is smart enough to deviate from the initial minimum and point to another one which, although "less minimum" for E, better minimizes the whole $\mathcal{F}(\chi, E)$.

Similar results are found with the two-target configuration in FIG. 3.38. In FIG. 3.39, the scatterers are very well separated with three hot spots each, while $\mathcal{F}$ and $g(E)$ show the same behavior just commented.

Dielectric targets

The configuration presented in FIG. 3.31(c) is used here to test the retrodiffusion and full

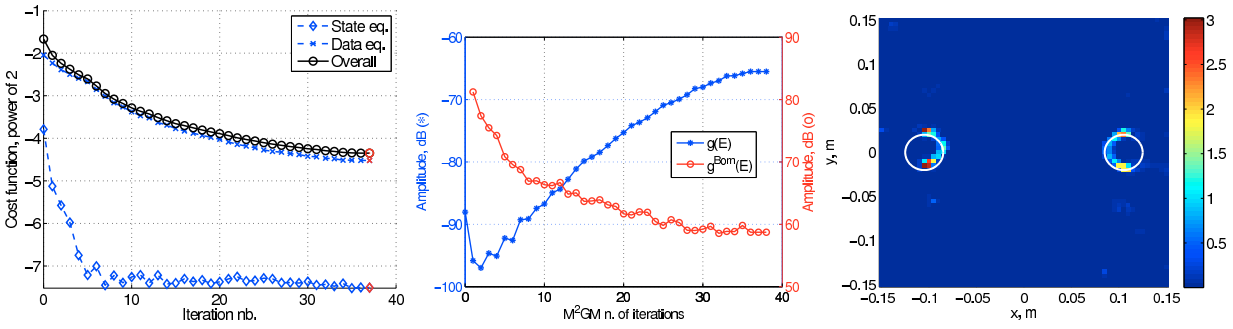

(a) $\mathcal{F}$ (b) $g(E), g^{\text{Born}}(E)$ (c) $d_{\text{pix}}/\delta_\infty$ @ 3 GHz

FIGURE 3.39: *Inversion of the configuration in* FIG. *3.38. Experimental results.*

configurations in the case of a purely dielectric target. With retrodiffusion data only, the inversion results are given in FIG. 3.40. The presence of two opposite arrays prevents the "focusing effect" observed in FIGS. 3.22-3.23 to occur. Nonetheless, two hot spots appear up and down the target location, and there is still ambiguity between real and imaginary parts of χ. Also, the shape of the target is not really retrieved.

Using full data improves the results, as shown in FIG. 3.41. The profiles are globally cleaner, and the shape of the target is better imaged; yet, parasite spots appear at a distance of 6-7 cm, probably linked (through a $\lambda_0/2$ relation) to a "dominant" frequency component between 2 and 2.5 GHz. A behavior similar to the one observed in the metallic

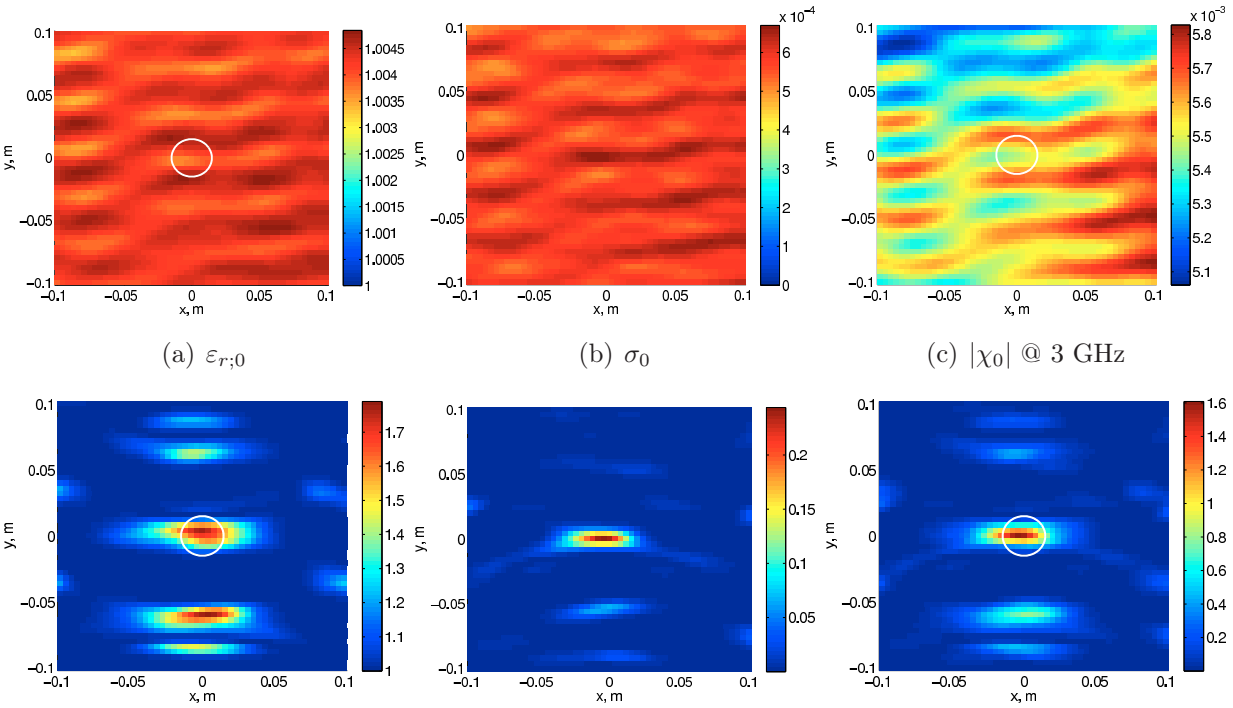

(a) $\varepsilon_{r;0}$ (b) σ_0 (c) $|\chi_0|$ @ 3 GHz

(d) $\varepsilon_{r;\infty}$ (e) σ_∞ (f) $|\chi|$ @ 3 GHz

FIGURE 3.40: *Inversion of the configuration in* FIG. *3.31(c). Retrodiffusion data only. Experimental results.*

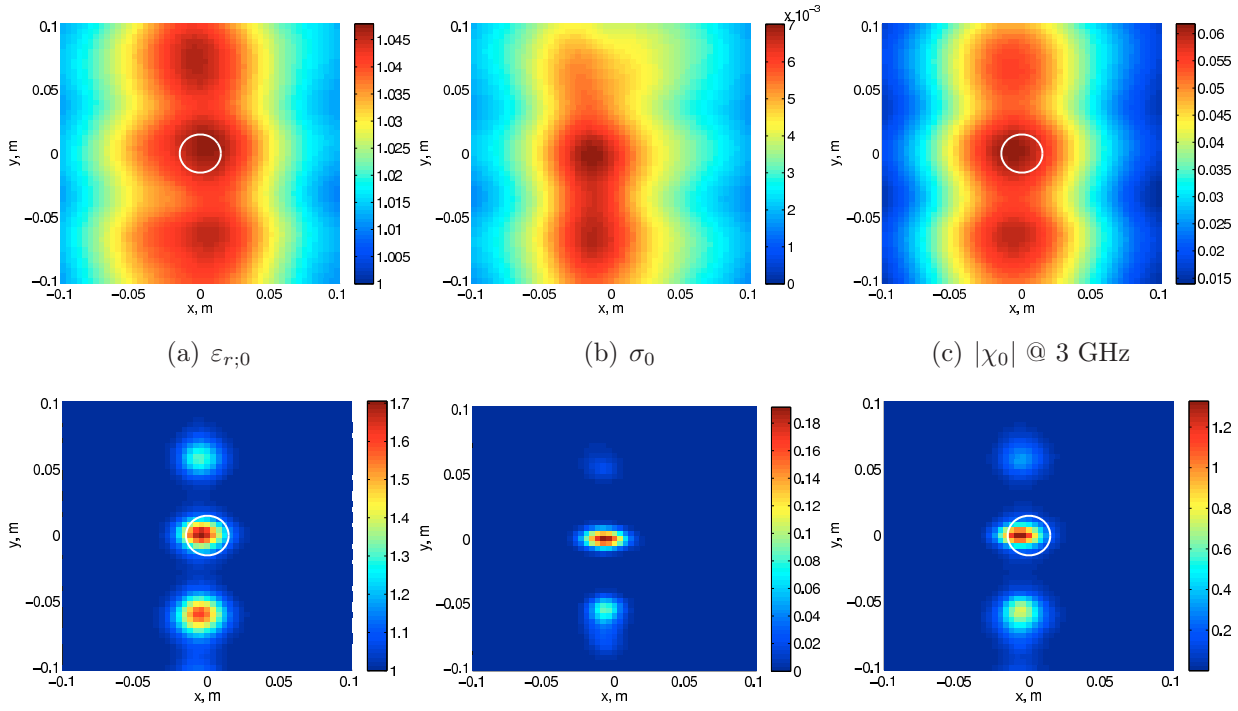

(a) $\varepsilon_{r;0}$ (b) σ_0 (c) $|\chi_0|$ @ 3 GHz

(d) $\varepsilon_{r;\infty}$ (e) σ_∞ (f) $|\chi|$ @ 3 GHz

FIGURE 3.41: *Inversion of the configuration in* FIG. *3.31(c). Full data. Experimental results.*

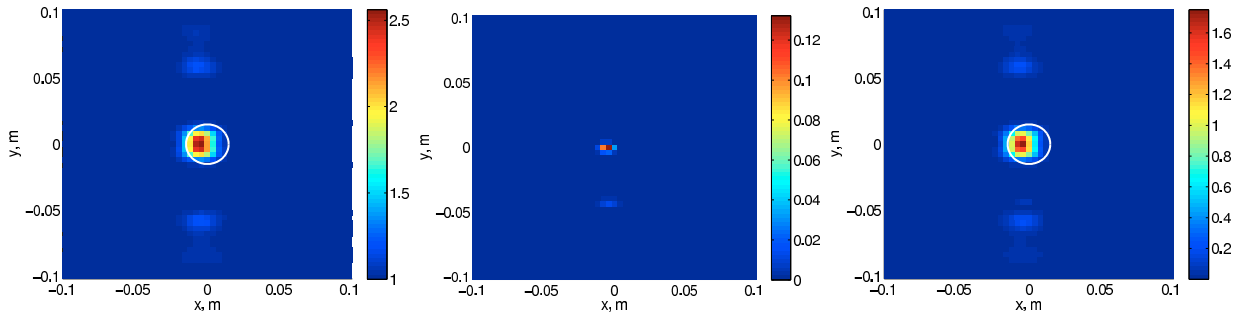

(a) $\varepsilon_{r;\infty}$ (b) σ_∞ (c) $|\chi_\infty|$ @ 3 GHz

FIGURE 3.42: *Inversion of the configuration in* FIG. *3.31(c). Full data. Synthetic results (ε_r=2).*

target case appears here: with synthetic data (FIG. 3.42), the absence of noise allows the algorithm to continue iterating and minimizing $\mathcal{F}$, leading to a reduction of the paraisite spots and to a cleaner image with a better estimate of the permittivity value. On the other hand, when noise is present, that is, in the experimental case, the algorithm reaches convergency before this refinement can take place.

Metallic and dielectric targets

Inverting a configuration with both a metallic and a dielectric target is a more difficult task. Whether the inversion procedure has enough resolution to resolve both, and whether the SNR is large enough for the same purpose, are the questions to be answered here.

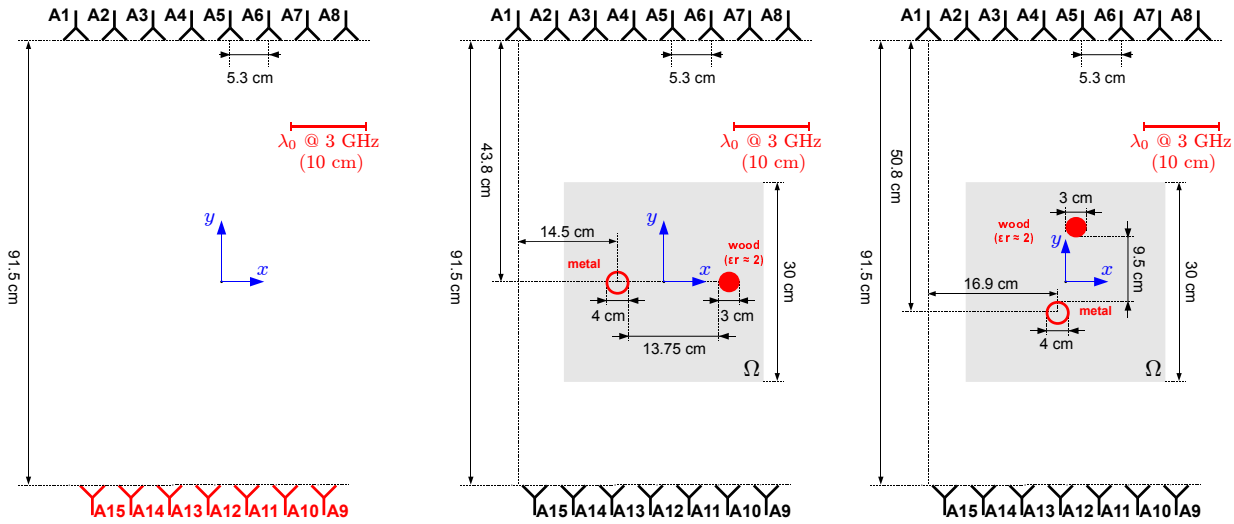

(a) Calibration (b) Scattering (cross-range configuration) (c) Scattering (down-range configuration)

FIGURE 3.43: *Inversion setup. Metllic and dielectric cylinders in full configuration.*

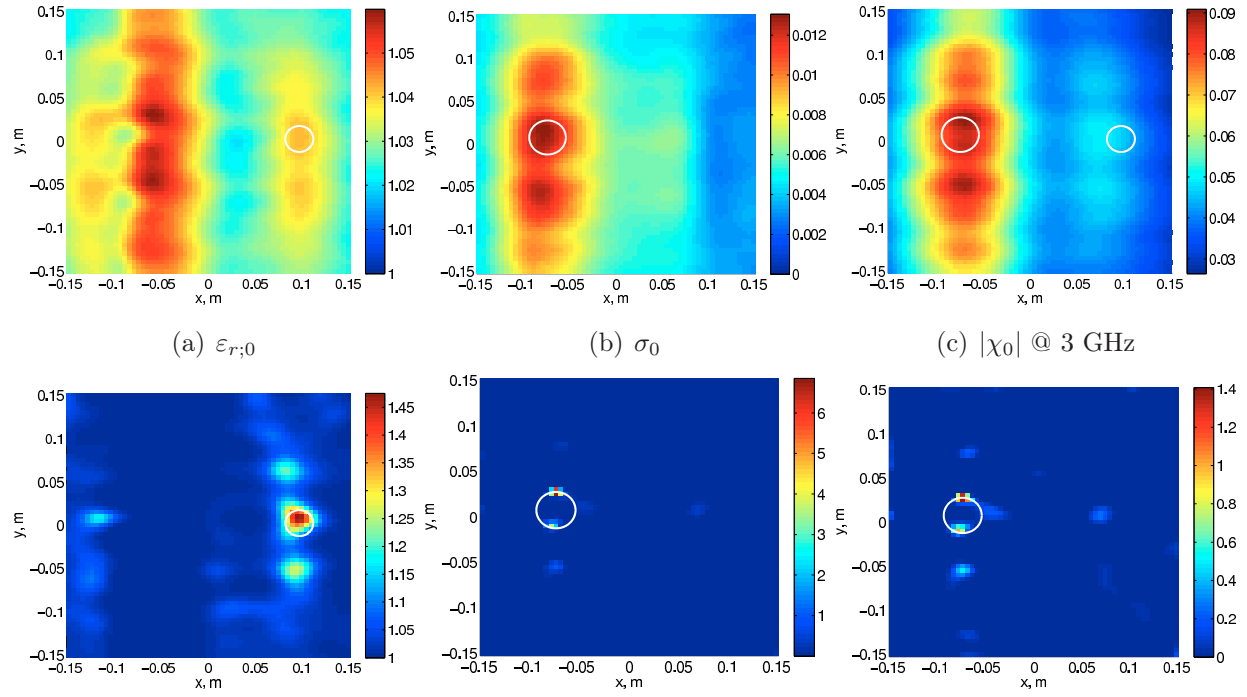

(a) $\varepsilon_{r;0}$ (b) σ_0 (c) $|\chi_0|$ @ 3 GHz

(d) $\varepsilon_{r;\infty}$ (e) σ_∞ (f) $d_{\text{pix}}/\delta_\infty$ @ 3 GHz

FIGURE 3.44: *Inversion of the configuration in* FIG. *3.43(b). Full data. Experimental results.*

The first configuration, shown in FIG. 3.43(b), has two targets spaced by 13.75 cm and placed roughly at mid-distance from the arrays. The experimental results are in FIG. 3.44. Since the back-propagation initial estimate, a hint on the nature of the targets seems to appear: although in FIG. 3.44(a) the metallic target position is "hotter" than the one of the wooden cylinder, due to the larger scattering power of the latter, the σ profile very well rejects the dielectric. As the iterations go, even the ϵ_r profile starts rejecting the metal,

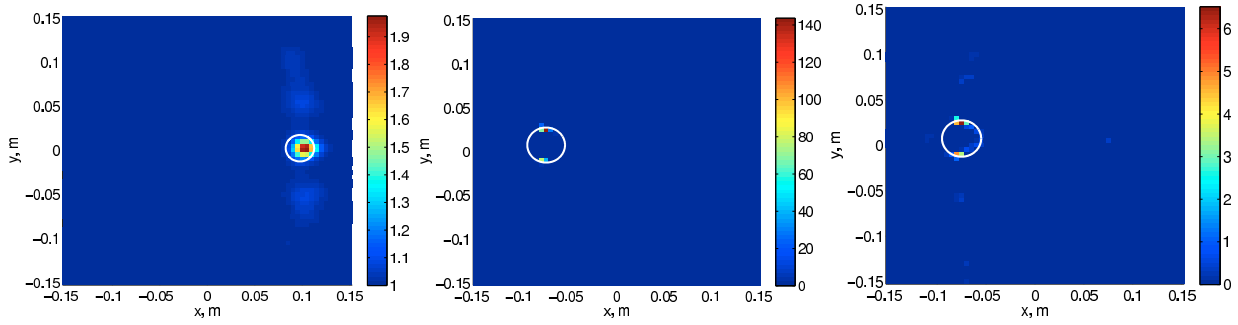

(a) $\varepsilon_{r;\infty}$ (b) σ_∞ (c) $d_{\text{pix}}/\delta_\infty$ @ 3 GHz

FIGURE 3.45: *Inversion of the configuration in* FIG. *3.43(b). Full data. Synthetic results ($\varepsilon_r = 2$ for the wooden cylinder).*

and finally both the targets are well imaged, at least coherently with the results of the single-target configurations just presented (FIG. 3.35 and FIG. 3.41). As for the synthetic data results in FIG. 3.45, they are of course much cleaner, because - as usual - the absence of noise allows the algorithm to perform additional iterations that refine further the retrieved profiles.

When the distance separating the targets is reduced, the results are still very good. As an example, in FIG. 3.46, the edge-to-edge distance is only 1 cm; still the targets are well separated (partially even from the very back-propagation) and their nature discriminated.

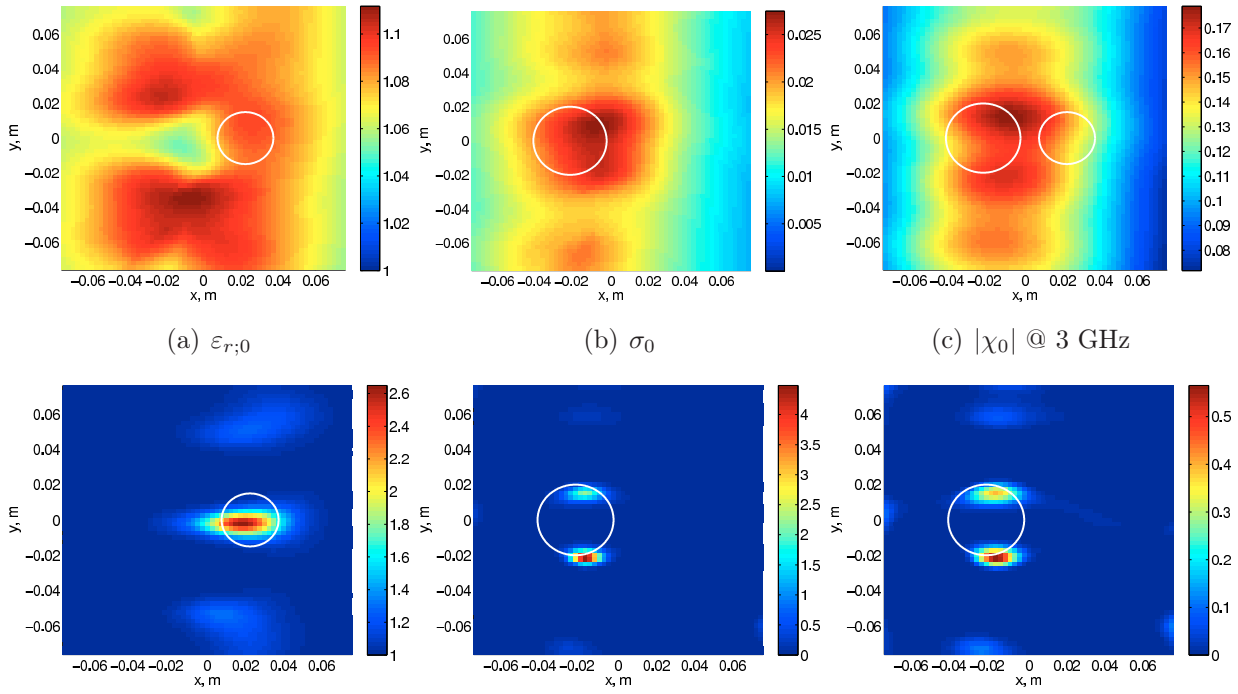

(a) $\varepsilon_{r;0}$ (b) σ_0 (c) $|\chi_0|$ @ 3 GHz

(d) $\varepsilon_{r;\infty}$ (e) σ_∞ (f) $d_{\text{pix}}/\delta_\infty$ @ 3 GHz

FIGURE 3.46: *Inversion of the configuration in* FIG. *3.43(b) but with an edge-to-edge target distance of 1 cm. Full data. Experimental results.*

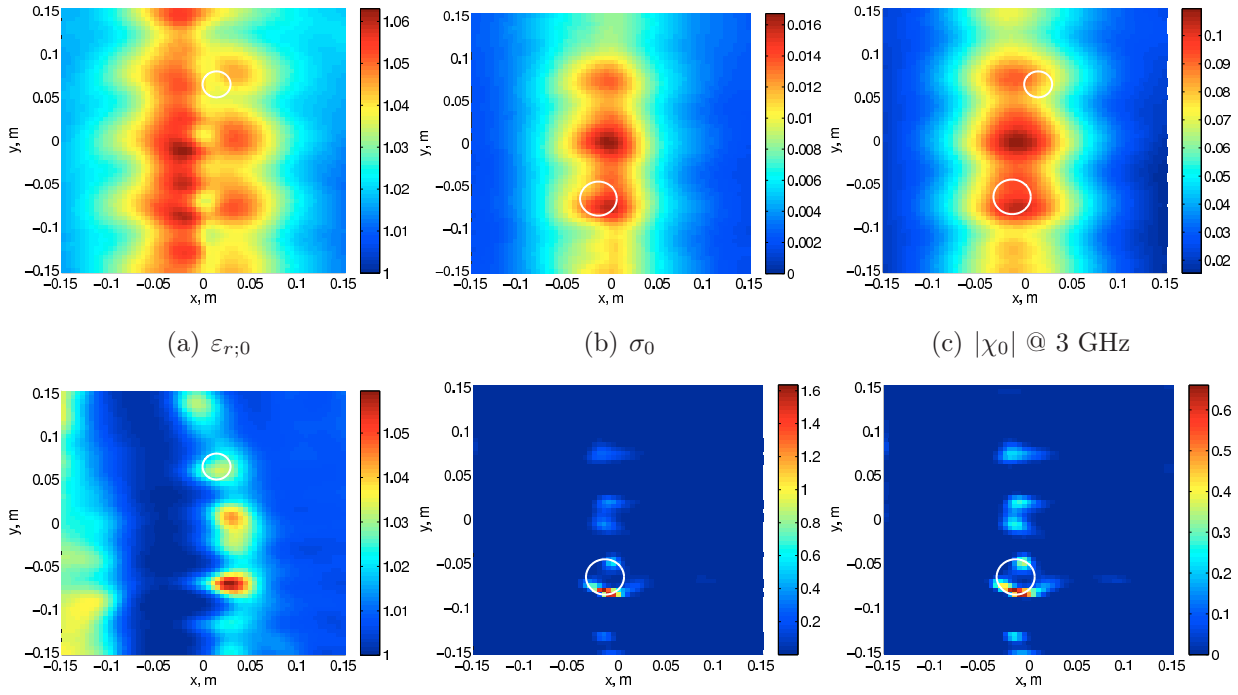

(a) $\varepsilon_{r;0}$ (b) σ_0 (c) $|\chi_0|$ @ 3 GHz

(d) $\varepsilon_{r;\infty}$ (e) σ_∞ (f) $d_{\text{pix}}/\delta_\infty$ @ 3 GHz

FIGURE 3.47: *Inversion of the configuration in* FIG. *3.43(c). Full data. Experimental results.*

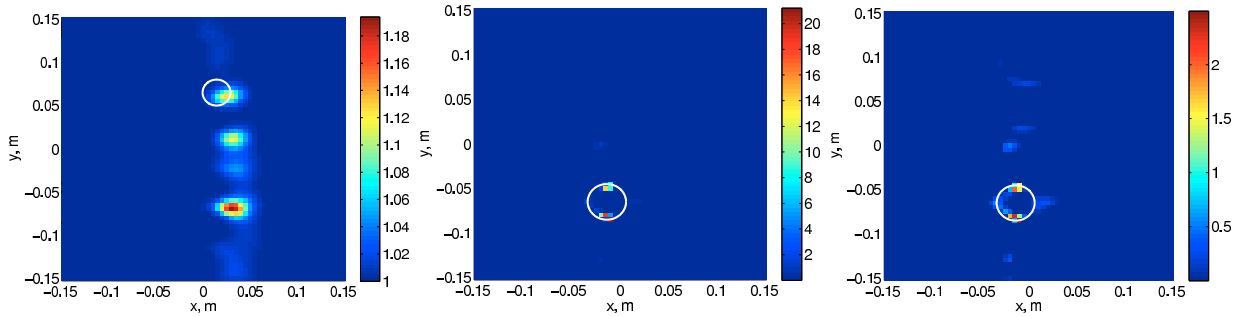

(a) $\varepsilon_{r;\infty}$ (b) σ_∞ (c) $d_{\text{pix}}/\delta_\infty$ @ 3 GHz

FIGURE 3.48: *Inversion of the configuration in* FIG. *3.43(c). Full data. Synthetic results ($\varepsilon_r = 2$ for the wooden cylinder).*

Similar results are also obtained if the distance is shrinked to 0 cm. When synthetic data are used (not shown), the results are in line with the previous ones, namely more iterations are performed before convergency and the retrieved profiles are cleaner than the experimental ones.

A different configuration is given in FIG. 3.43(c). The same targets are now placed along the down-range direction at a distance of 9.5 cm. Both the experimental results in FIG. 3.47 and the synthetic ones in FIG. 3.48 are not as good anymore. In fact, the targets shadow each other, due to the small array aperture, and the inversion works almost as if the wooden cylinder were only imaged by the upper array (array-1) and the metallic cylinder only by

the lower one (array-2).

In the down-range case, making the targets closer does not help the reconstruction. Still, the targets shadow each other and the dielectric one, in particular, is never imaged, not even with synthetic data.

Impact of the frequency bandwidth

Until now, the full available frequency band, namely [2-4] GHz, has been exploited for the inversion. Nonetheless, it must be understood how its width affects the results. Here, two among the previous test cases are considered. The metallic cylinder in reflection, whose configuration is in FIG. 3.13, and the metallic plus dielectric cylinders down-range setup with full data shown in FIG. 3.43(b). For both of them, the inversion has been run first at a single frequency, namely 2 GHz, then with 3 frequencies from 2 to 2.2 GHz, and finally with 11 frequency from 2 to 3 GHz, the frequency step being 10 MHz as for all the other results of the chapter.

The results, shown in FIGS. 3.49-3.50, attest the usefulness of an as-large-as-possible bandwidth. Indeed, especially for the full setup, the algorithm hardly performs any "significant" iteration when frequencies up to 2.2 GHz are employed. This is very different from the literature results obtaining satisfying reconstructions from singe-frequency data in circular configurations: here the small array configuration makes it mandatory to possess - and exploit - frequency diversity.

3.6.5 Conclusions

Several conclusions can be drawn from the results of this chapter. First of all, the incident field and far-field green function calibration seems very well suited to the line of measurement experimental setup. Its importance lies in the fact that the coefficients of the expansions are retrieved through experimental data measured in the same setup of the scattering experiment. Hence, antenna coupling and "interferences" of the medium are taken into account. The importance of modeling the receiving directivity of the antenna *via* a multipolar expansion of $\mathcal{G}^{\Gamma}$ is new and adds an important contribution to the calibration procedure, especially in the case of rather directive antennas as the ETS used here.

The inversion results based on this calibration have been classified according to the geometrical configuration of the array. It first appears that the reflection configuration, given a small measurement line with aperture angles around 40 deg, does not allow to retrieve enough information on the scatterers to reconstruct them properly. This can be expected for metallic targets, which because of their impenetrability are only partially retrieved. Nonetheless, dielectric targets are not properly imaged either, especially when their dimensions become comparable to λ_0.

Using transmission data only leads to completely wrong results. The data, again because of the small aperture, do not contain enough information for localizing the targets. Yet,

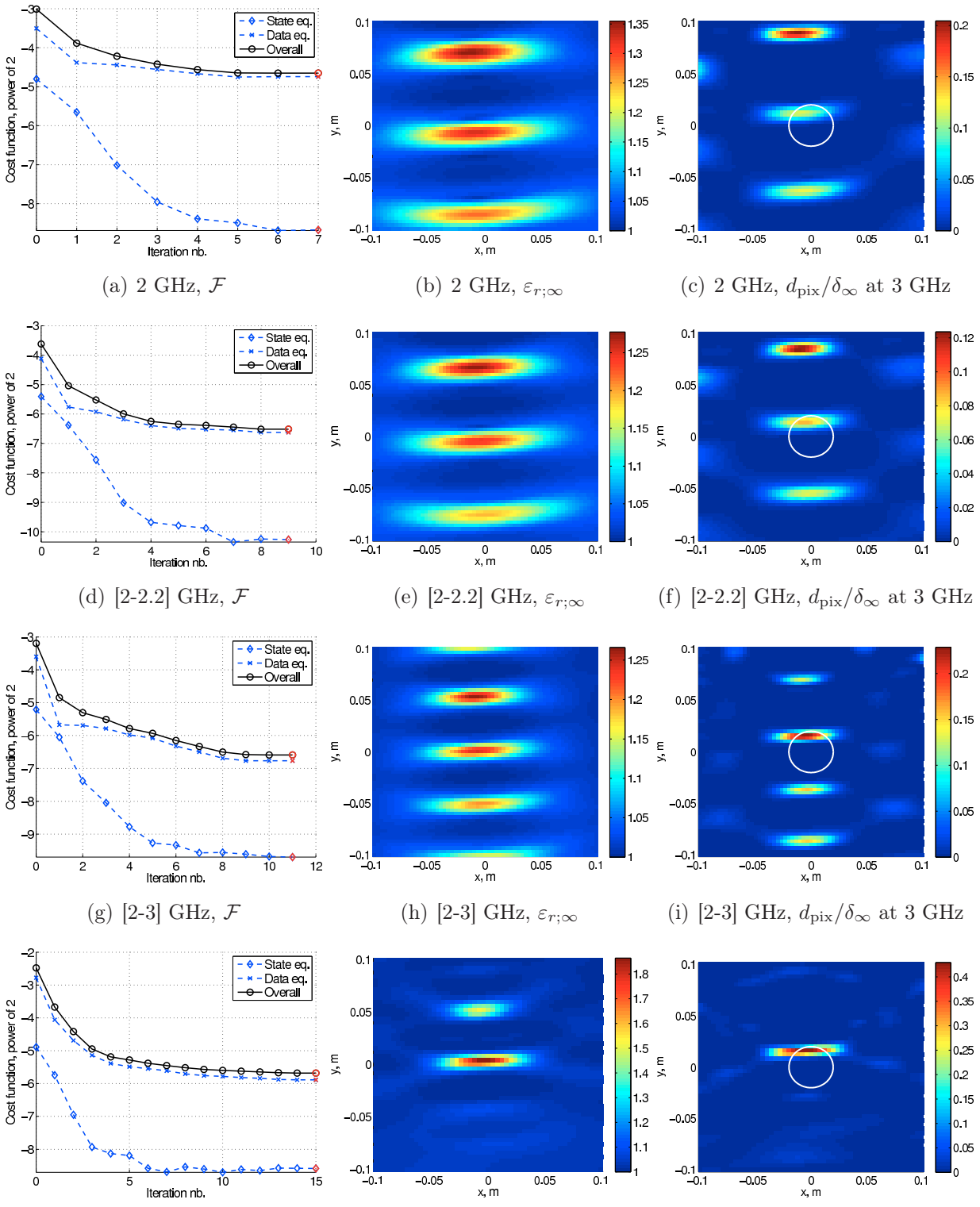

(a) 2 GHz, $\mathcal{F}$ (b) 2 GHz, $\varepsilon_{r;\infty}$ (c) 2 GHz, $d_{\text{pix}}/\delta_\infty$ at 3 GHz

(d) [2-2.2] GHz, $\mathcal{F}$ (e) [2-2.2] GHz, $\varepsilon_{r;\infty}$ (f) [2-2.2] GHz, $d_{\text{pix}}/\delta_\infty$ at 3 GHz

(g) [2-3] GHz, $\mathcal{F}$ (h) [2-3] GHz, $\varepsilon_{r;\infty}$ (i) [2-3] GHz, $d_{\text{pix}}/\delta_\infty$ at 3 GHz

(j) [2-4] GHz, $\mathcal{F}$ (k) [2-4] GHz, $\varepsilon_{r;\infty}$ (l) [2-4] GHz, $d_{\text{pix}}/\delta_\infty$ at 3 GHz

FIGURE 3.49: *Inversion of the configuration in* FIG. *3.13. Experimental results for four different frequency bands. Reflection data.*

when transmission data are added to the reflection, or retrodiffusion, ones, the results are satisfying. The algorithm can now image both dielectric and metallic targets, although

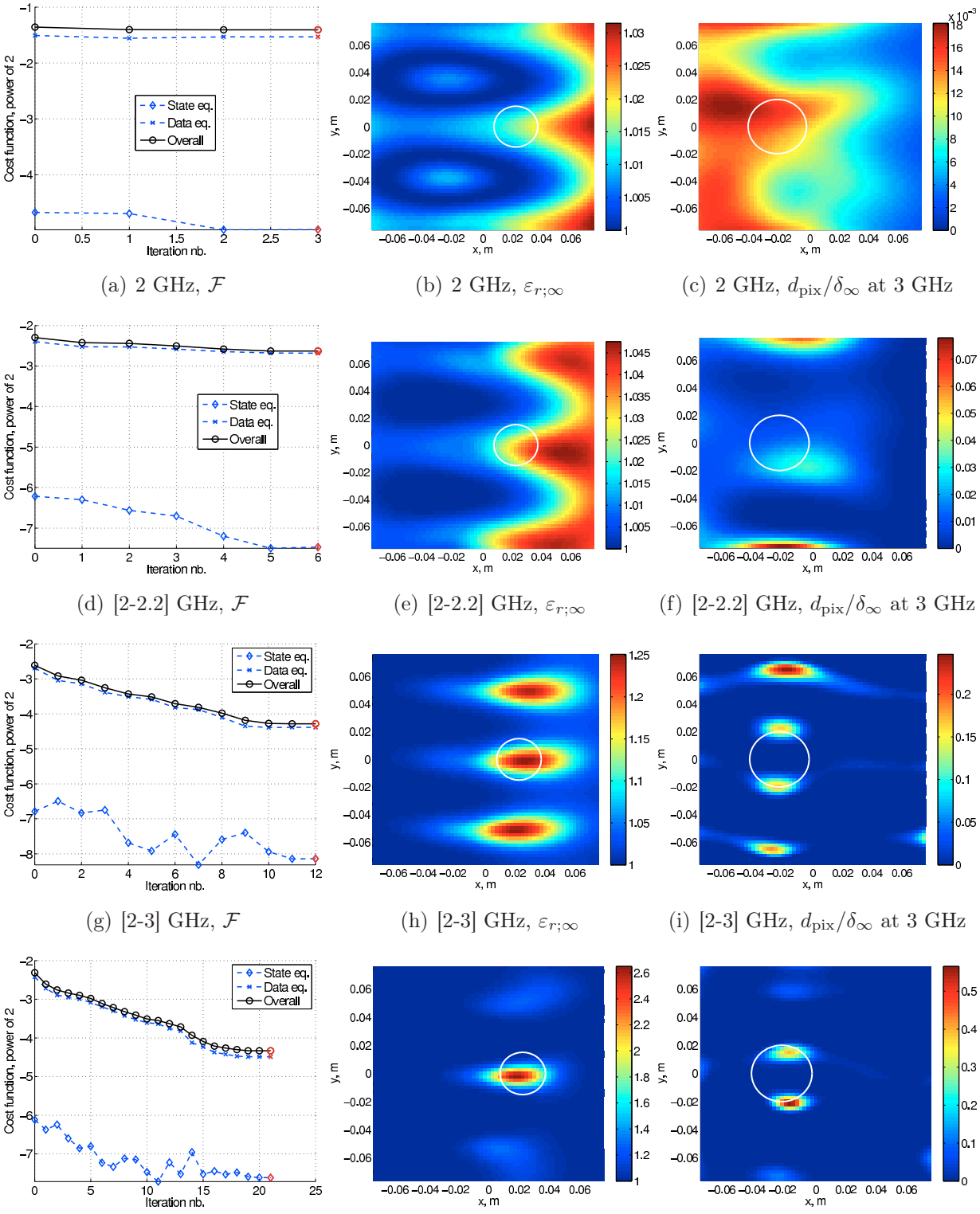

(a) 2 GHz, $\mathcal{F}$ (b) 2 GHz, $\varepsilon_{r;\infty}$ (c) 2 GHz, $d_{\text{pix}}/\delta_\infty$ at 3 GHz

(d) [2-2.2] GHz, $\mathcal{F}$ (e) [2-2.2] GHz, $\varepsilon_{r;\infty}$ (f) [2-2.2] GHz, $d_{\text{pix}}/\delta_\infty$ at 3 GHz

(g) [2-3] GHz, $\mathcal{F}$ (h) [2-3] GHz, $\varepsilon_{r;\infty}$ (i) [2-3] GHz, $d_{\text{pix}}/\delta_\infty$ at 3 GHz

(j) [2-4] GHz, $\mathcal{F}$ (k) [2-4] GHz, $\varepsilon_{r;\infty}$ (l) [2-4] GHz, $d_{\text{pix}}/\delta_\infty$ at 3 GHz

FIGURE 3.50: *Inversion of the configuration in* FIG. *3.43(b) but with an edge-to-edge target distance of 1 cm. Experimental results for four different frequency bands. Full data.*

for the latter a better SNR would help in retrieving the exact shape and in killing some

smaller, yet existing, parasite spots. Also, the resolution power is enough for distinguishing the nature of the scatterers in the case both metals and dielectrics are to be imaged. Yet, this all does not work when targets are placed in down-range, since they practically shadow each other due - again! - to the small array aperture.

A final comment on the effect of the bandwidth is of importance. Given the very small array aperture, frequency diversity plays an incontrovertible role in converging to a pertinent solution. This is not the case when complete data retrieved in a setup with antennas encircling the scatterers are used, since the availability of additional frequencies basically allows to retrieve finer details (making it possible, for instance, to adopt the frequency hopping approach) but does not radically change the convergency properties of the algorithm. Yet, it is not possible to conclude that frequency diversity supplies to the lack of aperture of the array. The Ewald's circle from a theoretical point of view (§3.4) and the experimental results show indeed that the missing spatial information is not equivalent to and is not brought back by additional frequencies.

Chapter 4

Inversion in cluttered media exploiting the DORT method

In the previous chapter it has been experimentally demonstrated that quantitative inversion methods are an effective tool for retrieving the properties of one or more scatterers. This is true as long as the quantity of retrieveable information in the available data is sufficient and as long as the SNR is high enough. As a consequence, when the scatterers to be imaged are in cluttered media, the signal scattered by clutter acts as noise on the data, seriously endagering the efficacity of non-linear inversion algorithms. In such cases, the most straightforward approach for the inversion consists in assuming free-space conditions or, in some cases, in modeling the propagating medium as a homogeneous one with a known background permittivity $\varepsilon_{r;\mathrm{b}} \neq 1$[1]. Yet, if the mismatch between this simplistic model and the real one, including multiple scattering between the target(s) of interest and the surrounding clutter, becomes too important, erroneous results are produced. Equivalently, it is the very low SNR - in this case Signal-to-Clutter Ratio (SCR) - that produces failure.

A classical approach to inversion in clutter consists in filtering the data to remove as much multiple-scattering as possible, enhancing in turn the SCR. The filtered data can then be inverted through a free-space model, leading in some cases to clean reconstructions. A remarkable example is *e.g.* given in the work by Aubry and Derode [158] that focuses on qualitative reconstructions. These filters, nevertheless, are based on statistical properties of clutter and their impact is more and more effective when the quantity of independent available data increases, *e.g.* in the case of a large array with many TX/RX antennas.

The approach that motivates this chapter relies on a purely deterministic frame. It is mainly based on the fact that the response to a wave focusing onto the target of interest contains less multiple-scattering, and has therefore a better SCR, than the response to a rather isotropic wave illuminating both the clutter and the target itself. As a consequence, inverting such a wave within a free-space model might lead to improved reconstructions of the scatterer onto which focusing occurs. As for the way of generating focusing waves, the

[1] In practice, this is simply done by modifying the Green function operators $\mathcal{G}^{\Gamma}$ and $\mathcal{G}^{\Omega}$.

effectiveness of Time Reversal-based methods has been validated in §2. The DORT method, in particular, is a good candidate for its time-harmonic nature - consistent with the multi-frequency inversion method - and for its ability to generate waves focusing selectively on different targets.

The starting point for this work are the results provided by Dubois *et al.* in [32], where the DORT method is used to regularize the inversion procedure. The geometrical configuration of interest, as done in [32], is here the measurement line (*e.g.* for subsurface sensing applications). Within this frame, the way a DORT-based cost function $\mathcal{F}^{\mathrm{DORT}}$ is built and, if needed, is used to regularize the "regular" one is first exposed. Then, several parametric analyses are carried on, each one validated using synthetic data. These include different usages of $\mathcal{F}^{\mathrm{DORT}}$ and the impact of the measurement line size.

4.1 The DORT cost function $\mathcal{F}^{\mathrm{DORT}}$

4.1.1 TX beamforming

Consider an antenna array with J antennas in reflection. In the case of one scatterer in a cluttered medium, it has been shown in §2.3.3 that the DORT method allows to retrieve, through the SVD of the inter-element matrix $\mathbf{K}$, a singular vector that, if back-propagated into the same medium, focuses onto the scatterer. Such vector, $\mathbf{v}_1$, is associated to the largest singular value, λ_1. While to each array antenna corresponds a vector of "regular" incident fields

$$\mathbf{E}^{\mathrm{i}}(\vec{r}) = \left[E_1^{\mathrm{i}}(\vec{r})\ E_2^{\mathrm{i}}(\vec{r})\ \ldots\ E_J^{\mathrm{i}}(\vec{r})\right]\ , \tag{4.1}$$

a unique *DORT incident field* can be defined as

$$E^{\mathrm{i;\,DORT}}(\vec{r}) \triangleq \sum_{j=1}^{J} v_{1;j} E_j^{\mathrm{i}}(\vec{r}) = \mathbf{v}_1^T \mathbf{E}^{\mathrm{i}}(\vec{r}) \quad \vec{r} \in \Omega\ . \tag{4.2}$$

The scattered fields associated to $E^{\mathrm{i;\,DORT}}(\vec{r})$ are then the components of the vector

$$\mathbf{E}^{\mathrm{s;\,DORT}}|_{\Gamma} = \left[E^{\mathrm{s;\,DORT}}(\vec{r}_1^{\,\Gamma})\ E^{\mathrm{s;\,DORT}}(\vec{r}_2^{\,\Gamma})\ \ldots\ E^{\mathrm{s;\,DORT}}(\vec{r}_J^{\,\Gamma})\right]^T \triangleq \mathbf{K}\mathbf{v}_1 = \lambda_1 \mathbf{u}_1\ , \tag{4.3}$$

where $\mathbf{K}$ is the measured inter-element matrix. A new cost function $\mathcal{F}^{\mathrm{DORT}}$ can therefore be built by replacing the "regular" incident field $E_{j,p}^{\mathrm{i}}$ and the measured scattered fields $E_{j,p}^{\mathrm{s;meas}}$ in (3.34) by the new DORT ones just defined.

From an implementation point of view, the DORT incident field must be evaluated through (4.2) before the iterative minimization starts; then, the whole algorithm is unchanged except that the number of views is now

$$J \leftarrow J^{\mathrm{DORT}} = 1\ . \tag{4.4}$$

4.1.2 RX beamforming

A slightly different approach also exists. Since DORT is essentially a beamforming method, it is possible to perform such beamforming at reception, rather than at transmission. Thus, for each incident field $E_j^{\mathrm{i}}(\vec{r})|_{j=1,\ldots,J}$, the received scattered fields $E_j^{\mathrm{s}}(\vec{r}_k^{\,\Gamma})|_{k=1,\ldots,K}$ ($K = J$ in a reflection configuration) can be recombined by

$$E_j^{\mathrm{s;\,DORT}} \triangleq \sum_{k=1}^{K} u_{1;k}^{*} E_j^{\mathrm{s}}(\vec{r}_k^{\,\Gamma}) \ , \tag{4.5}$$

forming the *DORT scattered field* row-vector

$$\mathbf{E}^{\mathrm{s;\,DORT}}|_{\Gamma} \triangleq \mathbf{u}_1^H \mathbf{K} = \lambda_1 \mathbf{v}_1^H \ . \tag{4.6}$$

Notice that due to reciprocity and linearity of the electric field, the scattered fields in (4.6) and (4.3) are identical.

From the implementation point of view, only the Green function operator $\mathcal{G}^{\Gamma}$ must be modified according to

$$E_j^{\mathrm{s;\,DORT}} = \sum_{k=1}^{K} u_{1;k}^{*} E_j^{\mathrm{s}}(\vec{r}_k^{\,\Gamma}) = \sum_{k=1}^{K} u_{1;k}^{*} \mathcal{G}_k^{\Gamma}\left(\chi E_j\right) = \mathcal{G}^{\Gamma;DORT}\left(\chi E_j\right) \ , \tag{4.7}$$

where, in virtue of the linearity of $\mathcal{G}^{\Gamma}$, the new DORT far-field Green operator is defined as

$$\mathcal{G}^{\Gamma;DORT} \triangleq \sum_{k=1}^{K} u_{1;k}^{*} \mathcal{G}_k^{\Gamma} \ . \tag{4.8}$$

While the number of views is still J, the number of receptions are now

$$K \leftarrow K^{\mathrm{DORT}} = 1 \ . \tag{4.9}$$

4.1.3 About the computational burden

Although TX and RX beamforming may seem equivalent as applied to the inversion frame, they are definitely not in terms of computational burden. Indeed, at least in the most common implementations of inverse algorithms, the number of operations to be performed increases much more rapidly with the number of sources than with the number of receivers. To show this, let us focus on the convolution products between the Green function operators, $\mathcal{G}^{\Gamma}$ and $\mathcal{G}^{\Omega}$, and the contrast χE. Such products are evaluated for the computation of the gradients and during the line search (*cf.* §3.3). Their number is

$$\begin{aligned} &\mathcal{G}^{\Gamma}(\chi E) : \text{one per source and per receiver} \\ &\mathcal{G}^{\Omega}(\chi E) : \text{one per source} \end{aligned} \tag{4.10}$$

where it should also be remarked that the latter computation is heavier since $\mathcal{G}^{\Omega}$ has a singularity requiring a "special" treatment (see *e.g.* [142]). With $J = K$ TX/RX antennas,

then, the standard inversion procedure requires $JK + J$ convolution products, whereas RX beamforming needs $2J$ and TX beamforming only $K + 1$. The gain in terms of operations reaches $(1 + K)/2$ and J for RX and TX beamforming, respectively.

In addition to this, TX beamforming is even more appealing when the M^{2}GM algorithm is used. The reason lies in the fact that at each CG iteration one state equation per source is solved, which despite the rapidity of the solver adds a non-negligeable burden.

4.2 Regularized cost function

As just discussed, running an inversion using $\mathcal{F}^{\mathrm{DORT}}$ is very appealing both from the computational and the theoretical point of view. Despite this, since the number of data is reduced by a factor J (at least if only one DORT singular space is used), it might be argued that the available information contained in the data undergoes the same scaling (*cf.* §3.4). Hence, a trade-off appears between the gain in SNR and the available information contained in the data. In order not to renounce to have the whole available information and an improved SCR, it might be a good idea to *regularize* the cost function $\mathcal{F}$ through the DORT one, $\mathcal{F}^{\mathrm{DORT}}$, as reported in [32].

The new cost function can then be written in one of two ways,

$$\mathcal{F}^{\mathrm{reg}} = \mathcal{F} + \kappa \mathcal{F}^{\mathrm{DORT}} \tag{4.11}$$

$$\mathcal{F}^{\mathrm{reg}} = \mathcal{F} \left(\mathcal{F}^{\mathrm{DORT}}\right)^{\kappa} \tag{4.12}$$

corresponding respectively to an additive and a multiplicative regularization approach with $0 < \kappa < \infty$. The gradients must of course be adapted to the new expression, as well as the line search procedure.

Concerning the choice of κ, the usual debate can be led. Nonetheless, it must be stressed out that although in the multiplicative approach κ is in most cases set to 1 "automatically" (see *e.g.* [132, 159]), it does play a role in the minimization and an optimal value should be sought. It could also be possible to have an iteration-dependent κ value, for instance by setting

$$\kappa_n = \kappa^{'} \frac{\mathcal{F}}{\mathcal{F}^{\mathrm{DORT}}} \ , \tag{4.13}$$

but still an optimal value for $\kappa^{'}$ shoud be identified.

Finally, notice that either the TX or the RX $\mathcal{F}^{\mathrm{DORT}}$ can be used in (4.11) and (4.12). The latter being advantageous from a computational point of view as just explained, and the data being the same in either case, the TX approach is the most suitable one.

4.3 Numerical experiments

The numerical experiments performed to validate the use of $\mathcal{F}^{\mathrm{DORT}}$ are relative to the measurement line setup in Fig. 4.1. An antenna array working in reflection images a

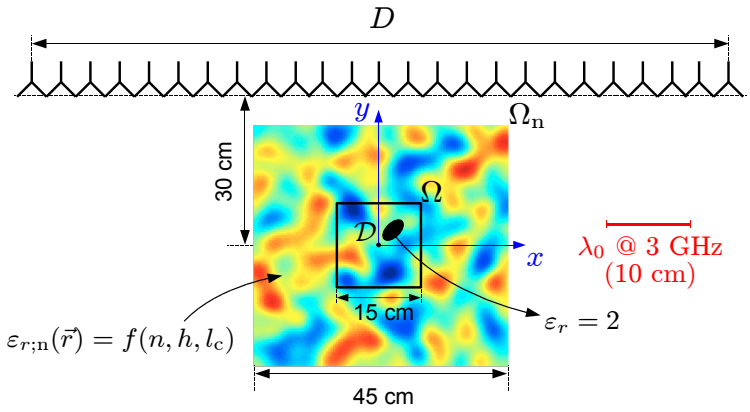

FIGURE 4.1: *Measurement line setup used for the numerical experiments. The noise profile is described by (4.14); the scatterer permittivity is* $\varepsilon_r = 2$.

decentrated and slanted elliptic scatterer with $\varepsilon_r = 2$ placed at slightly less than 30 cm down-range. The target is placed into a cluttered medium Ω_n whose dimensions are 45×45 cm^2. The inversion region Ω, where the object is sought, is much smaller than Ω_n and its size has been set to 15×15 cm^2 ($1/9^{\text{th}}$ the area of Ω_n).

Clutter is generated as follows. The conductivity is set to 0, whereas the real part of the permittivity is

$$\varepsilon_{r;n}(\vec{r}) = n + h\,a\,(\vec{r}) \quad \vec{r} \in \Omega_n - \mathcal{D}\ , \tag{4.14}$$

where n is the mean value of the profile, h its standard deviation, and a a random number with a centered gaussian distribution with standard deviation equal to 1. The spatial FFT of $a(\vec{r})$, hence of $\varepsilon_{r;n}$, has a gaussian shape ruled by the correlation length l_c, whose value determines the characteristic spatial scale of the profile. This choice for the noise profile is meant to mimick scenarii typical of medical imaging (*e.g.* breast imaging for cancer detection) or of subsurface imaging (*e.g.* geophysical prospection). An example of profile and distribution of $\varepsilon_{r;n}$ values for a given clutter realization is shown in FIG. 4.2(a) and FIG. 4.2(b), respectively. As for the parameters of the clutter realizations used in the chapter and summarized in TAB. 4.1, the chosen l_c values correspond to a clutter distribution in the resonance regime (large l_c, `noise3`), in the homogenization domain (small l_c, `noise2`), and in an intermediate regime between the two (`noise1`).

	n	h	l_c	λ_0/l_c at 2 GHz
`noise1`	1	0.08	2.5 cm	6
`noise2`	1	0.12	0.8 cm	≈ 19
`noise3`	1	0.15	7.5 cm	2

TABLE 4.1: *Parameters, with respect to (4.14), of the clutter realizations used in the following.*

The background relative permittivity outside the clutter domain is $\varepsilon_{r;b} = 1$ and, as in [32], it is assumed that the mean permittivity value of clutter is known. Hence, to be able to compare the results with those in [32] - where a subsurface configuration with

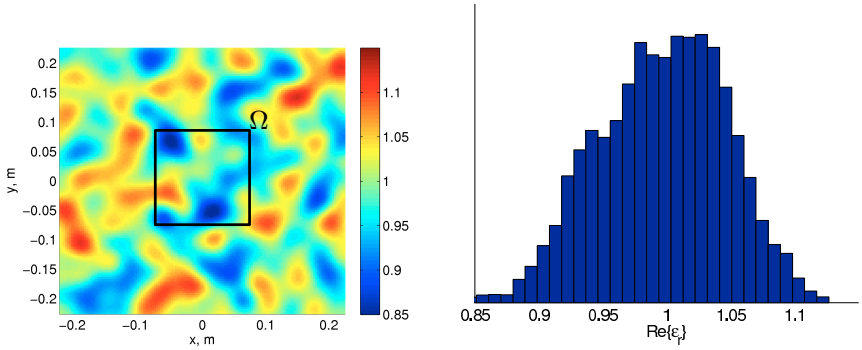

(a) (b)

FIGURE 4.2: *(a) Profile of the clutter realization* `noise1` *and (b) histogram of the* $\varepsilon_{r;\mathrm{n}}$ *values.*

$\varepsilon_{r;\mathrm{b}} = n > 1$ is used - n is set to 1. Although this choice leads to physically unrealistic $\varepsilon_{r;\mathrm{n}} < 1$ values, the behavior of the inversion algorithm is not altered from a numerical point of view.

As for the inversion algorithm, the multi-frequency formulation defined in §3.3.1 and applied throughout the previous chapter is used here. The positivity constraint, in particular, is imposed as done in [32] with respect to the $\varepsilon_{r;\mathrm{b}}$ value. Finally, due to the dielectric nature of the target and to the partial complementarity between real and imaginary parts of χ already observed in §3.6.4, the problem is regularized by restraining the inversion to purely dielectric scatterers. Although this choice does constitute a simplification, it does not result in a loss of generality when one keeps in mind the goal of this study, a comparison between DORT and standard inversion approaches.

4.3.1 Noiseless inversion: TX vs. RX beamforming

Regardless of the computational considerations discussed in §4.1.3, it is important to investigate which - if any - between the TX and RX beamforming approaches leads to better inversion results. Indeed, despite the DORT scattered field vectors (4.6) and (4.3) are identical, it might be that placing the diversity at reception (TX beamforming) be more advantageous than placing it at emission (RX beamforming), or vice versa (due *e.g.* to a different handling of sources and receivers within the inversion algorithm).

The geometric configuration is the one shown in FIG. 4.1. The array is made of 25 antennas and the aperture angle is as large as 127 deg, while the cross-range resolution limit, $\lambda_0 F/D$, goes from 3.75 cm at 2 GHz to 1.88 cm at 4 GHz. The major and minor axes of the ellipse are 7.2 and 3 cm long, respectively. With an appropriate scaling due to the different frequency bands, this setup is comparable to the one in [32].

First, noiseless data are inverted through the standard cost function $\mathcal{F}$ (FIG. 4.3), and through $\mathcal{F}^{\mathrm{DORT}}$ with TX (FIG. 4.5) and RX beamforming (FIG. 4.6). The symmetric singular value is used for both DORT-based approaches, easily trackable in FIG. 4.4 despite the crossing at around 3.6 GHz thanks to the symmetric/anti-symmetric features of the

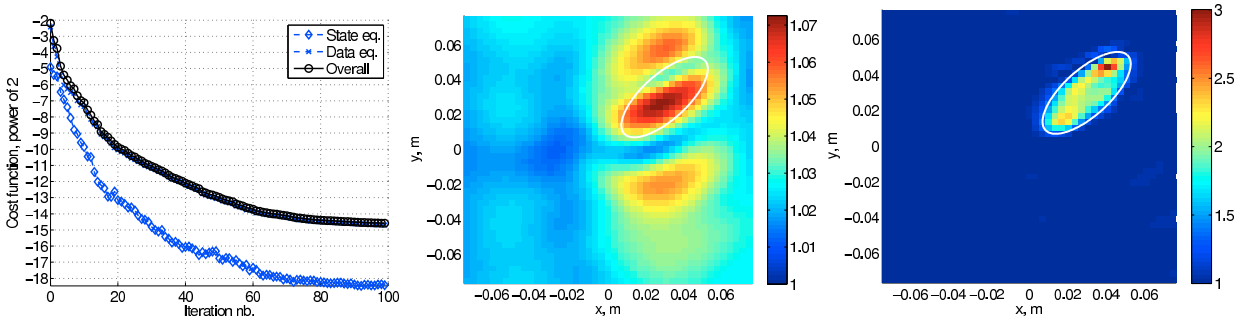

(a) $\mathcal{F}$ (b) $\varepsilon_{r;0}$ (c) $\varepsilon_{r;\infty}$

FIGURE 4.3: *Noiseless data. Inversion results with the standard cost function $\mathcal{F}$.*

respective singular vectors and field charts detailed in §2.3.3.1 (see *e.g.* FIG. 2.15).

In all cases, the retrieved profile matches rather well the real one, although, as already remarked in §3, adding to the cost function a regularization term based on the gradient of the retrieved profile would probably help in smooth the ε_r chart. Yet, the results are not exactly the same; it seems in particular that the reconstructed support is resolved more finely in the standard case, leading to the conclusion that using $\mathcal{F}^{\text{DORT}}$ with the symmetric singular space reduces the available information in the $\vec{k}$ plane.

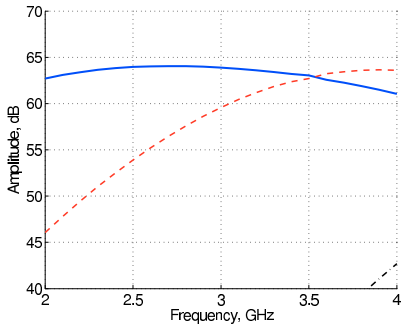

FIGURE 4.4: *Noiseless data. Singular values distribution versus frequency.*

Comparing FIG. 4.5 and FIG. 4.6, it appears immediately that RX beamforming has a much better initial guess (almost the same obtained throught the standard $\mathcal{F}$). This last point comes from the fact that in the back-propagation method described in §3.3.3 the received field is propagated back in the medium *for each view*. The more the available views, then, the more resolved in space the resulting image. Therefore, since with TX beamforming only one view exists, the initial guess in FIG. 4.5(b) is poorly resolved both in down- and cross-range, whereas the one obtained with RX beamforming in FIG. 4.6(b) is almost identical to the nice one obtained without beamforming in FIG. 4.3(b).

The analyses run with noisy data, whose results are not shown here for conciseness, confirm these findings while showing that none of the beamforming techniques appears more robust than the other. All these arguments suggests the following inversion strategy: use of TX beamforming, which executes much faster, starting from the initial estimation obtained with RX beamforming. This approach will be applied from now on.

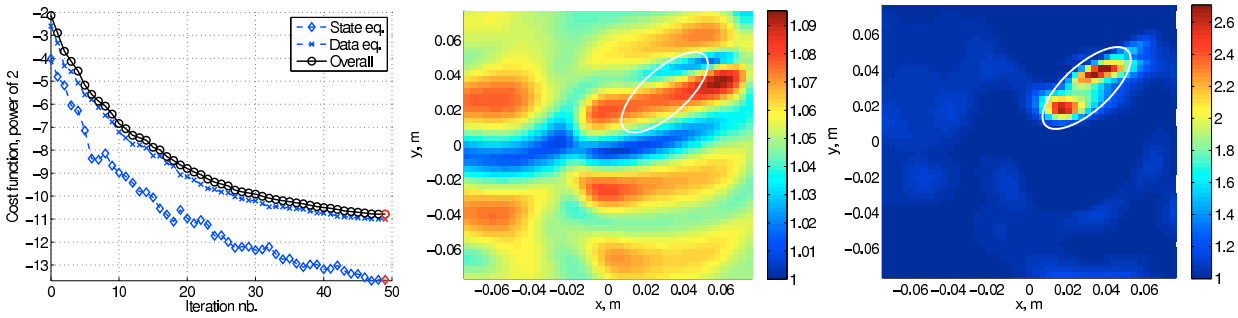

(a) $\mathcal{F}$ (b) $\varepsilon_{r;0}$ (c) $\varepsilon_{r;\infty}$

FIGURE 4.5: *Noiseless data. Inversion results with $\mathcal{F}^{\mathrm{DORT}}$ and TX beamforming.*

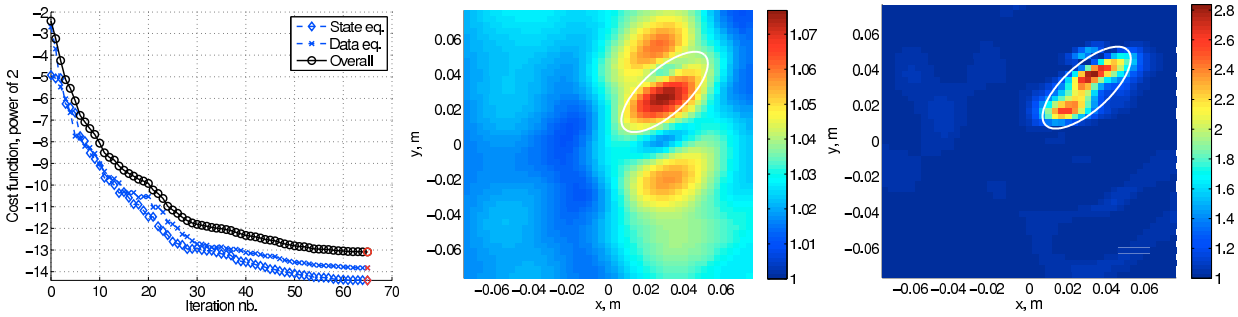

(a) $\mathcal{F}$ (b) $\varepsilon_{r;0}$ (c) $\varepsilon_{r;\infty}$

FIGURE 4.6: *Noiseless data. Inversion results with $\mathcal{F}^{\mathrm{DORT}}$ and RX beamforming.*

4.3.2 Influence of the spatial scale of clutter

In analogy with (3.77), it is possible to define a Signal-to-Clutter Ratio (SCR) as

$$\mathrm{SCR} \triangleq \frac{\sum_{j,p} \left\| \tilde{E}^{\mathrm{s}}_{j,p} \right\|_{\Gamma}^{2}}{\sum_{j,p} \left\| E^{\mathrm{s}}_{j,p} - \tilde{E}^{\mathrm{s}}_{j,p} \right\|_{\Gamma}^{2}} , \tag{4.15}$$

where $\tilde{E}^{\mathrm{s}}$ is the clean scattered field and E^{s} the one relative to the simulation with clutter[2]. Similarly, a $\mathrm{SCR}^{\mathrm{DORT}}$ can also be defined by replacing $\tilde{E}^{\mathrm{s}}_{j,p}$ and $E^{\mathrm{s}}_{j,p}$ in (4.15) by $\tilde{E}^{\mathrm{s;DORT}}_{j,p}$ and $E^{\mathrm{s;DORT}}_{j,p}$ defined in (4.3), respectively.

The first clutter setting to be inverted is `noise1`, shown in FIG. 4.2. The characteristic dimension of clutter, of the order of l_{c}, is comparable to the one of the target. The same geometry used in §4.3.1 is considered in the whole paragraph. The singular values distribution versus frequency, given in FIG. 4.7(a), must be compared to the one, obtained with noiseless data, in FIG. 4.4. While the symmetric singular value (full blue line) is rather unchanged, the anti-symmetric one (dashed red line) is significantly altered. This can be

[2]According to this expression, $\sqrt{SCR}$ is exactly the inverse of the error *err* defined in [32], eq. (28): $err = 100\%$ corresponds to SCR $= 0$ dB, and an increase of 3 dB of the latter gives an error reduction by a factor $\sqrt{2}$.

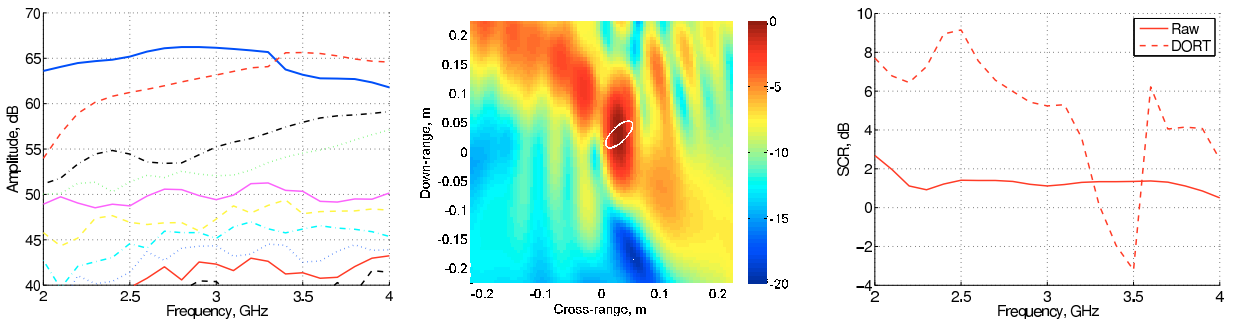

(a) (b) (c)

FIGURE 4.7: `noise1` *dataset. (a) Singular values distribution as a function of frequency, (b) incoherent sum of DORT field charts from 2 to 4 GHz built with* $(\lambda_1, \mathbf{v}_1)$*, and (c) SCR as a function of frequency for the raw and DORT scattered fields.*

explained by admitting that the scattering contribution associated to clutter has a symmetric and anti-symmetric components. Therefore, while the former is rather negligeable with respect to the stronger one associated to the target, the anti-symmetric component even dominates at the lower frequencies. Indeed, the crossing frequency is now shifted backwards to 3.4 GHz. Also, a tangle of clutter-related singular values grow up to 10 to 3 dB from the symmetric one. By incoherently adding the DORT field charts from 2 to 4 GHz ($I^{\mathrm{DORT}}_{\omega\omega}$ in (2.26)), it can be appreciated that the symmetric singular vector focuses

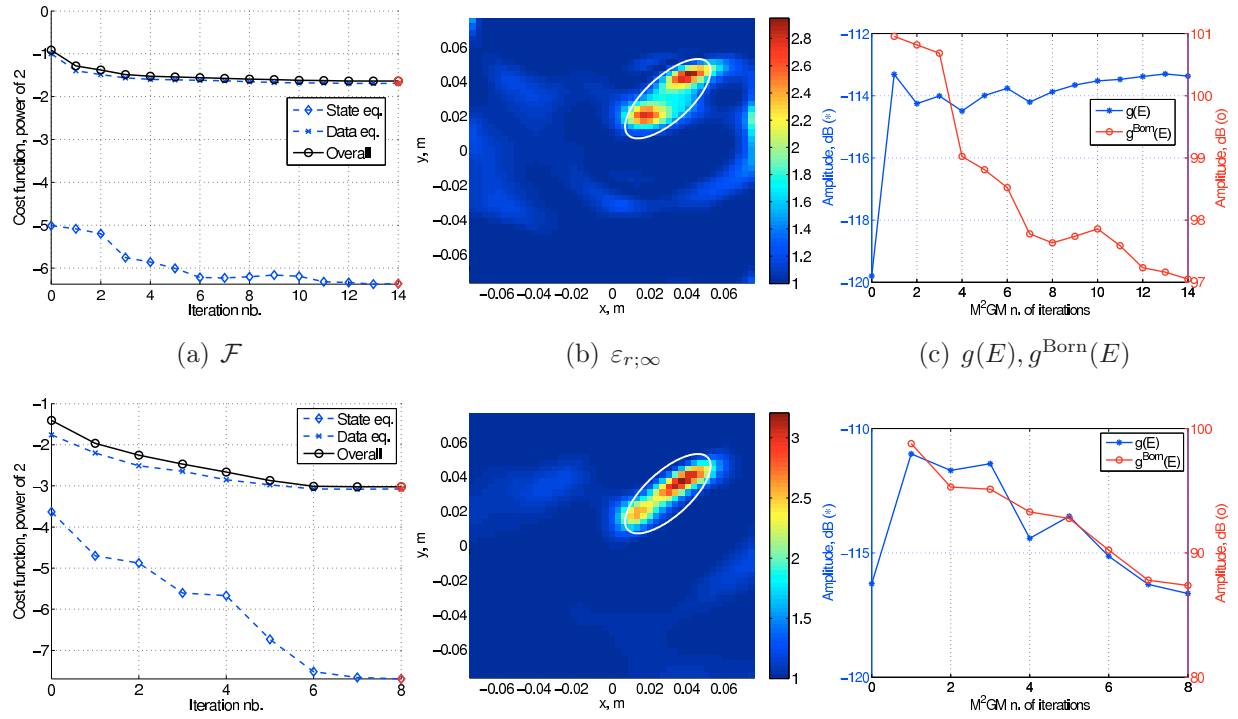

(a) $\mathcal{F}$ (b) $\varepsilon_{r;\infty}$ (c) $g(E), g^{\mathrm{Born}}(E)$

(d) DORT, $\mathcal{F}$ (e) DORT, $\varepsilon_{r;\infty}$ (f) DORT, $g(E), g^{\mathrm{Born}}(E)$

FIGURE 4.8: `noise1` *dataset. Inversion results with (top) the standard cost function* $\mathcal{F}$ *and (bottom)* $\mathcal{F}^{\mathrm{DORT}}$*.*

well onto the target (FIG. 4.7(b)). The resulting SCR and SCR^{DORT} are plotted in full and dashed line, respectively, in FIG. 4.7(c). Apart from the crossing region at around 3.4 GHz, where symmetric and anti-symmetric contributions mix up, the improvement goes from 2 to 6 dB.

The inversion results are shown in FIG. 4.8. In both cases, the ellipse is reconstructed with acceptable permittivity values, while as mentioned before the support displays finer details when the standard approach is used. On the other hand, in FIG. 4.8(c,f) the gradients $g(E)$ and $g^{\text{Born}}(E)$ defined in (3.80) are more regularly and more deeply minimized through the DORT approach. Similarly, the cost function decreases more when using $\mathcal{F}^{\text{DORT}}$, by a factor 3 versus the 1.5 factor of $\mathcal{F}$. Finally, the permittivity profiles, outside the support of the ellipse, are much less noisy with $\mathcal{F}^{\text{DORT}}$. This all testifies of an increased robustness to clutter.

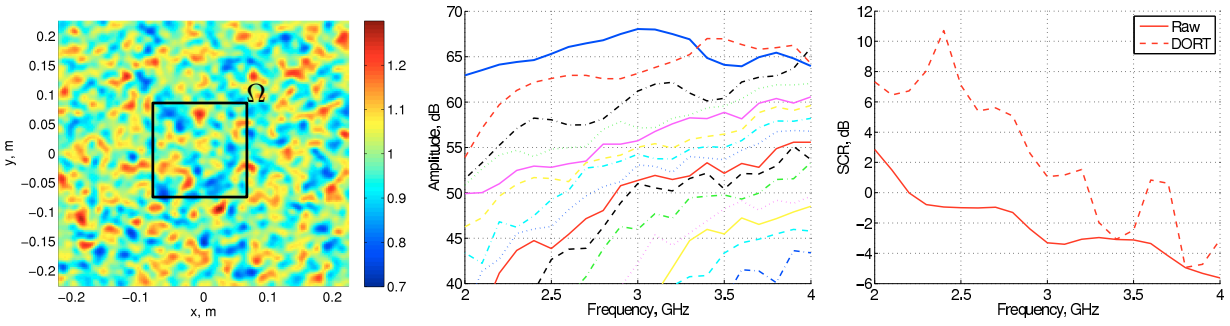

(a) (b) (c)

FIGURE 4.9: `noise2` *dataset. (a) Singular values distribution as a function of frequency and (b) SCR as a function of frequency for the raw and DORT scattered fields.*

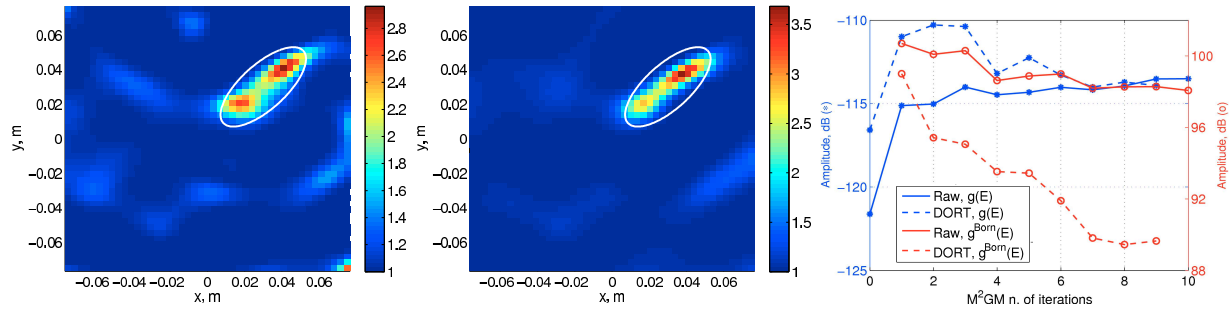

(a) $\varepsilon_{r;\infty}$ (b) DORT, $\varepsilon_{r;\infty}$ (c) $g(E), g^{\text{Born}}(E)$

FIGURE 4.10: `noise2` *dataset. Inversion results with* $\mathcal{F}$ *and* $\mathcal{F}^{\text{DORT}}$.

Similar conclusions can be drawn from the `noise2` dataset, where the small l_c value with respect to the wavelengths (0.8 cm or approximately $\lambda_0/19$ at 2 GHz) makes the clutter profile in FIG. 4.9(a) behave almost as a homogeneous one. From FIG. 4.10 it can indeed be noticed that while the target support is more finely and quantitatively better reconstructed when using $\mathcal{F}$, the DORT profiles have less artefacts (see *e.g.* at the bottom right corner of the charts). Again, the total field gradients are minimized more with $\mathcal{F}^{\text{DORT}}$.

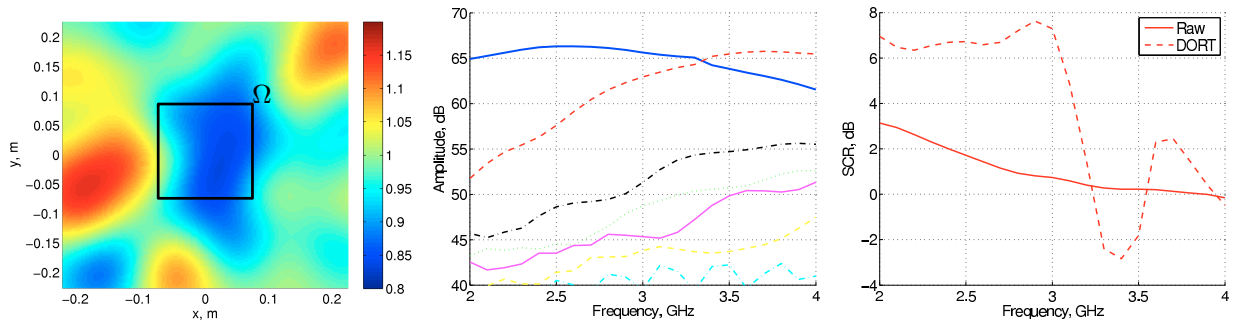

(a) (b) (c)

FIGURE 4.11: `noise3` *dataset. (a) Singular values distribution as a function of frequency and (c) SCR as a function of frequency for the raw and DORT scattered fields.*

In the last dataset, `noise3`, whose profile is shown in FIG. 4.11(a), the correlation length is of the order of $\lambda_0/2$ @ 2 GHz (7.5 cm). We are in the resonance domain and the impact of multiple-scattering is expected to be higher. With both approaches, the effect of such profile is a slightly wrong localization of the target in FIG. 4.10, found nearer to the array because of the $\varepsilon_{r,\mathrm{n}}(\vec{r}) < \varepsilon_{r,\mathrm{b}}$ values between the array and the object. Apart from such localization offset, the DORT inversion still seems more robust to clutter for the same reasons observed and discussed above.

From all these results, obtained for a geometric configuration comparable to the one used by Dubois *et al.* in [32], some tentative conclusions can then be drawn:

- using only $\mathcal{F}^{\mathrm{DORT}}$ seems to alter the information content of the data, resulting in particular in a decrease of the highest reconstructible spatial frequencies. For the configuration used in this section, though, such reduction is fairly acceptable;
- on the other hand, the DORT-based approach seems to be slightly more robust to clutter;
- for a comparable quality of the results, inverting $\mathcal{F}^{\mathrm{DORT}}$ is considerably faster than inverting $\mathcal{F}$. The gain in computation and speed is of the order of J/N_{tgt}, where J is the number of sources (*cf.* §4.1.3) and N_{tgt} is the number of targets, since one DORT

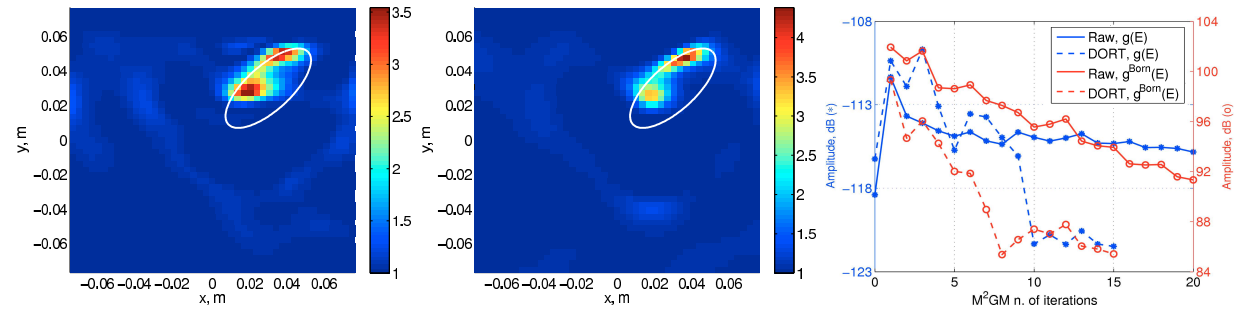

(a) $\varepsilon_{r;\infty}$ (b) DORT, $\varepsilon_{r;\infty}$ (c) $g(E), g^{\mathrm{Born}}(E)$

FIGURE 4.12: `noise3` *dataset. Inversion results with* $\mathcal{F}$ *and* $\mathcal{F}^{\mathrm{DORT}}$.

incidence per target should be considered in order to image all of them;

- if the amount of clutter increases, namely for a larger h value, the standard inversion might lead to erroneous results; on the other hand, the symmetric DORT singular value is most probably hidden in the tangle of clutter-related singular values, making it impossible to use $\mathcal{F}^{\mathrm{DORT}}$. Therefore, although for different reasons, both approaches fail in case of strong clutter;
- although no result has been provided here for conciseness, the regularization approach discussed in §4.2 does not really improve the reconstructions (regardless of the additive/multiplicative regularization choice and regardless of the κ value). Even if in [32] it is claimed that it is the DORT regularization that considerably improves the results, it should also be mentioned that the profiles retrieved with the standard approach *and* the positivity constraint are not shown in the paper. Therefore, assuming that such missing result is comparable to the one obtained with the DORT regularization, it might even be argued that the main regularization effect is brought by the positivity and not by the DORT fields.

4.3.3 Influence of the line size

Coherently with the experimental setup studied throughout this manuscript, it is interesting to observe the behavior of $\mathcal{F}^{\mathrm{DORT}}$ when a small measurement line is available. For this purpose, the number of antennas is reduced to 7 (the central ones with reference to Fig. 4.1), resulting in an aperture angle of 53 deg. The inversion results as well as the singular values distribution versus frequency are shown in Fig. 4.13 for noiseless data. The standard and the DORT-based approach give comparable results, both fair although much less clean than those obtained with the large-aperture setup in Figs. 4.3-4.5. This is of course due to the reduced aperture angle, leading to a reduced available information in the data according to the Ewald's circle theory developed in §3.4.

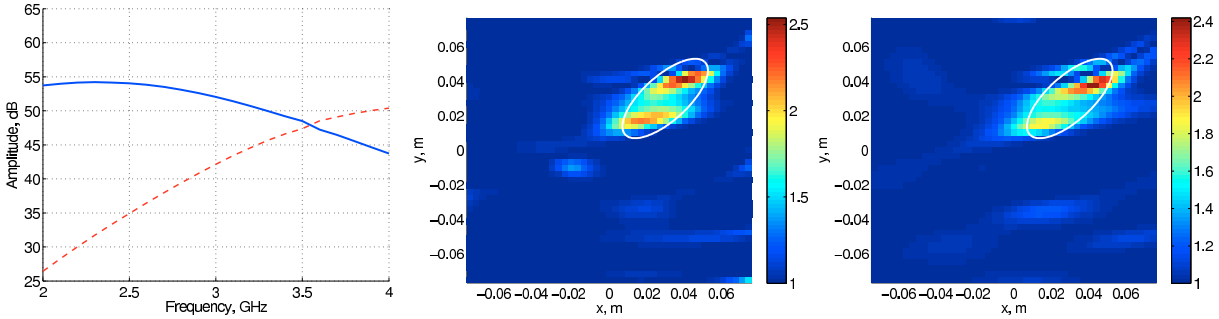

(a) (b) $\varepsilon_{r;\infty}$ (c) DORT, $\varepsilon_{r;\infty}$

Figure 4.13: *Noiseless data. (a) Singular values distribution as a function of frequency and (b,c) inversion results with $\mathcal{F}$ and $\mathcal{F}^{\mathrm{DORT}}$.*

When clutter is introduced, namely through the `noise1` setup, the inversion results are dramatically affected. In Fig. 4.14(c), it must first be noticed that apart from the [2.5-3] GHz

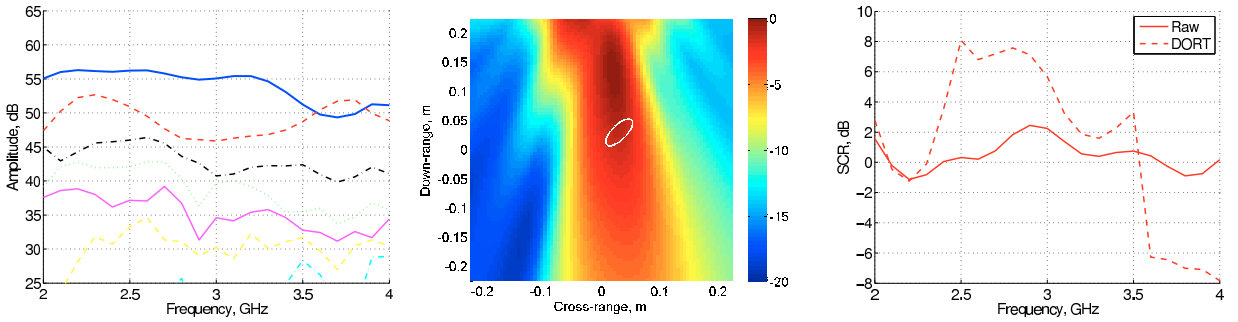

(a) (b) (c)

FIGURE 4.14: `noise1` *dataset. (a) Singular values distribution as a function of frequency, (b) incoherent sum of DORT field charts from 2 to 4 GHz built with* $(\lambda_1, \mathbf{v}_1)$*, and (c) SCR as a function of frequency for the raw and DORT scattered fields.*

frequency band, there is hardly an improvement in SCR (it actually gets 6 dB worse with DORT from 3.6 to 4 GHz, due to the crossing-coupling of the two largest singular values in FIG. 4.14(a)). This is due essentially to the fact that with a small line the resolution (both cross- and down-range) is generally poor - in this case it is equal to $\lambda_0(\omega)$ -, so that the focusing incident field cannot avoid illuminating also the clutter near the target. In effect, comparing FIG. 4.14(b) and FIG. 4.7(b), it is easy to see that while with the big line the hot spot of the DORT incident field is exactly over the target support, it is now located between the target and the array, where clutter is present. In addition, the cross-range hot region is now much larger.

The inversion results in FIG. 4.15 show first of all that the standard approach is more sensitive to clutter when the line is small, since the degradation from FIG. 4.13(b) to FIG. 4.15(b) is much worse than the one, relative to the large line setup, from FIG. 4.3(c) to FIG. 4.8(c). As for the DORT-based inversion, since the SCR is not really improved, the retrieved profile is not better than the one obtained by simply inverting $\mathcal{F}$.

To prove that the regularization approach described in §4.2 does not allow to improve the reconstructions of $\mathcal{F}$ and $\mathcal{F}^{\mathrm{DORT}}$, the result of the multiplicative regularization scheme with $\kappa = 1$ (cost function $\mathcal{F}\mathcal{F}^{\mathrm{DORT}}$) is shown in FIG. 4.16. The profile is not better than

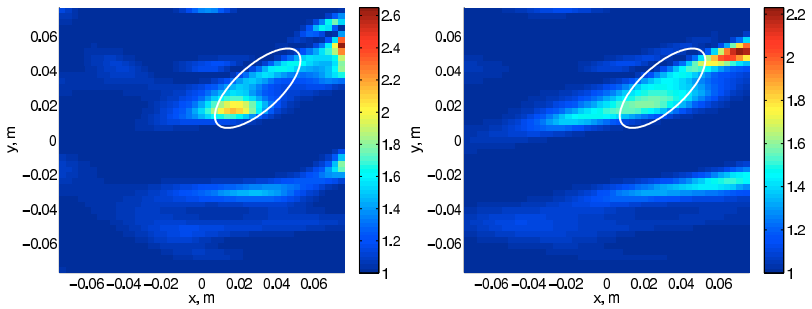

(a) $\varepsilon_{r;\infty}$ (b) DORT, $\varepsilon_{r;\infty}$

FIGURE 4.15: `noise1` *dataset. Inversion results with* $\mathcal{F}$ *and* $\mathcal{F}^{\mathrm{DORT}}$*.*

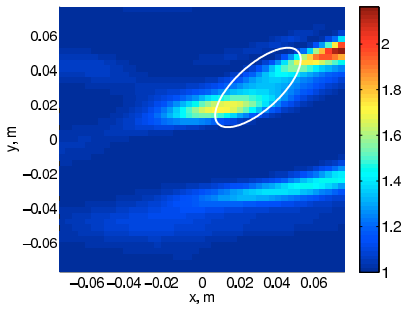

FIGURE 4.16: `noise1` *dataset. Inversion result* ($\varepsilon_{r;\infty}$) *with the regularized* $\mathcal{FF}^{\mathrm{DORT}}$ *cost function.*

any of the unregularized ones in FIG. 4.15. Also, there is hardly any improvement when changing the value of κ and/or employing the additive scheme.

For all these reasons, it can be concluded that the small line configuration is not well suited for the use of the DORT approach. The reason lies essentially in the poor resolution obtained with the DORT incident field, which does not really result in an improvement in SCR that could trade-off the reduced number of data. As a consequence, the regularization approach cannot improve the results either. Finally, since only a small line is experimentally available, this explains why no inversion from experimental data has been performed.

Conclusion and perspectives

The idea behind this work consisted, at the time I joined LSEET, in the realization of a microwave imaging prototype suited to experimentally test inversion methods. The hardware and software development necessary to have a running instrument, by themselves, have covered a large amount of time. The goal has been achieved and the laboratory now possesses a beamforming-capable system that can be used to characterize scatterers in the [2-4] GHz frequency band. In addition, a small anechoic chamber has been built.

The first approaches that have been implemented fall under the category of qualitative methods. The interest has been particularly put in studying the performances of Time Reversal as applied to electromagnetic waves. Indeed, in order both to test the beamforming performances of the prototype and to validate the improvement in resolution achieved with Time Reversal in disordered media [41], the following experiment has been realized. The field emitted by one antenna has been backpropagated by an array of antennas under two different propagation conditions: in free-space and in a medium with three metallic cylinders heavily perturbating the field radiated by the source antenna. In the latter case, an improvement in resolution of a factor 2.4 has been observed in the direction parallel to the array.

Then, detection and localization of passive targets have been tackled. With either one array in reflection, or with two arrays facing each other in transmission, Time Reversal-based methods such as DORT and Time Reversal-MUSIC (TR-MUSIC) have been applied to the experimental data. The effectiveness of these methods in selectively imaging well-separated targets has been confirmed for both configurations. In particular, it has been shown that whilst a classical method such as Kirchhoff migration fails in the transmission case, both DORT and TR-MUSIC don't. Their behavior is in fact the same in reflection and in transmission. The exploitation of the frequency bandwidth is not straightforward for any of these methods. An effective solution inspired by [99] has been succesfully applied to the DORT case. It is based on an arrival time estimation computed using the singular vectors, and leads to an improved rejection of clutter and parasite multiple-scattering. A solution also based on the arrival time estimation has been used for TR-MUSIC.

The prototype has then been employed in the quantitative inverse scattering frame. Namely, the Modified^2 Gradient Method [12] has been run with the multi-view multi-

static multi-frequency experimental data. The role played by the antenna modeling step, necessary to describe the incident field in the region under test, is here fundamental. A calibration procedure extracting the radiation pattern of the antennas from the same experimental data used for the inversion has thus been developed. This choice has the main advantage of taking into account the actual radiation patterns, hence including the effect of the proximity with the other array antennas. The calibration is based on a multipolar expansion of the field, and is applied to both the incident field (TX antennas) and the Green function linking the region under test and the receivers (RX antennas). To our knowledge, this might be spotted as an original contribution in the inverse scattering community.

The results show that the reflection configuration, as long as the array aperture is of the order of 40 deg, is not well suited for imaging, especially in the case of dielectric targets, whose profiles are systematically underestimated and their shape even badly reconstructed. As for metallic scatterers, due to their impenetrability, only the visible side is properly imaged. On the other hand, when two arrays are used and both the transmission and reflection data are considered, the results are satisfactory. The algorithm images well both metallic and sufficiently small dielectric targets ($d\sqrt{\varepsilon_r}$ of the order, at most, of $\lambda_0/3$, d being the largest dimension of the target, ε_r its permittivity, and λ_0 the wavelength at the smallest frequency) and is even capable of selectively resolve them.

In the final chapter, quantitative inversions using the incident and scattered fields issued from the DORT method have been run. The goal is to improve the robustness of the algorithm to clutter by exploiting the improved Signal-to-Clutter Ratio (SCR) of the DORT data. A new cost function, $\mathcal{F}^{\mathrm{DORT}}$, has thus been built and inverted. Two conclusions can be drawn from the results, obtained with synthetic data and for the reflection configuration. The first is that, as long as the target is sufficiently small, running an inversion with J "raw" incident fields gives a result almost identical to that obtained by using $\mathcal{F}^{\mathrm{DORT}}$. Only, the latter approach has only one incidence per target - the one associated with the symmetric DORT singular value -, hence it runs at least J/N_{tgt} times faster, N_{tgt} being the number of targets. Deceivingly, only a marginal improvement in clutter rejection can be observed. The second conclusion concerns the domain of applicability of this solution. The whole idea is based on the assumption that the DORT incident field focuses onto the target of interest. Nonetheless, in the case of a small aperture angle, the focusing spot is poorly resolved and not even centered upon the target location. Under these circumstances, typical of a small line configuration, there is therefore no improvement wahtsoever in SCR, and the use of $\mathcal{F}^{\mathrm{DORT}}$ is actually not advised.

A few general conclusions are due. First, the effectiveness of Time Reversal-based methods such as DORT and TR-MUSIC has been proved experimentally in the case of a small measurement line. The coherent exploitation of the frequency bandwidth is a crucial point at this purpose, and the arrival time estimation method proposed in §2.3.3.3 seems a very good candidate to achieve the task. The main issue with DORT and, in general, with

subspace-based methods, is still the classification of the singular spaces. How to automatically identify the symmetric singular value? How to automatically detect a crossing between singular values? Related to this problem, is the issue of de-correlating singular spaces that couple each other, typically in multi-target configurations. Effective answers to these problems would definitely cast DORT among the most effective localization methods, and I personally believe that further research in this direction is worth the effort.

As for the quantitative inversion experiments, they have shown that if a meticulous calibration procedure is implemented, it is possible to reconstruct small scatterers even with a small line, at least when reflection and transmission data are combined together. It would now be interesting to pursue the investigation in a 3D frame, adding namely the polarization diversity to the data.

Finally, the DORT-based inversion has given intriguing results. It should be proven through a more important number of test cases up to what extent it is possible to replace the classical multi-view inversion approach with a single-DORT-view one. The gain in execution time being remarkable, this might help in approaching the real-time paradigm. Concerning clutter rejection, the effectiveness of the DORT-based method seems related to the resolution and neatness of the focusing spot of the incident field. In virtue of its full aperture angle, the circular scanner configuration seems therefore a good candidate to evaluate the limits of the idea.

Bibliography

[1] O. Bucci and T. Isernia, "Electromagnetic inverse scattering: Retrievable information and measurement strategies," Radio Sci., vol. 32, no. 6, pp. 2123–2137, 1997.

[2] M. Fink, C. Prada, F. Wu, and D. Cassereau, "Self focusing in inhomogeneous media with time reversal acoustic mirrors," in Proc. IEEE Ultrasonics Symposium, vol. 2, Montreal, Que., Canada, Oct. 1989, pp. 681–686.

[3] C. Prada and M. Fink, "Eigenmodes of the time reversal operator: A solution to selective focusing in multiple-target media," Wave Motion, vol. 20, pp. 151–163, Sep. 1994.

[4] H. Lev-Ari and A. Devaney, "The time-reversal technique re-interpreted: subspace-based signal processing for multi-static target location," in Sensor Array and Multichannel Signal Processing Workshop. 2000. Proceedings of the 2000 IEEE, 2000, pp. 509–513.

[5] C. Prada and J.-L. Thomas, "Experimental subwavelength localization of scatterers by decomposition of the time reversal operator interpreted as a covariance matrix," J. Acoust. Soc. Am., vol. 114, no. 1, pp. 235–243, Jul. 2003.

[6] K. Belkebir and M. Saillard, "Special section: Testing inversion algorithms against experimental data," Inv. Probl., vol. 17, no. 6, pp. 1565–1571, Dec. 2001.

[7] ——, "Special section on testing inversion algorithms against experimental data: inhomogeneous targets," Inv. Probl., vol. 21, no. 6, pp. S1–S3, Dec. 2005.

[8] A. Litman and L. Crocco, "Testing inversion algorithms against experimental data: 3d targets," Inv. Probl., vol. 25, p. 020201, 2009.

[9] P. M. Meaney, M. W. Fanning, D. Li, S. P. Poplack, and K. D. Paulsen, "A clinical prototype for active microwave imaging of the breast," IEEE Trans. Microwave Theory Tech., vol. 48, pp. 1841–1853, 2000.

[10] B. Duchêne, A. Joisel, and M. Lambert, "Nonlinear inversions of immersed objects using laboratory-controlled data," Inv. Probl., vol. 20, pp. S81–S98, 2004.

[11] C. Gilmore, P. Mojabi, A. Zakaria, M. Ostadrahimi, C. Kaye, S. Noghanian, L. Shafai, S. Pistorius, and J. LoVetri, "A wideband microwave tomography system with a novel frequency selection procedure," IEEE Trans. Biomed. Eng., vol. 57, no. 4, pp. 894–904, 2010.

[12] K. Belkebir and A. G. Tijhuis, "Modified^2 gradient method and modified born method for solving a two-dimensional inverse scattering problem," Inv. Probl., vol. 17, no. 6, pp. 1671–1688, Dec. 2001.

[13] M. Bianchieri-Astier, "Conception d'un miroir à retournement temporel en micro-ondes," Stage de MASTER2 Recherche SMES ST, LSEET - Université du Sud Toulon-Var, fev-jun 2007.

[14] M. Fink, D. Cassereau, A. Derode, C. Prada, P. Roux, M. Tanter, J.-L. Thomas, and F. Wu, "Time-reversed acoustics," Rep. Prog. Phys., vol. 63, no. 12, pp. 1933–1995, Dec. 2000.

[15] C. Draeger and M. Fink, "One-Channel Time Reversal of Elastic Waves in a Chaotic 2D-Silicon Cavity," Phys. Rev. Lett., vol. 79, no. 3, pp. 407–410, Jul. 1997.

[16] W. A. Kuperman, W. S. Hodgkiss, T. A. H. C. Song, C. Ferla, and D. R. Jackson, "Phase Conjugation in the ocean: Experimental demonstration of an acoustic time-reversal mirror," J. Acoust. Soc. Am., vol. 103, pp. 25–40, Jan. 1998.

[17] Z. Bouchal and J. Perina, "Electromagnetic concept of phase conjugation," J. Modern Opt., vol. 45, no. 2, pp. 425–436, 1998.

[18] H. Tortel, G. Micolau, and M. Saillard, "Decomposition of the time reversal operator for electromagnetic scattering," J. Electromagn. Waves Appli., vol. 13, no. 5, pp. 687–719, Sep. 1999.

[19] D. H. Chambers and A. K. Gautesen, "Analysis of the Time-Reversal Operator for a Small Spherical Scatterer in an Electromagnetic Field," IEEE Trans. Antennas Propag., vol. 52, no. 7, pp. 1729–1738, Jul. 2004.

[20] G. Micolau and M. Saillard, "D.O.R.T. method as applied to electromagnetic subsurface sensing," Radio Sci., vol. 38, no. 3, p. 1038, May 2003.

[21] G. Micolau, M. Saillard, and P. Borderies, "DORT method as applied to Ultrawideband Signals for Detection of Buried Objects," IEEE Trans. Geosci. Remote Sens., vol. 41, no. 8, pp. 1813–1820, Aug. 2003.

[22] R. Carminati, R. Pierrat, J. de Rosny, and M. Fink, "Theory of the time reversal cavity for electromagnetic fields," Opt. Lett., vol. 32, no. 21, pp. 3107–3109, Nov. 2007.

[23] J. de Rosny, G. Lerosey, and M. Fink, "Theory of electromagnetic time-reversal mirrors," IEEE Trans. Antennas Propag., vol. 58, no. 10, pp. 3139–3149, Oct. 2010.

[24] G. Lerosey, J. de Rosny, A. Tourin, A. Derode, G. Montaldo, and M. Fink, "Time reversal of electromagnetic waves," Phys. Rev. Lett., vol. 92, no. 19, p. 193904, May 2004.

[25] G. Lerosey, J. de Rosny, A. Tourin, A. Derode, and M. Fink, "Time reversal of wideband microwaves," Appl. Phys. Lett., vol. 88, no. 15, p. 154101, Apr. 2006.

[26] S. Gupta and E. R. Brown, "Noise-correlating radar based on retrodirective antennas," IEEE Trans. Aerospace Electronic Systems, vol. 43, no. 2, pp. 472–479, 2007.

[27] A. Khaleghi, G. El Zein, and I. Naqvi, "Demonstration of Time-reversal in indoor Ultra-wideband Communication: Time Domain Measurement," in Proc. IEEE International Symposium on Wireless Communication Systems, Trondheim, Norway, 2007, pp. 465–468.

[28] D. Liu, S. Vasudevan, J. Krolik, G. Bal, and L. Carin, "Electromagnetic Time-Reversal Source Localization in Changing Media: Experiment and Analysis," IEEE Trans. Antennas Propag., vol. 55, no. 2, p. 344–354, Feb. 2007.

[29] A. Cresp, I. Aliferis, M. J. Yedlin, J.-Y. Dauvignac, and C. Pichot, "Time-domain processing of electromagnetic data for multiple-target detection," AIP Conf. Proc., 3rd Conference on Mathematical Modeling of Wave Phenomena, vol. 1106, no. 1, pp. 204–213, Mar. 2009.

[30] I. Naqvi, G. El Zein, G. Lerosey, J. de Rosny, P. Besnier, A. Tourin, and M. Fink, "Experimental validation of time reversal ultra wide-band communication system for high data rates," IET Microw. Antennas Propag., vol. 4, no. 5, pp. 643–650, May 2010.

[31] K. Belkebir, S. Bonnard, F. Pezin, P. Sabouroux, and M. Saillard, "Validation of 2d inverse scattering algorithms from multi-frequency experimental data," J. Electromagn. Waves Appl., vol. 14, no. 12, pp. 1637–1667, 2000.

[32] A. Dubois, K. Belkebir, and M. Saillard, "Localization and characterization of two-dimensional targets buried in a cluttered environment," Inv. Probl., vol. 20, no. 6, pp. S63–S79, Nov. 2004.

[33] P. Broche, P. Forget, J. C. D. Maistre, J. L. Devenon, and M. Crochet, "Vhf radar for ocean surface current and sea state remote sensing," Radio Sci., vol. 22, pp. 69–75, 1987.

[34] A. Allou, P. Forget, and J. L. Devenon, "Submesoscale vortex structures at the entrance of the gulf of lions in the northwestern mediterranean sea," Cont. Shelf Res., vol. 30, pp. 724–732, 2009.

[35] D. J. Daniels, Ground Penetrating RADAR, 2nd ed. London, U.K.: IEE, 2004.

[36] F. K. Gruber, E. A. Marengo, and A. J. Devaney, "Time-reversal imaging with multiple signal classification considering multiple scattering between the targets," J. Acoust. Soc. Am., vol. 115, no. 6, pp. 3042–3047, 2004.

[37] D. Colton and A. Kirsch, "A simple method for solving inverse scattering problems in the resonance region," Inv. Probl., vol. 12, pp. 383–393, 1996.

[38] M. Cheney, "The linear sampling method and the music algorithm," Inv. Probl., vol. 17, pp. 591–595, Aug. 2001.

[39] I. Catapano, L. Crocco, and T. Isernia, "On simple methods for shape reconstruction of unknown scatterers," IEEE Trans. Antennas Propagation., vol. 55, no. 5, pp. 1431–1436, 2007.

[40] M. Fink, "Time-reversal waves and super resolution," J. Phys.: Conf. Ser., vol. 104, p. 012004, 2004.

[41] G. Lerosey, J. de Rosny, A. Tourin, and M. Fink, "Focusing beyond the diffraction limit with far-field time reversal," Science, vol. 315, no. 5815, pp. 1120–1122, Feb. 2007.

[42] L. C. V. Atta, U.S. Patent 2 908 002, Oct. 6, 1959.

[43] C. Y. Pon, "Retrodirective array using the heterodyne technique," IEEE Trans. Antennas Propag., vol. 12, no. 2, pp. 176–180, 1964.

[44] Y. Chang, H. Fetterman, I. Newberg, and S. Panaretos, "Microwave phase conjugation using antenna arrays," IEEE Trans. Microwave Theory Tech., vol. 46, no. 11, pp. 1910–1919, 1998.

[45] C. Germond, F. Barbaresco, L. Allano, and M. Lesturgie, "Phase conjugation in radar," in EuRAD'05 Conference, Paris, Oct. 2005.

[46] E. R. Brown, E. B. Brown, and A. Hartenstein, "Ku-band retrodirective radar for ballistic projectile detection and tracking," in Proc. of IEEE Radar Conference, Washington, USA, 10-14 may 2010.

[47] V. Fusco and N. B. Buchanan, "High-performance IQ modulator-based phase conjugator for modular retrodirective antenna array implementation," IEEE Trans. Microwave Theory Tech., vol. 57, no. 10, pp. 2301–2306, 2009.

[48] M. Bocquet, C. Loyez, C. Lethien, N. Deparis, M. Heddebaut, A. Rivenq, and N. Rolland, "A multifunctional 60-ghz system for automotive applications with communication and positioning abilities based on time reversal," in Proceedings of the 7th European Radar Conference, Paris, Sep. 2010, pp. 61–64.

[49] A. Derode, A. Tourin, and M. Fink, "Time reversal versus phase conjugation in a multiple scattering environment," Ultrasonics, vol. 40, pp. 275–280, May 2002.

[50] M. Nieto-Vesperinas and E. Wolf, "Phase conjugation and symmetries with wave fields in free space containing evanescent components," J. Opt. Soc. Am., vol. 2, no. 9, pp. 1429–1434, 1985.

[51] E.-G. Paek, J. Y. Choe, and P. A. Bernhardt, "Over-the-horizon radars with multipath-enabled super-resolution using time-reversal," in Proc. of IEEE Radar Conference, Pasadena, CA, USA, 4-8 may 2009.

[52] B. E. Henty and D. D. Stancil, "Multipath-enabled super-resolution for rf and microwave communication using phase-conjugate arrays," Phys. Rev. Lett., vol. 93, p. 243904, 2004.

[53] F. Coppinger, A. Bhushan, and B. Jalali, "Time reversal of broadband microwave signals," Electronics Lett., vol. 35, no. 15, pp. 1230–1232, 1999.

[54] H. Zmuda, M. Fanto, and T. McEwen, "Experimental results for a photonic time reversal processor for adaptive control of an ultra wideband phased array antenna," in Enabling Photonics Technologies for Defense, Security, and Aerospace Applications IV, vol. 6975. Orlando, FL, USA: SPIE, 2008, p. 697504.

[55] E. Guillanton, J. Y. Dauvignac, C. Pichot, and J. Cashman, "A new design tapered slot antenna for ultra-wideband applications," Microwave Opt. Tech. Lett., vol. 19, no. 4, pp. 286–289, 1998.

[56] N. Maaref, P. Millot, X. Ferrières, C. Pichot, and O. Picon, "Electromagnetic imaging method based on time reversal processing applied to through-the-wall target localization," Prog. Electromagn. Res. M, vol. 1, pp. 59–67, 2008.

[57] K. Kurokawa, "Power waves and the scattering matrix," IEEE Trans. Micr. Theory & Tech., vol. 13, no. 2, pp. 194–202, Mar. 1965, article introducing S-parameters.

[58] VNA Dynamic Range and Linearity Accuracy (Application Note), Anritsu, 2008.

[59] C. Eyraud, J.-M. Geffrin, A. Litman, P. Sabouroux, and H. Giovannini, "Drift correction for scattering measurements," Appl. Phys. Lett., vol. 89, p. 244104, 2006.

[60] R. Mavaddat, Network scattering parameters. World Scientific Publishing Co., 1996, ch. 2, pp. 65–72.

[61] J.-M. Geffrin, C. Eyraud, A. Litman, and P. Sabouroux, "Optimization of a bistatic microwave scattering measurement setup: From high to low scattering targets," Radio Sci., vol. 44, p. RS2007, Mar. 2009.

[62] C. Eyraud, J.-M. Geffrin, P. Lewyllie, A. Franchois, and A. Dubois, "Target localization and measured scattered field pre-processing using spectral bandwidth minimization for shallowly buried target problems," Microwave Opt. Tech. Lett., vol. 52, no. 1, pp. 147–151, Jan. 2010.

[63] O. M. Bucci and G. Franceschetti, "On the spatial bandwidth of scattered fields," IEEE Trans. Antennas Propag., vol. 35, no. 12, pp. 1445–1455, Dec. 1987.

[64] O. M. Bucci, C. Gennarelli, and C. Savarese, "Representation of electromagnetic fields over arbitrary surfaces by a finite and nonredundant number of samples," IEEE Trans. Antennas Propag., vol. 46, no. 3, pp. 351–359, Mar. 1998.

[65] R. Bracewell, The Fourier Transform and its applications, McGraw-Hill, Ed. McGraw-Hill Book Company, 1965.

[66] F. de Coulon, Théorie et traitement des signaux, 1st ed. Lausanne: Presse polytechniques romandes, 1984, p. 220.

[67] C. A. Balanis, Antenna Theory, 2nd ed., 1997, ch. 2, pp. 79–81.

[68] J. D. Jackson, Classical Electrodynamics, 3rd ed. John Wiley & Sons, 1999.

[69] G. W. Stewart, Matrix Algorithms. New York: SIAM, 2001, vol. Volume II: Eigensystems.

[70] D. Franceschini, M. Donelli, and A. Massa, "On the effects of the electromagnetic source modeling in the iterative multiscaling method," Radio Sci., vol. 42, p. RS3020, Jun. 2007.

[71] G. Leone and F. Soldovieri, "Analysis of the distorted born approximation for subsurface reconstruction: Truncation and uncertainties effects," IEEE Trans. Geosci. Remote Sens., vol. 41, no. 1, pp. 66–74, 2003.

[72] R. Dubroca, N. Fortino, J.-Y. Dauvignac, L. Bellomo, S. Pioch, M. Saillard, T. Lepetit, J. de Rosny, C. Prada, P.Millot, N.Maaref, and B.Boudamouz, "Time reversal-based processing for human targets detection in realistic through-the-wall scenarios," in EuMW'11, Manchester, UK, 12-14 oct 2011.

[73] R. A. Fisher, Optical phase conjugation, A. Press, Ed., 1983.

[74] M. Fink, "Time reversal of ultrasonics fields. i. basic principles," IEEE Trans. Ultrason. Ferro. Freq. Contr., vol. 39, pp. 555–566, Sep. 1992.

[75] R. Carminati, J. J. Saenz, J.-J. Greffet, and M. Nieto-Vesperinas, "Reciprocity, unitarity, and time-reversal symmetry of the s matrix of fields containing evanescent components," Phys. Rev. A, vol. 62, p. 012712, 2000.

[76] F. Wu, J.-L. Thomas, and M. Fink, "Time reversal of ultrasonic fields. ii. experimental results," IEEE Trans. Ultrason. Ferro. Freq. Contr., vol. 39, no. 39, pp. 567–578, Sep. 1992.

[77] M. J. Yedlin, A. Cresp, C. Pichot, I. Aliferis, J.-Y. Dauvignac, S. Gaffet, and G. Sénéchal, "Ultra-wideband microwave imaging of heterogeneities," J. of Appl. Geophys., vol. 68, no. 1, pp. 17–25, May 2009.

[78] L. Bellomo, S. Pioch, M. Saillard, and E. Spano, "Time reversal experiments in the microwave range: description of the radar and results," Prog. Electromagn. Res., vol. 104, pp. 427–448, 2010.

[79] G. Montaldo, G. Lerosey, A. Derode, A. Tourin, J. de Rosny, and M. Fink, "Telecommunication in a disordered environment with iterative time reversal," Waves Random Media, vol. 14, pp. 287–302, 2004.

[80] C. Oestges, J. Hansen, S. M. Emami, A. D. Kim, G. Papanicolaou, and A. J. Paulraj, "Time reversal techniques for broadband wireless communication systems," in European Microwave Conference (Workshop), Amsterdam, The Netherlands, Oct. 2004, pp. 49–66.

[81] P. Kyritsi, G. Papanicolaou, P. Eggers, and A. Oprea, "Time reversal techniques for wireless communications," in Vehicular Technology Conference, 2004. VTC2004-Fall, vol. 1, 2004, pp. 47–51.

[82] R. C. Qiu, C. Zhou, N. Guo, and J. Q. Zhang, "Time reversal with miso for ultra-wideband communications: Experimental results," IEEE Ant. Wireless Prop. Lett., vol. 5, pp. 1–5, 2006.

[83] X. Liu, B.-Z. Wang, S. Xiao, and J. Deng, "Performance of impulse radio uwb communications based on time reversal technique," Prog. Electromagn. Res., vol. 79, pp. 401–413, 2008.

[84] N. Buchanan, V. Fusco, and P. Sundaralingam, "Fast response retrodirective radar," in Microwave Symposium Digest (MTT), 2010 IEEE MTT-S International, May 2010, pp. 153–156.

[85] P. Kosmas and C. M. Rappaport, "Time reversal with the fdtd method for microwave breast cancer detection," IEEE Trans. Microwave Theory Tech., vol. 53, no. 7, pp. 2317–2323, Jul. 2005.

[86] C. S. Larmat, J.-P. Montagner, M. Fink, Y. Capdeville, A. Tourin, and E. Clévédé, "Time-reversal imaging of seismic sources and application to the great sumatra earthquake," Geophysical Research Letters, vol. 33, p. L19312, 2006.

[87] C. S. Larmat, R. A. Guyer, and P. A. Johnson, "Time-reversal methods in geophysics," Phys. Today, vol. 63, no. 8, pp. 31–35, Aug. 2010.

[88] F. Lemoult, G. Lerosey, J. de Rosny, and M. Fink, "Resonant metalenses for breaking the diffraction barrier," Phys. Rev. Lett., vol. 104, p. 203901, 2010.

[89] ——, "Manipulating spatiotemporal degrees of freedom of waves in random media," Phys. Rev. Lett., vol. 103, p. 173902, 2009.

[90] J. Claerbout, Imaging the earth's interior, ser. Stanford Exploration project. Blackwell Scientific Publications, 1985.

[91] M. Cheney, "A mathematical tutorial on synthetic-aperture radar," SIAM review, vol. 43, no. 2, pp. 301–312, 2001.

[92] M. I. Skolnik, Introduction to RADAR Systems, ser. Electrical Engineering Series. McGraw-Hill, 1980.

[93] C. Prada, F. Wu, and M. Fink, "The iterative time reversal mirror: A solution to self-focusing in the pulse echo mode," J. Acoust. Soc. Am., vol. 90, no. 2, pp. 1119–1129, 1991.

[94] M. Abramowitz and I. Stegun, Handbook of mathematical functions with formulas, graphs, and mathematical tables. U.S. Govt. Print. Off., 1972, ch. 9, p. 363.

[95] R. Petit, Ondes électromagnétiques en radioélectricité et en optique. Dunod, 1997.

[96] A. Cresp, I. Aliferis, M. J. Yedlin, C. Pichot, and J.-Y. Dauvignac, "Investigation of time-reversal processing for surface-penetrating radar detection in a multiple-target configuration," in Proc. 5th European Radar Conference, Amsterdam, Netherlands, 2008.

[97] F. D. Philippe, C. Prada, D. Clorennec, M. Fink, and T. Folégot, "Construction of the temporal invariants of the time-reversal operator," J. Acoust. Soc. Am. Express Lett., vol. 126, no. 1, pp. EL8–EL13, Jul. 2009.

[98] M. E. Yavuz and F. L. Teixiera, "Space-Frequency Ultrawideband Time-Reversal Imaging," IEEE Trans. Geosci. Remote Sens., vol. 46, no. 4, pp. 115–1124, Apr. 2008.

[99] L. Borcea, G. Papanicolaou, C. Tsogka, and J. Berryman, "Imaging and time reversal in random media," Inv. Probl., vol. 18, no. 5, pp. 1247–1279, Oct. 2002.

[100] N. Mordant, C. Prada, and M. Fink, "Highly resolved detection and selective focusing in a waveguide using the d.o.r.t. method," J. Acoust. Soc. Am., vol. 105, no. 5, pp. 2634–2642, May 1999.

[101] F.-D. Philippe, "Caractérisation et détection de cibles en guide d'onde non stationnaire par décomposition de l'opérateur retournement temporel," Ph.D. dissertation, Université de Paris Diderot (Paris 7), 2008.

[102] M. Davy, J.-G. Minonzio, J. de Rosny, C. Prada, and M. Fink, "Experimental study of the invariants of the time-reversal operator for a dielectric cylinder using separate transmit and receive arrays," IEEE Trans. Antennas Propag., vol. 58, no. 4, pp. 1349 –1356, Apr. 2010.

[103] J.-G. Minonzio, C. Prada, A. Aubry, and M. Fink, "Multiple scattering between two elastic cylinders and invariants of the time-reversal operator: Theory and experiment," J. Acoust. Soc. Am., vol. 120, no. 2, pp. 875–883, Aug. 2006.

[104] J. F. Lingevitch, H. C. Song, and W. A. Kuperman, "Time reversed reverberation focusing in a waveguide," J. Acoust. Soc. Am., vol. 111, no. 6, pp. 2609–2614, Jun. 2002.

[105] T. Folégot, C. Prada, and M. Fink, "Resolution enhancement and separation of reverberation from target echo with the time reversal operator decomposition," J. Acoust. Soc. Am., vol. 113, no. 6, pp. 3155–3160, Jun. 2003.

[106] T. Folégot, J. de Rosny, C. Prada, and M. Fink, "Adaptive instant record signals applied to detection with time reversal operator decomposition," J. Acoust. Soc. Am., vol. 117, no. 6, pp. 3757–3765, Jun. 2005.

[107] G. Bienvenu and L. Kopp, "Optimality of high resolution array processing using the eigensystem approach," IEEE Trans. Acoust. Speech Signal Process., vol. 31, no. 5, pp. 1235–1248, 1983.

[108] R. O. Schmidt, "Multiple emitter location and signal parameter estimation," IEEE Trans. Antennas Propag., vol. 34, pp. 276–280, 1989.

[109] M. Davy, J.-G. Minonzio, J. de Rosny, C. Prada, and M. Fink, "Influence of noise on subwavelength imaging of two close scatterers using time reversal method: Theory and experiments," Prog. Electromagn. Res., vol. 98, pp. 333–358, 2009.

[110] M. L. Mehta, Random matrices. Elsevier/Academic Press, 2004.

[111] N. Thanh, L. van Kempen, T. Savelyev, X. Zhuge, M. Aftanas, E. Zaikov, M. Drutarovsky, and H. Sahli, "Comparison of basic inversion techniques for through-wall imaging using uwb radar," in 5th European Radar Conference - EuRAD, Oct. 2008, pp. 140–143.

[112] A. Kolmogorov and S. V. Fomine, Éléments de la Théorie des Fonctions et de l'Analyse Fonctionelle. Moscow: MIR, 1973.

[113] Z. Q. Meng, T. Takenaka, and T. Tanaka, "Image reconstruction of two dimensional impenetrable objects using genetic algorithm," J. Electromag. Waves Applicat., vol. 13, pp. 95–118, 1999.

[114] E. Bermani, S. Caorsi, and M. Raffetto, "An inverse scattering approach based on neural network technique for the detection of dielectric cylinder buried in a lossy half space," Progress Electromagn. Res., vol. 26, pp. 67–87, 2000.

[115] S. Caorsi, A. Massa, and M. Pastorino, "A crack identification microwave procedure based on a genetic algorithm for nondestructive testing," IEEE Trans. Antennas Propag., vol. 49, no. 9, pp. 1812–1820, 2001.

[116] A. Roger, "Newton-kantorovich algorithm applied to an electromagnetic inverse problem," IEEE Trans. Antennas Propag., vol. 29, no. 2, pp. 232–238, 1981.

[117] N. Joachimowicz, C. Pichot, and J. P. Hugonin, "Inverse scattering: An iterative numerical method for electromagnetic imaging," IEEE Trans. Antennas Propag., vol. 39, pp. 1742–1751, Dec. 1991.

[118] K. Belkebir, J.-M. Elissalt, J.-M. Geffrin, and C. Pichot, "Newton-kantorovich and modified gradient-inversion algorithms applied to ipswich data," IEEE Trans. Antennas Propag., vol. 38, no. 3, pp. 41–44, 1996.

[119] K. Belkebir, R. E. Kleinman, and C. Pichot, "Microwave imaging - location and shape reconstruction from multifrequency scattering data," IEEE Trans. Microwave Theory Tech., vol. 45, no. 4, pp. 469–476, 1997.

[120] R. F. Remis and P. M. van den Berg, "On the equivalence of the newton-kantorovich and distorted born methods," Inv. Probl., vol. 16, pp. L1–L4, 2000.

[121] W. C. Chew and Y. M. Yang, "Reconstruction of two-dimensional permittivity distribution using the distorted born iterative method," IEEE Trans. Med. Imaging, vol. 9, no. 2, pp. 218–225, 1990.

[122] A. G. Tijhuis, K. Belkebir, A. C. S. Litman, and B. P. de Hon, "Multiple-frequency distorted-wave born approach to 2d inverse profiling," Inv. Probl., vol. 17, p. 1635–1644, 2001.

[123] T. M. Habashy, R. W. Groom, and B. R. Spies, "Beyond the born and rytov approximation: A nonlinear approach to electromagnetic scattering," J. Geophys. Res., vol. 98, no. B2, pp. 1759–1775, 1993.

[124] A. Abubakar and T. M. Habashy, "A green function formulation of the extended born approximation for three-dimensional electromagnetic modelling," Wave Motion, vol. 41, pp. 211–227, 2005.

[125] R. E. Kleinman and P. M. van den Berg, "A modified gradient method for two-dimensional problems in tomography," J. Comput. Applied Math., vol. 42, pp. 17–35, 1992.

[126] ——, "Two-dimensional location and shape reconstruction," Radio Sci., vol. 29, no. 4, pp. 1157–1169, 1994.

[127] M. Lambert, D. Lesselier, and B. J. Kooij, "The retrieval of a buried cylindrical obstacle by a constrained modified gradient method in the h-polarization case and for maxwellian materials," Inv. Probl., vol. 14, no. 5, p. 1265, 1998.

[128] R. Kleinman and P. M. van den Berg, "A contrast source inversion method," Inv. Probl., vol. 13, pp. 1607–1620, 1997.

[129] T. Isernia, L. Crocco, and M. D'Urso, "New tools and series for forward and inverse scattering problems in lossy media," IEEE Geosci. Remote Sens. Lett., vol. 1, no. 4, pp. 327–331, Oct. 2004.

[130] L. Crocco, M. D'Urso, and T. Isernia, "Testing the contrast source extended born inversion method against real data: the tm case," Inv. Probl., vol. 21, no. 6, p. S33, 2005.

[131] I. Catapano, L. Crocco, M. D'Urso, and T. Isernia, "A novel effective model for solving 3-d nonlinear inverse scattering problems in lossy scenarios," IEEE Geosci. Remote Sens. Lett., vol. 3, no. 3, pp. 302–306, 2006.

[132] A. Abubakar and P. M. van den Berg, "Total variation as a multiplicative constraint for solving inverse problems," IEEE Trans. Image Process., vol. 10, no. 9, pp. 1384–1392, Sep. 2001.

[133] P. M. van den Berg and A. Abubakar, "Contrast source inversion method: state of art," Progress Electromagn. Res., vol. 34, pp. 189–218, 2001.

[134] A. Abubakar, P. M. van den Berg, and T. M. Habashy, "Application of the multiplicative regularized contrast source inversion method on tm- and te-polarized experimental fresnel data," Inv. Probl., vol. 21, no. 6, p. S5, 2005.

[135] P.-A. Barrière, J. Idier, J.-J. Laurin, and Y. Goussard, "Contrast source inversion method applied to relatively high contrast objects," Inverse Problems, vol. 27, no. 7, p. 075012, 2011. [Online]. Available: http://stacks.iop.org/0266-5611/27/i=7/a=075012

[136] H. Carfantan and A. Mohammad-Djafari, "A bayesian approach for nonlinear inverse scattering tomographic imaging," in Internation Conference on Acoustics, Speech, and Signal Processing, ICASSP-95, vol. 4, Detroit, MI, USA, May 1995, pp. 2311 – 2314.

[137] A. Baussard, D. Prémel, and O. Venard, "A bayesian approach for solving inverse scattering from microwave laboratory-controlled data," Inv. Probl., vol. 17, no. 6, pp. 1659–1669, 2001.

[138] Y. J. Yu, B. Krishnapuram, and L. Carin, "Inverse scattering with sparse bayesian vector regression," Inv. Probl., vol. 20, no. 6, pp. S217–S231, Dec. 2004.

[139] O. Féron, B. Duchêne, and A. Mohammad-Djafari, "Microwave imaging of inhomogeneous objects made of a finite number of dielectric and conductive materials from experimental data," Inv. Probl., vol. 21, no. 6, pp. S95–S115, 2005.

[140] C. Eyraud, A. Litman, A. Hérique, and W. Kofman, "Microwave imaging from experimental data within a bayesian framework with realistic random noise," Inv. Probl., vol. 25, no. 2, p. 024005, Feb. 2009.

[141] A. G. Tijhuis, K. Belkebir, A. C. S. Litman, and B. P. de Hon, "Theoretical and computational aspects of 2-d inverse profiling," IEEE Trans. Geosci. Remote Sens., vol. 39, no. 6, pp. 1316–1330, 2001.

[142] A. Dubois, "Étude de l'intéraction d'une onde électromagnétique avec une structure matérielle en régime temporel : problèmes directs et inverses," Ph.D. dissertation, Université Paul Cezanne Aix-Marseille III, 2005.

[143] A. J. Devaney and E. Wolf, "Radiating and nonradiating classical current distributions and the fields they generate," Phys. Rev. D, vol. 8, pp. 1044–1073, 1973.

[144] A. J. Devaney and G. C. Sherman, "Nonuniqueness in inverse source and scattering problems," IEEE Trans. Antennas Propag., vol. 30, no. 5, pp. 1034–1037, Sep. 1982.

[145] W. C. Chew and J. H. Lin, "A frequency-hopping approach for microwave imaging of large inhomogeneous bodies," IEEE Microw. Guid. Wave Lett., vol. 5, pp. 439–441, 1995.

[146] A. Dubois, K. Belkebir, and M. Saillard, "Retrieval of inhomogeneous targets from experimental frequency diversity data," Inv. Probl., vol. 21, no. 6, pp. S65–S79, Dec. 2005.

[147] A. Dubois, K. Belkebir, I. Catapano, and M. Saillard, "Iterative solution of the electromagnetic inverse scattering problem from the transient scattered field," Radio Sci., vol. 44, p. RS1007, 2009.

[148] A. van den Bos, "Complex gradient and hessian," IEE Proc.-Vis. Image Signal Process., vol. 141, no. 6, pp. 380–382, Dec. 1994.

[149] H. Li and T. Adali, "Complex-valued adaptive signal processing using nonlinear functions," EURASIP J. Adv. Signal Process., vol. 2008, 2008.

[150] W. H. Press, S. A. Teukolsky, W. T. Vetterling, and B. P. Flannery, Numerical Recipes in Fortran 90, 2nd ed. Cambridge University Press, 1996, vol. 2, ch. 10, pp. 402–408.

[151] J. Nocedal and S. J. Wright, Numerical optimization. New York, NY: Springer Verlag, 1999.

[152] P.-A. Barrière, J. Idier, Y. Goussard, and J.-J.Laurin, "On algorithms based on joint estimation of currents and contrast in microwave tomography," IRCCyN-EPM, Tech. Rep., Sep. 2008, http://arxiv.org/abs/0901.4723v1.

[153] I. Catapano, L. Crocco, M. D'Urso, and T. Isernia, "3D microwave imaging via preliminary support reconstruction: testing on the fresnel 2008 database," Inv. Probl., vol. 25, p. 0240002, 2009.

[154] X. Chen, "Application of signal-subspace and optimization methods in reconstructing extended scatterers," J. Acoust. Soc. Am. A, vol. 26, pp. 1022–1026, 2009.

[155] ——, "Subspace-based optimization method for solving inverse-scattering problems," IEEE Trans. Geosci. Remote Sens., vol. 48, no. 1, pp. 42–49, jan 2010.

[156] ——, "Subspace-based optimization method for inverse scattering problems with an inhomogeneous background medium," Inv. Probl., vol. 26, p. 074007, 2010.

[157] D. Colton and R. Kress, Inverse Acoustic and Electromagnetic Scattering Theory. Springer, Berlin, 1998, ch. 5, p. 133.

[158] A. Aubry and A. Derode, "Detection and imaging in a random medium: A matrix method to overcome multiple scattering and aberration," J. Appl. Phys., vol. 106, no. 4, p. 044903, 2009. [Online]. Available: http://link.aip.org/link/?JAP/106/044903/1

[159] A. Abubakar, P. M. van den Berg, and J. J. Mallorqui, "Imaging of biomedical data using a multiplicative regularized contrast source inversion method," IEEE Trans. Microwave Theory Tech., vol. 50, no. 7, pp. 1761–1771, Jul. 2002.

Appendices

Appendix A

Driving VNA and PIC from Matlab

Using the Instrument Control Toolbox, Matlab drives both the VNA and the PIC.

A.1 VNA

The chosen physical interface is the Ethernet cable. The following software tools must be installed in a Windows OS environment in order to set up and use the connection:

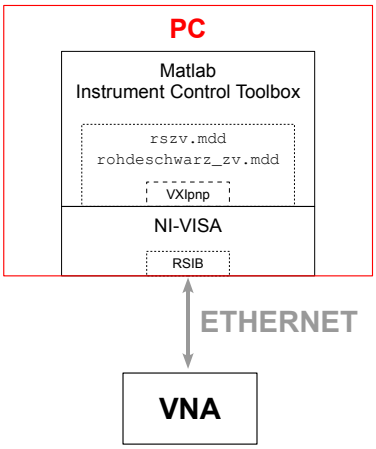

Figure A.1: *Simplified schematization of the way the PC communicates with the VNA.*

- National Instruments (NI) Virtual Instrument Software Architecture (VISA). It is an application programming interface (API) between instruments and development environments that supports interfaces such as GPIB, RS-232, USB (from version 3.0). It was created to be able to drive different vendor's instruments, independently from the physical interface and from the operating system, by using a common set of low-level I/O commands.
- Rohde & Schwarz RSIB passport. To use an Ethernet connection Rohde & Schwarz has its own protocol, based on TCP/IP, called RSIB; installing the passport allows VISA to recognize and communicate with Rohde & Schwarz RSIB instruments.

- VXIplug&play driver. This is a standardized driver, which mainly merges the low-level I/O commands available in NI-VISA to higher-level commands, thus further simplifying the control of instruments. Matlab's Instrument Control Toolobox supports this driver and the communication is based upon it.
- Matlab Instrument Control Toolobox `rszv.mdd` or `rohdeschwarz_zv.mdd`. These files, made available in the Matlab Central database, implement a yet higher-level VXIplug&play-based driver specific to Rohde & Schwarz ZV Network Analyzers. Using this driver, allows one to issue extremely simple commands within Matlab.

The whole scheme is sketched in Fig. A.1.

A.2 PIC microcontroller

The microcontroller is the PIC18F4550 from Microchip. It has been chosen because it is available with a development card, the PICDEM FS USB board, which greatly eases the development of applications based on a USB interface. In fact, Microchip also delivers a set of firmware code that can be used as a basis to develop the firmware for its own application. This firmware is written in a special version of C language enriched with the possibility of typing directly assembly lines, useful for instance to directly address physical memory locations. To develop and use its own firmware application, one needs to install:

- PICDEM FS USB board software. It is the software delivered with the board; it includes the graphical interface to download the firmware into the PIC and a demo application interface.
- MPLAB Integrated Development Environment (IDE). It is the PIC programming environment where one can write the firmware code, compile it, debug it, etc.
- Microchip C18 (MCC18) compiler. It is the C compiler specific to PIC's microcontrollers of the 18F family.

At the time the board was installed and developed, Microchip proposed firmwares for three USB classes: Communications Device Class (CDC), Human Interface Device (HID) and Mass Storage. In addition, a "raw" firmware was available, not belonging to any USB class. Two solutions were then available: either developing a USB Test and Measurement Control (TMC)-compliant firmware starting from the "raw" code, or using the available CDC firmware emulating a serial COM device. The first possibility is motivated by the fact that Matlab recognizes the TMC USB class (and only that) using the VISA standard; nevertheless, developing such a firmware would have been quite time-consuming since a deep knowledge (and implementation) of the USB standard would have been needed. On the other hand, using the serial emulator allows one to completely bypass the USB connection behavior: the board is recognized as a COM device and Matlab natively supports COM devices! The latter has thus been the simplest choice.

A.3 About the chosen OS

Finally, apart from the obvious choice of using the Windows OS to drive the instruments (obvious in the sense that all the softwares/drivers are delivered only for Windows), adopting Linux and namely the Ubuntu distribution was a tempting idea as well. The reasons why it was abandoned were mainly related to the control of the VNA, since very little information on the drivers were available at the time. I had even contacted Rohde & Schwarz for a Linux version of the RSIB passport, but they only supported Red Hat and Suse distributions (not Debian-based as Ubuntu). Concerning the PIC, MPLAB was not available at the time (I see today it is), nor was the PICDEM FS USB board software. Nevertheless some informations are today available on the Internet on how to use native Linux libraries and unofficial packages to make it to use the evaluation board (but I never tried it).

Appendix B

Resolution analysis

The resolution analysis for some of the methods described in §2 are carried out, with reference to the 3D setup in FIG. B.1, under the following hypotheses:

1. emitting and receiving antennas are infinitesimal dipoles (point sources/receivers);
2. the target is a point, located at $\vec{r}^* = (0, F)$, so that its scattering is described by a single constant coefficient $S_0(\omega) = S_0$;
3. the target is in far-field with respect to the array, that is, $F \gg D$ and $F \gg \lambda_{\max}$, where $\lambda_{\max}$ is the largest wavelength within the bandwidth used;
4. the target and the antennas lie in the same plane at $z = 0$.

Furthermore, a reflection configuration with N antennas is chosen and the frequency band is $[\omega_{\mathrm{m}}\ \omega_{\mathrm{M}}]$; hence, central frequency and bandwidth are, respectively, $\omega_{\mathrm{c}} = \frac{1}{2}(\omega_{\mathrm{m}} + \omega_{\mathrm{M}})$ and $\omega_{\mathrm{bw}} = \omega_{\mathrm{M}} - \omega_{\mathrm{m}}$.

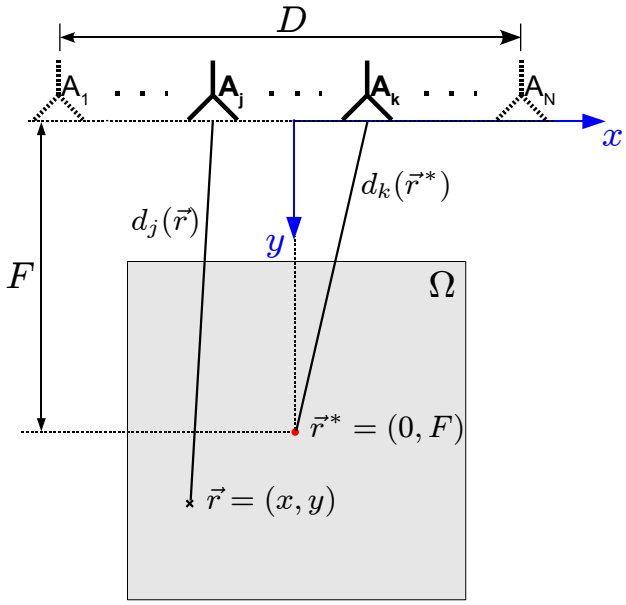

FIGURE B.1: *Configuration for the resolution analysis.*

In this frame, as usually done in literature, two distinct approximations concerning the antenna-investigation point and antenna-target distances $d_i(\vec{r})$ and $d_i(\vec{r}^*)$ (see FIG. B.1),

respectively, are made. For all delay and phase terms, it holds that, for $i = 1, N$,

$$d_i(\vec{r}) = \sqrt{(x_i - x)^2 + y^2} = y\sqrt{1 + \left(\frac{x_i - x}{y}\right)^2} \approx y\left[1 + \frac{1}{2}\left(\frac{x_i - x}{y}\right)^2\right] , \tag{B.1a}$$

and, similarly,

$$d_i(\vec{r}^*) = \sqrt{x_i^2 + F^2} \approx F\left[1 + \frac{1}{2}\left(\frac{x_i}{F}\right)^2\right] , \tag{B.1b}$$

whereas for amplitude factors the simpler approximation

$$d_i(\vec{r}^*) \approx d_i(\vec{r}^*) \approx F \tag{B.2}$$

is used.

B.1 Kirchhoff migration

The continuous approximation of the Kirchhoff migration image given in (2.7) is

$$I^{\mathrm{KM}}(\vec{r}) \approx \left| \int_{-D/2}^{D/2}\!\!\int \tilde{K}_{jk}\left[t_{jk}^d(\vec{r})\right] dx_j dx_k \right|^2 , \tag{B.3}$$

where the integration over the emitted pulse duration $2\delta t$ is removed for simplicity. At any rate, if the pulse length $2\delta t\, c$ is smaller than the resolution lengths found later on, its only effect is to smooth the image (B.3). The arrival time $t_{jk}^d(\vec{r})$ is expressed as the sum of the arrival times relative to each investigation point,

$$t_{jk}^d(\vec{r}) \triangleq t_j + t_k = \frac{d_j(\vec{r})}{c} + \frac{d_k(\vec{r})}{c} . \tag{B.4}$$

Now, the $(j,k)^{\mathrm{th}}$ element of the inter-element matrix $\mathbf{K}(\omega)$, $K_{jk}(\omega)$, can be written as

$$K_{jk}(\omega) = S_0 \frac{e^{-ikd_j(\vec{r}^*)}}{d_j(\vec{r}^*)} \frac{e^{-ikd_k(\vec{r}^*)}}{d_k(\vec{r}^*)} . \tag{B.5}$$

The complex envelope of its Fourier transform is then

$$\begin{aligned} \tilde{K}_{jk}(t) &= \int_{-\infty}^{\infty} K_{jk}(\omega)\, \Pi\left(\frac{\omega - \omega_{\mathrm{c}}}{\omega_{\mathrm{bw}}}\right) e^{i\omega t} d\omega \\ &= \frac{S_0 \omega_{\mathrm{bw}}}{d_j(\vec{r}^*) d_k(\vec{r}^*)}\ \delta\left[t - t_{jk}^{\mathrm{d}}(\vec{r}^*)\right] * \left[\mathrm{sinc}\left(\frac{1}{2}\omega_{\mathrm{bw}} t\right) e^{i\omega_{\mathrm{c}} t}\right] \\ &= \frac{S_0 \omega_{\mathrm{bw}}}{F^2}\ \mathrm{sinc}\left\{\frac{1}{2}\omega_{\mathrm{bw}}\left[t - t_{jk}^{\mathrm{d}}(\vec{r}^*)\right]\right\} e^{i\omega_{\mathrm{c}}\left[t - t_{jk}^{\mathrm{d}}(\vec{r}^*)\right]} , \end{aligned} \tag{B.6}$$

where, by analogy with (B.4), the arrival time $t_{jk}^d(\vec{r}^*)$ is defined as the sum of the antenna-target arrival times,

$$t_{jk}^d(\vec{r}^*) \triangleq \tau_j + \tau_k = \frac{d_j(\vec{r}^*)}{c} + \frac{d_k(\vec{r}^*)}{c} . \tag{B.7}$$

Finally, substituting (B.6) in (B.3), and applying the amplitude approximation (B.2), gives the final formula for the image:

$$I^{\mathrm{KM}}(\vec{r}) \propto \left| \iint_{-D/2}^{D/2} \mathrm{sinc}\left\{ \frac{1}{2}\omega_{\mathrm{bw}} \left[t_{jk}^{\mathrm{d}}(\vec{r}) - t_{jk}^{\mathrm{d}}(\vec{r}^{*}) \right] \right\} e^{i\omega_{\mathrm{c}}\left[t_{jk}^{\mathrm{d}}(\vec{r}) - t_{jk}^{\mathrm{d}}(\vec{r}^{*}) \right]} dx_j dx_k \right|^2 , \tag{B.8}$$

where the amplitude factor $|S_0\omega_{\mathrm{bw}}/F^2|^2$ has been removed for conciseness.

It is now interesting to study separately the resolution in down- and cross-range.

B.1.1 Down-range resolution

In down-range, the investigation domain reduces to a line along y at $x = 0$. The important quantity is the arrival times difference in (B.8), which, after tedious manipulations, becomes

$$t_{jk}^{d}(\vec{r}) - t_{jk}^{d}(\vec{r}^{*}) \approx \left(2 - \frac{1}{2}\frac{x_j^2 + x_k^2}{Fy} \right) \frac{y - F}{c} . \tag{B.9}$$

Eq. (B.8) with (B.9) cannot be solved explicitly unless the far-field hypothesis $F \gg D$ is "pushed to the limit" by observing that for any $(j,k)^{\mathrm{th}}$ term

$$2 \gg \frac{1}{2}\frac{x_j^2 + x_k^2}{Fy} , \tag{B.10}$$

that is, the array aperture has practically no impact on the down-range resolution. This leads to

$$I^{\mathrm{KM}}(y) \propto \left| \iint_{-D/2}^{D/2} \mathrm{sinc}\left[k_{\mathrm{bw}}(y - F) \right] dx_j dx_k \right|^2 = D^4 \mathrm{sinc}^2\left[k_{\mathrm{bw}}(y - F) \right] , \tag{B.11}$$

where k_{bw} and k_{c} represent the wavenumbers associated to ω_{bw} and ω_{c}, respectively. Notice that, apart from the D^4 term, (B.11) gives indeed the same result obtainable with a single measurement instead of with an $N \times N$ matrix. Finally, the image in down-range has a $|\mathrm{sinc}|^2$ profile, and the resolution $R_{\mathrm{dn}}^{\mathrm{KM}}$, that is, the distance between the maximum and the first zero of (B.11), is

$$\boxed{R_{\mathrm{dn}}^{\mathrm{KM}} \approx \frac{\lambda_{\mathrm{bw}}}{2}} . \tag{B.12}$$

B.1.2 Cross-range resolution

An image along x with $y = F$ must now be constructed. Again after some calculations,

$$t_{jk}^{d}(\vec{r}) - t_{jk}^{d}(\vec{r}^{*}) \approx \frac{x - x_j - x_k}{F}\frac{x}{c} , \tag{B.13}$$

and the result is

$$I^{\mathrm{KM}}(x) \propto \left| \iint_{-D/2}^{D/2} \mathrm{sinc}\left[\frac{1}{2}k_{\mathrm{bw}}\frac{x(x-x_j-x_k)}{F}\right] e^{ik_{\mathrm{c}}\frac{x(x-x_j-x_k)}{F}} dx_j dx_k \right|^2 . \tag{B.14}$$

In a general frame, this expression cannot be simplified anymore, since the role of the array aperture D is here fundamental. The cross-range resolution $R_{\mathrm{x}}^{\mathrm{KM}}$ is then a function of D, F, and both k_{bw} and k_{c}.

Nevertheless, if $\omega_{\mathrm{bw}} < \omega_{\mathrm{c}}$, it is possible to neglect the 'sinc' term in (B.14), since it oscillates with a frequency proportional to $1/2\,\omega_{\mathrm{bw}}$ whereas the 'exp' term oscillates at ω_{c} (in addition the 'sinc' function decreases slowlier than a simple 'sin' function for small arguments). Under this approximation, the following closed-form result is reached:

$$I^{\mathrm{KM}}(x) \approx \left| \iint_{-D/2}^{D/2} e^{ik_{\mathrm{c}}\frac{x(x-x_j-x_k)}{F}} dx_j dx_k \right|^2 = D^4 \mathrm{sinc}^4\left(k_{\mathrm{c}}\frac{xD}{2F}\right) , \tag{B.15}$$

giving the approximated down-range resolution

$$\boxed{R_{\mathrm{x}}^{\mathrm{KM}} \approx \frac{\lambda_{\mathrm{c}} F}{D}}_{\omega_{\mathrm{bw}}<\omega_{\mathrm{c}}} . \tag{B.16}$$

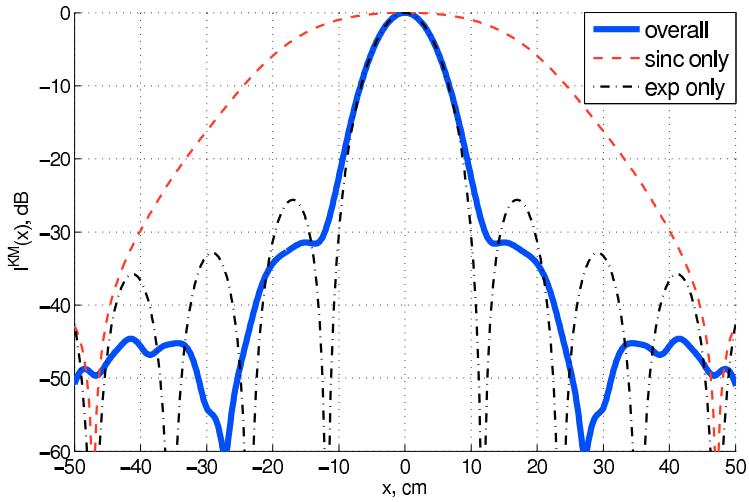

Figure B.2: *Cross-range resolution for the configuration parameters in (B.17).*

This result is well confirmed for a typical experimental configuration among those used in this manuscript. For instance, the one used in Fig. 2.8(a) has the following parameters:

$$\begin{cases} N = 8 \\ D = 37.1 \text{ cm} \\ F = 50 \text{ cm} \\ \omega_{\mathrm{bw}} = 2 \text{ GHz} \\ \omega_{\mathrm{c}} = 3 \text{ GHz} \end{cases} \tag{B.17}$$

The resolution profile is plotted in FIG. B.2, where the results for the 'sinc' and the 'exp' components separately are also presented. Indeed, the overall profile is dominated by the latter contribution, so that the resolution (at least at -30 dB) mainly depends on ω_c and equals about 13 cm ($\approx \lambda_c F/D$). A larger bandwidth increases the impact of the 'sinc' contribution, until for the limit case $\omega_{bw} = 2\omega_c$, it almost becomes the dominant one.

B.2 Time reversal or time-domain DORT

In Time Reversal, the array back-propagates the phase-conjugate of the received signal coherently at all the frequencies within the used bandwidth. For a point target, this corresponds to the time-domain DORT field chart (2.27), where the first singular vector $\mathbf{v}_1(\omega) = \hat{\mathbf{G}}^*(\omega; \vec{r}^*)$ is used.

Two possible imaging approaches based on DORT are studied here. The first (2.27) consists in the back-propagation of the time-domain singular vector associated to the target. A second strategy is inspired from the frequency-coherent TR-MUSIC method (2.42)-(2.43), where the focusing singular space must be used in spite of the noise subspace. It is presented here because interesting indications on the behavior of TR-MUSIC can be extracted from its analysis. In both cases, to proceed, the normalization of the Green function vectors as well as the $i\omega$ term are neglected. For the latter, the assumption of a not too large ω_{bw}/ω_c ratio (exactly as in §B.3) is implicitly made.

1. As just stated, the first solution (2.27) consists in steering the array with $\mathcal{F}^{-1}\left[\mathbf{v}_1(\omega)\right](t)$ and, from the resulting "movie" describing the propagation of the back-propagated wave, extracting the frame corresponding to the focusing instant t^{foc}. The choice of t^{foc} is linked in §2.3.3.2 to the SVD phase indetermination issue, which makes it impossible to predict the exact focusing instant. For simplicity, such issue is here assumed as solved, giving $t^{foc} = 0$, which is by the way the principle of Time Reversal. Then, the continuous version of (2.27) becomes

$$I^{DORT}(\vec{r}) \approx \left| \int_{-D/2}^{D/2} \mathcal{D}_1(t^{foc} = 0; \vec{r}) dx_j \right|^2 , \tag{B.18}$$

with

$$\begin{aligned}
\mathcal{D}_1(t; \vec{r}) &= \int_{-\infty}^{\infty} |S_0|^2 G^*(\omega; \vec{r}^*, \vec{r}_j) G(\omega; \vec{r}, \vec{r}_j) \, \Pi\left(\frac{\omega - \omega_c}{\omega_{bw}}\right) e^{i\omega t} d\omega \\
&= |S_0|^2 \int_{-\infty}^{\infty} \frac{e^{ikd_j(\vec{r}^*)}}{d_j(\vec{r}^*)} \frac{e^{-ikd_j(\vec{r})}}{d_j(\vec{r})} \, \Pi\left(\frac{\omega - \omega_c}{\omega_{bw}}\right) e^{i\omega t} d\omega \\
&= \frac{|S_0|^2 \omega_{bw}}{d_j(\vec{r}^*) d_j(\vec{r})} \; \delta\left[t - t_j^d(\vec{r}, \vec{r}^*)\right] * \left[\mathrm{sinc}\left(\frac{1}{2}\omega_{bw} t\right) e^{i\omega_c t}\right] \\
&\approx \frac{|S_0|^2 \omega_{bw}}{F^2} \; \mathrm{sinc}\left\{\frac{1}{2}\omega_{bw}\left[t - t_j^d(\vec{r}, \vec{r}^*)\right]\right\} e^{i\omega_c\left[t - t_j^d(\vec{r}, \vec{r}^*)\right]} ,
\end{aligned} \tag{B.19}$$

and where

$$t_j^{\mathrm{d}}(\vec{r},\vec{r}^{\,*}) \triangleq t_j - \tau_j = \frac{d_j(\vec{r})}{c} - \frac{d_j(\vec{r}^{\,*})}{c} \ . \tag{B.20}$$

As for Kirchhoff migration, the integration over the pulse duration has been removed for simplicity. Finally, substituting (B.19) in (B.18) gives

$$I^{\mathrm{DORT}}(\vec{r}) \propto \left| \int_{-D/2}^{D/2} \mathrm{sinc}\left[\frac{1}{2}\omega_{\mathrm{bw}} t_j^{\mathrm{d}}(\vec{r},\vec{r}^{\,AT\,*})\right] e^{-i\omega_{\mathrm{c}} t_j^{\mathrm{d}}(\vec{r},\vec{r}^{\,*})} dx_j \right|^2 \ . \tag{B.21}$$

2. The second solution (2.42)-(2.43), which has the advantage of naturally solving the SVD phase indetermination issue, is based on the concept of arrival time, similarly to Kirchhoff migration:

$$I^{\mathrm{DORT-AT}}(\vec{r}) \approx \left| \iint_{-D/2}^{D/2} \mathcal{D}_2\left[t_k^{\mathrm{d}}(\vec{r});\vec{r}\right] dx_j dx_k \right|^2 \ , \tag{B.22}$$

where the k^{th} antenna arrival time is

$$t_k^{\mathrm{d}}(\vec{r}) \triangleq t_k = \frac{d_k(\vec{r})}{c} \ . \tag{B.23}$$

The integrand of (B.22) writes as

$$\begin{aligned}
\mathcal{D}_2(t;\vec{r}) &= \int_{-\infty}^{\infty} |S_0|^2 G^*(\omega;\vec{r}^{\,*},\vec{r}_j) G(\omega;\vec{r},\vec{r}_j) G(\omega;\vec{r}^{\,*},\vec{r}_k)\, \Pi\left(\frac{\omega-\omega_{\mathrm{c}}}{\omega_{\mathrm{bw}}}\right) e^{i\omega t} d\omega \\
&= |S_0|^2 \int_{-\infty}^{\infty} \frac{e^{ikd_j(\vec{r}^{\,*})}}{d_j(\vec{r}^{\,*})} \frac{e^{-ikd_j(\vec{r})}}{d_j(\vec{r})} \frac{e^{-ikd_k(\vec{r}^{\,*})}}{d_j(\vec{r}^{\,*})}\, \Pi\left(\frac{\omega-\omega_{\mathrm{c}}}{\omega_{\mathrm{bw}}}\right) e^{i\omega t} d\omega \\
&= \frac{|S_0|^2 \omega_{\mathrm{bw}}}{d_j(\vec{r}^{\,*}) d_j(\vec{r}) d_k(\vec{r}^{\,*})}\ \delta\left[t - t_{jjk}^{\mathrm{d}}(\vec{r},\vec{r}^{\,*})\right] * \left[\mathrm{sinc}\left(\frac{1}{2}\omega_{\mathrm{bw}} t\right) e^{i\omega_{\mathrm{c}} t}\right] \\
&= \frac{|S_0|^2 \omega_{\mathrm{bw}}}{d_j(\vec{r}^{\,*}) d_j(\vec{r}) d_k(\vec{r}^{\,*})}\ \mathrm{sinc}\left\{\frac{1}{2}\omega_{\mathrm{bw}}\left[t - t_{jjk}^{\mathrm{d}}(\vec{r},\vec{r}^{\,*})\right]\right\} e^{i\omega_{\mathrm{c}}\left[t - t_{jjk}^{\mathrm{d}}(\vec{r},\vec{r}^{\,*})\right]} \ ,
\end{aligned} \tag{B.24}$$

where now

$$t_{jjk}^{\mathrm{d}}(\vec{r},\vec{r}^{\,*}) \triangleq t_j - (\tau_j - \tau_k) = \frac{d_j(\vec{r})}{c} - \left[\frac{d_j(\vec{r}^{\,*})}{c} - \frac{d_k(\vec{r}^{\,*})}{c}\right] \ . \tag{B.25}$$

The final image is then

$$I^{\mathrm{DORT-AT}}(\vec{r}) \propto \left| \iint_{-D/2}^{D/2} \mathrm{sinc}\left\{\frac{1}{2}\omega_{\mathrm{bw}}\left[t_k^{\mathrm{d}}(\vec{r}) - t_{jjk}^{\mathrm{d}}(\vec{r},\vec{r}^{\,*})\right]\right\} e^{i\omega_{\mathrm{c}}\left[t_k^{\mathrm{d}}(\vec{r}) - t_{jjk}^{\mathrm{d}}(\vec{r},\vec{r}^{\,*})\right]} dx_j dx_k \right|^2 \ . \tag{B.26}$$

B.2.1 Down-range resolution

For the down-range resolution analysis, $\vec{r} = (0, y)$ and the approximations (B.1) must be applied. A separate derivation for each solution is proposed in the following.

1. Eq. (B.20) becomes
$$t_j^{\mathrm{d}}(\vec{r}, \vec{r}^*) \approx \left(1 - \frac{1}{2}\frac{x_j^2}{Fy}\right)\frac{y - F}{c} \ . \tag{B.27}$$
As for Kirchhoff migration, (B.21) cannot be solved further without completely neglecting the effect of the array aperture. Since indeed
$$1 \gg \frac{1}{2}\frac{x_j^2}{Fy} \ , \tag{B.28}$$
(B.21) simply gives
$$I^{\mathrm{DORT}}(y) \propto D^2 \mathrm{sinc}^2\left[\frac{1}{2}k_{\mathrm{bw}}\left(y - F\right)\right] \ , \tag{B.29}$$
which, again as for Kirchhoff migration, only depends on the frequency bandwidth. The resolution is then
$$\boxed{R_{\mathrm{dn}}^{\mathrm{DORT}} \approx \lambda_{\mathrm{bw}}} \, , \tag{B.30}$$
that is, twice the resolution obtained with the Kirchhoff migration method.

This can be explained since, while DORT consists of beamforming the array either at emission with the right singular vectors $\mathbf{v}_l$, or at reception with the left ones, $\mathbf{u}_l$, Kirchhoff migration is based on beamforming *both* at emission and reception, which indeed halves the resolution. Mathematically, while with DORT focusing occurs when the *single* arrival times difference (B.20) is minimized, for Kirchhoff migration it is the *round-trip* arrival times (B.4) and (B.7) that tend to match at the target location.

2. Although the difference between (B.23) and (B.25) becomes
$$\begin{aligned} t_k^{\mathrm{d}}(\vec{r}) - t_{jjk}^{\mathrm{d}}(\vec{r}, \vec{r}^*) &\approx \left(1 + \frac{1}{2}\frac{x_k^2}{y^2}\right)\frac{y}{c} - \left[\left(1 + \frac{1}{2}\frac{x_j^2}{y^2}\right)\frac{y}{c} - \frac{1}{2}\frac{x_j^2 - x_k^2}{Fc}\right] \\ &= \frac{1}{2}\frac{x_k^2 - x_j^2}{Fy}\frac{F - y}{c} \ , \end{aligned} \tag{B.31}$$
it is again impossible to solve (B.26) when substituting (B.31). Nevertheless, neglecting the array aperture leads now to $t_k^{\mathrm{d}}(\vec{r}) - t_{jjk}^{\mathrm{d}}(\vec{r}, \vec{r}^*) \approx 0$, which leads to an infinitely large resolution in down-range:
$$\boxed{R_{\mathrm{dn}}^{\mathrm{DORT-AT}} \approx \infty} \, . \tag{B.32}$$
Notice also that re-introducing the effect of the array aperture brings $R_{\mathrm{dn}}^{\mathrm{DORT-AT}}$ to a finite, yet very large, value.

Such a poor resolution can easily be explained by the fact that for $I^{\mathrm{DORT-AT}}$ it is a *difference* of arrival times that is matched at the target location. Indeed,

$$t_k^{\mathrm{d}}(\vec{r}) - t_{jjk}^{\mathrm{d}}(\vec{r},\vec{r}^{\,*}) = t_k - t_j - (\tau_k - \tau_j) \ , \tag{B.33}$$

which is clearly near to zero along y since for any $(j,k)^{\mathrm{th}}$ pair the difference is very small.

B.2.2 Cross-range resolution

Again, the two strategies are handled separately imposing $y = F$.

1. The arrival time Eq. (B.20) becomes

$$t_j^{\mathrm{d}}(\vec{r},\vec{r}^{\,*}) \approx \frac{1}{2}\frac{x-2x_j}{F}\frac{x}{c} \ , \tag{B.34}$$

giving

$$I^{\mathrm{DORT}}(x) = \left| \int_{-D/2}^{D/2} \mathrm{sinc}\left[\frac{1}{4}k_{\mathrm{bw}}\frac{x(x-2x_j)}{F}\right] e^{-i\frac{1}{2}k_{\mathrm{c}}\frac{x(x-2x_j)}{F}} dx_j \right|^2 \ . \tag{B.35}$$

The behavior of (B.35) is very similar to the one found for Kirchhoff migration in §B.1.2. The cross-range resolution is in general a function of k_{bw}, k_{c}, D, and F. Nonetheless, if the ratio $\omega_{\mathrm{bw}}/\omega_{\mathrm{c}}$ is relatively small, then, especially for small arguments, the 'sinc' function can be neglected as compared to the 'exp' one. Then,

$$I^{\mathrm{DORT}}(x) \approx \left| \int_{-D/2}^{D/2} e^{-i\frac{1}{2}k_{\mathrm{c}}\frac{x(x-2x_j)}{F}} dx_j \right|^2 = D^2\mathrm{sinc}^2\left(k_{\mathrm{c}}\frac{xD}{2F}\right) \ , \tag{B.36}$$

which gives the well-known cross-range resolution formula

$$\boxed{R_{\mathrm{x}}^{\mathrm{DORT}} \approx \frac{\lambda_{\mathrm{c}}F}{D}}_{\omega_{\mathrm{bw}}<\omega_{\mathrm{c}}} \ , \tag{B.37}$$

exactly as for Kirchhoff migration.

2. A similar result holds for $I^{\mathrm{DORT-AT}}$. In effect, Eq. (B.25) gives

$$t_k^{\mathrm{d}}(\vec{r}) - t_{jjk}^{\mathrm{d}}(\vec{r},\vec{r}^{\,*}) \approx \frac{x_j - x_k}{F}\frac{x}{c} \ , \tag{B.38}$$

so that the final formula becomes

$$I^{\mathrm{DORT-AT}}(x) = \left| \iint_{-D/2}^{D/2} \mathrm{sinc}\left[\frac{1}{2}k_{\mathrm{bw}}\frac{x(x_j-x_k)}{F}\right] e^{-ik_{\mathrm{c}}\frac{x(x_j-x_k)}{F}} dx_j dx_k \right|^2 \ . \tag{B.39}$$

Again, the 'sinc' contribution can be neglected, resulting in

$$I^{\mathrm{DORT-AT}}(x) \approx \left| \iint_{-D/2}^{D/2} e^{-ik_{\mathrm{c}}\frac{x(x_j-x_k)}{F}} dx_j dx_k \right|^2 = D^4 \mathrm{sinc}^4\left(k_{\mathrm{c}}\frac{xD}{2F}\right) , \tag{B.40}$$

whose resolution is slightly better with respect to $I^{\mathrm{DORT}}(x)$ due to the 4^{th} versus the 2^{nd} 'sinc' power. Nonetheless, the distance from the maximum to the first zero of (B.40) is unchanged,

$$\boxed{R_{\mathrm{x}}^{\mathrm{DORT}} \approx \frac{\lambda_{\mathrm{c}} F}{D}}_{\omega_{\mathrm{bw}}<\omega_{\mathrm{c}}} . \tag{B.41}$$

B.3 3D vs. 2D resolution

The analysis carried out in this appendix covers the single-polarization 3D case. Under the 2D frame - wire sources/receivers and cylindrical target - the results are supposed to change. Indeed, the Green function is now the 0^{th}-order Hankel function of the second kind, which, with respect to the 3D case, introduces a $1/\sqrt{k}$ dependency. Thus, (B.5) as well as (B.19) and (B.24) are modified by a $1/k$ or $1/k^{1.5}$ factor.

This factor alters the resolution of the Inverse Fourier Transform (IFT) in (B.6) and (B.19)-(B.24), since their results should be convoluted to $\mathcal{F}^{-1}[1/k](t)$ or $\mathcal{F}^{-1}[1/k^{1.5}](t)$. Although these convolution products do not have closed-form solutions, it is possible to state that, if the operating bandwidth ω_{bw} is sufficiently small, *e.g.* one octave as in the experimental configurations studied in this manuscript, the result is very similar to the 3D one.

Appendix C

Construction of a field chart

Phase Conjugation, DORT or some of the other methods discussed in §2 produce a so-called *field chart*, *i.e.*, the distribution of the electric field $\vec{E}(\omega;\vec{r})$ over a given region when the antenna array is steered with a vector $\mathbf{v}(\omega)$. With reference to an experimental setup, such as the one described in §1, whose raw measurements are S-parameters, that is, voltage- or current-waves ratios, it is clear that feeding the j^{th} antenna with $v_j(\omega)$ actually means setting its feeding *current* $I_{\text{ant}}(\omega)$ to that value.

To build a field chart, it must be therefore possible to express the electric field $\vec{E}(\omega;\vec{r})$ given a current distribution $\vec{J}_{\text{ant}}(\omega;\vec{r})$, $\vec{r}$ being the position within the antenna support. Such current distribution is then the result, hence a function, of the current $I_{\text{ant}}(\omega)$ applied to the antenna. For simplicity, with a time dependency $e^{i\omega t}$, consider an electric dipole whose constitutive equations are

$$\begin{cases} \vec{J}_{\text{ant}}(\omega;\vec{r}) = i\omega\vec{P}_{\text{ant}}(\omega;\vec{r}) \\ \rho_{\text{ant}}(\omega;\vec{r}) = -\vec{\nabla}\cdot\vec{P}_{\text{ant}}(\omega;\vec{r}) \end{cases} , \tag{C.1}$$

where ρ_{ant} is the fictitious charge distribution [95] induced within the antenna support, and $\vec{P}_{\text{ant}}$ the electric moment (or polarization vector) of the dipole. In a 3D frame, the hypotheses used in this manuscript when dealing with synthetic data are

1. infinitesimal dipole, that is, infinitesimally small dipole located at $\vec{r} = \vec{r}_0 = (x_0, y_0, 0)$;
2. dipole oriented along the z-axis;
3. electric field sought at $z = 0$.

In formulae, since the electric moment can be written as

$$\vec{P}_{\text{ant}}(\omega;\vec{r}) = P_{\text{ant}}(\omega)\,\delta(\vec{r}-\vec{r}_0)\hat{z} , \tag{C.2}$$

the current distribution at the antenna becomes

$$\vec{J}_{\text{ant}}(\omega;\vec{r}) = I_{\text{ant}}(\omega)\delta(\vec{r}-\vec{r}_0)\hat{z} . \tag{C.3}$$

and finally

$$I_{\text{ant}}(\omega) = i\omega P_{\text{ant}}(\omega) . \tag{C.4}$$

In a homogeneous, non-magnetic, propagation medium with (possibly complex) relative permittivity ε_r, solving the Maxwell's equations including the source terms in (C.1) for $\vec{E}(\omega;\vec{r})$ leads to

$$\vec{E}(\omega;\vec{r}) = \frac{1}{\varepsilon_0\varepsilon_r}\left[\frac{\partial^2}{\partial x\partial z}\hat{x} + \frac{\partial^2}{\partial y\partial z}\hat{y} + \left(\frac{\partial^2}{\partial z^2} + k^2\right)\hat{z}\right] G(\omega;\vec{r}-\vec{r}_0)P_{\text{ant}}(\omega)\ , \tag{C.5}$$

where $G(\omega;\vec{r})$ is the Green function of the same medium defined in (3.5). The field has therefore three components oriented along the three axes. Nevertheless, since

$$\frac{\partial G(\omega;\vec{r})}{\partial z} = \frac{\partial G(\omega;\vec{r})}{\partial r}\frac{\partial r}{\partial z} = -G(\omega;\vec{r})\left(\frac{ik}{r} + \frac{1}{r^2}\right)z\ , \tag{C.6}$$

where $r = |\vec{r}|$, the first two terms of (C.5) become null on the plan $z = 0$. Concerning the third term, it holds that

$$\frac{\partial^2 G(\omega;\vec{r})}{\partial z^2} = G(\omega;\vec{r})\left[\left(-k^2 + \frac{3ik}{r} + \frac{3}{r^2}\right)\frac{z^2}{r^2} - \left(\frac{ik}{r} + \frac{1}{r^2}\right)\right]\ , \tag{C.7}$$

hence once again the first part of the sum equals zero at $z = 0$.

Recalling (C.4), the final complete expression for the electric field at $z = 0$ is then

$$\boxed{\vec{E}(\omega;\vec{r})|_{z=0} = -i\omega\mu_0\left(1 - \frac{i}{k|\vec{r}-\vec{r}_0|} - \frac{1}{k^2|\vec{r}-\vec{r}_0|^2}\right)G(\omega;\vec{r}-\vec{r}_0)I_{\text{ant}}(\omega)\hat{z}}\ . \tag{C.8}$$

The second and third terms within the $(\cdot)$ are the near-field contributions to the field, which indeed come from the $\partial^2/\partial z^2$ term in (C.5), whereas the first one is the "far-field" component, the former becoming negligeable as soon as $|\vec{r}-\vec{r}_0| \gg \lambda/2\pi$.

In a 2D frame, the infinitesimal dipole must be replaced by an infinitely long wire. The same reasoning holds, except the 3D Green function expression must be replaced by its 2D counterpart based on the 0^{th}-order Hankel function. Since in 2D any $\partial/\partial z$ term is null, the final expression is simply

$$\vec{E}_{\text{2D}}(\omega;\vec{r})|_{z=0} = -i\omega\mu_0 G_{\text{2D}}(\omega;\vec{r}-\vec{r}_0)I_{\text{ant}}(\omega)\hat{z}\ , \tag{C.9}$$

where the near-field contributions are "included" in the behavior of the Hankel function for $k|\vec{r}-\vec{r}_0| \ll \lambda/2\pi$.

Appendix D

Line search and Wolfe's conditions

At each iteration of an iterative function minimizing algorithm (*e.g.* Steepest Descent or Conjugate Gradient), a line search must be performed in order to produce a new estimate of the unknowns. Given a function $\mathcal{F}(\mathbf{x})$ to be minimized, calling $\mathbf{x}_n$ the vector of the variables at iteration n and $\mathbf{d}_n^x$ the vector of the descent directions with respect to each element of $\mathbf{x}_n$, the update rule writes

$$\mathbf{x}_{n+1} = \mathbf{x}_n + \lambda_n \mathbf{d}_{n+1}^x \ . \tag{D.1}$$

The line search, then, consists in finding the value λ_n that minimizes $\mathcal{F}(\mathbf{x}_{n+1})$. Many iterative methods exist for efficiently performing the line search. For any of them, instead of reaching the precision of the machine between two consecutive λ_n, it can be demonstrated that $\mathcal{F}$ will converge onto the same minimum if Wolfe's conditions are used to stop the search. Hence, less iterations are necessary for the line search and the whole minimization is more rapid without any degradation of the result. For the present case, Wolfe's condition write

$$\mathcal{F}(\mathbf{x}_{n+1}) \leq \mathcal{F}(\mathbf{x}_n) + c_1 \lambda_n \left(\mathbf{d}_{n+1}^x\right)^T \mathbf{g}_n^x \tag{D.2a}$$

$$\left|\left(\mathbf{d}_{n+1}^x\right)^T \mathbf{g}_{n+1}^x\right| \leq c_2 \left|\left(\mathbf{d}_{n+1}^x\right)^T \mathbf{g}_n^x\right| \ , \tag{D.2b}$$

where c_1 and c_2 are two empirical parameters set to 10^{-4} and 10^{-1} in [151] for a non-linear CG scheme as those presented in this manuscript in the frame of quantitative inverse scattering. The first condition, also known as Armijo rule, guarantees that the minimum necessary amount of reduction in $\mathcal{F}$ is obtained (remark that $\left(\mathbf{d}_{n+1}^x\right)^T \mathbf{g}_n^x$ is by definition a negative quantity). The second condition, also known as curvature condition or strong Wolfe condition, imposes that the slope of $\mathcal{F}$, which writes $\left(\mathbf{d}_{n+1}^x\right)^T \mathbf{g}_{n+1}^x$, should be small enough to guarantee the convergency of the descent algorithm.

Notice that, while the Armijo rule does not require the computation of any other quantity, the curvature condition requires the evaluation of $\mathbf{g}_{n+1}^x$ each time a new λ_n value is tested ($\mathbf{g}_n^x$ is considered as known since the descent direction $\mathbf{d}_{n+1}^x$ is usually a function of it).